APPLYING ROBOTICS AND AI IN PANDEMICS (COVID-19): DETECTION, DIAGNOSIS AND DELIVERY

EDITED BY: Bin Fang, Hang Su and John Oyekan

PUBLISHED IN: Frontiers in Robotics and AI

frontiers Research Topics

frontiers

ISSN 1664-8714
ISBN 978-2-83250-442-0
DOI 10.3389/978-2-83250-442-0

About Frontiers

Frontiers is more than just an open-access publisher of scholarly articles: it is a pioneering approach to the world of academia, radically improving the way scholarly research is managed. The grand vision of Frontiers is a world where all people have an equal opportunity to seek, share and generate knowledge. Frontiers provides immediate and permanent online open access to all its publications, but this alone is not enough to realize our grand goals.

Frontiers Journal Series

The Frontiers Journal Series is a multi-tier and interdisciplinary set of open-access, online journals, promising a paradigm shift from the current review, selection and dissemination processes in academic publishing. All Frontiers journals are driven by researchers for researchers; therefore, they constitute a service to the scholarly community. At the same time, the Frontiers Journal Series operates on a revolutionary invention, the tiered publishing system, initially addressing specific communities of scholars, and gradually climbing up to broader public understanding, thus serving the interests of the lay society, too.

Dedication to Quality

Each Frontiers article is a landmark of the highest quality, thanks to genuinely collaborative interactions between authors and review editors, who include some of the world's best academicians. Research must be certified by peers before entering a stream of knowledge that may eventually reach the public - and shape society; therefore, Frontiers only applies the most rigorous and unbiased reviews.
Frontiers revolutionizes research publishing by freely delivering the most outstanding research, evaluated with no bias from both the academic and social point of view. By applying the most advanced information technologies, Frontiers is catapulting scholarly publishing into a new generation.

What are Frontiers Research Topics?

Frontiers Research Topics are very popular trademarks of the Frontiers Journals Series: they are collections of at least ten articles, all centered on a particular subject. With their unique mix of varied contributions from Original Research to Review Articles, Frontiers Research Topics unify the most influential researchers, the latest key findings and historical advances in a hot research area! Find out more on how to host your own Frontiers Research Topic or contribute to one as an author by contacting the Frontiers Editorial Office: frontiersin.org/about/contact

APPLYING ROBOTICS AND AI IN PANDEMICS (COVID-19): DETECTION, DIAGNOSIS AND DELIVERY

Topic Editors:
Bin Fang, Tsinghua University, China
Hang Su, Tsinghua University, China
John Oyekan, The University of Sheffield, United Kingdom

Citation: Fang, B., Su, H., Oyekan, J., eds. (2022). Applying Robotics and AI in Pandemics (COVID-19): Detection, Diagnosis and Delivery.
Lausanne: Frontiers Media SA. doi: 10.3389/978-2-83250-442-0

Table of Contents

frontiers | Frontiers in Robotics and AI

TYPE Editorial
PUBLISHED 26 September 2022
DOI 10.3389/frobt.2022.1039273

OPEN ACCESS

EDITED AND REVIEWED BY
Med Amine Laribi,
University of Poitiers, France

*CORRESPONDENCE
Bin Fang,
fangbin@mail.tsinghua.edu.cn

SPECIALTY SECTION
This article was submitted to Biomedical Robotics,
a section of the journal
Frontiers in Robotics and AI

RECEIVED 08 September 2022
ACCEPTED 12 September 2022
PUBLISHED 26 September 2022

CITATION
Fang B, Su H and Oyekan J (2022), Editorial: Applying robotics and AI in pandemics (COVID-19): Detection, diagnosis and delivery.
Front. Robot. AI 9:1039273.
doi: 10.3389/frobt.2022.1039273

Editorial: Applying robotics and AI in pandemics (COVID-19): Detection, diagnosis and delivery

Bin Fang[1]*, Hang Su[1] and John Oyekan[2]

[1]Department of Computer Science and Technology, Tsinghua University, Beijing, China, [2]The Department of Automatic Control and Systems Engineering, The University of Sheffield, Sheffield, United Kingdom

KEYWORDS

autonomous agents, pandemics (COVID-19), detection, infection control, delivery

Editorial on the Research Topic
Applying Robotics and AI in Pandemics (COVID-19): Detection, Diagnosis and Delivery

The COVID-19 pandemic highlighted the fragility of the human response to pandemics on a global scale. First, the airborne transmission of the virus has led to a significant increase in infections. Weak medical systems ineffectively isolate the source of the disease. Second, close contact increases the probability of cross-infection and puts understaffed health workers at risk. In addition, the lack of detection devices limits tracking the health status of people and diagnosing cases in real time. Finally, the strict protection policy has led to a sharp decline in transportation efficiency and shortages of supplies. These factors make COVID-19 have an unprecedented impact on human society.

After 2 years of fighting COVID-19, humans are lessening the virus's influence with robotics and artificial intelligence (AI). Robots make up for the lack of professionals. It has unique advantages in improving work efficiency and blocking virus transmission. For example, temperature detection robots have tracked health status in public places. Telemedicine robots can reduce close interactions between caregivers and infected patients. The COVID-19 throat swab intelligent sampling robot has achieved a single sampling success rate of more than 95%, improving the standardization of biological sample Research Topic and ensuring specimen quality. In this Research Topic, we aim to collect current research around robotics and AI in the pandemic to overcome the challenges preventing wide-scale robotic deployment. Our purpose is to address the feasibility and impact of robotics in COVID-19 diagnosis and detection.

This Research Topic contains nine research articles that present the newest research achievements of robotic applications: four papers focus on detection methods and devices; three papers are on the diagnosis of symptoms or viruses; and the remaining two papers study the delivery of healthcare resources.

The first paper (Zhou et al.) proposes a cough recognition network (CRN) based on the CNN model and a Mel-spectrogram. CRN can achieve excellent performance in cough

recognition compared to other methods. The results of generalization tests show that CRN adapts to cough monitoring in complex scenes in daily life. It is expected to be a potential solution for disease management during the COVID-19 pandemic and to reduce health care workers' exposure.

The second paper (Jumlongku) presents the effectiveness of a new method of using robot-assisted surgery to cut the skull of a cadaver. Compared with the oscillating saw method, the noise level is reduced. It also limits the release of aerosol particles to levels similar to those of ordinary autopsy procedures. This method reduces fine infectious dust particles, especially during the COVID-19 pandemic.

The third paper (Al-Zogbi et al.) proposes an autonomous robotic solution enabling POCUS scanning of COVID-19 patients' lungs for diagnosis and staging. Under a CT scan, an algorithm is developed to estimate the optimal position and orientation of a US probe on a patient to image target points in the lungs. Without CT data, a deep learning algorithm can predict the 3D landmark positions of a ribcage given a torso surface model. The results demonstrate the preliminary feasibility of the system and its potential for offering a solution to help mitigate the spread of COVID-19 in vulnerable environments.

The fourth paper (McGinn et al.) presents the design of a robotic UVGI platform. It can be deployed alongside human workers and operate autonomously within cramped rooms. The results show that UVGI can effectively inactivate germs on commonly touched surfaces in radiology suites. Despite the short irradiation period, UVGI can inactivate microbes with more complex cell structures, thus indicating a high likelihood of effectiveness against COVID-19.

The fifth paper (Jumlongkul and Chutivongse) proposes an AMBU ventilator consisting of an automated AMBU bag ventilator, a negative pressure head box, and a transporting capsule. It allows the initial setting of the preliminary flow rate, rhythm, and volume of oxygen during the intubation period to protect medical colleagues from potential erosol infection. It is expected to block airborne transmission of COVID-19 viruses during the procedure.

The sixth paper (Akbari et al.) proposes a robot-assisted system that automatically scans tissue to enable isolation between patients and sonographers during the COVID-19 pandemic. This system automatically scans the tissue using a dexterous robot arm that holds the US probe and assesses the quality of the acquired US images in real time. According to the quality assessment algorithm, this system successfully maintains US image quality and is fast enough for use in a robotic control loop.

The seventh paper (Cheng and Tavakoli) reviewed applications requiring physiological organ motion compensation in the medical telerobotic system. Physical distancing restrictions cause significant effects on the delivery of physical healthcare procedures worldwide to limit the spread and transmission of the novel coronavirus. Medical telerobotic systems can play a positive role in the provision of telemedicine. This paper focuses on control-theoretic approaches to outline possible future directions of telerobotic systems in COVID-19 healthcare.

The eighth paper (Grimshaw and Oyekan) proposes a cable-driven parallel manipulator (CDPM) to balance an unstable load, a ball plate system. It consists of eight cables attached to the end effector plate. The hardware includes a reinforcement-learning trained neural network controller and nested PID controller to output the desired platform response. During the COVID-19 pandemic, this robotic device can reduce workers' exposure.

The ninth paper (Cheung et al.) surveys the available army doctrine of healthcare missions. The proposed framework adopts metrics of spacing error, separation distance, and string stability to compare the performance of autonomous convoys. According to hierarchical decision-making, this paper argues for using nonlinear battlefield techniques for delivering healthcare logistics to remote pandemic outbreak areas.

These nine articles are strictly selected based on many submissions. We hope that the discussion of recent advances in this area can promote an understanding of how robotics and AI can be used to diagnose and detect COVID-19 and provide a framework for how we can integrate smart systems to reduce pressure on healthcare systems during current and future pandemics.

Author contributions

BF writes the manuscript, JO and HS helped improve the paper.

Conflict of interest

The authors declare that the research was conducted in the absence of any commercial or financial relationships that could be construed as a potential conflict of interest.

Publisher's note

frontiers in Robotics and AI

MINI REVIEW
published: 09 November 2020
doi: 10.3389/frobt.2020.594673

COVID-19 Pandemic Spurs Medical Telerobotic Systems: A Survey of Applications Requiring Physiological Organ Motion Compensation

Lingbo Cheng[1,2] *and Mahdi Tavakoli*[2]*

[1] College of Control Science and Engineering, Zhejiang University, Hangzhou, China, [2] Department of Electrical and Computer Engineering, University of Alberta, Edmonton, AB, Canada

The coronavirus disease 2019 (COVID-19) pandemic has resulted in public health interventions such as physical distancing restrictions to limit the spread and transmission of the novel coronavirus, causing significant effects on the delivery of physical healthcare procedures worldwide. The unprecedented pandemic spurs strong demand for intelligent robotic systems in healthcare. In particular, medical telerobotic systems can play a positive role in the provision of telemedicine to both COVID-19 and non-COVID-19 patients. Different from typical studies on medical teleoperation that consider problems such as time delay and information loss in long-distance communication, this survey addresses the consequences of physiological organ motion when using teleoperation systems to create physical distancing between clinicians and patients in the COVID-19 era. We focus on the control-theoretic approaches that have been developed to address inherent robot control issues associated with organ motion. The state-of-the-art telerobotic systems and their applications in COVID-19 healthcare delivery are reviewed, and possible future directions are outlined.

Keywords: COVID-19, healthcare, physical distancing, teleoperation, telerobotics, telemedicine, motion compensation, robot control

OPEN ACCESS

Edited by:
Bin Fang,
Tsinghua University, China

Reviewed by:
Haiyuan Li,
Beijing University of Posts and Telecommunications (BUPT), China
Zhen Deng,
University of Hamburg, Germany

***Correspondence:**
Mahdi Tavakoli
mahdi.tavakoli@ualberta.ca

Specialty section:
This article was submitted to Biomedical Robotics, a section of the journal Frontiers in Robotics and AI

Received: *14 August 2020*
Accepted: *14 October 2020*
Published: *09 November 2020*

Citation:
Cheng L and Tavakoli M (2020) COVID-19 Pandemic Spurs Medical Telerobotic Systems: A Survey of Applications Requiring Physiological Organ Motion Compensation. Front. Robot. AI 7:594673. doi: 10.3389/frobt.2020.594673

INTRODUCTION

On January 30, 2020, the World Health Organization (WHO) officially declared the coronavirus disease 2019 (COVID-19) outbreak as a public health emergency of international concern (World Health Organization, 2020). Subsequently, the COVID-19 was assessed by WHO as a pandemic. The pandemic resulted in public health interventions to limit the spread and transmission of the novel coronavirus, causing significant effects on the delivery of physical healthcare procedures worldwide. For instance, to slow the spread of disease by stopping chains of transmission of COVID-19 and preventing new ones from appearing, social and physical distancing measures are strongly recommended globally, which resulted in dramatic reductions of in-person visits of patients to clinics or professionals. As this unprecedented crisis is likely to last for a long time and will possibly have multiple waves until a vaccine is available, rapidly seeking and developing a global solution to address this issue (i.e., physical distancing restrictions) will build confidence in delivering healthcare services either remotely or in-person while observing physical distancing.

Intelligent robotic systems, especially telerobotic systems, can play a positive role in this pandemic as they can effectively improve the *fully remote* or *physical distancing-aware* healthcare

procedures (Tavakoli et al., 2020). Specifically, robotic and telerobotic systems can significantly reduce the risk of infectious disease transmission to frontline healthcare workers by providing a way to triage, evaluate, monitor, and treat patients from a safe distance. Moreover, medical robots have inherent advantages including steady-hand, accuracy, motion scaling, and biomotion compensation, which lead them to be able to provide general support for patients and medical professionals and further alleviate the non-COVID-19 burden placed on healthcare systems during this crisis. In fact, given the growing demands for remote-based healthcare services in the age of COVID-19, a motivation to urgently develop and apply technologies for robotics-assisted surgery has emerged. Inspired by the abovementioned points, this paper focuses on a survey addressing the subject of teleoperation on medical applications.

Teleoperation naturally indicates operating at a distance, which can perfectly meet the requirements of fully remote or in-person distancing-aware healthcare services during the COVID-19 pandemic. Meanwhile, a medical telerobotic system is capable of extending the human capabilities such as the facilitation of motion and/or force scaling, offering advantages in minimally invasive surgery including repeatability, accuracy, dexterity, fine manipulation, etc. In a general single-master/single-slave medical telerobotic system, the human applies a force on the master consoler, which results in movement commands transmitted to the slave manipulator that in turn mimics the human's operations.

Designing a teleoperation system requires addressing many issues concerning sensors and actuators, communication media, time-delay problem, stability, and transparency. Most of the relevant work and surveys focused on teleoperation, which is assumed to include a stable environment on the slave site, aiming for perfect transparency, system stability, and solving time-delay-induced problems (Hokayem and Spong, 2006; Passenberg et al., 2010). However, a survey addressing problems for teleoperation with a moving environment is seldom studied. Differing from the most researched issues such as time-delay, stability, and transparency, the most critical problem for teleoperation with a moving environment is to synchronize the slave robot's motion with the movement of the object (the environment) so that the automatic robotic motion compensations can be deployed instead of manual ones by the human operators.

A typical application of teleoperation in the medical area is manipulating with physiological organ motion caused by cardiac and respiratory activity. The cardiac motion has important local effects on the heart and areas proximal to the heart. Respiratory motion affects the movement for the majority of the body, from the thorax to the abdomen (including heart, lungs, liver, pancreas, and kidneys), and from inside to outside (such as chest and breast) of the body. It has been reported that organ displacements may range from 10 to 40 mm in anterior–posterior, left–right, and superior–inferior directions during normal breathing (Keall et al., 2006). The physiological organ motion has significant effects on medical procedures such as (i) inside or outside moving-organ surgeries (the surgeon has to manually compensate for the organ motion), (ii) moving-organ evaluation (the ability to define accurate target volumes in radiation oncology is difficult), and (iii) image-based diagnosis and monitoring (image quality and quantitative accuracy are highly effected) (Uchinami et al., 2019). When the telerobotic systems (Ballantyne, 2002) are used for the applications requiring automatic organ motion compensation, the current medical performance may need to be improved.

Among many medical telerobotic systems (Avgousti et al., 2016; Evans et al., 2018), da Vinci® robot (Intuitive Surgical Inc.) is currently the most widespread robotic surgical system, which not only can be used for teleoperation over remote distance but also can perform a variety of surgeries, evaluations, diagnosis, and monitoring. Those functionalities involve scaling the operator's actions over a small distance and with a negligible communication delay. Experimentally, the communication delay will be kept within 5–10 ms, and the effects caused by communication delay is trivial and can be negligible. In the short-distance applications, the master console and the slave manipulators are generally placed in the same operating room or different operating rooms in the same clinic; the time-delay problem, therefore, is trivial and negligible.

In this paper, we narrow down the teleoperation systems to short-distance medical telerobotics with applications accompanied by physiological organ motion, and mainly focus on the issue of motion compensation. The aim of this survey is to present the state of the art of the medical telerobotic systems with applications requiring motion compensation and the related control strategies. The rest of the paper is organized as follows. Section Teleoperation for Organ Motion Compensation deals with the control strategies of robotic-assisted systems with an emphasis on the control for automatic motion compensation. Section Applications focuses on clinical applications with telerobotic systems and solutions to effectively deliver healthcare services during the COVID-19 pandemic. Section Discussions and Future Directions discusses the perspectives of future work and concludes the paper.

TELEOPERATION FOR ORGAN MOTION COMPENSATION

The mission of advancing medical telerobotic systems is to boost medicine performance by improving patient care, expanding access to high-quality therapy, and enhancing physician education, safety, and efficiency. For medical telerobotic systems with physiological organ motion such as respiratory and heartbeat motion, to minimize the risks of tool-tissue collision and tissue injury, an idea of automatic synchronization of the movement of robotic manipulator's end-tip with the moving organ is proposed. This inspires the development of telerobotic systems to provide compensation for the physiological organ motion to assist the human in performing operations accurately and safely. Indeed, if the robotic system can move a surgical instrument (e.g., catheter, ultrasound probe, forceps) in synchrony with the target tissue while the organ moves, it can provide significant benefits to the surgeon and give him/her a feeling of performing surgery on a stationary organ.

Teleoperation Systems

In a telerobotic system, the master console controls a remote slave robotic manipulator by sending position/velocity commands and receiving potential haptic/visual feedback signals, as well as the information of slave robot status. Teleoperation systems can be divided into three categories with their features: unilateral teleoperation systems, bilateral teleoperation systems, and multilateral teleoperation systems.

In a typical single-master/single-slave teleoperation system, if the slave does not possess a force sensor, which causes the human operator losing the sense of touch, then this system is called a unilateral teleoperation system. In contrast, if the slave possesses force sensors and is able to transmit the force feedback to the master, then this system is called a bilateral teleoperation system. In other words, the human can feel the interaction force between the slave robot and what it is touching, enabling the human to efficiently manipulate the master robot to provide appropriate commands. When a teleoperation system consists of more than one master console and/or slave manipulator and involves more than one sensed and command signal flow between the human operator and the environment, the system is called a multilateral teleoperation system. A multilateral framework not only allows for a one-to-one correspondence between the operator–master and the slave–environment sets but also realizes collaborative scenarios between multiple operator–master sets and/or multiple slave robots.

Physiological Organ Motion

The motion of a moving organ is primarily induced by respiratory and/or heartbeat motions with different frequency ranges. In order to mimic the physiological organ motion in experiments, the studies can be classified into two categories: organ simulators and living organ. By designing mechanical devices, the organ simulators can be controlled to mimic the moving organ's motion based on pre-acquired organ motion data (Yang et al., 2016; Cheng et al., 2019) or biological signals (Cheng and Tavakoli, 2018b). *In vivo* experiments use living porcine organ (Kesner and Howe, 2014) or dog organ (Mansouri et al., 2018) to demonstrate the control techniques. Specifically, in Yang et al. (2016), a stereo video of *in vivo* porcine heart, which recorded image sequence of a totally endoscopic coronary artery bypass graft from a da Vinci (Intuitive Surgical, CA) surgical platform, was used to measure the 3D heart positions offline by vision tracking. The quasi-periodic 3D heart motion signals were transmitted to a Motoman SIA-5F (Yaskawa America, Inc., Miamisburg, OH, USA) 7-DOF serial manipulator (Cheng et al., 2019) to control the manipulator to work as a real heart organ.

Motion Compensation Control Techniques

To compensate for the physiological organ motion and synchronize a robot's motion with the organ's motion, various control methods have been proposed for both handheld robotic systems (Yuen et al., 2009; Poulsen et al., 2012; Winter et al., 2015; Kolbitsch et al., 2018; Salehi et al., 2018; Ting et al., 2018) and telerobotic systems (Ginhoux et al., 2005; Gangloff et al., 2006; Cheng et al., 2018). In the paper, we mainly focus on motion compensation control methods for telerobotic systems, which generally falls into four categories: position control, force control, impedance control, and hybrid control.

Position Control

The position-based controllers need the real-time organ position and use that to synchronize the slave's movement with the organ's motion. For a teleoperation system, to further control the slave robot to mimic the human's operation, the summed positions of the master and the moving organ are used as a reference position for the slave robot to follow. A pure position-based telerobotic control system belongs to a unilateral teleoperation system as it provides the human without haptic feedback.

Before discussing robot controllers, a vital issue is to measure the moving organ position in real time. To this end, many image-based sensors have been widely used in research such as high-speed camera/laparoscopy (Nakajima et al., 2014), X-ray fluoroscopy (Ma et al., 2020), computed tomography (CT) (Su et al., 2013), magnetic resonance imaging (MRI) (Yang et al., 2014), positron emission tomography (PET) (Bettinardi et al., 2013), and ultrasound imaging (US) (Bowthorpe and Tavakoli, 2016a,b; Diodato et al., 2018). To get performance, hybrid imaging systems are also developed to measure precise organ motion including MRI/US imaging (Celicanin et al., 2018), MRI/CT imaging (Neumann et al., 2017), PET/CT imaging (Bettinardi et al., 2013; Pepin et al., 2014), and PET/MRI (Kolbitsch et al., 2018). The above-listed measurements have their advantages and limitations, which are elaborated in **Table 1**.

Non-image-based sensors have also been used to collect moving organ motion data such as sonomicrometric sensors (Bebek and Cavusoglu, 2007), optical measurement (Ruszkowski et al., 2016), and electromagnetic tracking system (Loschak et al., 2020).

Once the position of the moving organ is measured, robot controllers aimed for motion compensation can be deployed. Controllers for physiological organ motion compensation can be classified into error feedback controllers, predictive feedforward (prediction-based) controllers, and predictive feedback controllers, as elaborated in the following:

Error feedback controllers directly use the measured position as a reference signal for the medical robot. A proportional–integral–derivative (PID) controller is widely used to continuously calculate an error value (Murphy, 2004). However, the error feedback controller is found to be unable to reduce tracking error sufficiently if used solely.

Prediction-based controllers use the estimated current organ position as the setpoint to move the medical tools. It aims to develop accurate mathematical models of the organ's motion by using one or more previous measured motion dataset. The primary goal is to improve motion tracking performance by developing estimation methods. To this end, Taken's theorem (Ortmaier et al., 2005), artificial neural network (Cheng and Tavakoli, 2019b; Hirai et al., 2019), extended Kalman filter (EKF) (Liang et al., 2014), receding horizon model predictive controller (Bebek and Cavusoglu, 2007), and recursive least squares-based adaptive filter (Tuna et al., 2014) have been investigated in the developments of prediction-based controllers.

TABLE 1 | Advantages and disadvantages of medical imaging measurements.

Measurements	Advantages	Disadvantages
High-speed camera	Accurately measure real-time organ position by tracking points on the tissue	It only visualizes the outer surface of the moving organ and is not appropriate for surgeries performed inside of the organ.
X-ray fluoroscopy and CT	Cancerous organ scanning inside the body, such as of the thoracic and abdominal viscera. Precise.	It exposes patients to a dose of radiation that is capable of damaging cells and initiating changes leading to cancer.
MRI	Avoid radiation issue and can provide high-quality imaging, especially to discover tumors.	Expensive. Patients with iron-containing metallic implants cannot undergo MRI scanning because MRI machine can dislodge those implants.
US	Study heart function, blood flow in the neck or extremities, gallbladder disease, and fetal growth and development.	Image quality is heavily operator-dependent, and its sampling frequency is low.

Predictive feedback controllers not only need the organ's current position but also take the tracking error into account. By considering the physiological organ motion as periodic disturbances, controllers such as model predictive controllers (MPCs) (Gangloff et al., 2006; Vrooijink et al., 2017), Smith predictor-based controllers (Bowthorpe et al., 2013; Bowthorpe and Tavakoli, 2016a), generalized predictive controllers (GPCs) (Bowthorpe and Tavakoli, 2016b), and repetitive-GPC (R-GPC) (Ginhoux et al., 2005) were used. As these methods rely on the known organ motion model, the robustness of the system to irregular organ motion is challenging.

Force Control

For applications that require tool-tissue contact such as ablation and biopsy with controlled depth, a significant breakthrough in medical telerobotics is facilitated by force-reflecting haptic feedback, which allows the human to perceive the forces applied by the slave robot on the environment (a moving target). Force feedback (haptic feedback) increases the transparency of the teleoperation, which enhances human operator's immersive maneuver on the master consoler. Such function, as mentioned earlier in the paper, requires sensory feedback information. In other words, a force/torque sensor should be mounted on the slave side to measure and transmit slave–environment interaction forces. To simultaneously compensate for the physiological organ motion, various force-based control methods are proposed. The control goal is to keep the slave–environment interaction forces at a constant value so that the human can have a haptic feeling that the environment is motionless through force feedback.

Moreira et al. (2014) proposed a force control scheme using an active observer (AOB) based on a viscoelastic interaction model (soft tissue model) to compensate for the physiological motion. The model-based force control used the AOB to estimate the system states and an extra state, which is employed to compensate for system disturbances and modeling errors. Dominici and Cortesão achieved motion compensation by designing a cascade MPC architecture with a Kalman AOB (Dominici and Cortesão, 2014). The AOB inner loop provides stable closed-loop dynamics, and the MPC outer loop generates reference forces for AOB control for autonomous motion compensation. The authors further proposed another force control scheme by using a double AOB architecture (Cortesão and Dominici, 2017). In the work of Mohareri et al. (2014), the authors developed an asymmetric force feedback control system for bimanual telerobotic surgery using the da Vinci surgical system. To avoid instability issues caused by the closed-loop system, the authors proposed to use one hand to exert force through the master robot and use the other hand to perceive force feedback from the slave robot. He et al. (2019) proposed a neural network-based force control scheme to compensate for the eyeball motion in retinal surgery, in which the tool–eyeball interactive force is fed into the neural network and the latter is trained to command the robot manipulator to move according to the eyeball movements.

Impedance Control

Different from the position control and the force control, which are utilized to control position or force variables separately, impedance control is a compliant control, which is employed to achieve desirable dynamic interaction between a robot manipulator and its environment. In other words, impedance control can control the dynamic relationship between robot motion and robot–environment interaction force as desired. For a robotic manipulator aiming to compensate for the organ's motion, the robot and the moving organ can be expressed as impedance and admittance, respectively (Hogan, 1984, 1985). The goal of impedance control is to regulate the dynamic relationship to achieve the requirements of automatically compensating for the organ motion while keeping the interaction force in a safe range.

Florez et al. (2012) proposed a method that uses an impedance control on a handheld robotic instrument to compensate for physiological motion. The handheld system allows the human to perform low-frequency motions that correspond to the task. At the same time, the part of the instrument contacting the moving organ actively moves in synchronism with the organ's motion to keep a constant contact. Zarrouk et al. (2010) proposed an adaptive control architecture based on model reference adaptive control to solve the 3D physiological motion compensation in beating-heart surgery. A reference impedance model and an adaptive controller were designed for the surgical robot. The aforementioned impedance-controlled systems are developed for handheld medical robotics instead of teleoperated systems. In the work of Cheng (Cheng and Tavakoli, 2018a; Cheng et al., 2018, 2019) and Sharifi et al. (2018), the model reference adaptive control was applied to the bilateral teleoperation systems

separately. The authors designed two reference impedance models for the master and slave robots, respectively. The slave reference impedance model was used to make the slave robot compensate for the living organ's motion, while the master reference impedance model has the ability to ensure the human to perceive non-oscillatory robot–organ interaction force. The oscillatory haptic feedback caused by oscillatory motion and force sensor inertia is filtered out by the master reference impedance model.

Hybrid Control

Hybrid control combines two or more control schemes together, including hybrid position/force control, hybrid position/impedance control, etc. The goal of hybrid control is mainly to develop a compliant control scheme to achieve specific task requirements. In Yuen et al. (2010) and Kesner and Howe (2014), the authors separately incorporated position control and force control to achieve beating-heart motion compensation. These methods combined the US guidance with a force controller and are aimed to incorporate a feedforward term that contains the estimated motion of a beating heart. The US was used to measure the position of the moving organ, while the force controller was utilized to extend the device application from free motion to constrained contact motion. Nakajima et al. (2014) used visual servoing to compensate for the organ motion and performed haptic feedback using an acceleration-based bilateral control method. System stability was evaluated through frequency characteristics and root locus. In Cheng and Tavakoli (2018b), an impedance control combined with an US image-guided position control was developed in a teleoperation system. The US scanner estimated the moving organ position and transmitted it along with the master robot position to the slave robot as a position reference. For non-oscillatory haptic feedback, a reference impedance model was designed for the master robot to provide the human with a steady slave–organ interaction force.

APPLICATIONS

Significant interest has been documented for both interventional (e.g., therapeutic treatments such as surgery and protontherapy) and diagnostic (e.g., US scan, X-ray scan, and biopsy) applications (**Figure 1**).

The corresponding telerobotic systems can significantly reduce the risk of infectious disease transmission to frontline healthcare workers by making it possible to evaluate, monitor, and treat patients from a safe distance. Moreover, the teleoperation techniques are able to provide general support for patients and medical professionals, alleviating the non-COVID-19 burden placed on healthcare systems during this crisis. The latter, i.e., secondary prevention and disease management of non-COVID-19 individuals who need therapeutic treatments or diagnosis during this difficult time, is of equal importance. Telerobotic and autonomous systems can support healthcare staff such as physiotherapists and surgeons during the COVID-19 pandemic through facilitating fully remote or in-person distancing-aware physical treatments and diagnosis services.

Teleoperated Intervention

Telesurgery

Telerobotics applications mostly involve articulated robot configurations with an interchangeable surgical tool that is mounted on the end effector of the slave robot (surgical robot). Robot systems have been developed from the first functional telesurgery system—ZEUS—to the da Vinci surgical system; the latter is currently the only commercially available surgical robotic system. However, telerobotics for applications with physiological organ motion are mostly in the domain of research yet.

Most of the proposed systems are application-specific medical telerobots, such as the telerobots used for beating-heart surgery (mitral valve prolapses and repair, atrial septal defect, atrial fibrillation) and percutaneous nephrolithotomy surgery (kidney stones, kidney cysts, kidney blockage). Compared to conventional surgery operations, the surgeries assisted by telerobotic systems requiring organ motion have significant advantages. First, the master–slave system enables remote or physical distancing-aware surgical procedures during the COVID-19 pandemic. Second, automatic compensation for complex physiological organ motion greatly reduces the difficulty of operation for surgeons and increases surgical accuracy, which turns to improve patient safety. Third, advanced technique introduces minimally invasive robotic surgery, which can be used for the surgeries mentioned above with benefits including small incisions, little pain, low risk of infection, short recovery time, and reduced blood loss. Last but not least, specifically for beating-heart surgery, robotic surgery has been found to have additional advantages over the conventional arrested-heart surgery; the latter has to employ a heart–lung bypass machine (Angelini et al., 2002).

Teleradiotherapy

When a tumor locates close to the vital organs (heart, lung, etc.), radiation therapy is generally recommended as a useful treatment to destroy cancer cells and slow tumor growth without harming nearby healthy tissue. The goal of radiation therapy is to assess the true volume of the tumor and its real motion and to obtain an accurate target delineation and an accurate and personalized definition of the treatment plan (Khan and Gibbons, 2014). As the breathing-induced motion has significant effects on organs (e.g., liver, lung, breast, kidney, prostate, and pancreas), radiation therapy, accurately and automatically compensating for continuous physiological respiratory motion of organs, is necessary. Indeed, if not correctly compensated, organ motion can lead to a spreading of the thermal dose, which is the cause of two severe issues: (i) loss of treatment efficiency, and (ii) generation of unplanned lesions in adjacent healthy tissues. Moreover, teleradiotherapy will be useful to get rid of the side effects of radiation therapy to the physicians.

Telediagnosis

Tele-Echography

Ultrasound is an imaging modality that plays a significant role in medical emergency and surgical decision diagnosis. To compensate for the limited availability of ultrasound experts in isolated areas (such as physical distancing-aware caused by

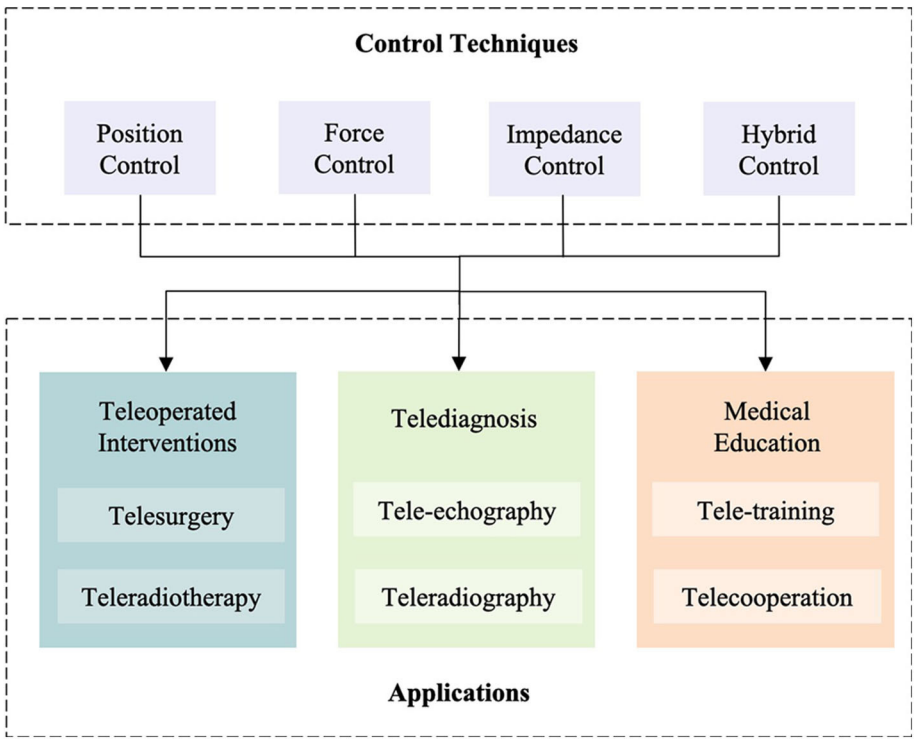

FIGURE 1 | Scheme of the control methods for physiological motion compensation and the potential applications.

COVID-19 pandemic), the use of robotic telemedicine systems is gaining attention. A commercial MELODY tele-ultrasound robotized system was developed by AdEchotech SME (France) (Vieyres et al., 2013) for long-distance US diagnosis. The slave robot is attached to an US probe through a probe holder. The human at the master site moves a fictive US probe as required for an echographic diagnosis. The MELODY system was designed to fulfill remote static organ diagnosis without considering issues such as moving organ motion compensation. Sharifi et al. (2017) developed a bilateral telerobotic system for echography in beating-heart surgery. Although it is just a proof of concept, the idea of the control scheme is worth to be considered for future commercial popularizing.

Teleradiography

Teleradiography allows radiologists or physicians to provide services without physically being at the location of the patient. Similar to tele-echography, by mounting the CT scanner or X-ray holder on the slave robot, the radiologists or physicians can remotely diagnose the patient's body without being exposed to radiation. Most importantly, robot-assisted organ motion compensation will be a benefit for accurate imaging and preventing the over-radiation of the patients.

Training and Education

The wide applicability of teleoperated interventions and telediagnosis will depend on not only the maturity of the technology but also the skill level of trained physicians. These applications require specialized skills compared to traditional methods. Moreover, it is essential that medical schools are equipped with such technologies to appropriately train physicians. Existing possibilities include the use of multilateral teleoperation systems with a multiple control console configuration to enable training or collaborative medical applications (Shahbazi et al., 2018; Cheng and Tavakoli, 2019a).

DISCUSSIONS AND FUTURE DIRECTIONS

Influenced by the COVID-19 pandemic, the presented review focuses on a potential solution for remote and physical distancing-aware healthcare delivery—medical telerobotics. The review studies the medical telerobotics for applications with physiological organ motion, and discusses control schemes for motion compensation, potential applications, and associated benefits. The medical telerobotics have been already employed in a wide range of diagnostic and interventional applications in different medical disciplines. To successfully apply medical telerobotic technologies to clinical practice, a significant issue is to develop appropriate control schemes for the specific application.

Solutions only involving visual servoing (image-based position control) are found to have several limitations: (i) artificial and natural landmarks occlusion will affect the measurements of the landmark-based sensors, (ii) tissue deformation during contact tasks will affect organ position measurement, and (iii) physiological motion induces oscillatory

force feedback and will affect human's performance. To deal with those issues, a latest research proposed a novel printing procedure to fabricate an electrical-impedance-tomography strain sensor on an ex-vivo breathing lung. The authors integrate a visual sensing system with a 3D printer to track the time-varying 3D geometry of the lung (Zhu et al., 2020). The method presented in the abovementioned research could aid modern medical treatments in myriad ways, such as printing electrode arrays for neural interfaces and printing bioscaffolds with engineered cells for tissue regeneration.

Another issue of position control is that when a position controller is used for contact tasks, the contact constraints will be treated as a disturbance resulting in increasing position tracking error, which probably leads to excessive interaction force. Therefore, a position control scheme in position tracking task works better in free motion than constrained motion. Applications such as biopsy and percutaneous puncture are more suitable to be performed by a position-based telerobotic control scheme.

In clinical practice, most medical interventions require direct interaction between one or more tools with the patient's organs. To assure the patient's safety and provide the surgeon with a comprehensive perception, force feedback is necessary for medical telerobotics during robotized interventions. In addition to the limitations of sensors and systems available for force feedback teleoperations, the force control scheme has its drawbacks as well. As the goal of pure force control is to keep the contact force as the reference without position limitations, it leads to force control working in constrained motion.

In fact, both position control and force control can be treated as extreme situations of impedance control. Specifically, the position controller has infinite impedance, while the force controller has zero impedance. Those controllers may be appropriate for applications in which the work exchanged between the robot and its environment is negligible. For applications where power exchange cannot be ignored, hybrid position/force interaction control or impedance control can be used to provide techniques to accommodate the side effects.

Medical telerobotics for applications requiring physiological organ motion have been developed considerably for the last 20 years, and they will be necessarily developed much further in the coming years, especially in the field of surgery and diagnosis. However, further efforts are required to address both clinical and technological challenges.

An existing difficulty for the adoption of medical telerobotic technologies is to deliver accuracy and precision medical procedures, which require particular effort to overcome. For instance, precise interaction and force applied on the tissue by the robotic instrument, accurate dose delivery to the patients, and limited radiation exposure of the patients should be strictly controlled according to specific medical practice. Considering and regulating applicable requirements and specifications for medical procedures and devices will be a benefit for bridging the gap between engineering and medicine. Both patients' and physicians' safety are always the priority in clinical practice. Therefore, when adopting a medical device in clinical practice, the stability of the system and the robustness and reliability to an unforeseeable emergency such as irregular organ motion should be of great concern.

Another significant issue that limits the spread of telerobotic system in clinical practice is the high cost of the medical devices. As the system development requires interdisciplinary knowledge including medicine, engineering, computer science, and mathematics, the challenges and costs are doubtless high. As a result, mature technology and standard requirements of specifications would be beneficial.

Ultimately, medical telerobotics is a promising technology, which has significant advantages for healthcare delivery and can play a positive role in the COVID-19 pandemic as it can effectively improve the remote or physical distancing-aware healthcare procedures. The present review study of teleoperation for medical applications requiring physiological motion shows that various control methods have been proposed for specific applications. As a result, preliminary research toward this direction has already been achieved, but the deep potential of medical telerobotics for applications requiring organ motion remains largely unexploited.

AUTHOR CONTRIBUTIONS

LC completed the work including literature review and preparation for the initial draft of the manuscript. MT provided guidance and valuable suggestions/discussions and was involved in the editing of the manuscript. All authors contributed to the article and approved the submitted version.

FUNDING

This work was supported by the Natural Sciences and Engineering Research Council (NSERC) of Canada under grants RGPIN-2019-04662 and RGPAS-2019-00106.

REFERENCES

Angelini, G. D., Taylor, F. C., Reeves, B. C., and Ascione, R. (2002). Early and midterm outcome after off-pump and on-pump surgery in Beating Heart Against Cardioplegic Arrest Studies (BHACAS 1 and 2): a pooled analysis of two randomised controlled trials. *Lancet* 359, 1194–1199. doi: 10.1016/S0140-6736(02)08216-8

Avgousti, S., Christoforou, E. G., Panayides, A. S., Voskarides, S., Novales, C., Nouaille, L., et al. (2016). Medical telerobotic systems: current status and future trends. *Biomed. Eng. Online* 15:96. doi: 10.1186/s12938-016-0217-7

Ballantyne, G. H. (2002). Robotic surgery, telerobotic surgery, telepresence, and telementoring. *Surg. Endosc. Other Intervent. Techn.* 16, 1389–1402. doi: 10.1007/s00464-001-8283-7

Bebek, O., and Cavusoglu, M. C. (2007). Intelligent control algorithms for robotic-assisted beating heart surgery. *IEEE Trans. Rob.* 23, 468–480. doi: 10.1109/TRO.2007.895077

Bettinardi, V., De Bernardi, E., Presotto, L., and Gilardi, M. C. (2013). Motion-tracking hardware and advanced applications in PET and PET/CT. *PET Clin.* 8, 11–28. doi: 10.1016/j.cpet.2012.09.008

Bowthorpe, M., and Tavakoli, M. (2016a). Physiological organ motion prediction and compensation based on multirate, delayed, and unregistered measurements in robot-assisted surgery and therapy. *IEEE/ASME Trans. Mech.* 21, 900–911. doi: 10.1109/TMECH.2015.2482391

Bowthorpe, M., and Tavakoli, M. (2016b). Generalized predictive control of a surgical robot for beating-heart surgery under delayed and slowly-sampled ultrasound image data. *IEEE Robot. Autom. Lett.* 1, 892–899. doi: 10.1109/LRA.2016.2530859

Bowthorpe, M., Tavakoli, M., Becher, H., and Howe, R. (2013). Smith predictor-based robot control for ultrasound-guided teleoperated beating-heart surgery. *IEEE J. Biomed. Health Inf.* 18, 157–166. doi: 10.1109/JBHI.2013.2267494

Celicanin, Z., Manasseh, G., Petrusca, L., Scheffler, K., Auboiroux, V., Crowe, L. A., et al. (2018). Hybrid ultrasound-MR guided HIFU treatment method with 3D motion compensation. *Magn. Reson. Med.* 79, 2511–2523. doi: 10.1002/mrm.26897

Cheng, L., Fong, J., and Tavakoli, M. (2019). "Semi-autonomous surgical robot control for beating-heart surgery," in *IEEE 15th International Conference on Automation Science and Engineering* (Vancouver, BC), 1774–1781. doi: 10.1109/COASE.2019.8843275

Cheng, L., Sharifi, M., and Tavakoli, M. (2018). Towards robot-assisted anchor deployment in beating-heart mitral valve surgery. *Int. J. Med. Rob. Comput. Assist. Surg.* 14:e1900. doi: 10.1002/rcs.1900

Cheng, L., and Tavakoli, M. (2018a). Switched-impedance control of surgical robots in teleoperated beating-heart surgery. *J. Med. Rob. Res.* 3:1841003. doi: 10.1142/S2424905X18410039

Cheng, L., and Tavakoli, M. (2018b). Ultrasound image guidance and robot impedance control for beating-heart surgery. *Control Eng. Pract.* 81, 9–17. doi: 10.1016/j.conengprac.2018.08.017

Cheng, L., and Tavakoli, M. (2019a). A multilateral impedance-controlled system for haptics-enabled surgical training and cooperation in beating-heart surgery. *Int. J. Intell. Robot. Appl.* 3, 314–325. doi: 10.1007/s41315-019-00099-y

Cheng, L., and Tavakoli, M. (2019b). "Neural-network-based heart motion prediction for ultrasound-guided beating-heart surgery," in *IEEE 15th International Conference on Automation Science and Engineering* (Vancouver, BC), 437–442. doi: 10.1109/COASE.2019.8843136

Cortesão, R., and Dominici, M. (2017). Robot force control on a beating heart. *IEEE/ASME Trans. Mech.* 22, 1736–1743. doi: 10.1109/TMECH.2017.2696259

Diodato, A., Cafarelli, A., Schiappacasse, A., Tognarelli, S., Ciuti, G., and Menciassi, A. (2018). Motion compensation with skin contact control for high intensity focused ultrasound surgery in moving organs. *Phys. Med. Biol.* 63:035017. doi: 10.1088/1361-6560/aa9c22

Dominici, M., and Cortesão, R. (2014). "Cascade robot force control architecture for autonomous beating heart motion compensation with model predictive control and active observer," in *IEEE RAS/EMBS International Conference on Biomedical Robotics and Biomechatronics* (São Paulo), 745–751. doi: 10.1109/BIOROB.2014.6913867

Evans, C. R., Medina, M. G., and Dwyer, A. M. (2018). Telemedicine and telerobotics: from science fiction to reality. *Updat. Surg.* 70, 357–362. doi: 10.1007/s13304-018-0574-9

Florez, J. M., Szewczyk, J., and Morel, G. (2012). "An impedance control strategy for a handheld instrument to compensate for physiological motion," in *IEEE International Conference on Robotics and Automation* (Saint Paul, MN), 1952–1957. doi: 10.1109/ICRA.2012.6225103

Gangloff, J., Ginhoux, R., de Mathelin, M., Soler, L., and Marescaux, J. (2006). Model predictive control for compensation of cyclic organ motions in teleoperated laparoscopic surgery. *IEEE Trans. Control Syst. Technol.* 14, 235–246. doi: 10.1109/TCST.2005.863650

Ginhoux, R., Gangloff, J., de Mathelin, M., Soler, L., Sanchez, M. M. A., and Marescaux, J. (2005). Active filtering of physiological motion in robotized surgery using predictive control. *IEEE Trans. Rob.* 21, 67–79. doi: 10.1109/TRO.2004.833812

He, C., Patel, N., Shahbazi, M., Yang, Y., Gehlbach, P., Kobilarov, M., et al. (2019). Toward safe retinal microsurgery: development and evaluation of an RNN-based active interventional control framework. *IEEE Trans. Biomed. Eng.* 67, 966–977. doi: 10.1109/TBME.2019.2926060

Hirai, R., Sakata, Y., Tanizawa, A., and Mori, S. (2019). Real-time tumor tracking using fluoroscopic imaging with deep neural network analysis. *Phys. Med.* 59, 22–29. doi: 10.1016/j.ejmp.2019.02.006

Hogan, N. (1984). "Impedance control: an approach to manipulation: Part I—theory," in *1984 American control conference* (San Diego, CA), 304–313. doi: 10.23919/ACC.1984.4788393

Hogan, N. (1985). Impedance control: an approach to manipulation: Part II—implementation. *J. Dyn. Syst. Meas. Control* 107, 8–16. doi: 10.1115/1.3140713

Hokayem, P. F., and Spong, M. W. (2006). Bilateral teleoperation: an historical survey. *Automatica* 42, 2035–2057. doi: 10.1016/j.automatica.2006.06.027

Keall, P. J., Mageras, G. S., Balter, J. M., Emery, R. S., Forster, K. M., Jiang, S. B., et al. (2006). The management of respiratory motion in radiation oncology report of AAPM Task Group 76 a. *Med. Phys.* 33, 3874–3900. doi: 10.1118/1.2349696

Kesner, S. B., and Howe, R. D. (2014). Robotic catheter cardiac ablation combining ultrasound guidance and force control. *Int. J. Rob. Res.* 33, 631–644. doi: 10.1177/0278364913511350

Khan, F. M., and Gibbons, J. P. (2014). *Khan's the Physics of Radiation Therapy*. Philadelphia, PA: Lippincott Williams and Wilkins.

Kolbitsch, C., Neji, R., Fenchel, M., Schuh, A., Mallia, A., Marsden, P., et al. (2018). Joint cardiac and respiratory motion estimation for motion-corrected cardiac PET-MR. *Phys. Med. Biol.* 64:015007. doi: 10.1088/1361-6560/aaf246

Liang, F., Yu, Y., Cui, S., Zhao, L., and Wu, X. (2014). Heart motion uncertainty compensation prediction method for robot assisted beating heart surgery-master-slave Kalman filters approach. *J. Med. Syst.* 38:52. doi: 10.1007/s10916-014-0052-y

Loschak, P. M., Degirmenci, A., Tschabrunn, C. M., Anter, E., and Howe, R. D. (2020). Automatically steering cardiac catheters *in vivo* with respiratory motion compensation. *Int. J. Rob. Res.* 39, 586–597. doi: 10.1177/0278364920903785

Ma, H., Smal, I., Daemen, J., and van Walsum, T. (2020). Dynamic coronary road mapping via catheter tip tracking in X-ray fluoroscopy with deep learning based Bayesian filtering. *Med. Image Anal.* 61:101634. doi: 10.1016/j.media.2020.101634

Mansouri, S., Farahmand, F., Vossoughi, G., and Ghavidel, A. A. (2018). A hybrid algorithm for prediction of varying heart rate motion in computer-assisted beating heart surgery. *J. Med. Syst.* 42:200. doi: 10.1007/s10916-018-1059-6

Mohareri, O., Schneider, C., and Salcudean, S. (2014). "Bimanual telerobotic surgery with asymmetric force feedback: a daVinci® surgical system implementation" in *IEEE/RSJ International Conference on Intelligent Robots and Systems* (Chicago, IL), 4272–4277. doi: 10.1109/IROS.2014.6943165

Moreira, P., Zemiti, N., Liu, C., and Poignet, P. (2014). Viscoelastic model based force control for soft tissue interaction and its application in physiological motion compensation. *Comput. Methods Programs Biomed.* 116, 52–67. doi: 10.1016/j.cmpb.2014.01.017

Murphy, M. J. (2004). Tracking moving organs in real time. *Semin. Radiat. Oncol.* 14, 91–100. doi: 10.1053/j.semradonc.2003.10.005

Nakajima, Y., Nozaki, T., and Ohnishi, K. (2014). Heartbeat synchronization with haptic feedback for telesurgical robot. *IEEE Trans. Ind. Electron.* 61, 3753–3764. doi: 10.1109/TIE.2013.2287258

Neumann, W., Lietzmann, F., Schad, L. R., and Zöllner, F. G. (2017). Design of a multimodal (1H/23Na MR/CT) anthropomorphic thorax phantom. *Z. Med. Phys.* 27, 124–131. doi: 10.1016/j.zemedi.2016.07.004

Ortmaier, T., Groger, M., Boehm, D. H., Falk, V., and Hirzinger, G. (2005). Motion estimation in beating heart surgery. *IEEE Trans. Biomed. Eng.* 52, 1729–1740. doi: 10.1109/TBME.2005.855716

Passenberg, C., Peer, A., and Buss, M. (2010). A survey of environment-, operator-, and task-adapted controllers for teleoperation systems. *Mechatronics* 20, 787–801. doi: 10.1016/j.mechatronics.2010.04.005

Pepin, A., Daouk, J., Bailly, P., Hapdey, S., and Meyer, M. E. (2014). Management of respiratory motion in PET/computed tomography: the state of the art. *Nucl. Med. Commun.* 35:113. doi: 10.1097/MNM.0000000000000048

Poulsen, P. R., Fledelius, W., Cho, B., and Keall, P. (2012). Image-based dynamic multileaf collimator tracking of moving targets during intensity-modulated arc therapy. *Int. J. Radiat. Oncol. Biol. Phys.* 83, e265–e271. doi: 10.1016/j.ijrobp.2011.12.053

Ruszkowski, A., Schneider, C., Mohareri, O., and Salcudean, S. (2016). "Bimanual teleoperation with heart motion compensation on the da Vinci® Research Kit: implementation and preliminary experiments." in *IEEE International Conference on Robotics and Automation* (Stockholm), 4101–4108. doi: 10.1109/ICRA.2016.7487601

Salehi, N., Rahmim, A., Fatemizadeh, E., Akbarzadeh, A., Farahani, M. H., Farzanefar, S., et al. (2018). Cardiac contraction motion compensation in gated

myocardial perfusion SPECT: a comparative study. *Phys. Med.* 49, 77–82. doi: 10.1016/j.ejmp.2018.05.004

Shahbazi, M., Atashzar, S. F., Ward, C., Talebi, H. A., and Patel, R. V. (2018). Multimodal sensorimotor integration for expert-in-the-loop telerobotic surgical training. *IEEE Trans. Rob.* 34, 1549–1564. doi: 10.1109/TRO.2018.2861916

Sharifi, M., Salarieh, H., Behzadipour, S., and Tavakoli, M. (2017). Tele-echography of moving organs using an Impedance-controlled telerobotic system. *Mechatronics* 45, 60–70. doi: 10.1016/j.mechatronics.2017.05.006

Sharifi, M., Salarieh, H., Behzadipour, S., and Tavakoli, M. (2018). Beating-heart robotic surgery using bilateral impedance control: theory and experiments. *Biomed. Signal Process. Control* 45, 256–266. doi: 10.1016/j.bspc.2018.05.015

Su, P., Yang, J., Lu, K., Yu, N., Wong, S. T., and Xue, Z. (2013). A fast CT and CT-fluoroscopy registration algorithm with respiratory motion compensation for image-guided lung intervention. *IEEE Trans. Biomed. Eng.* 60, 2034–2041. doi: 10.1109/TBME.2013.2245895

Tavakoli, M., Carriere, J., and Torabi, A. (2020). Robotics, smart wearable technologies, and autonomous intelligent systems for healthcare during the COVID-19 pandemic: an analysis of the state of the art and future vision. *Adv. Intell. Syst.* 2:2000071. doi: 10.1002/aisy.202000071

Ting, L. L., Chuang, H. C., Liao, A. H., Kuo, C. C., Yu, H. W., Zhou, Y. L., et al. (2018). Experimental king technique in radiation therapy. *Phys. Med.* 49, 11–18. doi: 10.1016/j.ejmp.2018.04.393

Tuna, E. E., Karimov, J. H., Liu, T., Bebek, Ö., Fukamachi, K., and Çavuşoglu, M. C. (2014). Towards active tracking of beating heart motion in the presence of arrhythmia for robotic assisted beating heart surgery. *PloS ONE* 9:e102877. doi: 10.1371/journal.pone.0102877

Uchinami, Y., Suzuki, R., Katoh, N., Taguchi, H., Yasuda, K., Miyamoto, N., et al. (2019). Impact of organ motion on volumetric and dosimetric parameters in stomach lymphomas treated with intensity-modulated radiotherapy. *J. Appl. Clin. Med. Phys.* 20, 78–86. doi: 10.1002/acm2.12681

Vieyres, P., Novales, C., Rivas, R., Vilcahuaman, L., Sandoval, J., Clark, T., et al. (2013). "The next challenge for world wide robotized tele-echography experiment (WORTEX 2012): from engineering success to healthcare delivery," in *Congreso Peruano De Ingeniería Biomédica, Bioingeniería, Biotecnología y Física Médica (TUMI II)* (Lima Peru).

Vrooijink, G. J., Denasi, A., Grandjean, J. G., and Misra, S. (2017). Model predictive control of a robotically actuated delivery sheath for beating heart compensation. *Int. J. Rob. Res.* 36, 193–209. doi: 10.1177/0278364917691113

Winter, J. D., Wong, R., Swaminath, A., and Chow, T. (2015). Accuracy of robotic radiosurgical liver treatment throughout the respiratory cycle. *Int. J. Radiat. Oncol. Biol. Phys.* 93, 916–924. doi: 10.1016/j.ijrobp.2015.08.031

World Health Organization (2020). *WHO Coronavirus Disease (COVID-19) Dashboard*. Available online at: https://covid19.who.int (accessed November 2, 2020).

Yang, B., Liu, C., Zheng, W., and Liu, S. (2016). Motion prediction via online instantaneous frequency estimation for vision-based beating heart tracking. *Inf. Fusion* 35, 58–67. doi: 10.1016/j.inffus.2016.09.004

Yang, B., Roys, S., Tan, U. X., Philip, M., Richard, H., Gullapalli, R., et al. (2014). Design, development, and evaluation of a master-slave surgical system for breast biopsy under continuous MRI. *Int. J. Rob. Res.* 33, 616–630. doi: 10.1177/0278364913500365

Yuen, S. G., Kettler, D. T., Novotny, P. M., Plowes, R. D., and Howe, R. D. (2009). Robotic motion compensation for beating heart intracardiac surgery. *Int. J. Rob. Res.* 28, 1355–1372. doi: 10.1177/0278364909104065

Yuen, S. G., Perrin, D. P., Vasilyev, N. V., Pedro, J., and Howe, R. D. (2010). Force tracking with feedforward motion estimation for beating heart surgery. *IEEE Trans. Rob.* 26, 888–896. doi: 10.1109/TRO.2010.2053734

Zarrouk, Z., Chemori, A., and Poignet, P. (2010). "Adaptive force feedback control for 3d compensation of physiological motion in beating heart surgery," in *IEEE/RSJ International Conference on Intelligent Robots and Systems* (Taipei), 1856–1861. doi: 10.1109/IROS.2010.5650684

Zhu, Z., Park, H. S., and McAlpine, M. C. (2020). 3D printed deformable sensors. *Sci. Adv.* 6:eaba5575. doi: 10.1126/sciadv.aba5575

Conflict of Interest: The authors declare that the research was conducted in the absence of any commercial or financial relationships that could be construed as a potential conflict of interest.

frontiers in Robotics and AI

ORIGINAL RESEARCH
published: 06 January 2021
doi: 10.3389/frobt.2020.590306

Exploring the Applicability of Robot-Assisted UV Disinfection in Radiology

Conor McGinn[1,2], Robert Scott[1], Niamh Donnelly[2], Kim L. Roberts[3], Marina Bogue[3], Christine Kiernan[4] and Michael Beckett[3]*

[1] School of Engineering, Trinity College Dublin, Dublin, Ireland, [2] Akara Robotics, Dublin, Ireland, [3] Department of Microbiology, Trinity College Dublin, Dublin, Ireland, [4] School of Medicine, Trinity College Dublin, Dublin, Ireland

The importance of infection control procedures in hospital radiology departments has become increasingly apparent in recent months as the impact of COVID-19 has spread across the world. Existing disinfectant procedures that rely on the manual application of chemical-based disinfectants are time consuming, resource intensive and prone to high degrees of human error. Alternative non-touch disinfection methods, such as Ultraviolet Germicidal Irradiation (UVGI), have the potential to overcome many of the limitations of existing approaches while significantly improving workflow and equipment utilization. The aim of this research was to investigate the germicidal effectiveness and the practical feasibility of using a robotic UVGI device for disinfecting surfaces in a radiology setting. We present the design of a robotic UVGI platform that can be deployed alongside human workers and can operate autonomously within cramped rooms, thereby addressing two important requirements necessary for integrating the technology within radiology settings. In one hospital, we conducted experiments in a CT and X-ray room. In a second hospital, we investigated the germicidal performance of the robot when deployed to disinfect a CT room in <15 minutes, a period which is estimated to be 2–4 times faster than current practice for disinfecting rooms after infectious (or potentially infectious) patients. Findings from both test sites show that UVGI successfully inactivated all of measurable microbial load on 22 out of 24 surfaces. On the remaining two surfaces, UVGI reduced the microbial load by 84 and 95%, respectively. The study also exposes some of the challenges of manually disinfecting radiology suites, revealing high concentrations of microbial load in hard-to-reach places. Our findings provide compelling evidence that UVGI can effectively inactivate microbes on commonly touched surfaces in radiology suites, even if they were only exposed to relatively short bursts of irradiation. Despite the short irradiation period, we demonstrated the ability to inactivate microbes with more complex cell structures and requiring higher UV inactivation energies than SARS-CoV-2, thus indicating high likelihood of effectiveness against coronavirus.

Keywords: UV robot, COVID-19, UVGI, radiology robot, disinfection methods, robotics, HCAI

OPEN ACCESS

Edited by:
John Oyekan, The University of Sheffield, United Kingdom

Reviewed by:
Luis J. Manso, Aston University, United Kingdom
Selene Tognarelli, Sant'Anna School of Advanced Studies, Italy

****Correspondence:***
Conor McGinn
mcginnc@tcd.ie

Specialty section:
This article was submitted to Biomedical Robotics, a section of the journal Frontiers in Robotics and AI

Received: *31 July 2020*
Accepted: *12 November 2020*
Published: *06 January 2021*

Citation:
McGinn C, Scott R, Donnelly N, Roberts KL, Bogue M, Kiernan C and Beckett M (2021) Exploring the Applicability of Robot-Assisted UV Disinfection in Radiology. Front. Robot. AI 7:590306. doi: 10.3389/frobt.2020.590306

1. INTRODUCTION

Infectious diseases cause significant clinical and economic burden. This has become increasingly apparent in recent months as the toll of coronavirus known as the severe acute respiratory syndrome coronavirus 2 (SARS-CoV-2) has continued to grow. However, the need for improved infection control methods is not exclusively motivated by the COVID-19 outbreak. A large body of literature illustrates the harmful and costly effects of hospital-acquired infections (HAIs). According to Guest et al. (2019), in an average NHS hospital with 510 beds, there may be 3,683 HAIs per year at a cost of £11.9 million, with 126 HAI-associated deaths. The same study estimated that 4.7% of adult hospitalized patients in the NHS would acquire a HAI during their stay, and 1.7% of frontline staff would acquire one annually.

Patients that contract an infectious disease are normally quarantined and subjected to strictly monitored isolation precautions (involving extensive disinfection protocols) in accordance with their condition. Infectious patients that require procedures (such as biopsy, X-ray, etc.) in other locations of the hospital create a significant logistical challenge as additional cleaning is mandated before and after these patients are treated in these rooms. This problem is especially pronounced in Radiology settings where, according to Mossa-Basha et al. (2020), disinfectant cleaning times can take between 30 and 60 minutes after each patient. These delays have had a devastating effect on patient workflow; NHS statistics show that between February and March 2020, the number of people waiting 6 weeks or more for a scan had nearly tripled. It is common practice for much of the disinfectant cleaning to be performed by radiographers (cleaning staff are rarely permitted to disinfect expensive medical equipment). This is problematic as it places additional pressures on the resources within a Radiology department. Disinfectant cleaning is also limited to surfaces only, since the use of aerosolized disinfectant chemicals would be likely to cause damage to any exposed electronic circuitry (PCs, medical equipment, etc.) in the room.

Advances in technology offers potential for improving standards of infection control, namely: (1) increased effectiveness, (2) reduce the time and resources it takes to perform disinfectant cleaning, and (3) reduce the risks incurred by healthcare workers (including cleaning staff) who are required to occupy the facilities. The third point seems especially important in light of findings by Huang et al. (2020), Chen et al. (2020), and others, that COVID-19 has had significant adverse effects on the mental health of front-line health workers.

Ultraviolet germicidal irradiation (UVGI) is a non-touch disinfection method that uses short-wavelength ultraviolet C (UV-C) light to kill or inactivate microorganisms by destroying nucleic acids and disrupting their DNA, leaving them unable to perform vital cellular functions. UVGI has many compelling advantages including the effectiveness against broad-spectrum organisms, lack of harmful residuals, reduced labor and consumable costs, and relative simplicity of operation within a healthcare environment. Despite a large body of scientific evidence demonstrating its efficacy against a wide range of pathogens, including coronavirus, to the best of the authors' knowledge, its effectiveness in radiology setting has not yet been tested. Furthermore, for reasons later outlined, few, if any, of the commercially available UV robot platforms are well suited for this application.

In this paper, we investigate the effectiveness and feasibility of using a UV disinfectant robot for applications in radiology settings. In so doing, we make three significant contributions. First, we propose a design for a UV robot that can actively control its field of UV irradiation, thereby if used in the manner intended, it may be safe for use around humans. Second, using an embodiment of the proposed design, we demonstrate the efficacy of UVGI in inactivating microorganisms from a wide range of commonly touched surfaces in hospital radiology suites. Third, we test the effectiveness of disinfecting a radiology suite comprising a CT scan machine in a period of <15 minutes, a 2-4X reduction on the time it presently takes according to relevant recent literature.

2. LIMITATIONS OF CURRENT DISINFECTION METHODS

The spread of germs, including SARS-CoV-2, can be reduced through improved hygiene practices (i.e., washing hands, social distancing), wearing PPE (i.e., facemasks) and frequent targeted disinfection cleaning. During the COVID-19 outbreak, global shortages of PPE were widely blamed for the high transmission rates among healthcare workers. Other potentially contributing factors, including poor adherence among healthcare workers to hand-washing protocols (Mortell, 2012 observes that this "theory-practice" gap has long existed) and limitations of conventional disinfection cleaning techniques, received relatively less attention.

The issues associated with current disinfection practices are more fundamental, and comprise both operational and scientific factors. Disinfectant cleaning is most commonly undertaken through the application of chlorine-based chemical agents. For best performance, it is normally recommended that surfaces must be first cleaned with a detergent prior to the application of the disinfectant. For a chemical disinfectant to be effective, it must remain wet on a surface for a pre-specified amount of time (normally around 10 minutes). This is difficult to control for in practice, however, as mops/cloths lose their wetness quickly and wetness can be difficult to gauge when wearing latex gloves. Certain germs may also develop resistance to disinfectant chemicals; for example, Edwards et al. (2016) showed that *Clostridium difficile* can develop resistance to household bleach.

Currently, visual inspection is the standard means of assessing the efficacy of cleaning in hospitals. However, since most common germs are <10 microns in size, it is impossible to tell with the naked eye whether a surface has been thoroughly disinfected or not. Sherlock et al. (2009) compared visual inspection against chemical (ATP), microbial methods, and aerobic colony count (ACC). It was found that visual assessment was an inadequate and subjective means of monitoring the cleanliness of hospitals and what appeared clean to the eye was often below acceptable thresholds under other means of analysis.

When disinfectant cleaning is performed, strict infection control protocols must be followed and cleaners are advised to wear gowns, gloves, protective eye-wear, and a mask at all times. In practice, especially in large rooms and those with many surfaces, the activity is time consuming, physically exerting (especially when wearing PPE) and difficult to perform systematically due to factors including the presence of patients, the coming-and-going of physicians, and myriad other things going on at any given time that can cause distractions.

Traditional methods of disinfectant cleaning are limited to surfaces only. Therefore, they can only be considered effective at protecting against fomite transmission. They are ineffective against aerosol and droplet transmission, which is concerning considering the growing evidence that SARS-CoV-2 is primarily transmitted in aerosol form. Santarpia et al. (2020) recently demonstrated the infectious nature of SARS-CoV-2 aerosol, suggesting that airborne transmission of COVID-19 is possible, and that aerosol prevention measures are necessary to effectively reduce the spread of SARS-CoV-2. Chemical disinfectant can be dispersed in the air using misting or vaporizing technologies, such as vaporized hydrogen peroxide (VHP). However, this process is highly time consuming (often takes several hours), resource intensive (vents/doors must be blocked) and logistically challenging as the room must be evacuated during use. Furthermore, there are many parts of the hospital where it is not possible to use chemical misting technologies; examples include public and communal areas that cannot be evacuated (such as hallways, waiting areas, ICU) or in rooms comprising equipment with exposed circuitry such as PCs, CT scanners, etc.

3. PRIOR WORK

UVGI technology has been successfully deployed in clinical settings for over a decade. The application of the technology has varied from decontaminating medical devices and PPE (see Kac et al., 2010; Moore et al., 2012), sterilizing ambulances (see Lindsley et al., 2018), air sterilization (see Ethington et al., 2018), to being deployed on mobile platforms (including robots) for the purposes of room disinfection (see Miller et al., 2015).

Several clinical studies have explored the effect of the introduction of UV disinfectant technology on clinical outcomes. In a long-term study spanning several years, Haas et al. (2014) found a correlation between the introduction of UV disinfection robot technology in an acute 643-bed medical center and reduced levels of Hospital Acquired Infections (HAIs). Murphy et al. (2019) report similar reductions in HAIs over a 36 month period after the introduction of a UV disinfectant robot in a bone marrow transplant unit.

Other studies have focused on scientific validation of the technology in the field. One study by Yang et al. (2019) found a substantial reduction in surface bacteria after deploying a mobile UV-C disinfection robot in vacated rooms of patients harboring Methicillin-resistant *Staphylococcus aureus* (MRSA), Vancomycin Resistant *Enterococcus* (VRE) and other nosocomial pathogens. Casini et al. (2019) demonstrated that a pulsed-xenon UV-C device was capable of significantly reducing the amount of microorganisms present on high-touch surfaces in several hospital settings including the Intensive Care Unit, operating theater, and patient rooms.

Research from Memarzadeh et al. (2010), Jinadatha et al. (2015), and Boyce (2016) suggests that UVGI is most effectively deployed in combination with conventional friction-based cleaning methods as the low penetrating power of UV-C limits the effectiveness of the systems in areas that are not first manually cleaned. In a study exploring the efficacy of UVGI systems in an ambulance patient compartment, Lindsley et al. (2018) suggest UVGI as a method of whole-compartment disinfection that would act as a supplement to standard cleaning procedure and allow manual cleaning to be focused on areas most prone to contamination.

Elgujja et al. (2020) reviewed the existing literature on UV surface decontamination in a 2020 publication. Several limitations to existing applications of UV surface decontamination are listed, with the key finding being that shadowed areas remain difficult to sterilize. Other limitations include the inability for UV to remove dust or dirt on surfaces, the need to vacate the room for most UVGI applications and high capital costs. The use of HPV as a disinfection agent has advantages in some areas over UV-C, although the process is time-consuming, cannot be used in an occupied room and HVAC systems must be covered during use. A commonly cited issue with existing UVGI systems is the lack of design against shadowed areas.

Research from van Doremalen et al. (2020) suggests the SARS-CoV-2 virus is detectable on hard surfaces up to 72 hours, and in the air for periods of more than 3 hours. Kampf et al. (2020) demonstrated that other human coronaviruses can persist on some surfaces for up to 9 days. Numerous studies have shown that UVGI is effective against viruses from the coronavirus family. Darnell et al. (2004) successfully inactivated SARS-CoV-1, irradiating liquid samples for 15 minutes at a distance of 3 cm, with a corresponding fluence of $3.6144 J/cm^2$. Eickmann et al. (2020) shows that UV-C irradiation led to the inactivation of three single-strand RNA viruses, including SARS-CoV-1. Walker and Ko (2007) demonstrated 254 nm UV-C inactivation of three viral aerosols: MS2 bacteriophage, adenovirus, and MHV coronavirus. The coronavirus was highly sensitive to UV radiation and was inactivated at a much lower irradiation intensity than the MS2 and the adenovirus. All three pathogens indicated a higher susceptibility to UV inactivation in aerosol form than when suspended in a liquid medium regardless of the size of the virus particle, the type of nucleic acid (DNA or RNA) and the viral structure (naked or enveloped). The finding that UV-C irradiation neutralizes aerosolized pathogens faster than surface-bound pathogens is supported by a study by Kesavan et al. (2014) which found that aerosolized spores were inactivated faster when compared to surface-fixed organism, even when accounting for variance in irradiation intensity observed in the aerosol chamber. More recently, Fischer et al. (2020) found that UV was comparable with hydrogen peroxide vapor (HPV) at inactivating SARS-CoV-2 on solid, non-porous surfaces.

In a review of UVGI technology, Miller et al. (2013) acknowledge that UV irradiation carries some potential health

risks. However, the paper states that health issues are rare and typically only occur due to improper maintenance procedures. In this article, the authors make reference to First et al. (2005) who examined eye and skin exposure across a range of settings where UVGI was being used, and showed that doses were well below the recommended level. This corresponds to findings by Lai et al. (2018) that also show applied UV fluences are well below the harmful threshold.

4. METHODS

4.1. Requirements Analysis

To understand the technical and operational requirements for a UV disinfectant solution, we engaged with Radiology departments in two Irish hospitals. We conducted several site visits to both hospitals and interviewed key staff including three consultant radiologists, a radiology services manager, four radiographers, and three infection control nurses. These interactions took place in March 2020, as the country was starting to deal with the toll of COVID-19. The infection control mandate in both hospitals was to thoroughly disinfect all accessible surfaces using a chlorine-based cleaning agent after the room was used by patients that had tested positive for COVID (or were suspected to have COVID). In the first hospital, the majority of the disinfectant procedure was carried out by contract cleaners; however, radiographers were still required to wipe down any medical equipment that was in the room. In the second hospital, a smaller regional hospital, all disinfectant cleaning was performed on-site by the radiographers. In both hospitals, according to the people we spoke with, the minimum time this procedure took was 30 minutes. In the larger hospital, we learned it often took far longer (up to 90 minutes) as room turnaround time was heavily dependent on the scheduling of the contract cleaners, who were in high-demand during the COVID-19 pandemic and often arrived late to the room. We learned that these long cleaning times were having a detrimental effect on patient workflow; in both hospitals, capacity of a CT scanner for COVID patients was 1 per hour, where as pre-COVID it was normal to process 4/5 patients in the same time.

Staff in both hospitals acknowledged that these disinfection periods were unsustainable. However, there was recognition that reducing disinfection times may have a limiting effect on the level of disinfection that was performed. One of the hospitals had considered the use of UV disinfectant technology in the past, and had facilitated a trial of the technology at the hospital. This evaluation process involved the formation of a committee (which included representatives of the Radiology department) which ultimately found that while UVGI technology seemed promising, they anticipated significant operational challenges of integrating currently available solutions into their clinical workflow. Issues identified that were of particular relevance for radiology settings included: (1) the majority of systems on the market were not autonomous and had to be pushed in place, increasing labor requirements, (2) the UVGI platforms were physically large, which made them difficult to maneuver around in smaller or cluttered rooms which are common in radiology settings, (3) they required the room to be evacuated during use, which added to the overall cleaning time since clinical staff were unable to prepare for the next patient until the robot had completed its procedure. They also expressed some high-level concerns regarding the effect that the UV irradiation might have on the equipment in the room.

4.2. UV Robot Design

Based on the insights gained during the consultancy phase, a list containing five high-level design requirements was formulated. These requirements were then used to benchmark the applicability of existing UV robot systems for potential use-cases in a Radiology setting (**Table 1**). It emerged that none of the existing off-the-shelf UV disinfectant robots were well suited for this application, as they were either too large to maneuver in tight spaces ($> 55 \times 55$ cm footprint), required rooms to be fully evacuated during use and/or produced light intensity levels (estimated by Lindblad et al., 2020 to be as

TABLE 1 | Benchmarking Violet and several existing UV robots against stated design requirements.

Robot model	 Xenex	 Tru-D	 Helios	 UVD	 Violet
Form factor (L × W × H)	76 × 51 × 97 cm	NA × NA × 168 cm	59 × 59 × 196 cm	93 × 66 × 171 cm	35 × 35 × 150 cm
Small form factor for operating in tight spaces	X	X	✓	X	✓
Can achieve a greater than 1-log reduction of most germs at distances of 1-2 m from the surface	✓	✓	✓	✓	✓
Can autonomously navigate (i.e., doesn't have to be pushed into place)	X	X	X	✓	✓
Cleaning staff can be deployed in the room at same time as robot	X	X	X	X	✓
UV lamp not too powerful to cause harm if exposed to skin/eyes for short period	X	X	X	X	✓

high as 1,068 mJ/cm^2) which indicated they would rapidly exceed the human occupational safety limits outlined in EU directive 2006/25/EC.

A prototype disinfectant robot was developed to overcome these limitations; our goal was to produce a system that could perform autonomously, was capable (at least potentially) of working safely alongside human cleaners, and that it possessed a small form factor which made it suitable for use in constrained spaces. Our design concept, which we subsequently named *Violet*, is shown in **Figure 1**. *Violet* comprises a differently driven robotic base equipped with a Hokoyu URG lidar and Intel Realsense D400 RGBD camera for autonomous navigation. It has one (or more as needed) vertically mounted UV lamps enclosed by a reflective shield. This shield serves two important purposes: (1) to reflect UV radiation emitted behind the robot, thus helping to amplify the total UV output (as shown by Miller et al., 2013 and several earlier studies), and (2) to control the parts of the room that are irradiated.

The *Violet* prototype was constructed using a Turtlebot 2 mobile base which mounted a vertical mercury vapor UV lamp (wavelength 254 nm). The lamp was powered through a DC-AC inverter which was connected with a 10Ahr Lithium Polymer battery pack. The robot and UV lamp were controlled using an on-board Hystou mini-pc (Intel i7 processor, 8 GB RAM). A wide angle logitech webcam was located at the front of the robot. The reflective shield was implemented using a folded piece of 1 mm Aluminum sheet metal. Fixtures for mounting the lamp, reflector and sensors were custom fabricated through a combination of laser cutting and 3D printing. The robot could be controlled manually using a Logitech handheld joystick, or autonomously using the Turtlebot's navigation stack which was openly available within the Robot Operating System (ROS) repository. Prior to deployment, the robot was tested in an anechoic chamber to ensure that it didn't produce any RF interference that would cause problems to hospital equipment.

4.3. Designing for Occupational Health and Safety

The UV-C output of an 8W (model: Philips TUV 8W FAM/10X25BOX) and 36W (Model: Philips TUV 36W SLV) lamp were measured empirically in a series of lab tests. Using a UV-C light intensity meter (Model: General UV254SD), the intensity of UV light was measured over distances of 1–5 m. To ensure that the light irradiated uniformly from the lamp, measurements were taken at 30 degree increments over a span of 120 degrees. Results from this experiment are plotted in **Figure 2** and tabulated in **Table 2**. The power intensity dropped significantly over distance for both 36 and 8 W bulbs. Based on its improved performance over distance, the 36 W lamp was selected for use on the *Violet* prototype.

The UV light intensity meter was also used to test the effectiveness of disposable gloves, a range of clothes fabrics and standard plastic PPE googles to shield UV rays. Our tests found that even at distances of just a few centimeters, the UV meter was unable to register a reading for any of the materials tested.

The legal daily exposure limit (over an 8 hour period) of unprotected skin and eyes, as per the EU Directive 2006/25/EC, is an effective radiant exposure value, H_{eff} of $30J/m^2$. For a UV-C light source, this can be calculated by the following equation:

$$H_{eff} = \Sigma_{\lambda=180nm}^{\lambda=400nm} E_\lambda \cdot S(\lambda) \cdot \Delta\lambda \cdot \Delta t \quad (1)$$

Where E_λ = spectral power density ($Wm^{-2}nm^{-1}$), $S(\lambda)$ = spectral weighting accounting for wavelength dependence of health effects of UV radiation on skin and eyes (dimensionless), $\Delta\lambda$ = bandwidth of measurement intervals (nm), and Δt = duration of exposure (s). Using the formula provided in Equation (1), it was estimated that if *Violet* was equipped with one Philips TUV226 36W SLV lamp, reaching this exposure limit would take 44 seconds at a distance of 1m, 2 minutes 37 seconds at 2 m, and 5 minutes 57 seconds at 3 m.

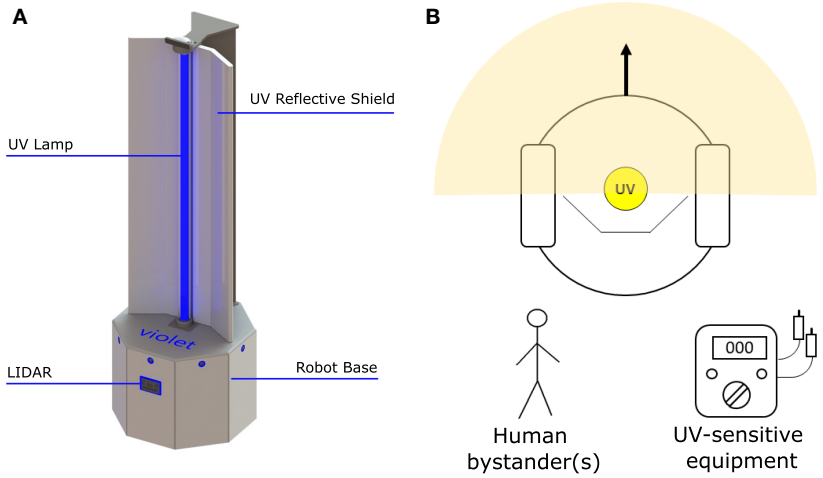

FIGURE 1 | The *Violet* robot platform. **(A)** Labeled image illustrating some of the robot's key features. **(B)** Plan view illustration of how *Violet* uses a physical barrier to shield bystanders and/or equipment from irradiation.

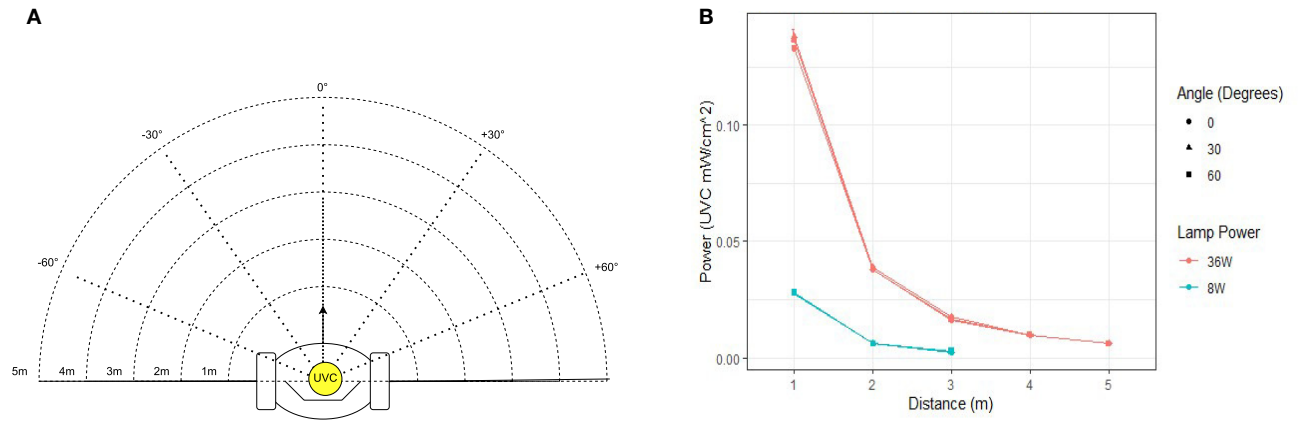

FIGURE 2 | Measured UV-C field in the region around the robot. **(A)** Measurements were taken at distances of 1–5 m at intervals of 30. **(B)** Graph illustrating the UV-C output of the 8 and 36 W lamp used in this study.

TABLE 2 | Instantaneous UV-C energy field around the robot for an 8 W (model: Philips TUV 8 W FAM/10X25BOX) and 36 W lamps (model: Philips TUV 36 W SLV).

		1 m [mW/cm^2]		2 m [mW/cm^2]		3 m [mW/cm^2]		4 m [mW/cm^2]		5 m [mW/cm^2]	
Angle	**Power (W)**	μ	σ	μ	σ	μ	σ	μ	σ	μ	σ
−60°	8	0.027	0.001	0.006	0.000	0.003	0.000	N/A	N/A	N/A	N/A
	36	0.132	0.000	0.038	0.000	0.017	0.001	0.010	0.000	0.006	0.000
−30°	8	0.027	0.000	0.006	0.000	0.003	0.000	N/A	N/A	N/A	N/A
	36	0.136	0.001	0.038	0.001	0.017	0.000	0.009	0.000	0.006	0.000
0°	8	0.028	0.000	0.006	0.000	0.002	0.000	N/A	N/A	N/A	N/A
	36	0.137	0.001	0.038	0.000	0.016	0.000	0.010	0.000	0.006	0.000
30°	8	0.028	0.000	0.006	0.000	0.002	0.001	N/A	N/A	N/A	N/A
	36	0.141	0.001	0.039	0.000	0.018	0.000	0.010	0.000	0.006	0.000
60°	8	0.029	0.000	0.006	0.000	0.003	0.000	N/A	N/A	N/A	N/A
	36	0.134	0.001	0.038	0.000	0.016	0.000	0.009	0.000	0.006	0.000

The highest detected output was 7.46 mW/cm^2, measured at a distance of approximately 5 mm from the 36 W lamp.

4.4. Sample/Data Collection and Analysis

The germicidal effectiveness of the *Violet* robot was examined at two hospital sites. Surfaces to be sampled were divided into eight 1 × 1 cm squares. Swabs, moistened with phosphate buffered saline (PBS), were used to sample 4 alternate squares before UV irradiation. Sample swabs were transferred to 1 ml PBS and stored on ice. After irradiation, surfaces were then re-sampled (using the four remaining squares at each sample location) using the same approach followed in the pre-treatment phase. Collected samples were diluted 1:10 in PBS and 100 μl was plated onto nutrient agar with four technical replicates and grown statically for 48 h at 37°C. Bacterial load was reported as colony forming units per square centimeter (cfu/cm^2) after correction for dilution and surface area.

5. RESULTS

A series of tests were undertaken within the Radiology departments of two Irish hospitals; a 500+ bed general hospital in Dublin (hospital 1) and a 250+ bed regional hospital (hospital 2). The first tests, performed at hospital 1, were designed with a focus on validating the germicidal efficacy of the *Violet* system. The second tests, which were performed in hospital 2, had a greater focus on validating the operational feasibility of using a UV robot to autonomously disinfect a room in a real-world, clinical radiology setting.

5.1. Experiment 1

The first experiment involved irradiating two radiology suites at hospital 1; a CT-scan room and X-ray room. Both rooms were estimated to be 34–40m^2 in area. The disinfection treatment involved navigating the robot to several locations (10 in CT scan room, 7 in the interventional suite) to irradiate nearby surfaces. To ensure repeatability and controllability of the experiment, the robot was manually controlled by a human operator. The robot stopped for a period of 3 minutes at each location. The stopping locations were chosen in advance, and selected as such that they irradiated many of the frequently touched surfaces in the room. Surfaces that were selected for swab testing had a high probability of human skin contact and were distributed through

the room. Surfaces of medical equipment (including the CT scanner tunnel) were not subjected to high doses of irradiation. This was introduced as precautionary measure in case that a high dosage of UVC light might have a degrading effect on medical equipment. Photographs of the surfaces sampled from the CT room and X-ray room of hospital 1 are given in **Figure 3**. A schematic illustrating the positioning of the swab points in each room, as well as the approximate locations of the robot during the experiment are presented in **Figure 4**.

Analysis of the swab samples revealed that, of the microbes present before the irradiation, a mix of both Gram positive and Gram negative bacteria was detected. Results from the swab testing indicates that UV irradiation successfully eliminated all of the measurable bacterial load on each of the different surfaces tested. The presence of *Staphylococcus aureus*, was detected on the door handle of the X-ray room (**Figure 3M**) prior to, but not after, UV irradiation. These results are shown in **Figure 5**.

5.2. Experiment 2

The second experiment investigated the germicidal effectiveness of a rapid (<15 minutes) CT room disinfection using the *Violet* robot. This experiment involved navigating the robot throughout the CT room, stopping at seven locations to irradiate nearby surfaces. The trajectory of the robot, including its irradiation

FIGURE 3 | Commonly touched surfaces chosen for swab testing in hospital 1: **(A–J)** CT scan room; **(K–Q)** interventional suite.

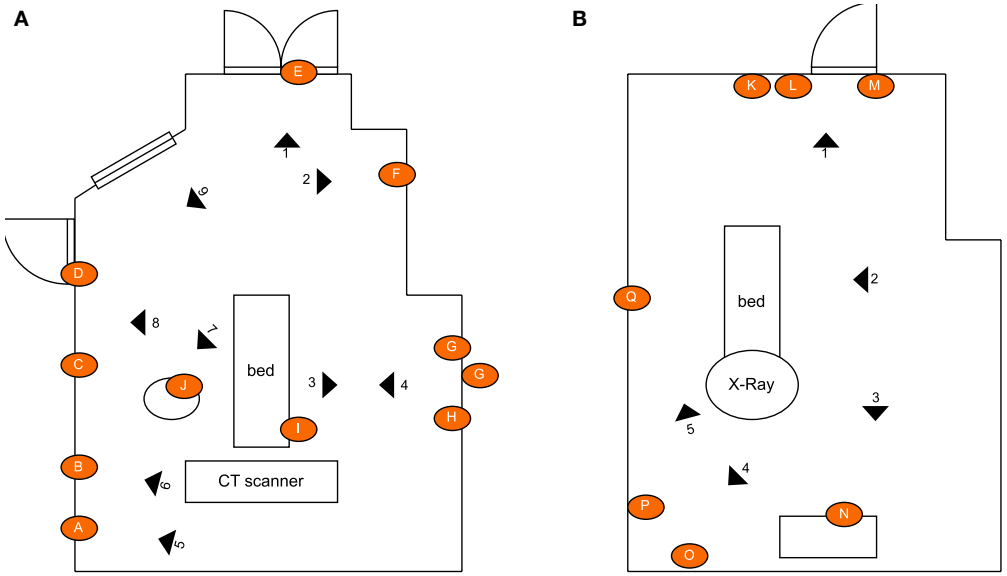

FIGURE 4 | Schematic illustrating the layout of the rooms, the location of the swab points in each room, and the approximate location of the robot during the defined irradiation periods: **(A)** CT scan room; **(B)** interventional suite. The swept area of the UV lamp is illustrated for location 1 to provide an indication of the volume of space covered. [Drawings not to exact scale].

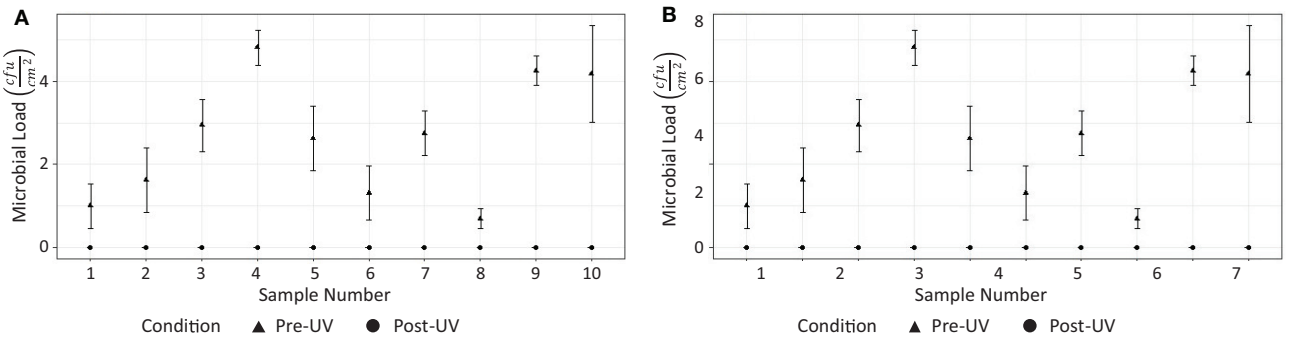

FIGURE 5 | Effectiveness of UV irradiation at eliminating on bacterial load on surfaces in hospital 1: **(A)** CT suite, **(B)** X-ray suite.

locations, were chosen in advance to maximize the total surface area exposed to UV irradiation. The robot stopped for a period of 2 minutes per location. The irradiation locations and the swab points were chosen independently of the route followed by the robot. To ensure repeatability and controllability of the experiment, the robot was manually controlled by a human operator. A schematic of the room, which shows the positioning of the swab points, as well as the approximate irradiation locations of the robot during the experiment are presented in **Figure 6**. Photos of the swab locations are given in **Figure 7**. The feasibility of autonomously performing the procedure was separately validated; a video showing *Violet* performing a similar route to the one described in the paper is given in the **Supplementary Material**.

Tests were performed on two occasions, 1 week apart. These results are shown in **Figure 8**. In the first test, swabs taken from two locations (**Figures 7C,F**) did not reveal the presence of any microbial load prior to the UV irradiation. On the second day, swabs from five locations (**Figures 7B–D,F,G**) did not reveal the presence of any bacteria prior to the UV irradiation. At the remaining locations, the UV irradiation was shown to be highly effective at eliminating microbial load. At one location, in a crevice on the bed of the scanner (**Figure 7E**), an especially high concentration of bacterial load was measured on both days; this included both *S. aureus* and *Staphylococcus epidermidis*. The UV irradiation eliminated 84% of the bacterial load at this location on testing day 1, and 95% of the bacterial load on testing day 2.

6. DISCUSSION

The results from our analysis indicate that robot-assisted UVGI can be an effective tool of reducing the presence of microorganisms in radiology departments. Our findings are likely the first to show effectiveness of UVGI in a

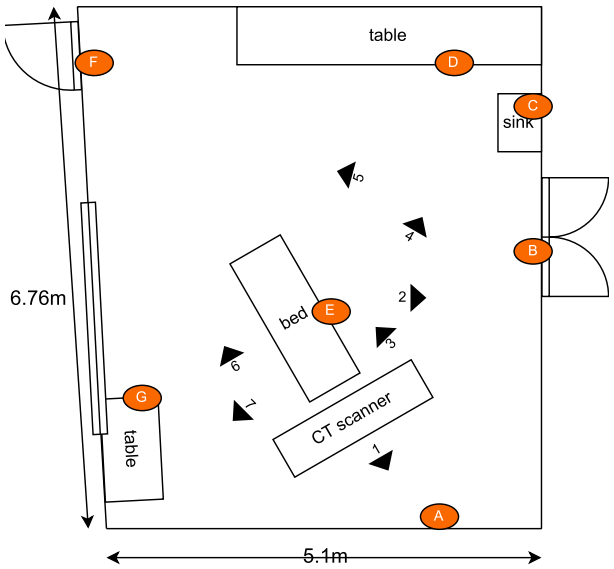

FIGURE 6 | Schematic illustrating the layout of the CT scan room used for the second hospital test. Indicated in the drawing are the locations of the swab points, and the approximate location of the robot during the defined irradiation periods. [Drawings not to exact scale].

radiology context, however they add to a growing body of research that demonstrates effectiveness of the technology within clinical settings.

Pre-UVGI swab testing revealed the presence of microbial load at (24/31) locations across three radiology suites. After UVGI treatment, microbial load was only detected at (2/24) locations. The location where the greatest concentration of microbial load was observed was on the patient bed in hospital 2, at a location adjacent to a crevice at the bed's lifting mechanism (**Figure 7E**). Both *S. auris* and *S. epidermidis* were also observed at this location. The high microbial load suggests that the site may have been inaccessible to human fingers during normal cleaning procedures. Although the UVGI didn't fully remove the microbial load at this location, it was successful in reducing it by >85% in both instances. The most plausible reason why the UVGI did not eliminate all bacteria at this location was due to shadowing in the vicinity of the crevice where the swab samples were taken. This limitation could be addressed through better placement of the UV lamp and/or a longer exposure time.

It was not possible to directly measure the effectiveness of *Violet* against coronavirus, since its presence in uncontrolled real-world settings is hard to quantify. However, we can estimate the likely performance by comparing the UV-C output of the robot with inactivation energy to kill the virus and based on its

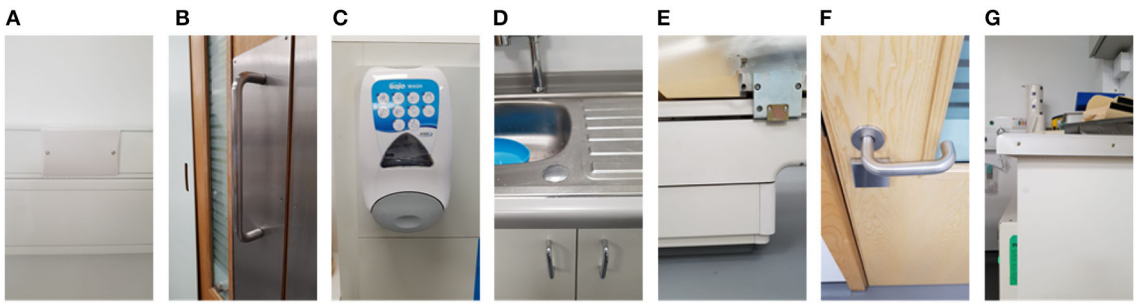

FIGURE 7 | Commonly touched surfaces **(A–G)** chosen for swab testing in CT scan room of hospital 2.

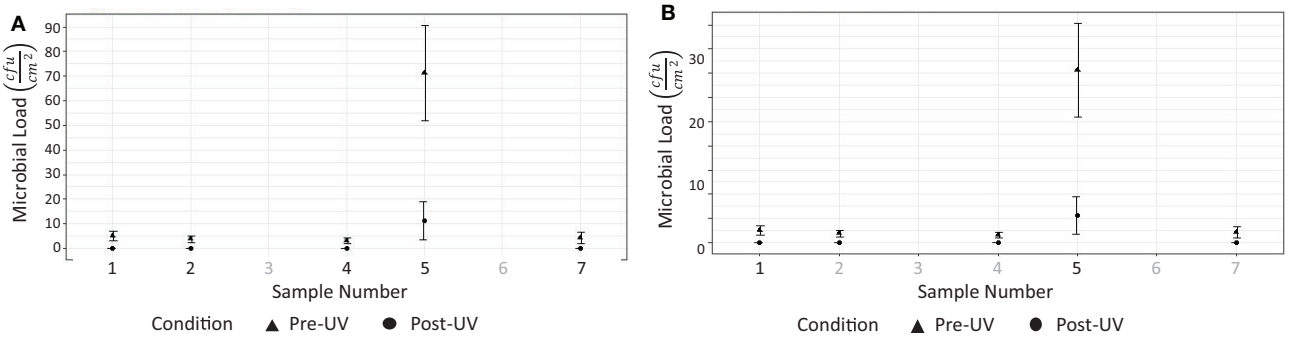

FIGURE 8 | Results from testing at hospital 2. **(A)** Reduction of measurable bacterial load on surfaces after 15 disinfection period (testing day 1). **(B)** Reduction of measurable microbial load on surfaces after 15 disinfection period (testing day 2).

performance at inactivating microbes with more complex cell structures. At a distance of 2 m, using the data given in **Figure 2**, we would expect *Violet* to generate a UV-C dose of approximately 4.2 mJ/cm^2 over a 2 minutes period. This is higher than the inactivation energy to achieve a log reduction of SARS-CoV-2, which was estimated by Heßling et al. (2020) to be 3.7 mJ/cm^2). Furthermore, we observed that the system was successful at inactivating *S. auris*, which, according to Kowalski (2010), has a UV inactivation energy for log reduction of 6.06 mJ/cm^2.

UVGI systems are widely used for air purification applications, so it is likely that a system like *Violet* will be effective at inactivate microbes in the air as well as on surfaces. However, the extent to which the methods used in this study may lead to measurable reductions of microbial load in air remains untested. As the distribution of microbes in the air is likely to fluctuate with changing air currents, measuring this would necessitate a different study design and was therefore beyond the scope of this paper. The authors think this would be an interesting piece of research for future work.

Our research provides evidence that relatively small doses of UV-C irradiation, suitably administered at short distances from target surfaces, can achieve significant reductions in microbial load. However, since relatively few studies have quantified the performance of manual disinfection methods, further work is needed in order to benchmark this performance with current disinfection standards. It is noted that in the preparation for this study, the authors performed a similar swab analysis to the one described in this work before and after a manual deep-clean of CT scan treatment room. We detected microbial load at four of the seven locations sampled. At these sample sites, the disinfectant cleaning only reduced the concentration by 10–30% at each location, indicating significantly worse performance than observed using UVGI in our experiments. It is not possible to draw conclusions from a single test, however this preliminary finding motivates follow-on work which should compare, where possible, the performance of UVGI relative to a benchmark of currently deployed cleaning methods.

It has been identified that a limitation of UVGI is that only surfaces that are in direct view of the light are irradiated, thus shadowing can prevent some surfaces being disinfected. Using a mobile robot base helped to mitigate this problem, since surfaces obscured when the robot was in one location, may not have been when the robot was in an adjacent position. However, there are certain features, such as the underside of door handles, where moving is not likely to affect things significantly. It may be possible to overcome this limitation with careful installation of reflective surfaces that could reflect UV light onto surfaces that may be otherwise obscured from the exposed lamp; the effectiveness of this approach merits further investigation. Similarly, it is conceivable that certain pieces of equipment, such as medical devices, may still necessitate manual cleaning regardless of whether they are irradiated by UV-C. Since these areas represent relatively small sections within the room, this should only demand to a small amount of human time. For example, we estimate in the radiology setting explored in this study, it would take approximately 1 minutes for a person to wipe down medical equipment and parts of the room that the light from the robot did not irradiate. This does, however, reinforce the need for coordination between the robot and the person tasked with cleaning the remaining parts of the room.

Through the addition of physical shielding on the robot, it was possible to control parts of the room that were irradiated with UV-C light. Since background radiation was found to be negligible, if implemented alongside suitable safety protocols, it's conceivable that a UVGI robotic system with a similar design may be deployed safely alongside staff, patients, or other hospital users. This feature would have an immediate advantage of increasing capacity within a radiology context, since it would enable staff to perform critical room preparation tasks at the same time that robot was disinfecting, thus shortening the turn-around time for the room. This capability may make the technology more accessible for use in settings like ICU where the incidence of HAIs is typically high and it is not normally possible to evacuate ventilated patients from the room to perform disinfectant cleaning. This design may also be advantageous for disinfecting public parts of the hospital (i.e., waiting areas, cafeterias, receptions, hallways) as well in non-clinical settings (i.e., trains, retail, airports) where frequent disinfection is needed but where it may not be possible to evacuate the space on a high-frequency basis.

The findings from this study raise several new research questions worth separate investigation. First, it would be interesting to know the time effects of UVGI treatment, namely if and for how long any germicidal effects of UVGI may persist after application. Second, with several different UV disinfectant robots on the market, and many with distinct designs, it would be of great interest to both the infection control community, as well as to hospital purchasing departments, to benchmark the germicidal performance of different UV disinfection robots from trials conducted in the field. It is noted that this paper is not the first to call for greater benchmarking; Masse et al. (2018) made the same observation and have already investigated the germicidal performance of two existing solutions (not capable of autonomous navigation) that are comparable with the robot in this study. Third, the findings in this work motivate a follow on clinical trial, whereby the germicidal performance of the UVGI system is measured directly against current disinfection procedures within radiology. Finally, while this study focused on a radiology department use-case, we have added to the body of scientific knowledge showing that the technology has the potential to be a powerful tool for limiting the spread of harmful pathogens, and may have a wide range of applications beyond radiography. As yet, few studies have yet investigated the effectiveness of UV disinfectant in non-clinical settings. The authors propose that testing in areas including on public transport, in nursing homes and long-term care, and in public buildings/schools/colleges would be interesting work.

7. CONCLUSIONS

Effectively preventing the spread of infectious diseases, such as COVID-19, requires the utilization of air/surface disinfectant practices as well as behavioral changes such as social distancing and cocooning. Currently, only chemical-based disinfectant practices are being widely used and recommended

by advisory groups such as the CDC and EPA. Alternative non-touch methods of disinfectant, such as ultraviolet germicidal irradiation, have the potential to overcome many of the practical limitations of chemical-based approaches, and may be automated for use in a much wider variety of settings where rigorous disinfectant protocols were previously not feasible, such as on public transport, nursing homes and in schools/universities. Our findings suggest that UVGI can effectively inactivate germs on commonly touched surfaces in radiology suites, even if the surfaces were not cleaned in advance and only exposed to relatively short bursts of irradiation. These results add to the growing body of scientific literature that supports the efficacy of UVGI in clinical settings. Our study also demonstrates the feasibility of using a bespoke robotic-UVGI system to reduce the time taken to disinfect rooms; in this study, we provide evidence that a comprehensive disinfectant procedure, that can operate in both the air and on surfaces, could feasibly be undertaken in 15 minutes or less. This new disinfectant approach is estimated to be between two and four times faster than currently-used chemical approaches. If such a system were implemented, it could both significantly improve workflow and machine utilization, and reduce exposure of front-line healthcare workers to infectious pathogens.

DATA AVAILABILITY STATEMENT

The raw data supporting the conclusions of this article will be made available by the authors, without undue reservation.

AUTHOR CONTRIBUTIONS

CM and MBe conceived of the presented idea. CM and ND developed robot used in the testing. CM, ND, MBe, and CK performed interviews and site visits to hospital locations. KR advised and assisted on the theory and analytical methods. CM and MBe conducted all microbial testing and analysis. All authors (including MBe and MBo) discussed the results and contributed to the final manuscript.

FUNDING

Funding for the project was provided from Science Foundation Ireland (SFI) under grant ID 20/COV/0021, as part of their COVID-19 Rapid Response initiative, as part of their COVID-19 Rapid Response Initiative.

ACKNOWLEDGMENTS

The authors would like to thank the Health Service Executive (HSE) as well as Midlands Regional Hospital, Tullamore for their involvement with the study.

SUPPLEMENTARY MATERIAL

The Supplementary Material for this article can be found online at: https://www.frontiersin.org/articles/10.3389/frobt.2020.590306/full#supplementary-material

REFERENCES

Boyce, J. M. (2016). Modern technologies for improving cleaning and disinfection of environmental surfaces in hospitals. *Antimicrob. Resist. Infect. Control* 5:10. doi: 10.1186/s13756-016-0111-x

Casini, B., Tuvo, B., Cristina, M. L., Spagnolo, A. M., Totaro, M., Baggiani, A., et al. (2019). Evaluation of an ultraviolet c (UVC) light-emitting device for disinfection of high touch surfaces in hospital critical areas. *Int. J. Environ. Res. Public Health* 16. doi: 10.3390/ijerph16193572

Chen, Q., Liang, M., Li, Y., Guo, J., Fei, D., Wang, L., et al. (2020). Mental health care for medical staff in china during the covid-19 outbreak. *Lancet Psychiatry* 7, e15–e16. doi: 10.1016/S2215-0366(20)30078-X

Darnell, M. E. R., Subbarao, K., Feinstone, S. M., and Taylor, D. R. (2004). Inactivation of the coronavirus that induces severe acute respiratory syndrome, SARS-CoV. *J. Virol. Methods* 121, 85–91. doi: 10.1016/j.jviromet.2004.06.006

Edwards, A. N., Karim, S. T., Pascual, R. A., Jowhar, L. M., Anderson, S. E., and McBride, S. M. (2016). Chemical and stress resistances of clostridium difficile spores and vegetative cells. *Front. Microbiol.* 7:1698. doi: 10.3389/fmicb.2016.01698

Eickmann, M., Gravemann, U., Handke, W., Tolksdorf, F., Reichenberg, S., Müller, T. H., et al. (2020). Inactivation of three emerging viruses–severe acute respiratory syndrome coronavirus, Crimean–congo haemorrhagic fever virus and nipah virus–in platelet concentrates by ultraviolet C light and in plasma by methylene blue plus visible light. *Vox Sang.* 115, 146–151. doi: 10.1111/vox.12888

Elgujja, A., Altalhi, H., and Ezreqat, S. (2020). Review of the efficacy of ultraviolet c for surface decontamination. *J. Nat. Sci. Med.* 3, 8–12. doi: 10.4103/JNSM.JNSM_21_19

Ethington, T., Newsome, S., Waugh, J., and Lee, L. D. (2018). Cleaning the air with ultraviolet germicidal irradiation lessened contact infections in a long-term acute care hospital. *Am. J. Infect. Control* 46, 482–486. doi: 10.1016/j.ajic.2017.11.008

First, M. W., Weker, R. A., Yasui, S., and Nardell, E. A. (2005). Monitoring human exposures to upper-room germicidal ultraviolet irradiation. *J. Occup. Environ. Hyg.* 2, 285–292. doi: 10.1080/15459620590952224

Fischer, R. J., Morris, D. H., van Doremalen, N., Sarchette, S., Matson, M. J., Bushmaker, T., et al. (2020). Assessment of n95 respirator decontamination and re-use for Sars-Cov-2. *MedRxiv [preprint]*. doi: 10.1101/2020.04.11.20062018

Guest, J. F., Keating, T., Gould, D., and Wigglesworth, N. (2019). Modelling the costs and consequences of reducing healthcare-associated infections by improving hand hygiene in an average hospital in England. *BMJ Open* 9:e029971. doi: 10.1136/bmjopen-2019-029971

Haas, J. P., Menz, J., Dusza, S., and Montecalvo, M. A. (2014). Implementation and impact of ultraviolet environmental disinfection in an acute care setting. *Am. J. Infect. Control* 42, 586–590. doi: 10.1016/j.ajic.2013.12.013

Heßling, M., Hönes, K., Vatter, P., and Lingenfelder, C. (2020). Ultraviolet irradiation doses for coronavirus inactivation-review and analysis of coronavirus photoinactivation studies. *GMS Hyg. Infect. Control* 15:doc08. doi: 10.3205/dgkh000343

Huang, J., Han, M., Luo, T., Ren, A., and Zhou, X. (2020). Mental health survey of 230 medical staff in a tertiary infectious disease hospital for covid-19. *Chin. J. Indust. Hyg. Occup. Dis.* 38, 192–195. doi: 10.3760/cma.j.cn121094-20200219-00063

Jinadatha, C., Villamaria, F., Restrepo, M., Ganachari-Mallappa, N., Liao, I.-C., Stock, E., et al. (2015). Is the pulsed xenon ultraviolet light no-touch

disinfection system effective on methicillin-resistant *Staphylococcus aureus* in the absence of manual cleaning? *Am. J. Infect. Control* 32, 878–881. doi: 10.1016/j.ajic.2015.04.005

Kac, G., Podglajen, I., Si-Mohamed, A., Rodi, A., Grataloup, C., and Meyer, G. (2010). Evaluation of ultraviolet c for disinfection of endocavitary ultrasound transducers persistently contaminated despite probe covers. *Infect. Control Hosp. Epidemiol.* 31, 165–170. doi: 10.1086/649794

Kampf, G., Todt, D., Pfaender, S., and Steinmann, E. (2020). Persistence of coronaviruses on inanimate surfaces and their inactivation with biocidal agents. *J. Hosp. Infect.* 104, 246–251. doi: 10.1016/j.jhin.2020.01.022

Kesavan, J., Schepers, D., Bottiger, J., and Edmonds, J. (2014). UV-C decontamination of aerosolized and surface-bound single spores and bioclusters. *Aerosol Sci. Technol.* 48, 450–457. doi: 10.1080/02786826.2014.889276

Kowalski, W. (2010). *Ultraviolet Germicidal Irradiation Handbook: UVGI for Air and Surface Disinfection*. Springer Science & Business Media. doi: 10.1007/978-3-642-01999-9

Lai, A. C. K., Nunayon, S. S., Tan, T. F., and Li, W. S. (2018). A pilot study on the disinfection efficacy of localized UV on the flushing-generated spread of pathogens. *J. Hazard. Mater.* 358, 389–396. doi: 10.1016/j.jhazmat.2018.07.003

Lindblad, M., Tano, E., Lindahl, C., and Huss, F. (2020). Ultraviolet-c decontamination of a hospital room: amount of UV light needed. *Burns* 46, 842–849. doi: 10.1016/j.burns.2019.10.004

Lindsley, W. G., McClelland, T. L., Neu, D. T., Martin, S. B., Mead, K. R., Thewlis, R. E., et al. (2018). Ambulance disinfection using ultraviolet germicidal irradiation (UVGI): effects of fixture location and surface reflectivity. *J. Occup. Environ. Hyg.* 15, 1–12. doi: 10.1080/15459624.2017.1376067

Masse, V., Hartley, M. J., Edmond, M. B., and Diekema, D. J. (2018). Comparing and optimizing ultraviolet germicidal irradiation systems use for patient room terminal disinfection: an exploratory study using radiometry and commercial test cards. *Antimicrob. Resist. Infect. Control* 7:29. doi: 10.1186/s13756-018-0317-1

Memarzadeh, F., Olmsted, R. N., and Bartley, J. M. (2010). Applications of ultraviolet germicidal irradiation disinfection in health care facilities: effective adjunct, but not stand-alone technology. *Am. J. Infect. Control* 38, S13–S24. doi: 10.1016/j.ajic.2010.04.208

Miller, R., Simmons, S., Dale, C., Stachowiak, J., and Stibich, M. (2015). Utilization and impact of a pulsed-xenon ultraviolet room disinfection system and multidisciplinary care team on *Clostridium difficile* in a long-term acute care facility. *Am. J. Infect. Control* 43, 1350–1353. doi: 10.1016/j.ajic.2015.07.029

Miller, S., Linnes, J., and Luongo, J. (2013). Ultraviolet germicidal irradiation: future directions for air disinfection and building applications. *Photochem. Photobiol.* 89, 777–781. doi: 10.1111/php.12080

Moore, G., Ali, S., Cloutman-Green, E. A., Bradley, C. R., Wilkinson, M. A., Hartley, J. C., et al. (2012). Use of UV-C radiation to disinfect non-critical patient care items: a laboratory assessment of the nanoclave cabinet. *BMC Infect. Dis.* 12:174. doi: 10.1186/1471-2334-12-174

Mortell, M. (2012). Hand hygiene compliance: is there a theory-practice-ethics gap? *Br. J. Nurs.* 21, 1011–1014. doi: 10.12968/bjon.2012.21.17.1011

Mossa-Basha, M., Meltzer, C. C., Kim, D. C., Tuite, M. J., Kolli, K. P., and Tan, B. S. (2020). Radiology department preparedness for covid-19: radiology scientific expert panel. *Radiology* 296:200988. doi: 10.1148/radiol.2020200988

Murphy, P., Kang, L., Fleming, M., Atkinson, C., Pryor, R., Cooper, K., et al. (2019). Effect of ultraviolet-c light disinfection at terminal patient discharge on hospital-acquired infections in bone marrow transplant and oncology units. *Am. J. Infect. Control* 48, 705–707. doi: 10.1016/j.ajic.2019.10.002

Santarpia, J. L., Herrera, V. L., Rivera, D. N., Ratnesar-Shumate, S., Denton, P. W., Martens, J. W., et al. (2020). The infectious nature of patient-generated SARS-CoV-2 aerosol. *medRxiv [preprint]*. doi: 10.1101/2020.07.13.20041632

Sherlock, O., O'Connell, N., Creamer, E., and Humphreys, H. (2009). Is it really clean? An evaluation of the efficacy of four methods for determining hospital cleanliness. *J. Hosp. Infect.* 72, 140–146. doi: 10.1016/j.jhin.2009.02.013

van Doremalen, N., Bushmaker, T., Morris, D. H., Holbrook, M. G., Gamble, A., Williamson, B. N., et al. (2020). Aerosol and surface stability of SARS-CoV-2 as compared with SARS-CoV-1. *N. Engl. J. Med.* 382, 1564–1567. doi: 10.1056/NEJMc2004973

Walker, C. M., and Ko, G. (2007). Effect of ultraviolet germicidal irradiation on viral aerosols. *Environ. Sci. Technol.* 41, 5460–5465. doi: 10.1021/es070056u

Yang, J.-H., Wu, U.-I., Tai, H.-M., and Sheng, W.-H. (2019). Effectiveness of an ultraviolet-C disinfection system for reduction of healthcare-associated pathogens. *J. Microbiol. Immunol. Infect.* 52, 487–493. doi: 10.1016/j.jmii.2017.08.017

Conflict of Interest: Two of the authors have involvement with a robotics company that are active in the development of a robotic disinfectant system. All work relating to the collection and analysis of data was performed by an author that is not involved in this company.

frontiers in Robotics and AI

METHODS
published: 29 January 2021
doi: 10.3389/frobt.2020.621580

Automated AMBU Ventilator With Negative Pressure Headbox and Transporting Capsule for COVID-19 Patient Transfer

Arnon Jumlongkul *

School of Medicine, Mae Fah Luang University, Chiang Rai, Thailand

Purpose: It is now clear that the COVID-19 viruses can be transferred via airborne transmission. The objective of this study was to attempt the design and fabrication of an AMBU ventilator with a negative pressure headbox linked to a negative pressure transporting capsule, which could provide a low-cost construction, flexible usage unit, and also airborne prevention that could be manufactured without a high level of technology.

Method: The machine consists of an automated AMBU bag ventilator, a negative pressure headbox, and a transporting capsule. The function and working duration of each component were tested.

Results: The two main settings of the ventilator include an active mode that can be set at the time range of 0 s–9 h 59 min 59 s and a resting mode, which could work continuously for 24 h. The blower motor and battery system, which were used to power the ventilator, create negative air pressure within the headbox, and the transporting capsule, could run for at least 2 h without being recharged. The transporting capsule was able to create an air change rate of 21.76 ACH with-10 Pa internal pressure.

Conclusion: This automated AMBU ventilator allowed flow rate, rhythm, and volume of oxygen to be set. The hazardous expired air was treated by a HEPA filter. The patient's transporting capsule is of a compact size and incorporates the air treatment systems. Further development of this machine should focus on how to link seamlessly with imaging technology, to verify standardization, to test using human subjects, and then to be the commercialized.

Keywords: automated AMBU, COVID-19, HEPA filter, negative pressure air, transporting capsule

OPEN ACCESS

Edited by:
John Oyekan,
The University of Sheffield,
United Kingdom

Reviewed by:
Selene Tognarelli,
Sant'Anna School of Advanced Studies, Italy
Muhammad Jawad Khan,
National University of Sciences and Technology (NUST), Pakistan

***Correspondence:**
Arnon Jumlongkul
arnon.jum@mfu.ac.th

Specialty section:
This article was submitted to Biomedical Robotics, a section of the journal Frontiers in Robotics and AI

Received: *26 October 2020*
Accepted: *21 December 2020*
Published: *29 January 2021*

Citation:
Jumlongkul A (2021) Automated AMBU Ventilator With Negative Pressure Headbox and Transporting Capsule for COVID-19 Patient Transfer. Front. Robot. AI 7:621580. doi: 10.3389/frobt.2020.621580

INTRODUCTION

The COVID-19 situation has resulted in the changing of many standard intubation and transportation procedures. Viruses can easily transmit via the airborne route and so many scientists have tried to create medical devices that can restrict the spread of COVID-19. Certain issues have to considered for the transport of critically ill COVID-19 patients, these include transport equipment pre-arrangements (e.g., portable ventilator, bag-valve-mask with oxygen tubing, infusion pump), preparations before transport (e.g., team coordination, limiting to essential medical

personnel), transport process (e.g., appropriate PPE, droplet precautions), then after arrival, post-transfer decontamination (e.g., a housekeeping team equipment as well as appropriate PPE to remove contaminations from the transfer route, patient's room, transport ambulance, and also preparing for the next mission), respectively (Yousuf et al., 2020). The concept of a mechanical ventilator started in the 14th century and the use of a positive-pressure mechanical ventilator became common around 1940. A typical mechanical ventilator consists of a control unit, blender, valves/turbine, and sensors. The construction of the ventilation mode should involve three elements, including, ventilator breath control variable (volume and pressure control), breath sequence, and targeting scheme (Dellaca' et al., 2017). In mass casualty cases, low-cost portable mechanical ventilators have proved to be essential. The ventilator mainly assists breathing using compression of a conventional bag valve mask (BVM) with an electric motor, an over-pressurization alarm system, and microcontroller board (Al Husseini et al., 2010). Due to the lack of adequate supplies of mechanical ventilators, exposed by the COVID-19 pandemic, a new portable ventilator design is suggested. The concept of this ventilator is the addition of a DC motor as a primary air compressor. Additional components also include a temperature sensor, heating resistor, pressure sensor, battery supply, audio alarms, LCD, and a start/stop system (El Majid et al., 2020). This provides the energy to overcome the BVM/air tank resistance in our prototypes, the estimation of tidal volume is then measured indirectly.

One of the interesting technologies that protect against COVID-19 spread is the use of negative pressure systems. According to the recommendations of the World Health Organization, probable or confirmed COVID-19 cases should avoid being moved or transported out of their area unless absolutely necessary, at which time availability of portable equipment becomes essential. Adequate ventilation is considered to be 6–12 air changes per hour (ACH) with a negative pressure difference of at least 2.5 Pa. Installation of exhaust fans and high-efficiency particulate air (HEPA) filters is required for environmental control (World Health Organization, 2020). For patient-care areas, the time required for airborne-contaminant removal by 99%, with 99.9% efficiency when the airflow is set as 12 ACH, is 23 min and 35 min, respectively, (Center for Disease Control and Prevention, 2019). One technique, which has been used to protect us from hazardous and dangerous situations, is the insulated patient transport capsule. Such systems can help protect medical personnel and patients against chemical, biological, radiological, and nuclear (CBRN) materials. The design concept of the CBRN transport capsule aimed to make the patient feel more secure, to promote trust, protection, and a blue color, which represents a feeling of calm (İşbilir et al., 2018). As there is a potential for clusters of COVID-19 patients, the design of containment capsules for COVID-19 patients must involve foldable, easy to construct structures that are easily transportable. The materials of the capsule must be light, have anti-corrosion properties, and be rigid during use. The use of aluminum tubes as the main structural component is an alternative way to create the capsule (Iván Cifuentes et al., 2020). Due to cost issues and availability mass production of the transporting capsule using aluminum as the predominant material may not appropriate for some developing countries, especially in Thailand.

In this pandemic, we also have found no complete protective-assisted ventilating device that can be used during the pre-intubation period, while waiting for invasive mechanical ventilation, and following the intubation period. Medical personnel, including the nurse operating the AMBU bag, the physician who inserts the endotracheal tube, and anyone who stays within that unit, must necessarily potentially be exposed to secretions from the patient. Even though some institutes have used an intubation acrylic box covered the patient's head during intubation, following the procedure exhaled and therefore infected air can spread. During the intubation period, airborne particle sizes of 0.3–2.5 μm can be decreased when using the sealed intubation box with suction, on the contrary, the erosol box solely showed an increase in 1.0–5.0 μm when compared with no device used (Simpson et al., 2020). Therefore, the objective of this article was to discuss the design and fabrication of an AMBU ventilator with a negative pressure headbox, incorporated with a negative pressure transporting capsule. This dual machine, which could provide a low-cost construction, ease of use, and easy to fabricate without a high level of technology, could then be used to protect medical personnel during periods of intubation as well as transport between units.

MATERIALS AND METHODS

This article was an experimental and pilot study. The tests of this dual machine also included continuous working, functions, battery endurance, and negative air pressure test. To prevent the spread of COVID-19, these anti-airborne system consists of three parts, including, a mechanical ventilator for the pre-intubation and intubation periods before using a standard mechanical ventilator, a negative pressure headbox for the post-intubation period, and finally a transporting capsule, which will be used during a patient's transfer. All materials within the ventilating system were certified as medical-grade products to make sure that patients will not suffer from any allergic conditions. The details of mechanical systems are shown below;

Automated AMBU bag Ventilator

Oxygen within a pipeline or a tank initially passes through an air filter and then into the ventilating system. A 12 V DC brushless motor for medical equipment, max power consumption 18 W, was used as a blower motor. In general, according to standard respiratory physiology, the tidal volume, which means the volume of each respiration, is usually 500 ml with a rate of 12 breaths min^{-1} (Carroll, 2007). Therefore, mechanical ventilation should be able to be adjusted to both higher and lower levels than the standard volume and rate. To control flow rate, rhythm, and volume of oxygen, three electrical circuits, including, a speed control circuit, a timer circuit, and a battery protection circuit,

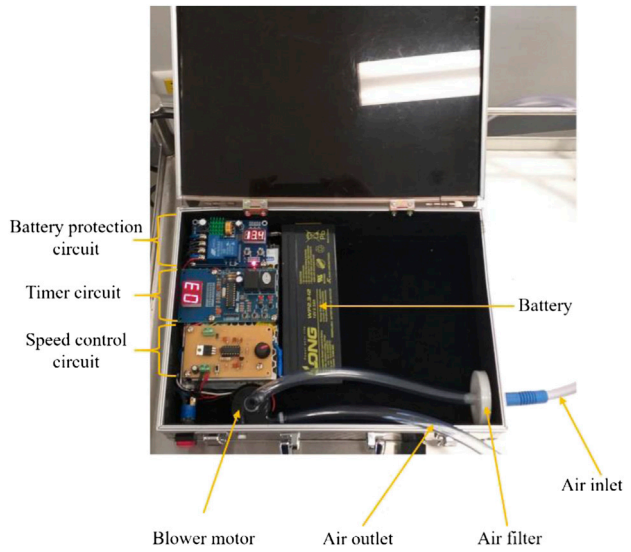

FIGURE 1 | The prototype of the mechanical ventilator.

were incorporated with the blower. A pressure release valve, set to operate if the air pressure exceeds 40 cm H_2O, was fitted to the AMBU bag. A 12 V 2.3 Ah rechargeable sealed lead-acid battery was used as the main power supply. The machinery functions and working duration were tested. A mechanical ventilator prototype is shown in **Figure 1**.

Negative Pressure Headbox

The headbox, which was mainly made of a PVC transparent sheet 0.5 cm thickness, was used as air-borne protective equipment. Four waterproof zippers were amalgamated with the headbox for hand and/or tube insertion. After the intubation procedure, hazardous air within the box was treated by HEPA filter and a blower motor that had the same specification as the mechanical ventilator. A 12 V 7 Ah lithium battery powered this machine. For ease of use all components of the headbox, except the HEPA filter, can be cleaned by any disinfectants. The blower and battery workings were tested. The negative pressure headbox model is shown in **Figure 2** while the combination of an automated AMBU ventilator with a negative pressure headbox is shown in **Figure 3**. The set of HEPA filter, blower motor, and battery are shown in **Figure 4**.

Negative Pressure Transporting Capsule

Similar with the negative pressure headbox, a semi-circular cylindrical transporting capsule, measuring 0.28 m^3 in volume (where: r = 0.3 m and L = 2.0 m), which is shown in **Figure 5**, was made of PVC materials and waterproof zippers. The design of the capsule was of a compact size, which could be loaded into either an ambulance or CT scan. The set-up of the HEPA filter, blower motor, and the battery was the same as for the negative pressure headbox. A digital airflow anemometer Model GM8901, measurement range 0–45 m s^{-1} (accuracy ±3%), was used for air velocity measurement within the closed system. The calculation of air changes per hour used the following formula:

$$ACH = \frac{3600 \cdot Q}{Vol}$$

Where:

- ACH = number of air changes per hour
- Q = volumetric flow rate of air in cubic meter per second
- Vol = space volume in a cubic meter

The pressure of the inside as well as outside capsule was measured using a portable multifunction digital LCD barometer that has a measurement range of 300 to 1,000 hPa.

According to the situation being, in Chiang Rai Province, Thailand, all COVID-19 patients have been sent to the Chiangrai Prachanukroh Hospital, which is the biggest medical center in Chiang Rai Province. By the way, no COVID-19 case has been detected at the Mae Fah Luang University Medical Center Hospital. We are therefore unable to test these instruments with COVID-19 patients at this moment. We will test the ventilator and capsule function absolutely in a real case as soon as possible. This step also only described how to fabricate and test in a preliminary laboratory scale. This experiment is only a design, fabrication, and test of machines without human participation. At this moment, the ethical committee review, therefore, was unnecessary.

RESULTS

The dual prototype of an automated AMBU ventilator and transporting capsule was fabricated and tested. The preliminary outcomes showed that each mechanical system could work for more than 24 h continuously. The summary of the system architecture diagram of both machines is shown in **Figure 6**. The results are shown below.

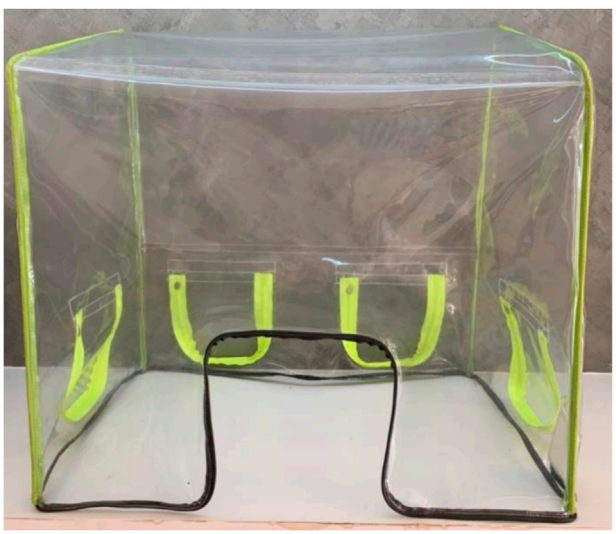

FIGURE 2 | The prototype of the negative pressure headbox.

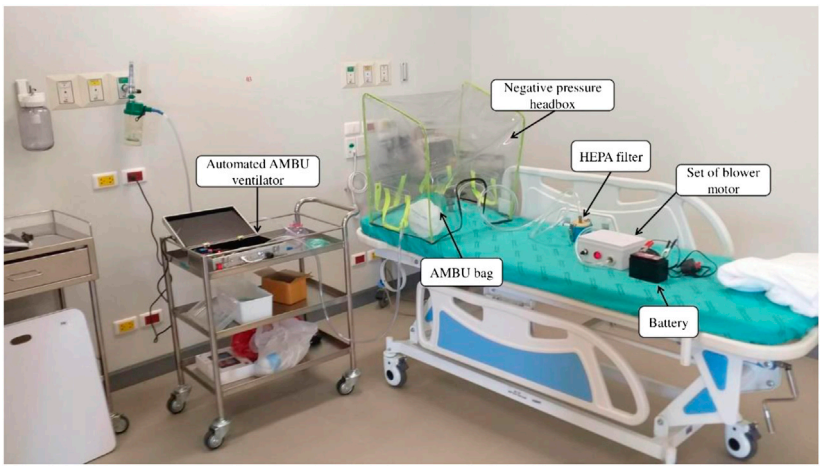

FIGURE 3 | The prototype of the automated AMBU ventilator with the negative pressure headbox.

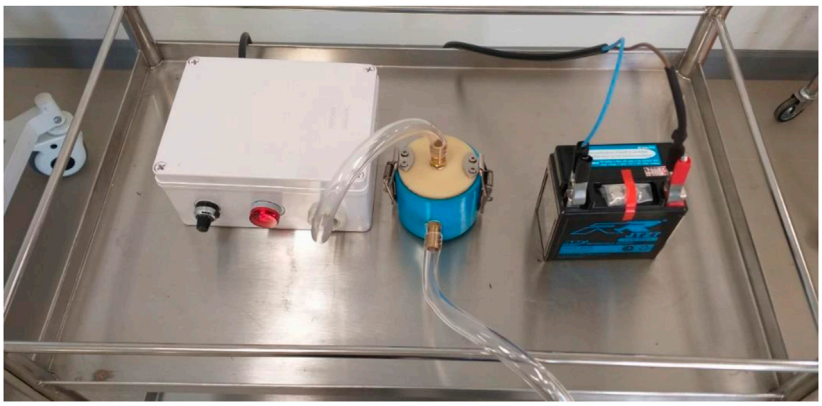

FIGURE 4 | The set of blower motor within the box (left), HEPA filter (middle), and battery (right).

FIGURE 5 | Model of the negative pressure transporting capsule with the set of the blower motor.

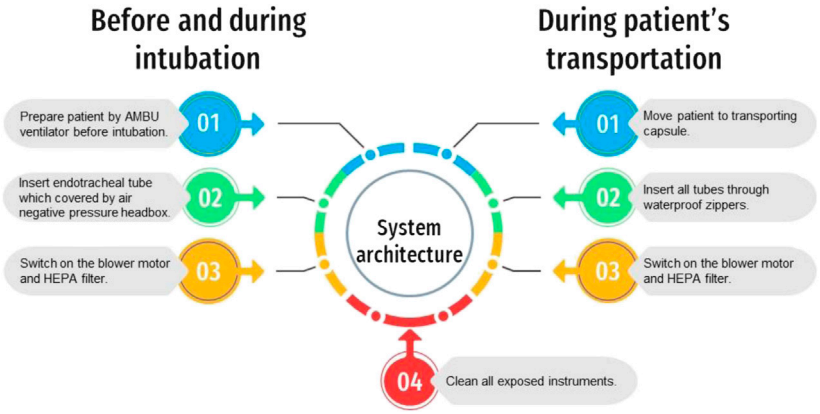

FIGURE 6 | The system architecture diagram of the mechanical ventilator and the transporting capsule.

Functional and Endurance Test

The mechanical ventilator speed control circuit can be adjusted from 0 to 100%. The two main functions of the ventilator include, firstly, an active mode, which can be adjusted at the resolution of 1 s and can be set to cover a range of 0 s–9 h 59 min 59 s. The delay time of the blower motor is approximately 1 s. Secondly, a rest mode can be controlled as an active mode without delay time. At maximum power the blower filled a 2,000 ml reservoir bag within 1.5 s. It was confirmed that the battery system could operate for up to 2 h without recharging.

The blower motor and battery system, which were used to create negative air pressure within a headbox as well as the transporting capsule, were also able to run for at least 2 h without recharging, which is a sufficient time for transferring patient between units.

Negative air Pressure Test

The transporting capsule was used for the negative air pressure experiment. The maximum air velocity at the end of the blower tube, measuring 1.905 cm in diameter, was 6 m s^{-1}. Therefore, this capsule also showed 21.76 ACH, which was more than 2–3 times greater than that of the World Health Organization's recommendations for such a system.

Air pressure within the capsule was approximately 10 Pa lower than the outside environment, when measured at 27.8°C, confirming that this method can create the required negative pressure for safe usage.

In case of any unforeseen issues, for example, if the mechanical ventilator cannot run, or maybe some accidents occur within the ventilation system, the user can pull the oxygen supply extension tubing off, then, connect it to the AMBU bag within the negative pressure headbox directly. The blower motor and the HEPA filter system of both the negative pressure headbox and the transporting capsule can be switched to another machine together. Therefore, medical personnel can use these air purifier systems simultaneously or individually.

DISCUSSION

All inventions that were fabricated in this study, were created within a time limit according to the COVID-19 situation. All development has been carried out at the Mae Fah Luang University Medical Center Hospital, Chiang Rai Province, Thailand, which is far away from the capital city. We have suffered with a lack of raw materials as well as monetary resources. These machines can run at least 24 h continuously. The mechanical ventilator can be used during pre-intubation and intubation period to control air flow rate, rhythm, and volume of oxygen in primary. The transporting capsule is of a compact size and incorporates the air treatment systems. Air pressure within the capsule was lower than the required negative pressure for safe usage. The hazardous expired air from the PVC headbox and also the transporting capsule was treated by a HEPA filter, which was able to run for at least 2 h without recharging. The author received a budget, to include the costs for fabrication and transportation, of 36,000 Thai Baht (THB) for the transporting capsule as well as 60,000 THB for the automated ventilator. As part of the ongoing development of the AMBU ventilator, a microcontroller should be incorporated to feedback any signals from the patient. For example, respiratory rate, positive end-expiratory pressure (PEEP), oxygen fraction, inspired tidal volume, expired tidal volume, peak pressure, etc. Then all parameters should be expressed on an LCD monitor and evaluated to provide optimum ventilation for each patient (Govoni et al., 2012).

A preliminary design of the transporting capsule focused on the overall utility of the machine, which should be able to be used within an ambulance or CT scanner. However, as a result of the COVID-19 travel restriction and state quarantine policies of Thailand, the inventor could not source suitable plastic materials to create the frame of this capsule. As a result thin wire had to be substituted to preserve the shape of the capsule. Other parts of the capsule that also had to be made from metal, were the waterproof zippers. In a second prototype it should be made of 100% plastic-based materials, without metal components, to allow compatibility of use with any diagnostic imaging devices. All devices should be able to be stored within a compact unit, so be portable and foldable.

Finally, these machines were fabricated and tested during the rush hour of the COVID-19 pandemic, they were also declared as the prototype scale. When the prototype concepts are finalized, they will be certified by national standard organizations (e.g., Thai

Food and Drug Administration, ISO 13485, ISO 15189) and then testing of the machines with human subjects will commence.

CONCLUSION

In summary, the automated AMBU ventilator allows the initial setting of preliminary flow rate, rhythm, and volume of oxygen during the intubation period, so protecting medical colleagues from potential erosol infection, but this first version has no ability to respond to respiratory feedback from the patients. The hazardous expired air is collected within the transparent PVC headbox and filtered through a HEPA filter, amalgamated with a blower motor, so returning fresh air to the environment. After intubation, patients can be transferred within the transport capsule, which has a compact size and contains the air treatment systems, including the negative pressure headbox, all constructed of PVC based materials. These machines, except some electronic parts that are separated from the contaminated airway systems and also have never exposed to viruses, can be cleaned by the same disinfectants as previous devices, for example, ethyl alcohol, sodium hypochlorite solution, calcium hypochlorite solution, hydrogen peroxide, etc. However, heat sterilization should be avoid because almost all headbox and also capsule materials were made of PVC sheet. Only the set box for housing HEPA filter can be treated using hot steam. This dual machine is safe, and can be fabricated easily in low and middle-income countries while the traditional ventilator systems also need some advanced technologies, followed by high-priced machines as well as the huge customary transport capsules that have been usually designed for transferring the patients between units, but also they cannot be entered into either an ambulance or CT scan. In the future all metal parts need to be replaced with plastic-based materials, operating standards need to be verified, testing on human subjects must be completed, and then the system needs to be properly marketed.

DATA AVAILABILITY STATEMENT

The original contributions presented in the study are included in the article/Supplementary Material, further inquiries can be directed to the corresponding author.

AUTHOR CONTRIBUTIONS

The author confirms being the sole contributor of this work and has approved it for publication.

FUNDING

These inventions are supported by the Princess Srinagarindra's Centenary Celebrations Foundation, Memorandum No. 28/2563 as well as the Mae Fah Luang Intellectual Property Management and Innovation Division, fiscal year 2020.

ACKNOWLEDGMENTS

The author would like to thank Watchara Jamnuch, an electrical engineer, for technical support, also Roger Timothy Callaghan, School of Medicine, Mae Fah Luang University for grammatical approval.

REFERENCES

Al Husseini, A. M., Lee, H. J., Negrete, J., Powelson, S., Servi, A. T., Slocum, A. H., et al. (2010). Design and prototyping of a low-cost portable mechanical ventilator. *J. Med. Dev. Trans. ASME* 4 (2), 027514. doi:10.1115/1.3442790

Carroll, R. G. (2007). "Pulmonary system," in *Elsevier's integrated physiology*. 1st End. Greenville, NC: Mosby Elsevier, 356.

Center for Disease Control and Prevention (2019). Appendix B. Air guidelines for environmental infection control in health-care facilities. Available at: https://www.cdc.gov/infectioncontrol/guidelines/environmental/appendix/air.html (Accessed July 22, 2003).

Dellaca, R. L., Veneroni, C., and Farre', R. (2017). Trends in mechanical ventilation: are we ventilating our patients in the best possible way? *Breathe* 13 (2), 84–98. doi:10.1183/20734735.007817

El Majid, B., El Hammoumi, A., Motahhir, S., Lebbadi, A., and El Ghzizal, A. (2020). Preliminary design of an innovative, simple, and easy-to-build portable ventilator for COVID-19 patients. *Euro-Med. J. Environ. Integ.* 5 (2), 23. doi:10.1007/s41207-020-00163-1

Govoni, L., Penuelas, O., Artigas, A., Dellaca, R. L., Bellani, G., Ferrer, M., et al. (2012). Actual performance of mechanical ventilators in ICU: a multicentric quality control study. *Med. Dev. Evid. Res.* 5, 111–119. doi:10.2147/MDER.S35864

Iván Cifuentes, J., Cabrera, L., Aguilar, F., Mendizabal, L., Perez, L., de la Cruz, C., et al. (2020). Design of containment capsule for covid-19 patients transport. *Res. Med. Eng. Sci.* 9 (1), 932–934. doi:10.31031/RMES.2020.09.000701

İşbilir, F., Kaynak, M. F., and Kesemen, M. A. A. (2018). Insulated patient transport capsule for chemical, biological, radiological and nuclear (CBRN) contamination cases. *Eur. Mech. Sci.* 2 (4), 133–139. doi:10.26701/ems.464243

Simpson, J. P., Wong, D. N., Verco, L., Carter, R., Dzidowski, M., and Chan, P. Y. (2020). Measurement of airborne particle exposure during simulated tracheal intubation using various proposed aerosol containment devices during the COVID-19 pandemic. *Anaesthesia* 75 (12), 1587–1595. doi:10.1111/anae.15188

World Health Organization (2020). Infection prevention and control during health care when coronavirus disease (COVID-19) is suspected or confirmed. Available at: https://apps.who.int/iris/rest/bitstreams/1284718/retrieve (Accessed June 29, 2020).

Yousuf, B., Sujatha, K. S., Alfoudri, H., and Mansurov, V. (2020). Transport of critically ill COVID-19 patients. *Inten. Care Med.* 46 (8), 1663–1664. doi:10.1007/s00134-020-06115-1

Conflict of Interest: The author declares that the research was conducted in the absence of any commercial or financial relationships that could be construed as a potential conflict of interest.

frontiers in Robotics and AI

ORIGINAL RESEARCH
published: 17 February 2021
doi: 10.3389/frobt.2020.622083

Robotic-Assisted Surgery for Cadaveric Skull Opening: A New Method of Autopsy Procedure

Arnon Jumlongkul[1]* *and Panuwat Chutivongse*[2]

[1]School of Medicine, Mae Fah Luang University, Chiang Rai, Thailand, [2]Department of Forensic Medicine, Faculty of Medicine, Chulalongkorn University, Bangkok, Thailand

Background: Sawing of bone is an essential part of an autopsy procedure. An oscillating saw always generates noise, fine infectious dust particles, and the possibility of traumatic injuries, all of which can induce occupational hazard risks to autopsy workers, especially during the COVID-19 pandemic.

Objectives: The first goal of this study was to explore the production of noise and bone dust emission, comparing an oscillating saw and a robotic autopsy saw during an autopsy. The second goal was to evaluate the performance of a new robotic autopsy method, used during skull opening. The third goal was to encourage mortuary workers to use robotic technology during the autopsy procedure to protect us away from occupational injuries as well as airborne infections.

Materials and Methods: The experiments involved a comparison of noise levels and aerosol production during skull cutting between the oscillating saw and the robotic autopsy saw.

Results: The results confirmed that noise production from the robotic autopsy saw was lower than the oscillating saw. However, the bone dust levels, produced by the robotic autopsy saw, were greater than the oscillating saw, but were not greater than the dust concentrations which were present before opening the skull.

Conclusions: The use of a new robotic system might be an alternative choice for protecting against occupational damage among the healthcare workers. Further research might attempt to consider other healthcare problems which occur in the autopsy workplace and apply the robotic-assisted technology in autopsy surgery.

Keywords: aerosol, autopsy noise, bone dust, oscillating saw, robotic-assisted surgery, robotic autopsy saw

OPEN ACCESS

Edited by:
John Oyekan,
The University of Sheffield,
United Kingdom

Reviewed by:
Changsheng Li,
Beijing Institute of Technology, China
Yue Chen,
University of Arkansas, United States

***Correspondence:**
Arnon Jumlongkul
arnon.jum@mfu.ac.th

Specialty section:
This article was submitted to Biomedical Robotics, a section of the journal Frontiers in Robotics and AI

Received: *27 October 2020*
Accepted: *22 December 2020*
Published: *17 February 2021*

Citation:
Jumlongkul A and Chutivongse P (2021) Robotic-Assisted Surgery for Cadaveric Skull Opening: A New Method of Autopsy Procedure. Front. Robot. AI 7:622083. doi: 10.3389/frobt.2020.622083

INTRODUCTION

'Autopsy' is a surgical procedure performed by pathologists, the purpose of which is to discover the cause of death, the manner of death, the mechanism of death, and any other issues related to the death. The autopsy must be done even though the COVID-19 situation has been going on. There are two types of autopsies, namely a medico-legal or forensic autopsy (i.e., autopsy, which is performed for legal purposes) and a clinical or academic autopsy (i.e., autopsy that is requested by physicians for reasons other than those required for legal purposes). An autopsy includes the external examination

of the body and dissection of internal organs from many sites of body cavities, namely cranial, thoracic, abdominal, and pelvic cavities (Ayoub and Chow, 2008; Pluim et al., 2018). To make the external cranial examination, the pathologists usually inspect and clarify the features of the cadaver's head, identify any external wounds, take photographs, and incise the scalp across the posterior vertex from behind the ears. The tissues are reflected in the lower forehead and occiput for preparing the bone cut. The skull is sawn by hand or power tools and the calvarium is then removed after this cut is completed. To start the intracranial examination, the dura is incised to allow brain removal, and the base of the skull is examined. The brain is brought into a pan for measuring and weighing before further dissection and tissue fixation (Pekka Saukko, 2015).

The human skull was originally cut using a hand saw, which consumed considerable time and labor. Occasionally, a slippery skull could not be held firmly, causing accidental operator injuries. Therefore, many types of electric autopsy saws were developed for this work, including both band and circular saws, but these are prone to causing hand injuries. Oscillating saws, which are routinely used during autopsy operation, always generate aerosol production from bone cutting and so can spread hazardous pathogens, such as Human Immunodeficiency Virus (HIV), Hepatitis B and C, Streptococci, etc. In post-mortem COVID-19 cases, SARS-CoV-2 and its viral protein could be found in the brains and cranial nerves, respectively (Matschke et al., 2020). Sometimes airborne infections, especially tuberculosis, can involve the human skull, also called 'calvarial tuberculosis'(Rosli and Harun, 2016). Saw blade frequency and saw blade contact loads on the bone affect the production of these aerosols. However, almost all forensic autopsies have operated for either unnatural or sudden death cases that we also do not know their COVID-19 exposed histories. Consequently, mortuary staff may expose any hazardous micro-organisms inevitably.

Vast amounts of aerosol particles can be produced by the oscillating saw, measuring 0.3–10 μm, while the bone band saw generates respirable aerosolized particles between 0.3 and 5 μm in diameter (Wenner et al., 2017; Pluim et al., 2018). For human safety, oscillating saws are used for skull cutting, but still produce heavy noise pollution and bone dust. The modified type of 'oscillating saw with spray-tube' and 'oscillating saw with exhauster' were invented to help prevent co-workers exposure to airborne infection (Kernbach-Wighton et al., 1996; Kernbach-Wighton et al., 1998). Additionally the noise hazard in an operating room can adversely affect the inner ear structure and can cause noise-induce hearing loss (NIHL) among surgeons and their colleagues. The peak sound level in an operating theater may exceed 140 dBA. To reduce the intensity of the noise from bone surgery, the use of oscillating tip saw systems are preferred to oscillating saw blade systems (Peters et al., 2016; Razali et al., 2017).

According to the development of robotic-assisted surgery, previous studies showed some advanced surgical technologies, for instance, firstly, the use of an improved recurrent neural network (RNN) scheme for controlling the trajectory of redundant robot manipulators, which has been used for the surgical tasks related to tumor resection skills (Su et al., 2020a). Secondly, the teleoperated Minimally Invasive Surgery (MIS) using an improved human-robot collaborative control (IHRCC) scheme, this technique can improve the accuracy of both a remote center of motion (RCM) constraint and also surgical tip (Su et al., 2019). Thirdly, the incorporation of an Internet of Things and Robot-assisted Minimally Invasive Surgery, which can improve the RCM constraint as well as surgical tip (Su et al., 2020b). Although massive articles have focused on the improvement of surgical technique within a human, unfortunately, medical personnel and also engineers scarcely think about how to apply human-robot interaction for mortuary tasks.

Nowadays the most commonly used autopsy saw is an oscillating saw, without spray-tube or suction, and the workers are therefore still exposed to the risk of injuries, pathogens from bone dust and secretions, and loud noise pollution. Therefore, the first goal of this study was to explore the production of noise and bone dust emission between a traditional oscillating saw and a robotic autopsy saw, which the authors just made before, when used in an autopsy room during the autopsy. The second goal was to evaluate the performance of robotic autopsy saw which represents a new method of skull opening. Finally, to encourage mortuary workers to use robotic technology to protect us away from occupational injuries as well as airborne infections, especially tuberculosis and also COVID-19.

MATERIALS AND METHODS

According to the lack of robotic study in the field of forensic medicine, then, this article was a pilot and an experimental study. The tests of the 2-machine also included average noise levels and also the number of aerosol particles. Experimental details are shown below.

Subjects

Cadaveric subjects, who died from May 2018 to January 2019 as a result of unnatural deaths, were brought to the Department of Forensic Medicine, Faculty of Medicine, Chulalongkorn University, Bangkok, Thailand for a forensic autopsy. The inclusion criteria were as follows:

1. The cadavers were adult 20–70 years old;
2. There was no history of osteoporosis or disease related to malformation of bone.

The exclusion criteria also included

1. Either the scalp or skull presented pathologic or traumatic findings when inspected by gross examination.

Ten corpses were selected for this research. Eight deceased subjects were male (age 23–57 years, mean age 42.6 years) and two cadavers were female (age 56 and 65 years, mean age 60.5 years). The complete forensic autopsies were performed at the Chulalongkorn Forensic Medicine Center, Department of

FIGURE 1 | The plastic head model, which in place of the human skull, was set in a supine position.

Forensic Medicine, Faculty of Medicine, King Chulalongkorn Memorial Hospital. This research was permitted by the Institutional Review Board of the Faculty of Medicine, Chulalongkorn University, Bangkok, Thailand (COA No. 880/2016, IRB No. 557/59). Written informed consent was obtained from the corpse's legal guardian/next of kin for the publication of any potentially identifiable images or data included in this article.

Experimental Setup

The cadavers were divided into two groups; five cadavers for oscillating saw testing and five cadavers for robotic autopsy saw testing. The deceased subjects were positioned in a supine position. Scalp opening was done. There was no autopsy procedure before, during, and after each experiment for at least 30 min. All experiments were performed on the same autopsy bed which was 80 cm high. Both the sound level meter and real-time dust monitor were placed at the same reference point, at a distance of 100 cm away from the calvarium on the horizontal axis and parallel to the calvarium. All skull cutting procedures, except the forensic physicians, were done by the same mortuary team. The position of cadaver is shown in **Figure 1**.

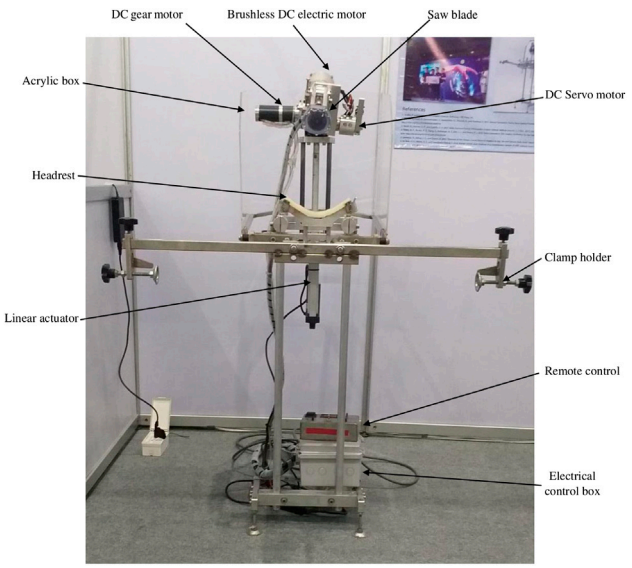

FIGURE 2 | The entire part of the robotic autopsy saw.

Autopsy Saw Instruments

Oscillating Saw

An oscillating autopsy saw (SG-700–01, SCHREIBER GmbH), 220–240 V 50 Hz 250 W strokes 12,000–21,000/min with segment saw blade (model SG-400–08), was used for this research. The sawing rotation and the saw blade depth were controlled at the surgical site (SCHREIBER GmbH, 2012).

Robotic Autopsy Saw

As part of mechanical design, this robot machine consists of four parts. Firstly, the rotary direction set, for controlling the speed of the saw frame, from 0 to 1 RPM. Secondly, the circular saw blade set, for adjusting the speed of the saw blade from 0 to 6,300 RPM. Thirdly, the saw blade depth, which is controlled from 0 to 20 mm. Finally, the electrical circuit is attached to a battery, which works by an analog signal with Pulse width modulation (PWM) for stabilizing the signal. The remote control system is housed in the high-grade aluminum electrical control box, which consists of a digital battery voltage indicator with an LCD display, the buttons for controlling the speed of the saw blade, the depth of the saw blade, the rotation of the saw frame, and also the emergency STOP push button. The autopsy operator can stand

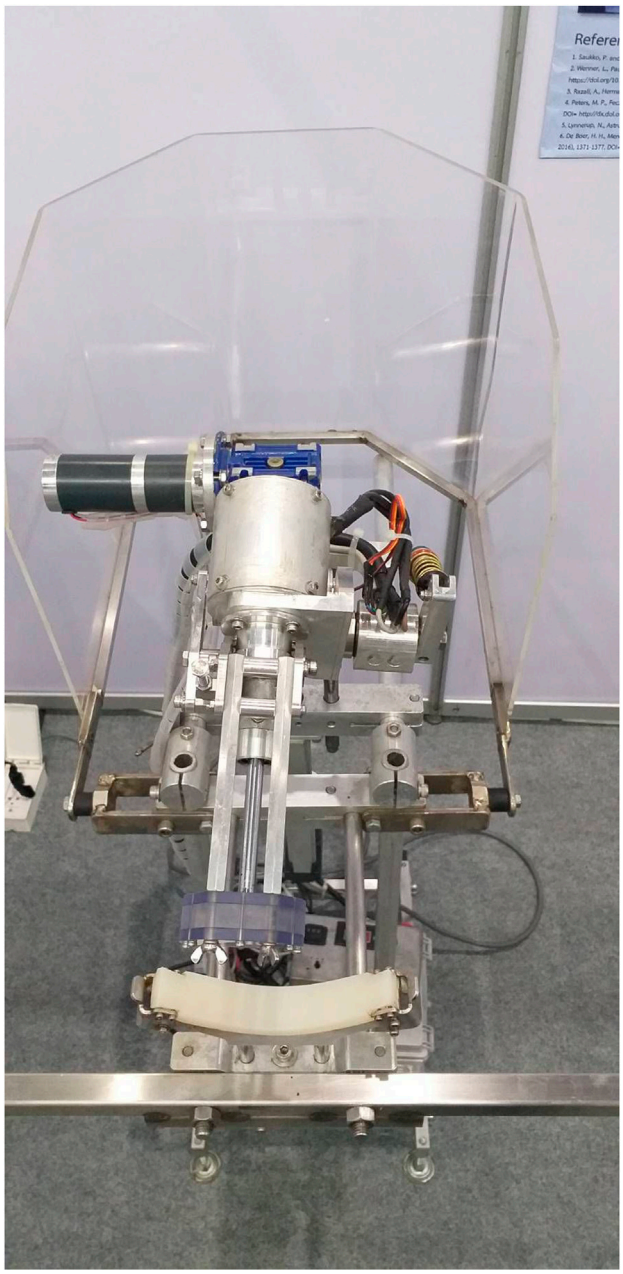

FIGURE 3 | The saw frame set of the robotic autopsy saw which can turn around the cadaveric skull.

away from the robotic autopsy saw and regulate it, from a radius of 2 m or further, depending on the cable length. The robotic autopsy saw was designed and tested with plastic skull models to ensure that it could cut the cadaveric skull perfectly (Jumlongkul and Chutivongse, 2019). The prototype of this machine is shown in **Figures 2–4**.

Acoustic Measurement

All noise measurements were carried out during the skull cutting with a sound level meter (model TES-1351, resolution 0.1 dB, range from 35 to 130 dB, accuracy ±1.0 dB), which converts an acoustic wave to a unit of sound measurement (dB) (TES Electrical Electronic Corp, 2014). Two kinds of acoustic measurements were tested, including a peak sound level and a time-weighted average (TWA) over 30 s for each cadaver. These were analyzed by comparison of two cadaveric groups with an arithmetic mean ± SD using Microsoft Excel Office 365.

The continuous steady or fluctuating noise over 1 h was calculated from the equivalent noise level in 1 h (LAeq, Tr), calculated as follows:

$$\mathrm{LAeq,\,Tr} = \mathrm{LAeq,\,Tm} + 10\,\mathrm{Log10}\left(\mathrm{Tm}/\mathrm{Tr}\right)$$

Where Tr is the average noise level (60 min), Tm is the actual time (0.5 min), and LAeq Tm is the specific noise over a representative period, which reflects variations from the specific source (dBA).

The continuous steady or fluctuating noise (LAeq, Ts), measured 5 times for each cadaveric group. was corrected using:

$$\mathrm{LAeq,\ Ts} = 10\ \mathrm{Log}\ 10\left\{\left(\frac{1}{\mathrm{Tm}}\right)\sum Ti10^{0.1\mathrm{LAeq,Ti}}\right\}$$

Where Ti is the duration of time from the origin of a source at i (min). LAeq, Ts was corrected with the constant volume adjustment and noted as LAeq, Tm in formula 1, which would be investigated for LAeq, Tr.

In all the experiments, the noise dosimeter was calibrated daily before collecting sound levels for each sample (Belcham, 2015).

Aerosol Measurement

The aerosol particles, present in the air during the experiments, were detected using a portable real-time dust monitoring device (CASELLA CEL Micro Dust Pro, measuring range 0.001 mg/m^3 to 250 g/m^3) which samples total, respirable, PM2.5 or PM10 with an optional adaptor. This dust collector machine can detect the aerosol particles using a forward light scattering method which converts the signal to a unit of dust per volume (mg/m^3) (CASELLA CEL Inc, 2012). Peak dust concentration levels and mean levels of dust concentration, over 30 s, during the experiments were collected. The data from each group was calculated and interpreted using an arithmetic mean ± SD by Microsoft Excel Office 365.

RESULTS

All the experiments were conducted by the same mortuary technician. From a total of ten cadaveric skulls, five were cut by the oscillating saw and five by the robotic apparatus. The auditory and dust measurements were as follows;

Acoustic Profiles

The average noise levels in an autopsy room, during usual operations without machine saws working, were measured over 30 s at 71.7 dBA (data not shown in **Table 1**). The average noise levels during every experiment (LAeq, Tr) in the robotic autopsy saw group, measuring 58.9 dBA, was lower than the oscillating saw group, measuring

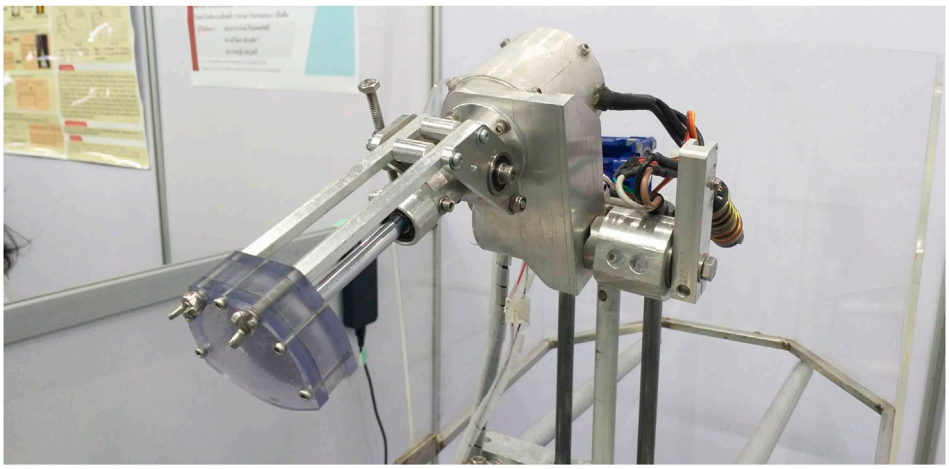

FIGURE 4 | Closed-up view of the circular saw blade set covered by an acrylic protector for human safety and prevent secretion spreading.

TABLE 1 | The noise exposures in an operating room during skull cutting. Measurements of the noise levels (Peak Level and LAeq, Tr) for each experiment, and the average noise level (Total LAeq, Tr) of the oscillating saw as well as the robotic autopsy saw.

Procedure	Average peak level (Min-Max) (dBA)	LAeq, tr in each cadaver (dBA)				Total LAeq, tr (dBA)
		Min	Max	Mean	SD	
Oscillating saw	94.0 (88.1–99.7)	64.6	71.4	67.5	±3.2	75.5
Robotic autopsy saw	86.9 (81.0–90.7)	44.2	67.6	58.9	±9.7	70.9

67.5 dBA, as well as Total LAeq, Tr (70.9 dBA with robotic autopsy saw and 75.5 dBA with oscillating saw, respectively). It should be noted that the total noise level (Total LAeq, Tr) for the robotic system did not exceed that of the usual noise level conducted without an electric saw. During parts of both of the saw procedures, the noise levels were low. However, the highest peak sound level was 99.7 dBA, which occurred during operation of the oscillating saw while the lowest peak was reported during the robotic procedure, measured at 81.0 dBA. The peak sound levels were in excess of 90 dBA in both groups. The calculated data were shown in **Table 1**.

Aerosol Particles

From **Table 2**, before the skull cutting experiments of two cadaveric groups, the average peak concentration of dust in the autopsy room, detected over 30 s, was 1.853 mg/m^3 (the minimum value of 0.018 mg/m^3 and the maximum value of 2.750 mg/m^3, respectively) which was the greatest value when compared with the oscillating saw and robotic autopsy saw. The average peak aerosol concentration of the oscillating saw, measured at 0.431 mg/m^3, was higher than the robotic machine procedure (0.346 mg/m^3). Importantly, the average aerosol concentration before skull cutting was 0.153 mg/m^3 (the minimum value of 0.016 mg/m^3 and the maximum value of 0.299 mg/m^3, respectively) which was the highest value among both of oscillating saw and robotic autopsy techniques. Nevertheless, the average aerosol concentration of the oscillating saw procedure, approximately 0.030 mg/m^3 (the minimum value of 0.014 mg/m^3 and the maximum value of 0.056 mg/m^3, respectively), was at a lower level than the dust generated by the robotic method, measuring 0.106 mg/m^3 (the minimum value of 0.016 mg/m^3 and the maximum value of 0.148 mg/m^3, respectively.

TABLE 2 | Dust concentrations before skull cutting and during two different skull cutting procedures: oscillating saw and robotic autopsy saw. The peak concentrations, mean values, standard deviations, minimum and maximum levels of dust per volume over ten subjects.

Procedure	Peak concentration (mg/m^3)		Dust per volume (mg/m^3)	
	Mean (Min-Max)	SD	Mean (Min-Max)	SD
Before skull cutting	1.853 (0.018–2.750)	±1.276	0.153 (0.016–0.299)	±0.100
Oscillating saw	0.431 (0.116–0.706)	±0.221	0.030 (0.014–0.056)	±0.021
Robotic autopsy saw	0.346 (0.018–0.852)	±0.350	0.106 (0.016–0.148)	±0.052

DISCUSSION

Nowadays, the conventional procedure, which has been routinely applied for human skull cutting in forensic examinations, is an oscillating saw system. The robotic autopsy saw is recent development, using a robotic-assisted surgical technique. The first goal of this study, the measurement of noise pollution from the oscillating saw, was found to be greater than the robotic autopsy saw in all parameters. This might result from different techniques applied to

the bone. The robotic saw blade system was designed based on a circular saw system which needs only a slow rotational speed of saw blade to cut the cadaveric skull while the oscillating saw uses a vibration method for breakthrough of solid objects. Therefore, the machinery strokes of the oscillating saw must be over 10,000/min, inevitably causing high noise generation (SCHREIBER GmbH, 2012). As suggested by the National Institute for Occupational Safety and Health (NIOSH) and the Occupational Safety and Health Administration (OSHA), total LAeq, Tr in both groups and the average noise level without saws working should not exceed the recommended exposure limits (REL) for noise, over an 8-h average (85 dBA suggested by NIOSH and 90 dBA by OSHA, respectively) and noise over a 15-min average (100 dBA suggested by NIOSH and 115 dBA by OSHA, respectively) while the skull cutting operations of this study did not exceed 3 min/test (Centers for Disease Control and Prevention, 2018).

In addition, the result of inhaled particle measurement in this study deviated from the hypothesis which we had proposed, that the robotic autopsy saw might reduce the rate of aerosol generation. Although the autopsy robotic machine worked with the dust collector covering the saw blade and the acrylic box covering a cadaveric head, which was designed to confine the bone dust particles, it still generated a peak dust concentration and dust per volume greater than the oscillating saw. Despite the results contrasted with the presumption before testing, the aerosol pollution, which came from skull cutting by the robotic autopsy machine, as well as the oscillating saw, were not greater than the dust concentrations before skull cutting. The described skull cutting procedures do not generate greater amounts of bone dust compared with the usual autopsy condition. The portable real-time dust monitoring device was 1 m away from the operation site, as is standard operating procedure, therefore, the bone dust might have had too far to diffuse to get into the probe chamber and so could not be adequately detected by the modulated laser light source.

As regards to the second goal of this study, trialing the replacement of the conventional oscillating saw with the robotic-assisted surgical technique, using the robotic autopsy saw. A new skull opening procedure to address concerns about the health and safety of forensic pathologists and their colleagues. This robotic machine works on a basis of remote control and electronic systems so the co-workers must be trained before using this application. The prototype of the robotic autopsy saw is very large when compared to the oscillating saw. The robotic autopsy machine should be modified into a much more compact size, linked with either a mobile phone application or other wireless application, and have a wider application which is not limited only for skull opening. To solve these problems, the cadaveric skull and tissue cutting manipulator was designed, fabricated, and preliminarily tested. This robot should be used as a comparative machine for the next experiment (Jumlongkul, 2020).

Future studies should attempt to evaluate the relevance of short-term and long-term effects, related to health problems and the type of machines used in an autopsy room, for example; occupational lung diseases, musculoskeletal disorders, occupational psychosis, and occupational infectious diseases in the workplace. The evidence of disease development in forensic healthcare workers must be considered and we will consider any idea, using robotic technology, to raise the standard of healthcare worker safety.

CONCLUSION

In conclusion, this research study examined the effectiveness of a new method to cut the cadaveric skull, using robotic-assisted surgery, which resulted in decreased noise levels when compared with the oscillating saw method. This robotic machine, which is an optimal machine for post-mortem examination, also limited the release of aerosol particles to a level similar to common autopsy procedures not involving the use of operation of calvarial cutting tools. Nevertheless, further study is necessary to improve the appropriate autopsy instruments and we hope that this research will inspire many researchers to further consider the safety of health care workers.

DATA AVAILABILITY STATEMENT

The original contributions presented in the study are included in the article/Supplementary Material, further inquiries can be directed to the corresponding author.

ETHICS STATEMENT

The studies involving human participants were reviewed and approved by the Institutional Review Board of the Faculty of Medicine, Chulalongkorn University, Bangkok, Thailand . The patients/participants provided their written informed consent to participate in this study.

AUTHOR CONTRIBUTIONS

AJ created the conception, design, fabrication of the robotic machine, and also drafted the manuscript. PC tested the machine and collected data. All the authors approved the final version submitted for publication and take responsibility for statements made in the published article.

FUNDING

This study was supported by the Ratchadapiseksompoch Fund, Faculty of Medicine, Chulalongkorn University, Contract Number CU-GFI_60_02_30_01, the fiscal year 2017, and also Mae Fah Luang University

ACKNOWLEDGMENTS

We would like to thank Kullaya Saricheewin, Faculty of Engineering, and Apirom Chumeka, Faculty of Technical Education, Rajamangala University of Technology Thanyaburi for technical support, Metinee Romphothong for collecting data, Watchara Jamnuch and Thanat Srisuksan for creating and testing the robotic autopsy saw, and Roger Timothy Callaghan, School of Medicine, Mae Fah Luang University for language corrections.

REFERENCES

Ayoub, T., and Chow, J. (2008). The conventional autopsy in modern medicine. *J. R. Soc. Med.* 101 (4), 177–181. doi:10.1258/jrsm.2008.070479

Belcham, A. (2015). *Manual of environmental management*. London: Routledge.

CASELLA CEL Inc (2012). *CEL-712 microdust Pro real-time dust monitor HB4048-01 user manual*. New York

Centers for Disease Control and Prevention (2018). NOISE and hearing loss prevention Guidance and regulations. Available at: https://www.cdc.gov/niosh/topics/noise/reducenoiseexposure/regsguidance.html (Accessed April 29, 2019).

Jumlongkul, A. (2020). Cadaveric skull and tissue cutting manipulator: autopsy equipment that provides safety against airborne infection and COVID-19. *Res. Biomed. Engg.* [Epub ahead of print]. doi:10.1007/s42600-020-00104-5

Jumlongkul, A., and Chutivongse, P. (2019). Design and fabrication of robotic autopsy saw. *Proc. Int. Conf. Biomed. Engg. Technol. ICBET*' 19, 1–5. doi:10.1145/3326172.3326177

Kernbach-Wighton, G., Kuhlencord, A., Rossbach, K., and Fischer, G. (1996). Bone-dust in autopsies: reduction of spreading. *Forensic Sci. Int.* 83 (2), 95–103.

Kernbach-Wighton, G., Kuhlencord, A., and Saternus, K. S. (1998). [Sawdust in autopsies: production, spreading, and contamination]. *Pathologe* 19 (5), 355–360.

Matschke, J., Lütgehetmann, M., Hagel, C., Sperhake, J. P., Schröder, A. S., Edler, C., et al. (2020). Neuropathology of patients with COVID-19 in Germany: a post-mortem case series. *Lancet Neurol.* 19 (11), 919–929. doi:10.1016/S1474-4422(20)30308-2

Pekka Saukko, B. K. (2015). *Knight's forensic pathology*. 4th Edn. Boca Raton: CRC Press.

Peters, M. P., Feczko, P. Z., Tsang, K., van Rietbergen, B., Arts, J. J., and Emans, P. J. (2016). Noise exposure in TKA surgery; oscillating tip saw systems vs oscillating blade saw systems. *J. Arthroplasty* 31 (12), 2773–2777. doi:10.1016/j.arth.2016.05.030

Pluim, J. M. E., Jimenez-Bou, L., Gerretsen, R. R. R., and Loeve, A. J. (2018). Aerosol production during autopsies: the risk of sawing in bone. *Forensic Sci. Int.* 289, 260–267. doi:10.1016/j.forsciint.2018.05.046

Razali, A., Herman, H. P., and Zulkifly, A. H. (2017). Noise exposure during orthopaedics surgery. *Sci. Heritage J.* 1 (2), 32–33. doi:10.26480/gws.02.2017.32.33

Rosli, F., and Harun, R. (2016). Tuberculosis of the skull mimicking a bony tumor. *Asian J. Neurosurg.* 11 (1), 68. doi:10.4103/1793-5482.172594

SCHREIBER GmbH (2012). *Instruction of use for oscillating plaster- and autopsy saw SG-700*. Fridingen, Germany

Su, H., Yang, C., Ferrigno, G., and De Momi, E. (2019). Improved human–robot collaborative control of redundant robot for teleoperated minimally invasive surgery. *IEEE Rob. Autom. Lett.* 4 (2), 1447–1453. doi:10.1109/LRA.2019.2897145

Su, H., Hu, Y., Karimi, H. R., Knoll, A., Ferrigno, G., and De Momi, E. (2020a). Improved recurrent neural network-based manipulator control with remote center of motion constraints: experimental results. *Neural Network* 131, 291–299. doi:10.1016/j.neunet.2020.07.033

Su, H., Ovur, S. E., Li, Z., Hu, Y., Li, J., Knoll, A., et al. (2020b). Internet of Things (IoT)-based collaborative control of a redundant manipulator for teleoperated minimally invasive surgeries. *IEEE Int. Conf. Rob. Autom* 2020, 9737–9742. doi:10.1109/ICRA40945.2020.9197321

TES Electrical Electronic Corp (2014). Sound level meter. Available at: http://www.tes.com.tw/en/product_detail.asp?seq=389 (Accessed April 30, 2019).

Wenner, L., Pauli, U., Summermatter, K., Gantenbein, H., Vidondo, B., and Posthaus, H. (2017). Aerosol generation during bone-sawing procedures in veterinary autopsies. *Vet. Pathol.* 54 (3), 425–436. doi:10.1177/0300985816688744

Conflict of Interest: The authors declare that the research was conducted in the absence of any commercial or financial relationships that could be construed as a potential conflict of interest.

frontiers in Robotics and AI

ORIGINAL RESEARCH
published: 22 February 2021
doi: 10.3389/frobt.2020.611203

Applying Deep Reinforcement Learning to Cable Driven Parallel Robots for Balancing Unstable Loads: A Ball Case Study

*Alex Grimshaw and John Oyekan**

The Department of Automatic Control and Systems Engineering, The University of Sheffield, Sheffield, United Kingdom

The current pandemic has highlighted the need for rapid construction of structures to treat patients and ensure manufacturing of health care products such as vaccines. In order to achieve this, rapid transportation of construction materials from staging area to deposition is needed. In the future, this could be achieved through automated construction sites that make use of robots. Toward this, in this paper a cable driven parallel manipulator (CDPM) is designed and built to balance a highly unstable load, a ball plate system. The system consists of eight cables attached to the end effector plate that can be extended or retracted to actuate movement of the plate. The hardware for the system was designed and built utilizing modern manufacturing processes. A camera system was designed using image recognition to identify the ball pose on the plate. The hardware was used to inform the development of a control system consisting of a reinforcement-learning trained neural network controller that outputs the desired platform response. A nested PID controller for each motor attached to each cable was used to realize the desired response. For the neural network controller, three different model structures were compared to assess the impact of varying model complexity. It was seen that less complex structures resulted in a slower response that was less flexible and more complex structures output a high frequency oscillation of the actuation signal resulting in an unresponsive system. It was concluded that the system showed promise for future development with the potential to improve on the state of the art.

Keywords: deep reinforcement learning, manufacture, pandemic, construction, cable robotics, q-learning, load, CDPR

OPEN ACCESS

Edited by:
Noman Naseer,
Air University, Pakistan

Reviewed by:
Muhammad Jawad Khan,
National University of Sciences and Technology (NUST), Pakistan
Umar Shahbaz Khan,
National University of Sciences and Technology (NUST), Pakistan

****Correspondence:***
John Oyekan
oyekanjohn@gmail.com
j.oyekan@sheffield.ac.uk

Specialty section:
This article was submitted to Biomedical Robotics, a section of the journal Frontiers in Robotics and AI

Received: *28 September 2020*
Accepted: *09 December 2020*
Published: *22 February 2021*

Citation:
Grimshaw A and Oyekan J (2021) Applying Deep Reinforcement Learning to Cable Driven Parallel Robots for Balancing Unstable Loads: A Ball Case Study. Front. Robot. AI 7:611203. doi: 10.3389/frobt.2020.611203

INTRODUCTION

The current pandemic has highlighted the need for rapid construction of structures to treat patients and ensure manufacturing of health care products such as vaccines. To achieve this, currently, a large manpower is needed to achieve this. Nevertheless, this exposes the workers to the danger of catching a virus or acting as a carrier to future patients. In this work, we propose the use of a robotic platform called a cable driven parallel manipulator (CDPM) to rapidly build structures. Toward this, a control strategy is required to control the end effector of the robotic platform. Having been utilized since the 1950's, reinforcement learning is one of the oldest fields of machine learning and artificial intelligence, yet in recent years it has been experiencing a resurgence as a framework for learning sequential decision tasks (Garychl, 2018). At the same time, cable driven parallel manipulators (CDPMs)—where flexible

cables replace rigid links as robot actuators—are becoming increasingly popular for their numerous benefits (Saber, 2015). This project aims to introduce reinforcement learning into a CDPM to balance an object on a platform as it is moved from one location to another, with the hope of improving upon the state of the art. Specifically, a ball is to be balanced on a flat plate, controlled by eight cables spaced in pairs at equidistant intervals in a workspace that are driven by motors.

The developments of this project have the potential to improve the performance of cable balancing systems in areas such as warehouse swarm robot optimization, shipyard container movement management, drone auto-balancing and general robotic balancing (Gullapalli et al., 1994; NIST, 1994; Lachevre et al., 2017) by reducing operational times and failure rates. In this work, our contributions is as follows: We make use of reinforcement learning to enable the transport of a continuous moving load, a ball in this case, which could be highly unstable at large speeds during transport. This is important especially when CDPM are to be used in rapid construction of emergency structures.

BACKGROUND AND LITERATURE REVIEW

Cable Driven Parallel Manipulators

As defined by Gallardo-Alvarado (2016), a Parallel Manipulator (PM) is a mechanical system formed by two linked platforms, namely, the fixed platform and the moving platform. The moving platform is connected to the fixed platform by at least two independent computer-controlled serial chains or limbs working in parallel. Cable Driven Parallel Manipulators (CDPM) are a subsidiary of the standard parallel manipulator where rigid limbs are replaced with retractable cables allowing for varying limb length.

The properties of PMs and CDPMs provides unique advantages when applied in robotics. Patel and George (2012) discussed in their 2012 paper how parallel manipulators offer a greater load carrying capacity, low inertia, higher structural stiffness, and a reduced sensitivity to certain errors. Generally, parallel manipulators provide a clear advantage over most serial manipulation robots in that they control end effector position with a high degree of precision (Tannous et al., 2014), which makes them excellent for use in invasive surgical procedures where a high degree of precision is mandated (Beira et al., 2011). However, parallel manipulators have smaller and less dextrous workspaces due to link interference, where coupling of link actuation is resistive due to counteractive movement. When compared to PMs, CDPMs offer additional advantages due to the properties of the cables. These include a higher payload to weight ratio, larger workspace, higher end-effector speed and acceleration, and being easy to reconfigure and implement (Tang, 2014; Qian et al., 2018). Replacing rigid links with cables does introduce new challenges in their design, particularly in the precise control of the end-effector position (Tang, 2014; Qian et al., 2018), which becomes difficult to ensure due the need for cables to be constantly under tension (Bosscher and Ebert-Uphoff, 2004; Qian et al., 2018) and the elastic nature of cables. This problem can be partly mitigated through more complex controller design and specific material design choices.

The need for ever increasing load capacities and workspaces is motivating further research on CDPMs which has led to implementation in interesting and challenging industrial and research scenarios. Perhaps the most recognisable application is the SkyCam (Brown, 2019), a camera mount system used in large sports venues and stadiums for live broadcasting (**Figure 1A**). The system consists of four motorised reels fixed to the corners of the venue that retract or extend the four cables attached to the camera. This allows for three-dimensional control with camera translation speeds of up to 44.8 km/h (Qian et al., 2018) whilst maintaining constant orientation. More recent developments have focused on industrial applications, such as cooperative cable driven crane systems (Qian et al., 2018) (**Figure 1**), which utilise the large tensile strength of the cable actuators to move heavy payloads. In academia, research at the National Institute of Standards and Technology (NIST) has led to development of the NIST Robocrane, a novel three cable system that has seen many uses including shipping container management on large vessels, load stabilization during transport, and even as a potential modification to lunar rovers for exploration of the moon (NIST, 1994).

Control Systems for CDPM

As mentioned, replacing rigid links with cables leads to challenges that complicate the design of control systems for CDPMs. Perhaps the most commonly implemented control method is PID control. Khosravi and Taghirad proposed a robust PID controller for a CDPM that controlled the length of each cable, with a corrective term to account for cable elasticity (Khosravi and Taghirad, 2016). The generated controller could stabilize the end effector and showed good orientation control, although desired positional control was not achieved and displayed erratic behaviour. Taking a different approach, Alp and Agrawal proposed a nested closed loop controller based on Lyapunov design and feedback linearization that would output the desired tension in each cable for a given end effector position and orientation (Alp and Agrawal, 2002). This control design allowed for adept positional control with a fast response time and minimal error, but the end effector failed to maintain accurate orientational control. In addition, the controller was complex in design and was hindered by large cable friction during operation. Both of the PID control methods discussed utilised indirect sensing, suffering from a need to estimate the end effector Cartesian pose (position and orientation) from complete knowledge of the inverse kinematics of the cable system, which is highly complex and missing in parts (e.g., Alp and Agrawal did not consider the cable friction in the kinematic model). Newer approaches now consider visual servoing techniques, utilizing computer vision to identify the end effector pose. This simplifies the kinematic model by removing the need to model complex dynamics and instead using simple closed loop feedback techniques to minimize end effector pose error. Dallej et al. reviewed current visual servoing techniques and developed and proposed a vision based PID control system for a ReelAx8 CDPM that was simpler to design and showed good results when assessing the pose errors over time (Dallej et al., 2011).

Previous research was performed on the specific cable rig used in this project by Hong (2019), who was able to design a real time

FIGURE 1 | Examples of CDPM systems in use. **(A)** The SkyCam in use at the Washington Huskies Stadium. Image reprinted from Brown (2019). **(B)** A cooperative crane system being used to move an heavy object.

auto tuning PID controller for control of end effector position within the workspace. Here, a Simulink PID auto tuner model was implemented to tune and return optimal gain values for four motors simultaneously in real time. His research showed that a controller was able to able to control the speed the motors attached to each cable with good rise and settling times and minimal steady state error when tested on hardware.

Ball Balancing Skill Acquisition

The problem of balancing a ball on a plate is an extension of the 2D traditional nonlinear ball on beam balancing problem that is often used as a benchmark in control design theory (Kostamo et al., 2005). The task consists of providing rotational actuation to a beam, where the ball is only free to travel in one axis. For a plate system the ball is free to travel in two axes. With both systems, the goal is to move the ball to a specific location and then maintain its position. As proven by derivation in Awtar et al. (2002) and further documented by Ali and Aphiratsakun (2015), the ball on plate system can be viewed as two independent ball on beam systems provided the plate has mass symmetry about its x-z and y-z axis. As such, both ball on plate and ball on beam systems and control schemes are discussed in this section (**Supplementary Figure S1**).

Classical Control Methods

Multiple attempts have been made to implement PID controllers on both balancing systems with varying degrees of success (Ali and Aphiratsakun, 2015) implemented a basic PID controller onto a ball-plate system that balanced a ball on the center of a plate from a random initial location, and then attempted to recover positional control of the ball after an external disturbance to the plate. The controller performed acceptably and was able to balance the ball in reasonable time for both cases, however the response was extremely oscillatory and took over 30 s to recover positional control from the disturbance. This is likely due to the controller design taking a model free approach and instead tuning the PID controller parameters on the hardware.

Taking a slightly different approach (Shih et al., 2017) developed an embedded PID/PD controller for a ball-beam system. The control structure consisted of a PD controller to choose the desired platform response and then a series of individual PID controllers on each motor to realize the idealized platform response by actuation of the motors. The ball-beam PD controller was tuned on a model of the ball dynamics that was estimated by collecting data on the positional response of the ball to varying inputs. The controller was then tested by placing the ball at one end and having the controller attempt to balance the ball at various locations. It was seen that whilst the controller performed worse when the desired ball location is further from the start point, generally the controller performed well and was able to balance the ball in less than 10 s for all scenarios. The controller did however show consistent initial overshoot in the range 10–20%, indicating the potential for improvement to the control system.

Other attempts have also been made using conventional control theory. In Ryu and Oh (2011), they discuss how estimation of the ball velocity is often a large source of error in ball-beam control systems as it is often estimated as the derivative of the measured ball position. He proposes a state space Linear Quadratic Regulator (LQR) controller as a potential solution to these problems and as a general improvement over standard PID control. The designed controller utilised state estimation of the ball position and velocity to optimize the feedback control system and was then tested by disturbing the balanced system and viewing the ball state reaction. It could be seen that the state estimation for the velocity of the ball was significantly less noisy that than when estimated *via* differentiation. This allowed for a much quicker response, with the ball returning to its balanced position in less than 5 s each time. The results do show small amounts of constant oscillation of the ball position around the set point, but the author suggests this is likely due to friction on the system that has not been modeled.

By studying the above literature, it was discovered that the ball position, its velocity as well as the position of the plate system were crucial when building the above mentioned controllers for balancing the ball. This information served as a bootstrap in defining the reward functions for our reinforcement learning approach.

Intelligent Methods

More modern approaches to controller design have focused on producing an "intelligent"' controller that is better suited to the unstable nonlinear system. Rahmat et al. (2010) designed a neural network-based controller and then compared its performance to both PID and LQR controllers on a ball-beam system. The approach consisted of designing a neural network to model the ball dynamics that took inputs of the current ball and beam states and output the future ball states. The model was trained *via* backpropagation. This had the benefit of a model free approach where the dynamics of the ball did not have to be derived, which can often be difficult to quantify. A separate neural network was also designed to control the actuation of the beam orientation based upon the expected output of the model network that was trained using the quasi-Newton backpropagation optimization method. The PID, LQR, and neural network controllers were then all tested and compared. It was seen that whilst all three controllers could successfully balance the ball in less than 5 s with minimal steady state error, the PID controller performance was superior to both other controller types, and the LQR controller was able to achieve a faster response while sacrificing some positional overshoot. This suggested that neural network approaches have the potential to be a valid control solution to this problem but require more work before its performance can be superior to conventional methods. Alternatively, Keshmiri et al. (2012) attempted to combine both traditional control strategies with newer intelligent optimization techniques to develop a superior LQR controller that's parameters were trained using genetic algorithms. As discussed in the paper, genetic algorithms are a class of stochastic search optimization methods based on random number generation, in this case the search algorithm attempts to find the optimal LQR parameters that minimize the error in position of the ball. The genetic LQR controller was then compared to a PID controller trained using the Ziegler-Nichols method and a normal LQR controller that was trained through trial and error. It was seen in testing that the application of the genetic algorithms allowed for a superior controller that responded faster than PID and LQR controllers with a lower steady state error.

At the forefront of current research is the design of end-to-end neural network controllers. Research on the topic is sparse, showing a clear opportunity to develop a novel solution to this traditional problem. In 2013, a publication by Bigharaz et al. (2013) discussed a neural network-based controller for application to a ball-plate system. It received the ball and plate states as inputs as well as motor control signals as outputs. The paper suggested the neural network controller performs almost as well as a generic PID or fuzzy controller, but the research is limited in its testing and does not discuss the method with which the neural network is trained.

When considering training neural networks, there are predominantly two main methods: optimization and machine learning. Examples of optimization methods are discussed previously, however there is minimal research on the application of machine learning. Machine learning methods consist of training the neural network based upon large sets of data related to the system. In the scenario of the ball-plate system this raises an issue as any dataset is unique to the system it is collected from, and this lack of available data leads to reinforcement learning being a promising method for training neural networks for ball-plate systems.

Publications are sparse on implementation of reinforcement learning to ball-beam or ball-plate systems. This sparsity is surprising due to the current popularity of reinforcement learning which has led to it being applied to a plethora of systems, from goal scoring football robots (Asada et al., 1996) to synthetic human speech bots that are indistinguishable from real voices (Arik et al., 2017).

Its potential benefits in CDPMs are obvious and build upon the benefits of visual servoing, by reducing the need to model and understand the kinematics of the system. Instead, a black box type approach can be taken. By simply monitoring the input and related output (and having an understanding of what the desired output is) a controller can be developed through repeated training that can perform the desired task. Of the limited research performed into the topic, some results show promise for its application. For example, Gullapalli et al. used an unsupervised, direct reinforcement learning algorithm to balance a ball on a one Degree of Freedom (DOF) platform (Gullapalli et al., 1994). Here the system reads the ball position from a series of pressure plates and uses it (along with historic data) to estimate the ball velocity. This, along with the current platform orientation and rate of change of orientation is fed into a neural network trained by a reinforcement learning algorithm that outputs the recommended new orientation, with the goal of returning the ball to the center of the platform. After 700 attempts, the controller learns to balance the ball with no further failures and can run for an indefinite amount of time. No comparison is made to alternate control techniques. Here no modeling has been performed on the ball or platform dynamics, allowing for a much simpler design process.

There is a noticeable gap in research into the application of reinforcement learning to control ball-beam and ball-plate systems, which this paper aims to explore. Developments in this topic could result in improved performance of balancing tasks and control of CDPMs which have many applications in the real world, as discussed throughout this section. This research will also aim to encourage future work on the topic that can further build on the developments made.

METHODOLOGY

System Overview

The idealized system that meets the aims and objectives set out in *Introduction* section would operate following the system diagram set out in **Figure 2**. The Agent is the reinforcement learning trained neural network that outputs the desired platform response at the start of each action phase (0.5 s). This is passed to a nested PID controller that realizes the desired platform response for each action phase by controlling the speed of each motor. The nest PID controllers were implemented as a black box with the boxes taking commands from our RL framework. The plant is the physical ball-plate-cable rig.

In **Figure 2**, the agent receives the platform and ball states. These are used to define reward functions that are then used by the Deep Q learning algorithms to derive a policy that balances the ball (Géron, 2017; Lachevre et al., 2017). In order to balance the ball, the desired direction and rotational speeds are derived by the Q learning algorithm in the form of an optimal policy for use

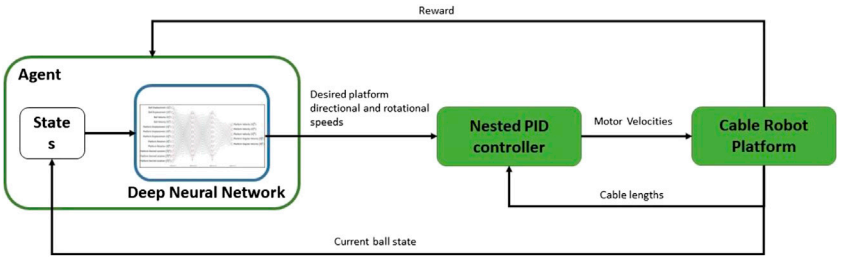

FIGURE 2 | Deep reinforcement learning system diagram for the ball balancing cable robot plant.

by the Nested PID controller. The Nested PID controller converts these values into motor velocities for use on the cable robot plant. The cable robot plant responds by adapting the length of each cable. *Hardware Design, Ball State Sensing Design, Platform Control Design, and Nested PID Cable Controller Design* sections details the work carried out to realize this system.

Hardware Design

A preassembled rig was provided at the start of the project that had been used for other CDPM projects. The rig consisted of a fixed frame with a XYZ workspace of 1 m × 1 m × 0.6 m. Fixed above the rig sat a Lego Ev3 Mindstorm microcomputer connected to four Ev3 Large Servo Motors (**Supplementary Figure S2**). Spools of cable were attached to the motors that extended to the top four corners of the frame. The cables then extended into the workspace where they were connected to another Lego Ev3 Mindstorm. Significant work was carried out on this rig to outfit it for the desired application.

Cable Design

As discussed in *Control Systems for CDPM* section one difficult aspect of control for CDPMs is the elasticity of the cables. To avoid the need to model cable elasticity, the first change made was to replace the 0.3 mm diameter string cables with 1 mm nylon cables to significantly reduce cable deformation. The original string material was unknown.

Cable Spool Design

The spools used to hold the cables had a diameter of 31.83 mm to achieve 100 mm of cable release per revolution. To achieve a faster system response, the spools were redesigned using CAD software, with roughly twice the diameter of 60 mm to achieve 188.5 mm of cable release per revolution. The designed spools were then 3D printed in polylactide (PLA) plastic (**Supplementary Figure S3**). In addition, to obtain complete six Degree of Freedom (DoF) control the system needs cable redundancy, as discussed by Enrico Sammarchi. Six DoF is necessary to achieve orientational and positional control of the platform. As such, the number of cables needs to be increased to more than six (since six DoF control is required). Therefore, four additional cables (eight total) were added at the bottom four corners of the workspace that are attached to four additional Lego Large Ev3 motors, making the CDPM a Redundantly Restrained Positioning Mechanism (RRPM) system (Sammarchi, 2019).

Platform Design

The current end-effector attached to the cables was an additional Lego Ev3 Mindstorm, which needed to be replaced with a flat plate (**Supplemetary Figure S4**). The plate was designed in CAD software and laser cut from a 5 mm acrylic sheet. Acrylic was used as it provides a smooth surface and would not flex or crack under usage. The plate was then painted matt black to reduce its reflectiveness to aid ball state extraction *via* image processing by providing a greater contrast with the white ball.

Camera Mount Design

Next, to enable identification of ball states, a webcam was obtained with a large field of view (FOV). A large FOV was necessary to reduce the height of the camera mount above the plate and hence reduce its obtrusiveness in the workspace. The mount was designed for the camera in CAD software, and fixes to the underside of the platform. It was designed symmetrically to minimize impact on platform center of gravity and hence bias any motor. The mount fixes to the corners of the plate underside to reduce the likelihood of collision with the ball. The components were then 3D printed in PLA (**Supplementary Figures S5, S6**).

Completed Hardware Model

The final modified hardware system was assembled. The kinematic model of the system and variable definitions can be seen in **Figure 3**. **Tables 1, 2** show the variable associated with the workspace and the platform references. **Figure 4** shows a diagram of the ball-plate system for reference.

Ball State Sensing Design

For closed loop feedback control of the ball position, its states need to be identified at the end of every action phase. For state sensing, options such as pressure pads where considered, as used by Gullapalli in his one DOF ball balancing robot (Gullapalli et al., 1994). However, this idea was disregarded due to concerns with compatibility with the Ev3 Brick and the impact it would have on platform design. Instead, a webcam is used alongside an image recognition system.

As Ev3 motor control is being performed in MATLAB, it was decided to also develop the image recognition system using MATLAB and using the Image Processing Toolbox a program was written that takes a still image from the webcam and computes the ball states. The ball position is found by

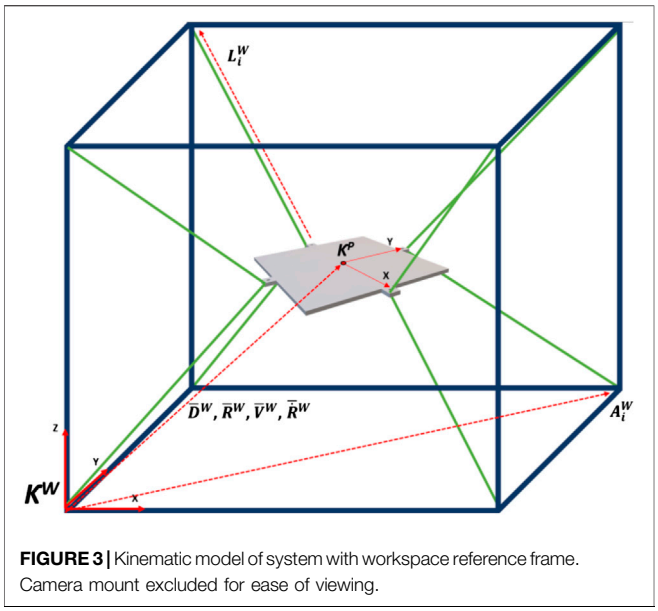

FIGURE 3 | Kinematic model of system with workspace reference frame. Camera mount excluded for ease of viewing.

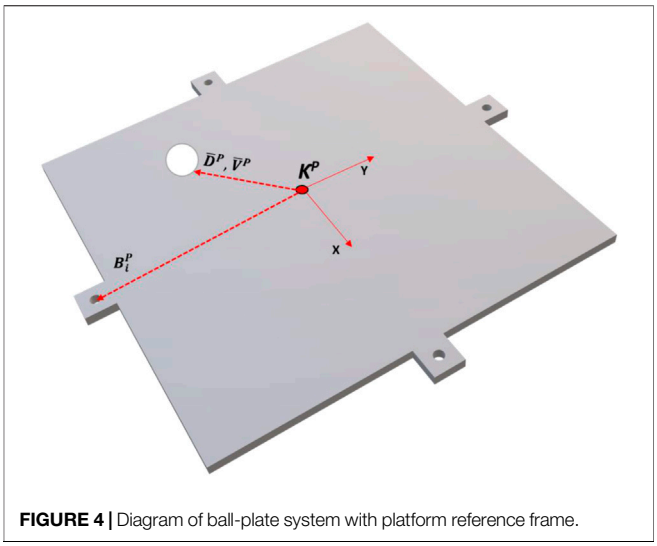

FIGURE 4 | Diagram of ball-plate system with platform reference frame.

TABLE 1 | Showing workspace reference frame variables.

Platform X displacement: (D_X^W)
Platform Y displacement: (D_Y^W)
Platform Z displacement: (D_Z^W)
Platform displacement vector:
$\bar{D}^W = \begin{bmatrix} D_X^W & D_Y^W & D_Z^W \end{bmatrix}^T$
Platform X velocity: (V_X^W)
Platform Y velocity: (V_Y^W)
Platform Z velocity: (V_Z^W)
Platform velocity vector:
$\bar{V}^W = \begin{bmatrix} V_X^W & V_Y^W & V_Z^W \end{bmatrix}^T$

Platform X rotation: (R_X^W)
Platform Y rotation: (R_Y^W)
Platform rotation vector:
$\bar{R}^W = \begin{bmatrix} R_X^W & R_Y^W & 0^T \end{bmatrix}$
Platform X angular velocity: $(\dot{R}_X^W)$
Platform Y angular velocity: $(\dot{R}_Y^W)$
Platform angular velocity vector:
$\bar{\dot{R}}^W = \begin{bmatrix} \dot{R}_X^W & \dot{R}_Y^W & 0^T \end{bmatrix}$

Cable workspace origins matrix:

$$\bar{A}^W = \begin{bmatrix} 0 & 1000 & 1000 & 0 & 0 & 1000 & 1000 & 0 \\ 0 & 0 & 1000 & 1000 & 0 & 0 & 1000 & 1000 \\ 0 & 0 & 0 & 0 & 600 & 600 & 600 & 600 \end{bmatrix}$$

$= [A_1^W \ldots\ldots A_8^W]$

Cable lengths matrix:

$$\bar{L}^W = \begin{bmatrix} L_{1,X}^W & L_{2,X}^W & & L_{8,X}^W \\ L_{1,Y}^W & L_{2,Y}^W & \ldots & L_{8,Y}^W \\ L_{1,Z}^W & L_{2,Z}^W & & L_{8,Z}^W \end{bmatrix}$$

$= [L_1^W \ldots . L_8^W]$

TABLE 2 | Showing platform reference frame variables.

Ball X displacement: (D_X^P)
Ball Y displacement: (D_Y^P)
Ball displacement vector:
$\bar{D}^P = \begin{bmatrix} D_X^P & D_Y^P & D_Z^P \end{bmatrix}^T$

Ball X velocity: (V_X^P)
Ball Y velocity: (V_Y^P)
Platform velocity vector:
$\bar{V}^P = \begin{bmatrix} V_X^P & V_Y^P & 0 \end{bmatrix}^T$

Plate = 200 mm × 200 mm with 10 mm extensions on each edge for connecting cables. Each connection point is 110 mm from the plate center and is rotated 45° from workspace reference frame. Two cables are connected to each connection point

Cable plate connection points:

$$\bar{B}^P = \begin{bmatrix} 0 & 110 & 0 & -110 & 0 & 110 & 0 & -110 \\ -110 & 0 & 110 & 0 & -110 & 0 & 110 & 0 \\ 0 & 0 & 0 & 0 & 0 & 0 & 0 & 0 \end{bmatrix}$$

$= [B_1^P \ldots B_4^P \; B_1^P \ldots B_4^P]$

converting the image to a binary image (dependant on pixel luminosity) and examining the binary value of adjacent pixels to identify the "edge" of the ball. Then, using the "regionprops" function the center position of the ball is located. A demonstration of this process can be seen in **Supplementary Figure S7**. The ball velocity is identified by assessing the change in ball position since the last action phase.

Platform Control Design

In this section, we design a reinforcement learning trained deep neural network controller that output the desired positional and rotational response to changing ball states at the start of each action phase. This neural network controller is referred to as "the agent."

Neural Network Structure

The structure of the neural network agent is shown in **Figure 5**. The input layer of the network contains the twelve input states to the system: the ball and plate states and the target end platform location. Two hidden layers are used to make it a deep neural network. Finally, the five node output layer outputs the desired platform response. Note that there is no output function for angular velocity in the *Z* axis as Z orientation is kept constant at the origin, as this offers no benefit in the balancing task. Rectified Linear Units (ReLU) were used as the activation functions. To assess the impact of model complexity on performance, three different model structures were assessed. Each model structure had a varying number of activation functions on each hidden layer: 10, 100, and 500, with an increasing number of activation functions resulting in an increase in model complexity. The weights on each input to each activation function were trained using reinforcement learning.

Policy Training Method—Q-Learning and Policy Gradients

As mention in *Ball Balancing Skill Acquisition* section, the process of training a neural network to perform a ball balancing task lends itself naturally to reinforcement learning due to the lack of

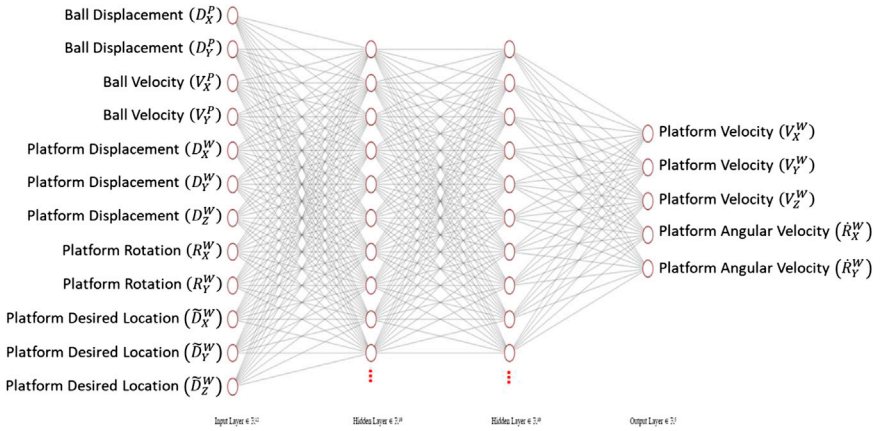

FIGURE 5 | Agent neural network structure for 10 node system.

availability of an appropriate dataset of system responses. It is generally accepted that the two leading approaches for model free reinforcement learning are Q-learning and policy gradients (PG) (DeepMind Technologies, 2014; Lillicrap et al., 2016; Cornell University, 2018).

Q-learning is a reinforcement learning method first introduced in 1989 by Watkins and Dayan (1992) that aims to approximate the Q function of each state-action pair through interacting with the environment. The Q function is the expected sum of future rewards if the policy is followed. Each time the agent interacts with the environment a data point is collected:

$$< s, a, r, s' >$$

s = the current state of the environment. a = the action taken by the agent. r = the reward from the environment. s' = the new state of the environment.

The Q function can be iteratively approximated using the Bellman equation through temporal difference learning (Yu, 2017). Once the Q function has been approximated for all state-action pairs, the optimal policy that the agent should take for any given current state can be decided by finding the action that provides the maximum Q function value. It was a deep Q-learning Network (DQN) that famously learned to play a wide range of ATARI games (Mnih et al., 2015) and helped re-popularize the field of reinforcement learning. One of the key drawbacks of Q-Learning is that the Q function needs to be learnt for discrete state-action pair. This means that environments with continuous action spaces require discretization of the states and actions, resulting in a loss of precision of the data (Hodge and Austin, 2012).

Alternatively, PG methods can operate in continuous or discrete action spaces (DeepMind Technologies, 2014) and are becoming the preferred choice for reinforcement learning tasks (Karpathy, 2016). Karpathy suggested that the reason PG methods are becoming favoured is because it is an end-to-end method: there's an explicit policy and a principled approach that directly optimizes the expected reward (Karpathy, 2016). Instead of estimating the future reward for every state-action pair based upon the data points collected, we estimate the future reward of the policy based on the policy parameters. This then becomes a gradient ascent task where the parameters are tuned to maximize the policy reward (Pseudocode 1). This, alongside the fact that the system operates in a continuous domain (e.g., platform X velocity can be any continuous value in the range of −50 to 50 mm/s) is why a policy gradient method was used for this project.

Simulated Environment Design

Whilst this project takes a model free approach to RL agent operation, the ball-plate environment needs to be modeled to allow for training of the agent on simulation. Simulated environment training offers benefits over a purely hardware-based training program in that simulations run drastically faster, can run training exercises simultaneously and require no supervision once initiated.

As discussed in *Background and Literature Review* section, the XYZ ball-plate system can be viewed as two independent ball-beam systems operating in the X-Z and Y-Z planes. This ball-beam system is shown in **Figure 6**. The assumptions which formulate the ball-beam system model are as follows:

(1) The ball is always in contact with the plate and does not bounce.
(2) There is no slipping motion between the ball and plate
(3) Resistive forces on the ball including air resistance and rolling friction are negligible
(4) The only force acting on the ball is its weight and the associated reaction force
(5) At the start of each action phase, the beam is assumed to undergo an instantaneous change in translational and rotational velocity to the exact desired position. (i.e., the motor response ins assumed to be perfect)
(6) The beam maintains its exact desired velocity for the entirety of the action phase
(7) Complete knowledge of the ball states is known at all points

Through assumptions 5 and 6, the plate is modeled to have constant velocity and no acceleration, therefore inertial forces

PSEUDOCODE 1 |
Input: Policy parameterisation $\pi(a|s,\theta)$
Input: Reward function definitions $R[s,\pi(s)]$
Parameters: Step size $\propto > 0$
Loop until number of max episodes:
Generate state-action pairs $s_0\, a_{01}\, r_{01}$, $s_0\, a_{02}\, r_{02}$ ..... $s_0\, a_{0n}\, r_{0n}$
For each state-action pair calculate the expected reward:

$$V^{\pi} = R[s,\pi(s)] + \gamma \sum_{s'} P[s'|s,\ \pi(s)] V^{\pi}(s')$$

$$V^{\pi *} = \max_{a} \left[R(s,a) + \gamma \sum_{s'} P(s'|s,\ a) V^{\pi *}(s') \right]$$

$$\theta \leftarrow \theta + \propto \nabla \pi^{*}(a|s,\theta)$$

from the plate movement on the ball are ignored. Whilst these assumptions are not strictly correct, they are appropriate as the physical plate is limited to small changes in velocities between action phases, and the motors used have high rotational speed so changes in velocity can be assumed close to instantaneous.

From assumption 4, the acceleration of the ball is defined:

$$\dot{V}^{P}_{X,Y}(t) = g * \sin\left[R^{W}_{X,Y}(t)\right] \quad for\ t\ \in \{0, 0.5\} \tag{1}$$

Hence the velocity of the ball is found as the Euler integration of **Eq. 1**

$$V^{P}_{X,Y}(t) = V^{P}_{X,Y}(0) + \dot{V}^{P}_{X,Y}(t) * t \quad for\ t\ \in \{0, 0.5\} \tag{2}$$

And finally, the ball position is found by the Euler integration of **Eq. 2**:

$$D^{P}_{X,Y}(t) = D^{P}_{X,Y}(0) + V^{P}_{X,Y}(t) * t \quad for\ t\ \in \{0, 0.5\} \tag{3}$$

From assumptions 6 and 7 the plate dynamical model is seen as:

$$D^{W}_{X,Y,Z}(t) = D^{W}_{X,Y,Z}(0) + V^{W}_{X,Y,Z} * t \quad for\ t\ \in \{0, 0.5\} \tag{4}$$

$$R^{W}_{X,Y}(t) = R^{W}_{X,Y}(0) + \dot{R}^{W}_{X,Y} * t \quad for\ t\ \in \{0, 0.5\} \tag{5}$$

Substituting **Eq. 5** into **Eq. 1** and subsequently **Eqs. 2** and **3** gives:

$$\dot{V}^{P}_{X,Y}(t) = g * \sin\left[R^{W}_{X,Y}(0) + \dot{R}^{W}_{X,Y} * t\right] \quad for\ t\ \in \{0, 0.5\} \tag{6}$$

$$V^{P}_{X,Y}(t) = V^{P}_{X,Y}(0) + \left\{g * \sin\left[R^{W}_{X,Y}(0) + \dot{R}^{W}_{X,Y} * t\right]\right\} * t \quad for\ t\ \in \{0, 0.5\} \tag{7}$$

$$D^{P}_{X,Y}(t) = D^{P}_{X,Y}(0) + \left[V^{P}_{X,Y}(0) + \left\{g * \sin\left[R^{W}_{X,Y}(0) + \dot{R}^{W}_{X,Y} * t\right]\right\} * t\right] * t \quad for\ t\ \in \{0, 0.5\} \tag{8}$$

Hence the ball states for any given plate action are given in **Eqs. 7** and **8**.

This was modeled in a MATLAB environment that was simulated for training.

Training Episode Reward

To promote positive actions by the agent, the training process must reward "good" actions and penalise "bad" actions. Toward this, reward functions were defined by taking into consideration the various parameters involved in ensuring the balancing of an unstable load. This included the position of the load, the speed of the load and how the platform positon and orientation affect the load. This resulted in defining three reward components: Ball Position Reward, Ball Speed Reward and Platform Position Reward. For this system, the reward structure was designed to promote balancing of the ball as the platform moves to the target location. As a result, for each action taken in the system, the agent receives a reward consisting of three components:

- **Ball Position Reward:** a reward in the range of (0–1) based upon the Euclidian distance of the ball from the center of the platform, that exponentially decays as the ball moves further from the center
- **Ball Speed Reward:** a reward in the range of (0–1) based on the Euclidian speed of the ball that exponentially decays as the ball speed increases
- **Platform Position Reward:** a reward in the range of (0–1) based on the Euclidian distance of the platform from its desired location that linearly decays

Hence the ball position and speed rewards promote balancing the ball as quickly as possible and the platform position reward promotes transportation of the load as quickly as possible.

The total reward for each action is then the weighted sum of the three components: Action Reward = 6 × Ball Position Reward + 2 × Ball Speed Reward + 2 × Platform Distance RewardAs such each action receives a score between (0–10). If the ball falls off the platform the episode receives a −3,000 reward and the episode is ended.

The reward is weighted to place a larger emphasis on preventing the ball from being dropped as in real world

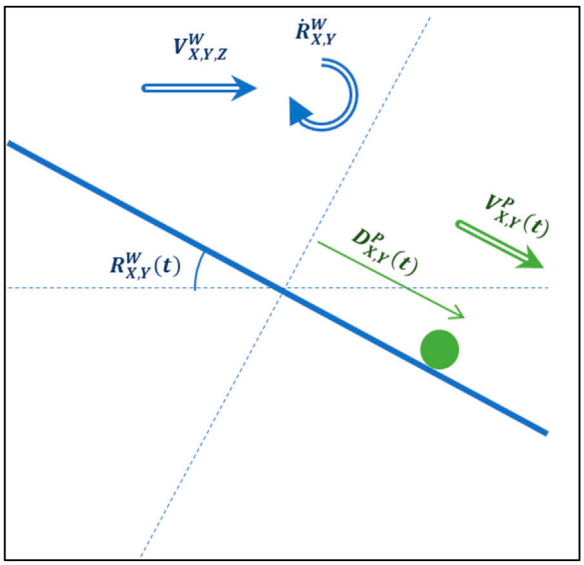

FIGURE 6 | Model of the ball dynamics for the system.

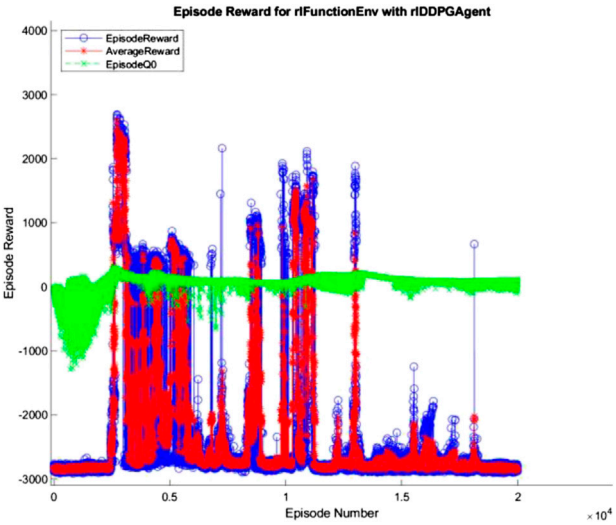

FIGURE 7 | 10 node network training progress.

applications dropping the load would cause a larger problem than the speed at which it is delivered. The ball rewards exponentially decay to prioritize keeping the ball away from the platform edge over balancing at the center to prevent episode failure.

Agent Training

The 10, 100, and 500 node networks were then trained over 20,000 simulated episodes each, with each episode attempting to balance the ball and transport it for 3 min. To accelerate training, four pool parallel processing was used along with GPU acceleration where appropriate. The training progress of each network is shown in **Figures 7–9** (The "AverageReward" is a 50-episode rolling average). As each action phase lasts 0.5 s, there are 360 action phases per episode, with a max reward of 3,600 per episode. During training, any agent with an episode reward greater than 2,000 was saved.

All three networks structures can be seen to be erratic between episodes, often identifying strategies that increased episode reward before altering the policy that results in a decrease in performance. The erratic nature of the training suggests the agent struggles to encapsulate the complexity of the system in its policy, with the randomly changing initial conditions of the episode being sufficient variation to cause failure of the controller. Whilst the 100 and 500 node networks also have periodic peaks in performance, the 10 node networks show larger periods between peaks. This suggests increasing model complexity results in an increase in frequency of optimal policy discovery. Overall, all three structures show an inability to consistently converge given an infinite number of training episodes.

Nested PID Cable Controller Design

As described in the system overview (*System Overview* section), every 0.5 s the agent will output a new desired platform response. This response is actuated through control of the eight motors connected to each of the eight cables, therefore the desired platform response needs to be converted into a desired motor speed.

The first step was to calculate the cable states from the platform states; therefore, the inverse kinematics of the platform were calculated. A reminder of the kinematic model of the system can be seen in **Figure 3**. It can be seen from literature (Gallardo-Alvarado, 2016; Sammarchi, 2019) that the inverse kinematics for an over defined CDPM is defined as:

$$\overline{L}^w = \overline{A}^w - \overline{D}^W - \overline{R}^W\overline{B}^P \tag{9}$$

Where $\overline{L}^w$ is a 3×8 array of vector lengths of each cable (each row is X/Y/Z and each column is a specific cable). The desired length of each cable can then be calculated as the Euclidian distance:

$$\left|L_i^W\right| = \sqrt{\left(L_{i,X}^W\right)^2 + \left(L_{i,Y}^W\right)^2 + \left(L_{i,Z}^W\right)^2} \tag{10}$$

To convert between desired platform and motor response the desired platform location at the start and end of each action phase is calculated and **Eqs. 9** and **10** are used to identify the desired initial and final cable lengths. From this the desired motor speed is calculated as:

$$\omega = \frac{L^w_{final} - L^w_{initial}}{0.5 * r} \tag{11}$$

Where r denotes the radius of the cable spool.

The system was initially designed to utilise the Ev3 inbuilt Tacho feedback that Lego claims performs closed loop control of the motor speed to ensure optimal performance. However, previous research by Hong (2019) on the system revealed consistent steady state error with a poor transient performance. Instead Wei designed and tested a real-time PID controller for motor speed control. This controller was utilized in this project and extended to all eight motors.

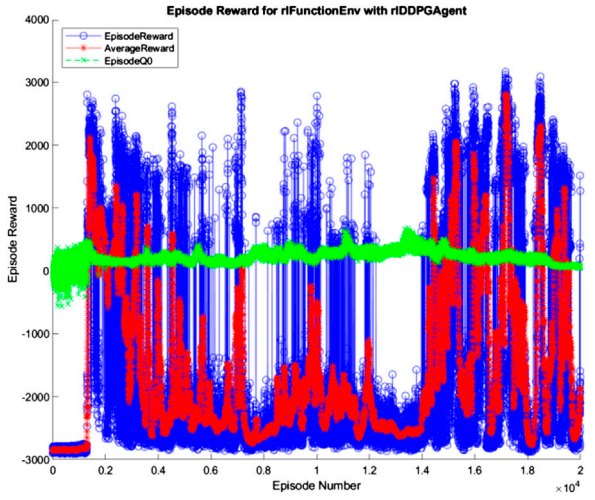

FIGURE 8 | 100 node network training progress.

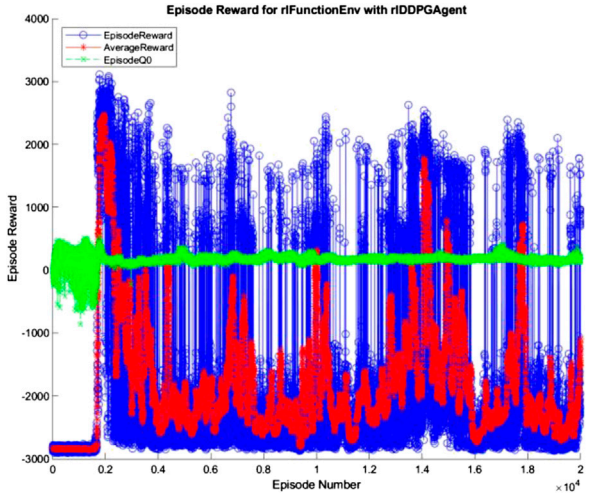

FIGURE 9 | 500 node network training progress.

IMPLEMENTATION, TESTING AND RESULTS

Image Recognition System Testing

The image recognition system was implemented on the system once the hardware had been constructed. The image recognition system was tested and it was seen that light reflected on the plate resulting in low accuracy for ball position identification. The camera image brightness was reduced, and contrast was increased to mitigate this. In addition, the required gray level for conversion to binary image was increased until the system worked ideally, and was able to identify the ball position in 10 different images.

It is notable that changing the location of the rig would likely result in readjustment of the above parameters which limits the applicability of the system.

Platform Response Controller Testing

For each network structure, all saved agents were assessed over 500 simulated episodes to identify the agent with the highest average reward for each network structure.

Each simulation started by placing the platform at the center of the workspace with no deviation in orientation. The ball was then placed on the platform at a random position with no initial velocity. The target platform location was randomized within the workspace. The simulation lasted 3 min, or until the ball leaves the platform.

The best performing agent for each network structure was then simulated over a further 10,000 episodes to analyze their performance. The rewards of this testing can be seen in **Table 3**.

From these results it can be seen that the 100-node structure achieved a higher average reward than both other network structures. This indicates a superior performance and ability to balance the ball while moving to the desired location. The 10 node and 500 node networks achieved similar average rewards, but the 500-node network failed to balance the ball for the duration of the episode 0.56% of the time. Whilst this is a relatively small failure chance, the consequence of a dropped payload is significant when utilized in industry, and can result in increased costs and risk to personal safety. As such, the 10-node network is superior to the 500-node network. To help understand the actions of each network structure and the systems response the best and worst performing episodes of each structure were further analyzed.

10-Node Agent

As can be seen in **Figures 10–12**, the 10-node network is capable of balancing the ball, however there is a constant steady state error from the origin, which increases with the balls starting displacement. This error is likely caused by the exponential nature of the reward prescribed based on the balls distance from the origin, described in *Training Episode Reward* section. This in itself is not necessarily a problem, as the ball is balanced somewhere on the platform for the duration of the journey. However, the controller is extremely slow in its ability to reach a steady state ball position and is damped and oscillatory. This is a significant problem as the controller would struggle to respond quickly to any disturbances or knocks it receives during operation. The most notable problem with the controller is that it actively moves the platform away from the target location. As such the controller fails to achieve its key goal of balancing the load as it is transported from one location to another.

100-Node Agent

It can immediately be seen in **Figures 13–15** that the ball response to the 100-node network is much more oscillatory when compared to the 10-node network. Here, the ball fails to reach a stable position and instead continuously oscillates around the origin. Interestingly, the network can control the Y axis ball position better than the X axis position, with smaller oscillations and a damped response to larger displacements. This highlights a flaw in the design choice to have a single complex network to control x-z and y-z states codependently instead of two identical simpler networks controlling x-z and y-z states independently.

TABLE 3 | Results of agent training and best episode testing.

Network hidden layer node count	10	100	500
Number of agents with reward > 2,000	31	877	604
Training time	15 h 0 min	66 h 29 min	63 h 55 min[a]
Best performing agent average reward over 10,000 tests	2,681.1	2,812.6	2,670.3
Number of tests where the best performing agent dropped the ball	0	0	56

[a]*Five-hundred node network trained utilizing four pool parallel processing and GPU acceleration for accelerated training.*

The higher frequency of platform oscillation suggests a system more capable of adapting to disturbances, however it also suggests a more unstable controller that may fail under more fringe circumstances. When considering the system's ability to move the platform between two locations, the 100-node network controller does show slight improvements as can be seen by the best episode showing an initial reduction in platform distance. However over time the platform moves further away from the target, so still fails to transfer the load from one location to another.

500-Node Agent

For the 500-node network, the worst response recorded was when the ball fell off the platform from the positive X axis edge. The ball states are noticeably less oscillatory when compared to the 100-node network, however the platform response is extremely responsive with high frequency, low amplitude oscillations dominating the orientation response. This platform response results in a slow responding low frequency oscillatory response from the ball as it does not have time between samples to achieve

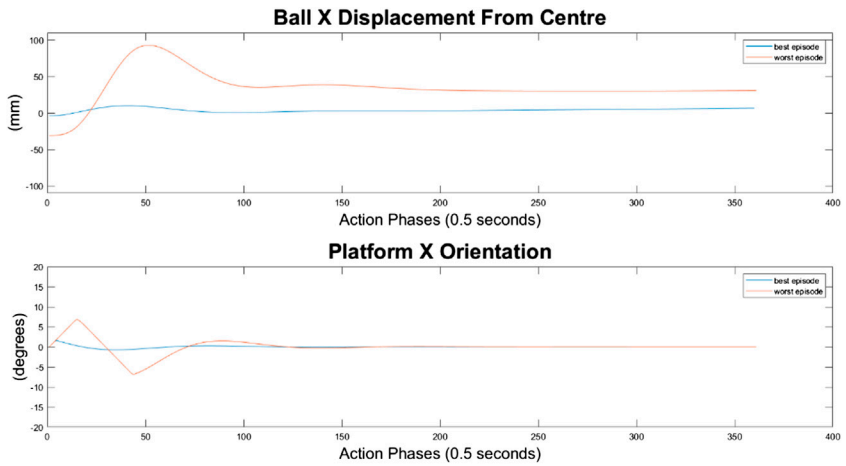

FIGURE 10 | Ball response and change in platform orientation in the *x* axis for the 10 node network.

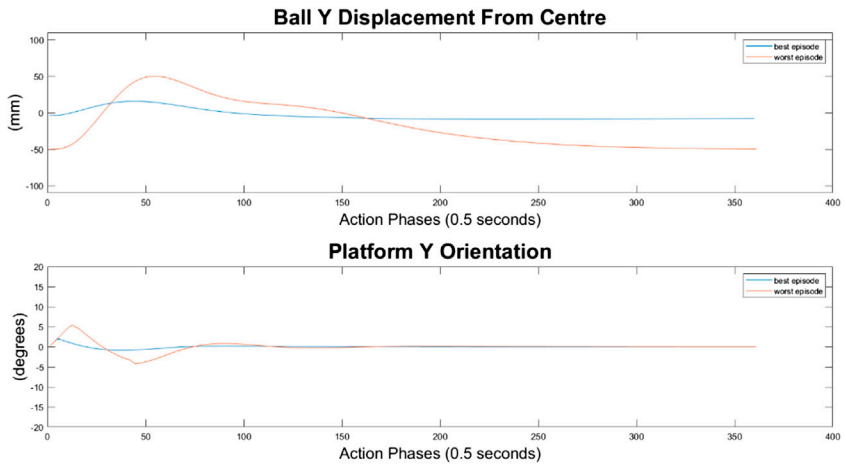

FIGURE 11 | Ball response and change in platform orientation in the *y* axis for the 10 node network.

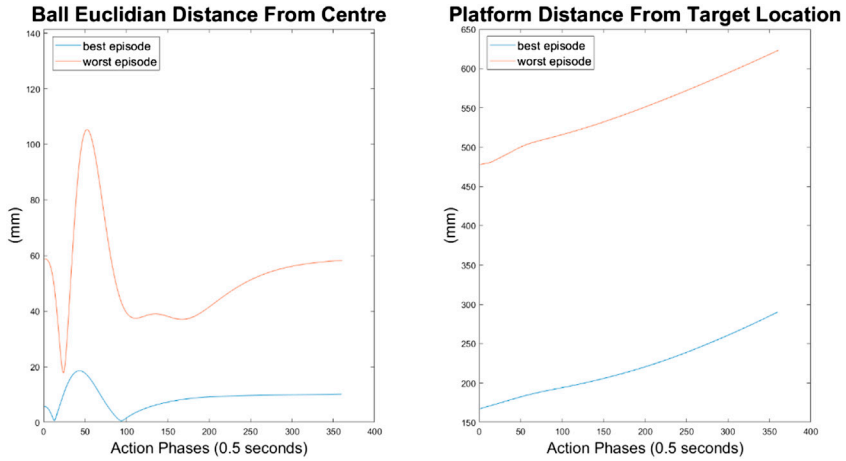

FIGURE 12 | Ball and platform Euclidian distance response for the 10 node network.

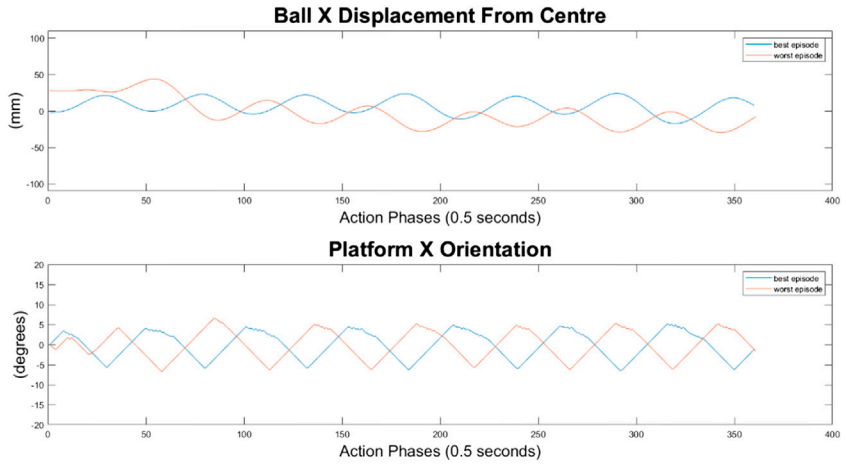

FIGURE 13 | Ball response and change in platform orientation in the *x* axis for the 100 node network.

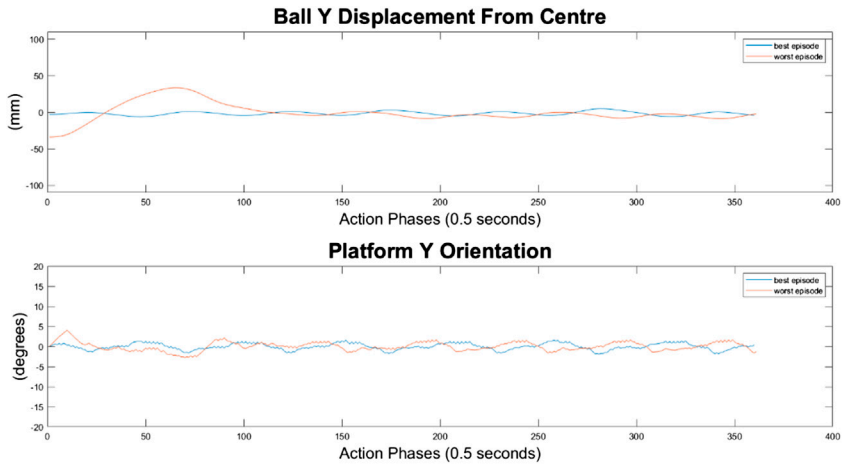

FIGURE 14 | Ball response and change in platform orientation in the *y* axis for the 100 node network.

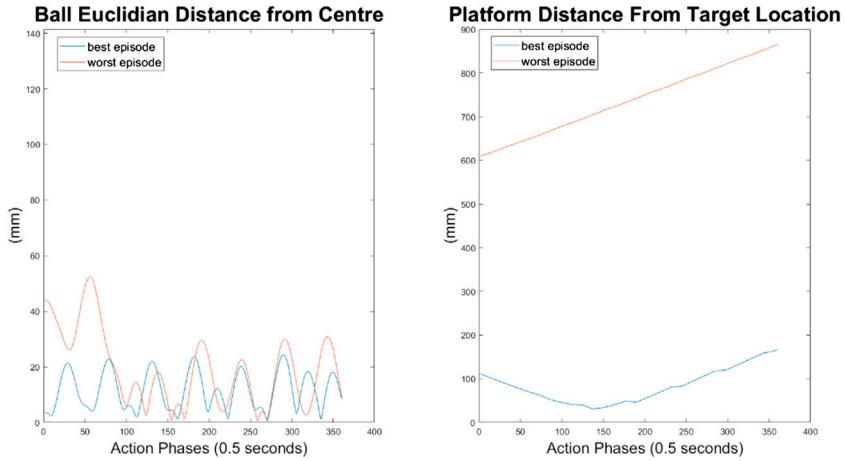

FIGURE 15 | Ball and platform Euclidian distance response for the 100 node network.

any noticeable velocity. Disregarding the failure cases, the 500-node networks appears to achieve a relatively minimal steady state error in ball position, as can be seen in **Figures 16–18**. In addition, it shows promise when analyzing its ability to move the platform to the desired location, but the platform's failure to always balance the load suggests it is an inferior controller to the 10 and 100-node networks.

DISCUSSION

The results of the performed testing suggest that whilst the reinforcement learning controller showed promise for balancing a load on a CDPM, in its current state it is not an improvement on the state of the art. The controller failed to outperform in key performance metrics including rise time and steady state error.

Alex Irpan, a software engineer on the robotics team at Google Brain, explained how important having a well-designed reward criteria is for RL (Irpan, 2018), describing how it has a tendency to overfit to your reward. In post-review of this project, one area of fault may be the reward structure. Since RL aims to achieve the highest reward possible, the reward function should capture the exact desired outcome. This was not the case in this project, as too high a priority was placed upon the system's ability to balance the ball instead of transporting the load. In addition, the velocity-based reward was unnecessary and counterproductive as it discouraged the system from attempting to move the ball closer to the center of the platform quickly. With the overfitting nature of RL to the reward in mind, a simpler reward function may improve training, where the velocity reward is removed, and the ball and plate displacement rewards are weighted equally. The complexity of the reward structure can be seen in the training progress described in **Figures 7–9** in *Hardware Design* section, where the reward was erratic and unsustainable, suggesting the existence of multiple local optima for the problem.

This project was a great exercise in the impact of model complexity on performance. It could be seen how less complex models produced less complex actions (i.e., smaller changes in output), whereas more complex models were erratic and responsive, sometime to their own detriment. Nevertheless, overly simple models also lead to underfitted controllers whose response are not adequate. Whilst no testing was performed on hardware, we suspect that the more complex controllers would see the greatest drop in performance from the simulated testing as the varied environment would likely expose instability within the controller. The controller would likely be overfitted to the reward structure and modeled environment, which was not absolutely true to the real world. On the flipside, the simpler agent structures struggled to wholly capture the simulated environment which led to a worse performing system as it was slower to respond.

Agent performance on the actual rig will vary due to assumptions made during environment modeling. As discussed, the model assumed no inertial forces on the ball due to platform displacement. These assumptions where justified in *Platform Control Design* section, and we maintain the belief that these assumptions are valid, however it is worth noting that as the system response increases in magnitude then the assumptions become less valid, limiting the applicability of this work.

The design process for this system was laboured and highlighted how implementation of intelligent systems on custom build hardware can often be the most time-consuming task in prototype-based research projects. The use of CAD and 3D printing is highlighted throughout this project and made a noticeable difference on our ability to complete the design and build tasks in a reasonable timeframe.

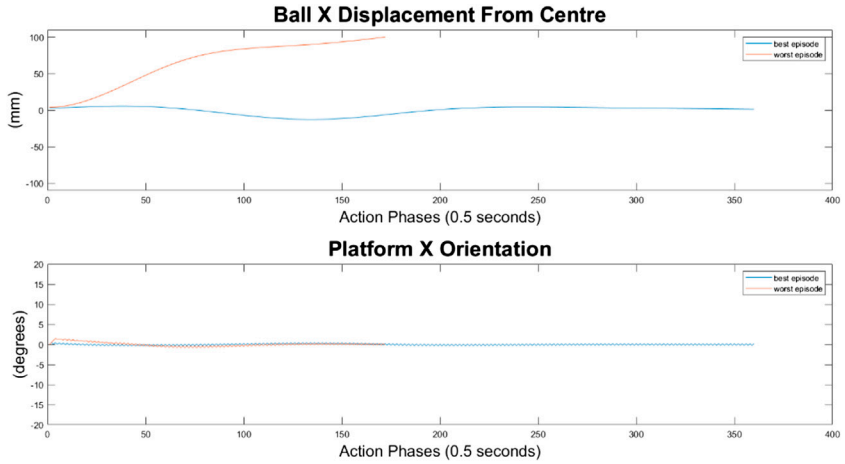

FIGURE 16 | Ball response and change in platform orientation in the *x* axis for the 500 node network.

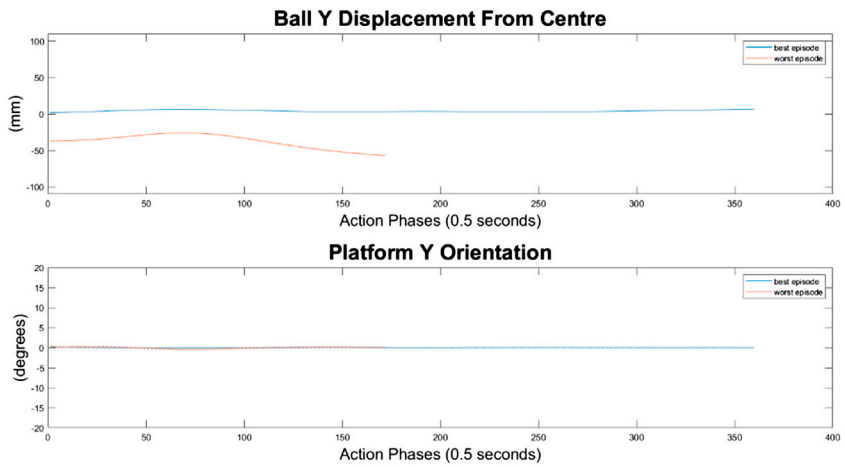

FIGURE 17 | Ball response and change in platform orientation in the *y* axis for the 500 node network.

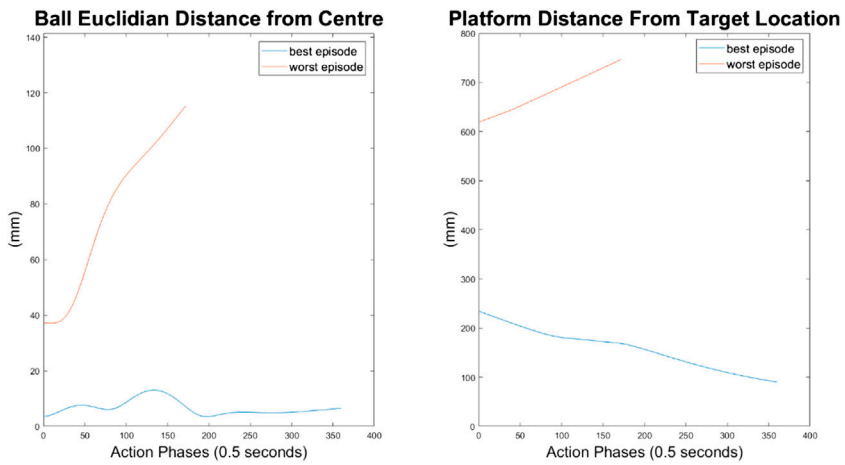

FIGURE 18 | Ball and platform Euclidian distance response for the 500 node network.

CONCLUSION

In the future, structures might need to be constructed rapidly in response to emergencies such as Pandemics. In order to reduce infection rates, worker's exposure to dangerous environments and build rapidly, robotic devices such as Cable Driven Parallel Manipulators could be deployed. These devices would need to deal with a variety of challenges including transporting highly unstable loads. In this work, we have designed and built a CDPM controlled by a neural network reference controller with a nested PID controller, to balance a load on a platform as it is transferred from one location to another. The neural network controller was a two-layer deep network with varying model complexity that was trained using a Deep Deterministic Policy Gradient (DDPG) reinforcement learning algorithm. The neural network controller was trained and assessed over a simulated environment. The system utilized image recognition techniques to identify the states of the loads for feedback and platform states were identified by calculating the cable inverse kinematics.

The image recognition system was able to accurately identify the ball states, however the system was vulnerable to calibration problems due to changing lighting conditions. This may affect the applicability of the system, but would not cause an issue if used in environment with a consistent light source, such as an enclosed warehouse.

Assessments of network complexity showed how precise choosing of model parameters is needed to ensure adequate capturing of the real system, and how overfitting and underfitting are likely when training is performed entirely on simulation. In the future, we plan to investigate how neural network complexity contributes to controller efficiency.

In this work, it was seen that the neural network controller was capable of balancing a load, however the performance did not show any significant improvements on the state of the art. In addition, the controller failed to transport the load, which was a key requirement. The attempt showed how there was still promise for the utilization of RL in ball balancing tasks but highlighted how design of RL systems is difficult and often leads to ineffective solutions, especially for complex systems.

Future work on the system should firstly prioritize testing and implementation of the system on the real rig. Additional work may wish to look at redesigning the reward structure and network for simpler performance. Furthermore, identification of the forward kinematics (i.e., calculating the platform pose from the cable lengths) could lead to the removal of the nested PID controller and introduce an end-to-end neural network controller that would output direct motor control signals. Also, investigating and comparing the combination of RL with other heuristics in the policy search, such as the bacterial foraging algorithm (Oyekan and Hu, 2010; Oyekan et al. 2013), will be carried out in the future.

DATA AVAILABILITY STATEMENT

The raw data supporting the conclusions of this article will be made available by the authors, without undue reservation.

AUTHOR CONTRIBUTIONS

All authors listed have made a substantial, direct, and intellectual contribution to the work and approved it for publication.

SUPPLEMENTARY MATERIAL

The Supplementary Material for this article can be found online at: https://www.frontiersin.org/articles/10.3389/frobt.2020.611203/full#supplementary-material.

REFERENCES

Ali, E., and Aphiratsakun, N. (2015). "AU ball on plate balancing robot," in IEEE international conference on robotics and biomimetics (ROBIO) Zhuhai, China, December 6–9, 2015, 2031–2034. Available at: https://ieeexplore.ieee.org/abstract/document/7419072 (Accessed March 9, 2020).

Alp, A., and Agrawal, S. (2002). "Cable suspended robots: feedback controllers with positive inputs," in Proceedings of the 2002 American control conference (IEEE Cat. No.CH37301), Anchorage, AK, May 8–10, 2002. Available at: https://ieeexplore.ieee.org/document/1024915 (Accessed December 9, 2019).

Arik, S. O., Chrzanowski, M., Coates, A., Diamos, G., Gibiansky, A., Kang, Y., et al. (2017). "DeepVoice: real-time neural text-to-speech," in 34th international conference on machine learning, Sydney, Australia, November 13–15, 2017, 195–204.

Asada, M., Noda, S., Tawaratsumida, S., and Hosoda, K. (1996). Purposive behaviour acquisition for a real robot by vision-based reinforcement learning. *Mach. Learn.* 23 (2-3), 279–303. doi:10.1007/bf00117447

Awtar, S., Bernard, C., Boklund, N., Master, A., Ueda, D., and Craig, K. (2002). Mechatronic design of a ball-on-plate balancing system. *Mechatronics* 12 (2), 217–228. doi:10.1016/S0957-4158(01)00062-9

Beira, R., Santos-Carreras, L., Rognini, G., Bleuler, H., and Clavel, R. (2011). Dionis: a novel remote-center-of-motion parallel manipulator for minimally invasive surgery. *Appl. Bionics Biomech.* 8 (2), 191–208. doi:10.3233/ABB-2011-0020

Bigharaz, M., Safaei, F., Afshar, A., and Suratgar, A. (2013). "Identification and nonlinear control of a ball-plate system using neural networks," in The 3rd international conference on control, instrumentation, and automation, Tehran, Iran, December 28–30, 2013, 260–262. Available at: https://ieeexplore.ieee.org/abstract/document/6912845 (Accessed March 9, 2020).

Bosscher, P., and Ebert-Uphoff, I. (2004). "Wrench-based analysis of cable-driven robots," in IEEE international conference on robotics and automation, 2004. Proceedings ICRA '04, New Orleans, LA, April 26–May 1, 2004. Available at: https://ieeexplore.ieee.org/abstract/document/1302502 (Accessed December 8, 2019).

Brown (2019). "SkyCam." Skycam tv. Available at: http://www.skycam.tv/ (Accessed Dec 08, 2019).

Cornell University (2018). *Equivalence between policy gradients and soft Q-learning*. Cornell, NY: Cornell University.

Dallej, T., Gouttefarde, M., Andreff, N., Michelin, M., and Martinet, P. (2011). "Towards vision-based control of cable-driven parallel robots," in 2011 IEEE/RSJ international conference on intelligent robots and systems, San Francisco, CA, September 25–30, 2011. Available at: https://ieeexplore.ieee.org/abstract/document/6094591/references#references (Accessed December 9 2019).

DeepMind Technologies (2014). *Deterministic policy gradient algorithms*. London, United Kingdom: University College London.

Gallardo-Alvarado, J. (2016). *Kinematic analysis of parallel manipulators by algebraic screw theory*. 1st Edn. Cham, CH: Springer, 19–28.

Garychl (2018). "Applications of reinforcement learning in real world." Towards Data Science. Available at: https://towardsdatascience.com/applications-of-

reinforcement learning-in-real-world-1a94955bcd12 (Accessed December 06, 2019).

Géron, A. (2017). *Hands-on machine learning with scikit-learn and TensorFlow*. 6th Edn. Newton, MA: O'Reilly Media, Inc., 445–478.

Gullapalli, V., Franklin, J., and Benbrahim, H. (1994). Acquiring robot skills *via* reinforcement learning. *IEEE Control Syst.* 14 (1), 13–24. doi:10.1109/37.257890

Hodge, V., and Austin, J. (2012). Discretisation of data in a binary neural k-nearest neighbour algorithm. *Knowl. Inf. Syst.* 8 (3), 276–291. Available at: http://eprints.whiterose.ac.uk/89484/ (Accessed March 8, 2020).

Hong, W. (2019). *Under-constrained 4-cable driven parallel robot for automated parts retrieval and storage using LEGO MINDSTORMS EV3 M.Sc*. Sheffield, United Kingdom: The University of Sheffield.

Irpan, A. (2018). Deep reinforcement learning doesn't work yet. Sorta Insightful.

Karpathy, A. (2016). "Deep reinforcement learning: pong from pixels," in Andrej Karpathy Blog. Available at: http://karpathy.github.io/2016/05/31/rl/.

Keshmiri, M., Jahromi, A., Mohebbi, A., Hadi Amoozgar, M., and Xie, W. (2012). Modeling and control of ball and beam system using model based and non-model based control approaches. *Int. J. Smart Sens. Intell. Syst.* 5 (1), 14–35. doi:10.21307/ijssis-2017-468

Khosravi, M., and Taghirad, H. (2016). Stability analysis and robust PID control of cable-driven robots considering elasticity in cables. *Amirkabir Int. J. Electr. Electron. Eng.* 48 (2), 113–125. doi:10.22060/EEJ.2016.821

Kostamo, J., Hyotyniemi, H., Kuosmanen, P., and Design, M. (2005). "Ball balancing system: an educational device for demonstrating optimal control," in 2005 international symposium on computational intelligence in robotics and automation, Espoo, Finland, June 27–30, 2005. Available at: https://ieeexplore.ieee.org/abstract/document/1554306 (Accessed March 9, 2020).

Lachevre, P., Sagastuy, J., Fournier-Bidoz, E., and Assad, A. (2017). *Balancing an inverted pendulum on a quadcopter with reinforcement learning*. Stanford, CA: Stanford University.

Lillicrap, T., Hunt, J., Pritzel, A., and Heess, N. (2016). "Continuous control with deep reinforcement learning," in ICLR, San Juan, May 2–4, 2016.

Mnih, V., Kavukcuoglu, K., Silver, D., Rusu, A. A., Veness, J., Bellemare, M. G., et al. (2015). Human-level control through deep reinforcement learning. *Nature* 518, 529–533. doi:10.1038/nature14236

National Institute of Standards and Technology (1994). *Applications of the NIST Robocrane*. Maui: NIST.

Oyekan, J., Gu, D., and Hu, H. (2013). Visual imaging of invisible hazardous substances using bacterial inspiration. *IEEE Trans. Sys. Man Cybern. Syst.* 43 (5), 1105–1115. doi:10.1109/TSMCA.2012.2231410

Oyekan, J., and Hu, H., (2010). "A novel bacterial foraging algorithm for automated tuning of PID controllers of UAVs," in IEEE international conference on information and automation, Harbin, China, June 20–23, 2010 693–698.

Patel, Y., and George, P. (2012). Parallel manipulators applications—a survey, *Modern Mech. Eng.* 02 (3), 57–64. doi:10.4236/mme.2012.23008

Qian, S., Zi, B., Shang, W., and Xu, Q. (2018). A review on cable-driven parallel robots. *Chin. J. Mech. Eng.* 31 (1), 66. doi:10.1186/s10033-018-0267-9

Rahmat, M., Wahid, H., and Wahab, N. (2010). Application of intelligent controller in a ball and beam control system. *Int. J. Smart Sens. Intell. Syst.* 3 (1), 45–60. doi:10.21307/IJSSIS-2017-378

Ryu, K., and Oh, Y. (2011). "Balance control of ball-beam system using redundant manipulator," in 2011 IEEE international conference on mechatronics, Istanbul, Turkey, April 13–15, 2011, 403–408. Available at: https://ieeexplore.ieee.org/abstract/document/5971319/references#references (Accessed March 9, 2020).

Saber, O. (2015). A spatial translational cable robot. *J. Mech. Robotics* 7 (3), 031006. doi:10.1115/1.4028287

Sammarchi, E. (2019). *Dynamic modelling and simulation of a cable-driven parallel robot for rehabilitation applications*. Bologna, Italy: Università di Bologna.

Shih, C. L., Hsu, J. H., and Chang, C. J. (2017). Visual feedback balance control of a robot manipulator and ball-beam system. *J. Comput. Commun.* 5 (9), 8–18. doi:10.4236/jcc.2017.59002

Tang, X. (2014). An overview of the development for cable-driven parallel manipulator. *Adv. Mech. Eng.* 6, 823028. doi:10.1155/2014/823028

Tannous, M., Caro, S., and Goldsztejn, A. (2014). Sensitivity analysis of parallel manipulators using an interval linearization method. *Mech. Mach. Theory* 71, 93–114. doi:10.1016/j.mechmachtheory.2013.09.004

Watkins, C., and Dayan, P. (1992). Q-Learning. *Machine learning* 8 (34), 279–292. doi:10.1007/BF00992698

Yu, F. (2017). Deep Q network vs policy gradients—an experiment on VizDoom with keras.

Conflict of Interest: The authors declare that the research was conducted in the absence of any commercial or financial relationships that could be construed as a potential conflict of interest.

frontiers in Robotics and AI

ORIGINAL RESEARCH
published: 22 March 2021
doi: 10.3389/frobt.2021.645424

Robotic Ultrasound Scanning With Real-Time Image-Based Force Adjustment: Quick Response for Enabling Physical Distancing During the COVID-19 Pandemic

Mojtaba Akbari[1]*, *Jay Carriere*[1], *Tyler Meyer*[2], *Ron Sloboda*[3], *Siraj Husain*[2], *Nawaid Usmani*[3] *and Mahdi Tavakoli*[1]

[1] Telerobotic and Biorobotic System Group, Electrical and Computer Engineering, University of Alberta, Edmonton, AB, Canada, [2] Division of Radiation Oncology, Tom Baker Cancer Centre, Calgary, AB, Canada, [3] Department of Oncology, Cross Cancer Institute, Edmonton, AB, Canada

OPEN ACCESS

Edited by:
John Oyekan,
The University of Sheffield,
United Kingdom

Reviewed by:
Chueh-Hung Wu,
National Taiwan University Hospital,
Taiwan
Changsheng Li,
Beijing Institute of Technology, China

***Correspondence:**
Mojtaba Akbari
akbari@ualberta.ca

Specialty section:
This article was submitted to Biomedical Robotics, a section of the journal Frontiers in Robotics and AI

Received: 23 December 2020
Accepted: 25 February 2021
Published: 22 March 2021

Citation:
Akbari M, Carriere J, Meyer T, Sloboda R, Husain S, Usmani N and Tavakoli M (2021) Robotic Ultrasound Scanning With Real-Time Image-Based Force Adjustment: Quick Response for Enabling Physical Distancing During the COVID-19 Pandemic. Front. Robot. AI 8:645424. doi: 10.3389/frobt.2021.645424

During an ultrasound (US) scan, the sonographer is in close contact with the patient, which puts them at risk of COVID-19 transmission. In this paper, we propose a robot-assisted system that automatically scans tissue, increasing sonographer/patient distance and decreasing contact duration between them. This method is developed as a quick response to the COVID-19 pandemic. It considers the preferences of the sonographers in terms of how US scanning is done and can be trained quickly for different applications. Our proposed system automatically scans the tissue using a dexterous robot arm that holds US probe. The system assesses the quality of the acquired US images in real-time. This US image feedback will be used to automatically adjust the US probe contact force based on the quality of the image frame. The quality assessment algorithm is based on three US image features: correlation, compression and noise characteristics. These US image features are input to the SVM classifier, and the robot arm will adjust the US scanning force based on the SVM output. The proposed system enables the sonographer to maintain a distance from the patient because the sonographer does not have to be holding the probe and pressing against the patient's body for any prolonged time. The SVM was trained using bovine and porcine biological tissue, the system was then tested experimentally on plastisol phantom tissue. The result of the experiments shows us that our proposed quality assessment algorithm successfully maintains US image quality and is fast enough for use in a robotic control loop.

Keywords: medical image quality assessment, medical robotic, ultrasound scanning, artificial intelligence, robotics for COVID-19

1. INTRODUCTION

Ultrasound (US) image acquisition is a popular medical imaging method because it does not involve radiation (like x-ray or CT do), is generally regarded as safe, has a low cost compared to other medical imaging methods and is widely available. For a healthcare system that is struggling with COVID-19, US scanning is a way for COVID-19 diagnosis (Buda et al., 2020; McDermott et al., 2020), especially in developing countries where access to the lab kit is very limited. But there are some factors regarding the US scanning procedure during COVID-19 pandemic that need to be addressed. The first factor is the close contact between sonographers and patients; it is very important to minimize contact between sonographers and patients during the COVID-19 pandemic. It has been proven that close person/person contact is the main way for the transmission of the virus (Jarvis et al., 2020; Jin et al., 2020; Morawska and Milton, 2020; Zu et al., 2020). The second factor is related to COVID-19 patients with underlying conditions such as heart conditions. These patients are at heightened risk, and some of these underlying conditions need US imaging, like echocardiography. The third factor is that US imaging can also be quite time-consuming. Most US scans last between 15 and 45 min (NHL, 2018). For example, echocardiography takes almost 20 min (Ebadollahi et al., 2001). Because of this, we need a system that helps a sonographer to scan tissue and decreases the contact duration (i.e., allows for greater distancing) between sonographers and patients. This paper proposes a quick, low-cost, and deployable solution for the problem mentioned above as a consequence of the COVID-19 pandemic. Robots can be very useful for solving this problem. The part of the scanning that requires experience and knowledge of the sonographer can be done the normal way, and the parts that put the sonographer at an increased risk of contacting the virus can be delegated to the robotic system just like the way x-ray systems work. Using robots during the COVID-19 pandemic can significantly decrease the risk of virus transmission (Tavakoli et al., 2020) particularly because the proposed robotic system can be sanitized between each US scanning procedure.

The assessment of image quality is essential in developing robotic US scanning. Image quality assessment has been a challenging topic in medical image processing, and different methods have been proposed in the literature. There are three different categories of image quality assessment algorithm based on the availability of reference images or other supplementary information. The first category is called full-reference image quality assessment. A reference image (high-quality image) is available in this category, and the quality assessment metric is implemented by comparing a given image to the reference image. The second category is called semi-reference image quality assessment, in which the algorithm has access only to some information about the reference image, such as important features in the image. For instance, Chen et al. (2020) uses the visual features (statistical features from contourlet transform) that are critical for both human perception and object recognition for sonar image quality assessment, but the reference image is not available. Semi-reference methods are more challenging than full-reference algorithms, and how to utilize the additional information is an important question for these algorithms. The final category is called no-reference image quality assessment, in which the algorithm does not have access to the reference image or any additional information related to it. This category is the most challenging but is very important and useful for medical image quality assessment (Chow and Paramesran, 2016). Being as typically we do not have access to quality reference images, the crucial part of no-reference image quality assessment is developing the quality metrics. Quality metrics should be based on features that are present in either high-quality or low-quality images. The extracted features need to be combined to build a quality metric that creates an image quality score.

The problem with US images processing is the inherent noise in the images, making it difficult for a physician to interpret them. This makes US image quality assessment a very complicated task. In this paper, we propose a method for assessing the US image's quality when a robotic arm is holding the US probe. We will incorporate the algorithm in the robot control loop for automatic scanning of tissue. An admittance-based controller will be used for the robot and automatically control the probe's scanning force applied to the tissue. The admittance controller produces a desired position using a predefined relationship between the position and measured force (Zeng and Hemami, 1997; Fong and Tavakoli, 2018). The US scanning assistant is shown in **Figure 1**. The sonographer uses a handle to position the robot by incorporating a robot's built-in admittance control, and the robot adjusts the US scanning force applied to the tissue by analyzing the quality of the acquired image. This system reduces contact time and mitigates the risk of virus transmission between the sonographer and the patient. Being as the system scans the tissue based on image quality assessment feedback, the sonographer does not need to be next to the patient for the whole duration of the scanning.

The outline of the paper is as follows. In section 2, we will give a brief review of previous medical image quality assessment algorithms, robot-assisted sonography and robotic admittance control applications. We will address the contributions of this paper in section 2.4. We develop our proposed image quality assessment algorithm in section 3 by giving details of the algorithm and discussing the specific image features it uses. In section 4, we will give the details of the robotic admittance controller used in the system to adjust the US scanning force applied to the tissue. The experimental setup and the experimental results are presented in section 5. We will conclude our method and its advantages in section 6.

2. PRIOR WORK

In this section, we will talk about previous work that has been done in medical image quality assessment, robot-assisted sonography, and robotic admittance control. We will talk about our contribution and novelty in the last paragraph of this section.

2.1. Medical Image Quality Assessment

Medical image quality assessment is a broad topic across multiple imaging modalities, with each imaging modality having its

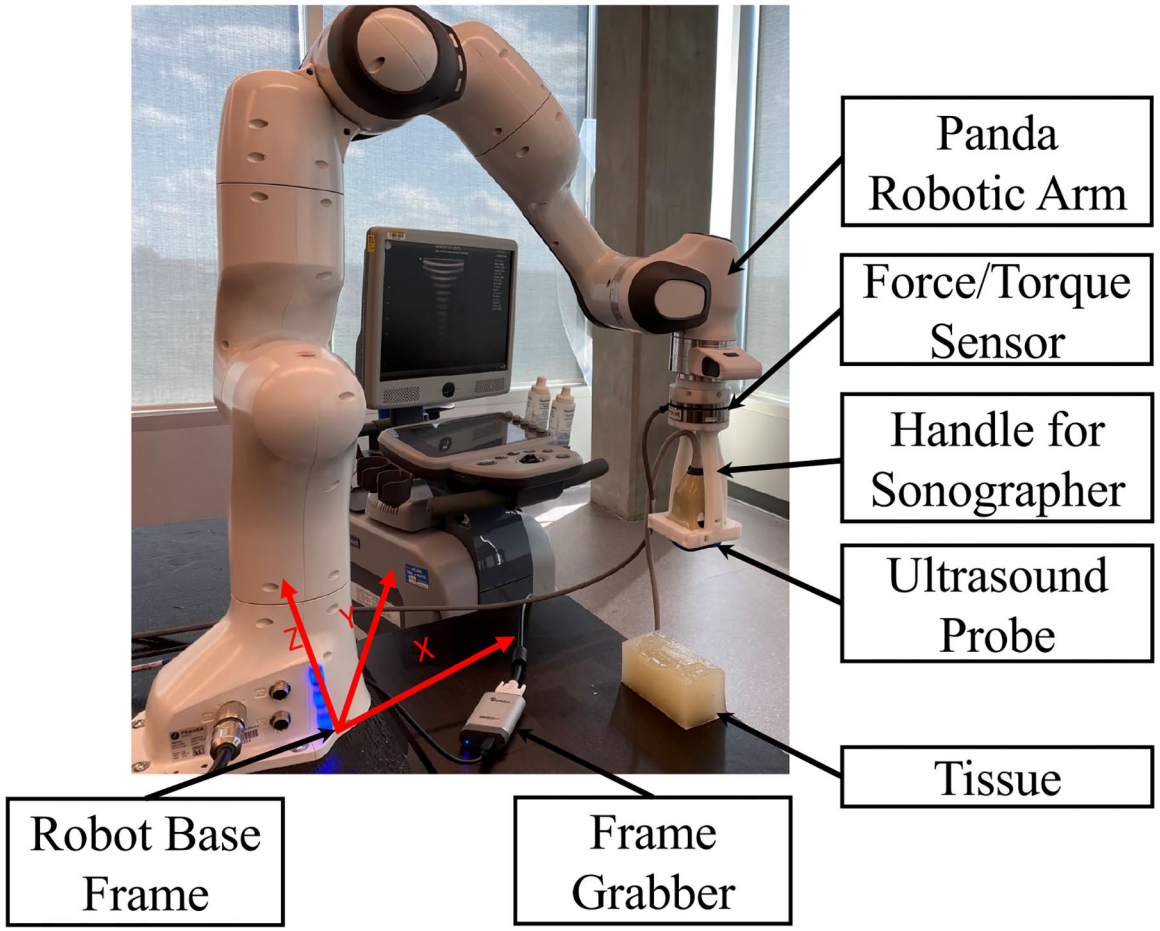

FIGURE 1 | US scanning assistant including Panda robot arm, US probe, handle for sonographer, tissue phantom, frame grabber, and robot base frame.

features and characteristics that need to be considered. A review of different medical image quality assessment algorithms and their corresponding imaging modalities can be found in Chow and Paramesran (2016). The most crucial problem in medical image quality assessment is the unavailability of reference data, and most methods are based on no-reference image quality assessment algorithms. We can classify no-reference medical image quality assessment methods into model-based and image-based methods. The algorithm is based on modeling both images and noise in a model-based image quality assessment algorithm, such as the method proposed in Zemp et al. (2003). On the other hand, in image-based quality assessment algorithms, metrics are present to assess the image's quality.

In US image quality assessment, different methods have been proposed for modeling image and noise. In Zemp et al. (2003), the author uses Noise-Equivalent Quanta (NEQ) that models noise based on US machine parameters and tissue physical property information; an improved version of the signal-to-noise ratio. Structural Similarity Index Measure (SSIM) is a very famous image quality assessment metric and has been used in many different applications. The method proposed in Renieblas et al. (2017) uses SSIM as the main quality assessment criteria and incorporates specific image features like preserved edges, structural similarity, and textures in the image.

Image-based quality assessment methods propose criteria that formalize critical features for quality assessment. The method proposed in Hemmsen et al. (2010) uses data management and data acquisition techniques to formalize the quality assessment metrics for US images. The authors of Abdel-Hamid et al. (2016) use five important features of transformed images for building a quality assessment metric. These five features are sharpness, illumination, homogeneity, field definition, and content. The method proposed in Abdel-Hamid et al. (2016) uses the wavelet transform and extracts the five image features from the transformed image, and combining them to create a formula for image quality assessment of human retina images.

As one modality of medical imaging, US poses many challenges in terms of image quality assessment. These challenges come primarily from the noisy nature of the US images. US image's quality is usually defined as an ability to see some tissue features or organs in the image. The method proposed in Zhang et al. (2017) developed a method of segmenting the fetus in an US

image, using a texton method on the image. The texton method performs segmentation and feature extraction, and a random forest classifier assesses the quality of the image based on the extracted features. Schwaab et al. (2016) proposes the extraction of three features from breast US images and uses a random forest for classification of those. These features are the nipple position, the shadow caused by the nipple, and the breast contours' shape. Schinaia et al. (2017) used a method similar to Schwaab et al. (2016), but incorporated 14 features and a correlation matrix for quality assessment. Deep Convolutional Neural Networks (CNN) have also proven to perform well for complicated tasks like this. Wu et al. (2017) uses two deep convolutional neural networks called C-CNN and L-CNN for quality assessment. L-CNN finds an ROI (Region Of Interest) in the image, and C-CNN evaluates the quality of the image based on the extracted ROI. The output of C-CNN is the binary label segmentation of the US image. The method proposed in Chatelain et al. (2015) and Welleweerd et al. (2020) use confidence map, which was proposed in Karamalis et al. (2012) for orienting and moving the US probe during scanning of the tissue. Confidence map methods are based on US signal propagation model inside of the tissue and the outcome is a map that can be used for feature extraction. The extracted features are the inputs to the controller and the output is the control signals for controlling the probe's orientation and position.

2.2. Robot-Assisted Sonography

Robots can be very helpful to a sonographer during US scanning. Many methods have been proposed to facilitate the process of sonography using robots. Najafi and Sepehri (2011) developed a robotic wrist to perform US imaging on a patient at remote sites. This system has four degrees of freedom and has been used for US imaging of the liver and kidney. The device developed in AbbasiMoshaii and Najafi (2019) is placed on the patient's body by an operator, and US expert controls the device's motion to obtain US image. The paper focuses on the robotic mechanism that performs US imaging. The mechanism keeps the US probe in contact with the patient's body and facilitates the sonographer's US scanning procedure. Fang et al. (2017) proposes a cooperatively robotic US system to reduce the force sonographers apply. This system consists of a six-axis robotic arm that holds and actuates the US probe. A dual force sensor setup enables cooperative control and adaptive force assistance using admittance force control. Antico et al. (2019) prepared a good review of different methods proposed in robot-assisted US intervention, and Moshaii and Najafi (2014) is a good review of the mechanical details of robot-assisted US scanning.

Tele-sonography is developed for scanning the tissue using remote robot. Sharifi et al. (2017) developed an impedance-controlled teleoperation system for robot-assisted tele-echography of moving organs such as heart, chest, and breast compensating for their natural motions. This system proposes two impedance models for master and slave robots. The slave robot follows the master robot's trajectory but complies with the oscillatory interaction force of moving organs, and the sonographer receives feedback from the slave robot. Sartori et al. (2019) proposes a solution for energy consumption in tele-echography on the master site based on properly scaling the energy exchanged between the master and the slave site. There are many challenges in designing tele-sonography system. The most important one is the high cost of the system and haptic feedback required in the master site. Using haptic feedback causes time delay in the system that may result discrepancy between sonographer and US probe during scanning. Our proposed method can be used as a local controller in the slave site to overcome this problem.

2.3. Robot Admittance Control

Admittance controller uses a predefined relationship between force and position. Authors in Carriere et al. (2019) use admittance control to ensure compliance in a co-manipulated US scanning system controlling the force applied to the tissue and reducing exerted force from the sonographer. The method proposed in Piwowarczyk et al. (2020) uses an admittance controller to scale the force applied by the user on the robot in relation to force applied to the environment. The stability of admittance-controlled robots and their ability to cope with different environmental forces have been investigated in Ferraguti et al. (2019). Admittance control was used in Li et al. (2018) for an exoskeleton robot to create a reference trajectory based on measured force. Dimeas and Aspragathos (2016) analyzes the stability of admittance control by detecting unstable behaviors and stabilizing the robot using an adaptive online method to tune the admittance control gains. The stabilization of the robot is based on monitoring high-frequency oscillations in the force signals. This idea was also used in Landi et al. (2017) for stabilizing the admittance control when interacting with humans. The idea of incorporating neural networks and admittance control for robot trajectory tracking is developed in Yang et al. (2018), in which the trajectory tracking is guaranteed by using a neural network while admittance control regulates torques to follow the desired trajectory. Authors in Keemink et al. (2018) prepared a very good review of different applications of admittance control in robotics.

2.4. Contributions of This Paper

As we mentioned in section 2.3, different methods and applications have been proposed for medical image quality assessment and robotic admittance control but all of them do not consider image feedback in admittance controllers. The idea of combining image feedback and admittance controller in the US scanning procedure is the first novelty of this paper. We also allow for collaboration between humans and the robot to keep the sonographer in the loop during the US scanning procedure. The proposed method uses a real-time image quality assessment algorithm to inform the robotic system. The real-time nature of the proposed image quality assessment algorithm makes it suitable for the clinician in the loop robot-assisted medical applications. The combination of admittance control and online image quality assessment algorithm in the robotic arm ensures social distancing during the COVID-19 pandemic and has not been explored before in the literature.

The second novelty of this paper is to propose a very quick, low-cost, and deployable solution for the COVID-19 pandemic that can be trained based on the preferences of the sonographers in terms of how US scanning is done in different applications. The training phase requires nothing more than the commodity hardware (e.g., a personal computer). This is a very important advantage of the proposed system over the method mentioned in section 2.1. The proposed method has the ability to consider the preferences of the sonographers for different applications by incorporating it in the training phase. The sonographer can manually classify the training set and the system will tune the parameters for the sonographer's preferences. To the best of our knowledge, this ability has not been investigated in the previous methods.

The third novelty of the proposed method is the ability to be used in unilateral tele-sonography as a controller on the patient side. In a tele-sonography modality, the sonographer moves the robot to the desired position using a master robot. The sonographer needs to feel the contact force between the tissue and the probe during scanning. The system should have a haptic interface on the master site to enable this feature for the sonographer. Using a haptic interface could cause a time delay in the system during scanning as discussed in Najafi and Sepehri (2011), Sharifi et al. (2017), Moshaii and Najafi (2014), and AbbasiMoshaii and Najafi (2019). The low-cost and better solution is using a unilateral tele-sonography system with a local controller on the patient site that adjusts the force applied to the tissue during scanning based on acquired image's quality. Our proposed method can be incorporated as a local controller in the slave site to adjust the force applied to the tissue based on the preferences of the sonographers. This feature will remove the essence of having haptic feedback in the tele-sonography system and will decrease the cost of the system.

3. IMAGE QUALITY ASSESSMENT ALGORITHM

As previously mentioned, US images are usually very noisy, and therefore, the tissue is not very clear in the images. This problem makes the automated assessment of US images complicated. A US image quality assessment algorithm should distinguish between different features in an image and decide on image quality based on the acquired features. For our proposed image quality assessment method, we will use a Support Vector Machine (SVM) classifier, which is compatible with small training sets and has proven to have a good ability to solve complicated problems, especially in medical applications.

3.1. Image Quality Assessment Metrics

We propose three distinct features for estimating the quality of the image. The first feature is based on the contact between the probe and the tissue. The second feature computes the level of compression caused by the US scanning force applied to the tissue. The third feature is an estimation of the noise level in the image. The noise level is estimated based on the statistical features of the noise in the US image. We will discuss each of the features in-depth in the following sub-sections.

3.1.1. Correlation

We use image correlation for modeling the contact between the tissue and probe. When there is no contact (or proper contact) between the probe and tissue, the US image will only consist of patterns of arcs; see **Figure 2A**. When we have sufficient contact, however, actual tissue will be visible in the image. In **Figure 2A**, the image captured by the US machine was defined as no-contact image I_{nc} in the sense that probe is not contacting the tissue when the image is captured. We define the contact feature as the correlation of no-contact image I_{nc} with an image captured by the US machine I_k in every time step k of the experiment. The contact feature c_k gives us a good estimation of the sufficiency of contact and $c_k \in [0, 1]$. The mathematical details of how the correlation between the images is calculated and how contact between the probe and the tissue is defined are as follows:

$$\mathrm{corr}(\mathrm{I_k}, \mathrm{I_{nc}}) = \frac{\sum_{p_x=1}^{M}\sum_{p_y=1}^{N}(I_k(p_x,p_y)-\overline{I_k})(I_{nc}(p_x,p_y)-\overline{I_{nc}})}{\sqrt{(\sum_{p_x=1}^{M}\sum_{p_y=1}^{N}(I_k(p_x,p_y)-\overline{I_k})^2)(\sum_{p_x=1}^{M}\sum_{p_y=1}^{N}(I_{nc}(p_x,p_y)-\overline{I_{nc}})^2)}} \quad (1)$$

$$c_k = \begin{cases} 1, & \mathrm{if corr}(\mathrm{I_k}, \mathrm{I_{nc}}) \geq \mathrm{t_{corr}} \\ 0, & \mathrm{if corr}(\mathrm{I_k}, \mathrm{I_{nc}}) < \mathrm{t_{corr}} \end{cases} \quad (2)$$

Here, the contact feature c_k is the value of the correlation between the two images. (p_x, p_y) is the location of pixels in the image frame, and M and N are the height and width of input images, respectively. $\overline{I_k}$ and $\overline{I_{nc}}$ are the average of the pixels' intensities in the acquired image and the image with no contact with the tissue, respectively, and t_{corr} is the threshold for determining the contact level. **Figure 2** shows two images, in which **Figure 2A** was captured when there is not enough contact between the tissue and the probe, and **Figure 2B** was conducted with sufficient contact. The x-y axis in the image frame is shown in **Figure 2A** and it is the same for all images in this paper.

3.1.2. Compression

The level of compression is a very important feature in US image acquisition. When the robot applies force to the tissue, it causes deformation. More force causes greater distortion/deformation. This causes pain for the patient, and may lead to wrong clinical diagnosis (Fang et al., 2017). The proposed compression feature is the difference between the maximum and minimum index of the pixels brighter than the threshold t_{comp}, relative to the image's size in the vertical direction. The mathematical expression for calculating the image compression feature is as follows:

$$\begin{aligned} U &= \max(p_y), \text{ where } I_k(p_y, \forall p_x \in I_k) \geq t_{comp} \\ L &= \min(p_y), \text{ where } I_k(p_y, \forall p_x \in I_k) \geq t_{comp} \\ f_c &= \frac{U-L}{M} \end{aligned} \quad (3)$$

In (3), U and L are the maximum and minimum location of the pixels having intensity higher than t_{comp}. We define f_c as the

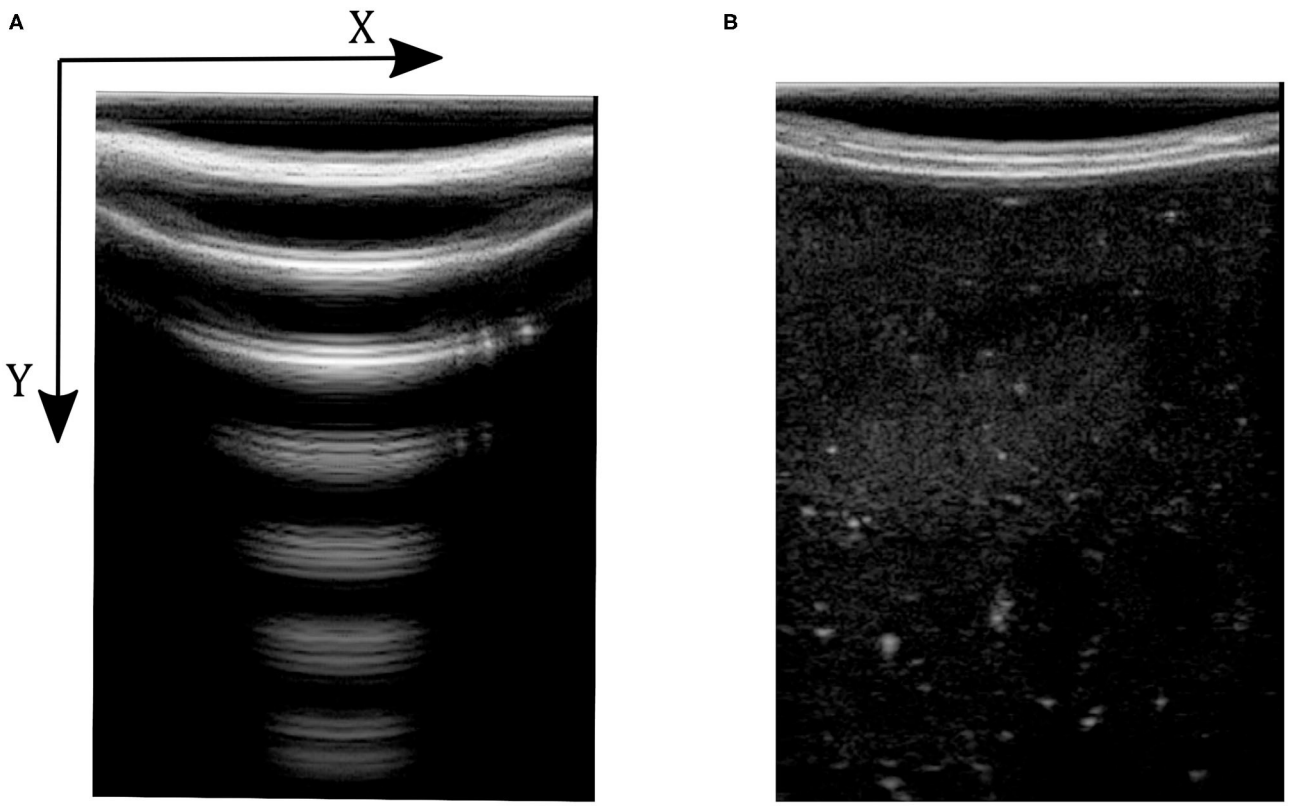

FIGURE 2 | Ultrasound images with and without contact between tissue and probe. **(A)** Ultrasound image with no contact. **(B)** Ultrasound image with sufficient contact.

compression feature in (3). M is the height of the image along the y direction. **Figure 3** shows two images with different levels of compression. **Figure 3A** is the US image with a high level of compression, and **Figure 3B** is the US image with a low level of compression. We have also shown a variation of f_c with respect to measured force in the z direction of the force sensor frame $F_{Z|k}$ (this is aligned with the y direction in image frame) in **Figure 4**.

3.1.3. Noise

As we mentioned earlier, the US image is very noisy. The noise comes from the manner in which US captures an image. This noise feature is also very important for the quality assessment of US images. As a first step, we use a Wiener filter for removing speckle noise from the US image. The calculation of the Wiener filter is based on Lim (1990). The US image's noise level can be estimated by the mean and standard deviation of the difference image between the original image I_k and the filtered image $I_{k,f}$. Equations (5) to (8) show the mathematical explanation of using a Wiener filter to remove noise from the US image and calculate the noise feature.

$$\mu = \frac{\sum_{p_x \in \eta} \sum_{p_y \in \eta} I_k(p_x, p_y)}{P \times Q} \tag{4}$$

$$\sigma^2 = \frac{\sum_{p_x \in \eta} \sum_{p_y \in \eta} I_k(p_x, p_y)^2}{P \times Q} - \mu^2 \tag{5}$$

$$I_{k,f}(p_x, p_y) = \mu + \frac{\sigma^2 - \nu^2}{\sigma^2}(I_k(p_x, p_y) - \mu) \tag{6}$$

$$I_n = I_k - I_{k,f} \tag{7}$$

$$f_n = \overline{I_n} + \sigma_n \tag{8}$$

Here, η is the neighborhood with the size of $P \times Q$ around each pixel of the noisy image and $I_k(p_x, p_y)$ is the intensity of each pixel in the noisy US image. μ is the average of pixel intensity in the original US image, and σ^2 is the corresponding variance value in (6). $I_{k,f}(p_x, p_y)$ is the intensity of the US image after removing the noise using Wiener filter and ν^2 is the noise variance in the image in (7). Equation (8) finds the difference between US image I_k and filtered image $I_{k,f}$ to find the US image's noise. In (8), $\overline{I_n}$ is the average of noise in the image and σ_n is the corresponding standard deviation value. **Figure 5** shows two images with high level (**Figure 5A**) and low level (**Figure 5B**) of noise. We have also shown in **Figure 6**, the variation of the noise feature f_n in the US image with respect to measured force $F_{Z|k}$.

3.2. Support Vector Machine (SVM)

The compression and noise features mentioned above will be used as an input to the SVM classifier (e.g, taking the output of the image feature calculation, Equations (3) and (8), for I_k we then calculate the SVM score) and the correlation feature works as a gate. SVM classifier tries to find a line that separates

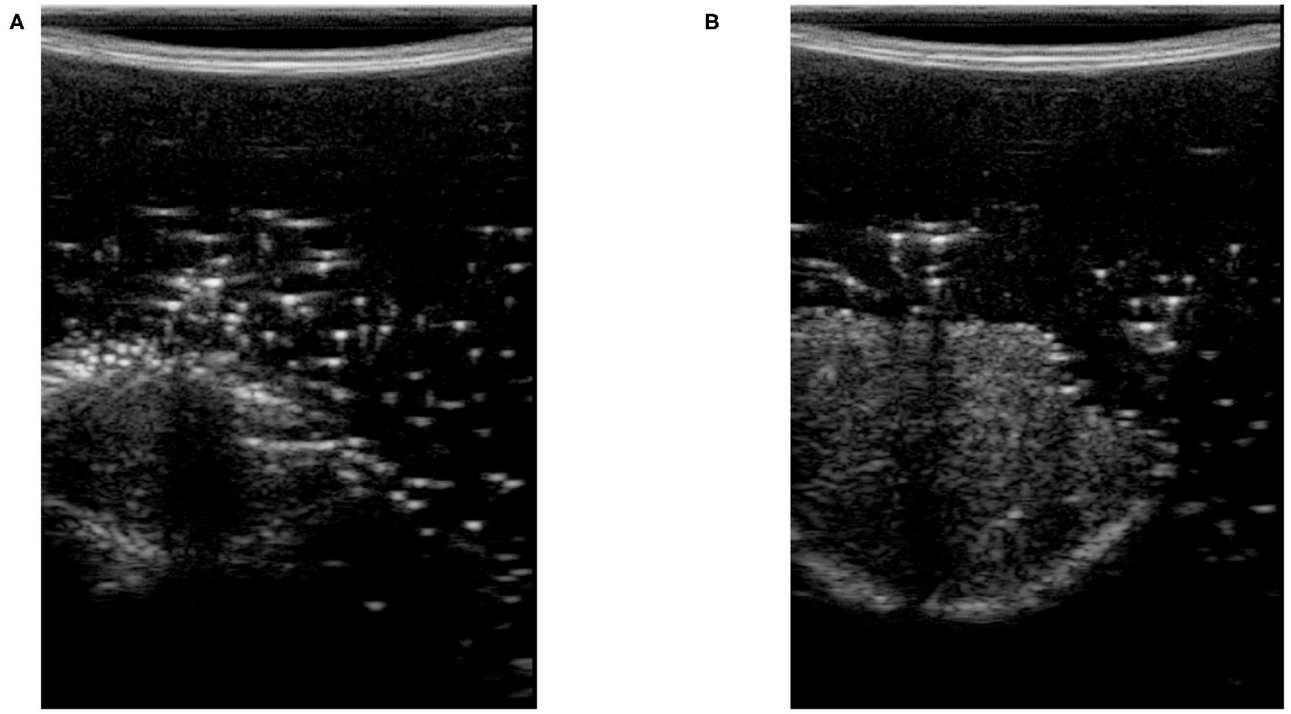

FIGURE 3 | Ultrasound images with high and low level of compression. **(A)** Ultrasound image with high tissue compression. **(B)** Ultrasound image with low tissue compression.

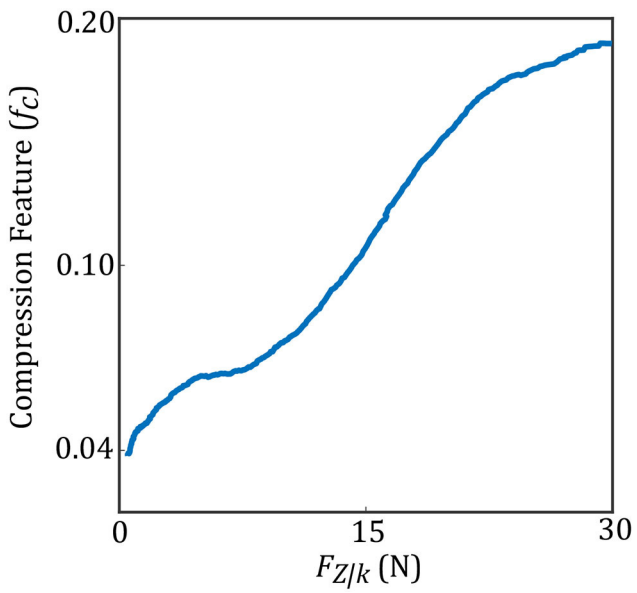

FIGURE 4 | Compression feature with respect to measured force.

two classes based on the features in feature space. SVM finds this line by optimizing a cost function based on the margin between two classes in feature space. There may be a need to increase the features' dimension to find this line in a higher dimensional space.

We tested the SVM using cross-validation. We used two different tissue phantoms to train and test the SVM, meaning we trained the SVM using one of the phantoms and tested it on the other phantom. The phantoms were biological porcine and bovine tissue. We trained the SVM using bovine phantom, and the trained SVM was tested on porcine tissue and vice versa. We will use the output of the SVM for robotic control.

We created an image database for training and testing the SVM. To create a database, we used a robot arm to scan bovine and porcine tissue phantoms by scanning multiple points on these tissues automatically by increasing force values at each point. The scanning procedure started from one side of the tissue and continued by dividing them to many points and increasing the US scanning force applied to the tissue from 1 to 20 N with an increment of 0.25 N. The force increment was based on force control feedback in the robotic arm by increasing the tissue indentation until the force value reached the desired force. This procedure was just used for creating a bovine and porcine image database. The images captured at each point on the tissue and the forces' value were saved using a computer. A trained non-medical user then manually classified all images and a subset of 1,000 images selected with 500 high-quality images and 500 low-quality images from the tissue phantoms' US images for different force values. The images were classified subjectively by the user, and the images were determined to be high quality if there is sufficient contact between tissue and the probe and tissue is visible without

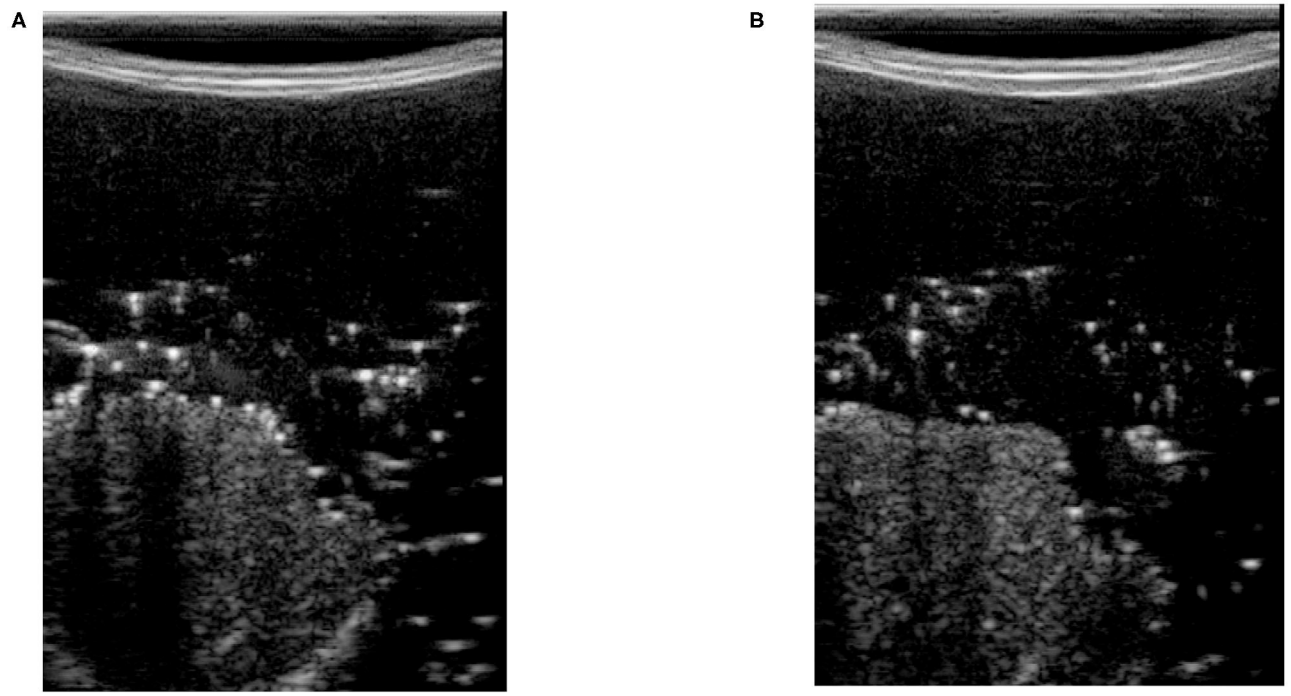

FIGURE 5 | Ultrasound images with high and low levels of noise. **(A)** Ultrasound image with a high levels of noise. **(B)** Ultrasound image with a low levels of noise.

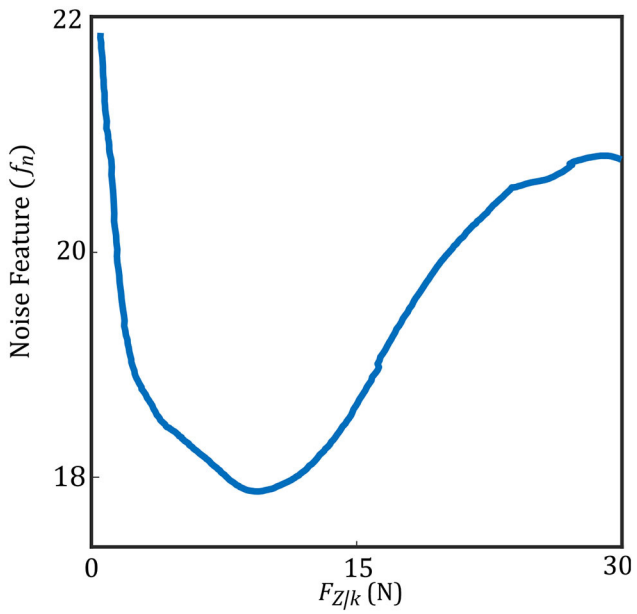

FIGURE 6 | Noise feature with respect to measured force.

significant deformation within the US image. The variation of the pixel intensity in the frame with respect the background was also been considered for image classification. The SVM was trained using 800 images with equal probability weighting in each of the two classes. The trained SVM was tested on the remaining 200 images. After training, the SVM has reached an accuracy (a ratio of the number of correct labels to all labels) of 96% on our test database. **Figure 7** shows the procedure of training SVM using biological porcine and bovine tissue.

The rule for updating the force's value based on the output of the image quality assessment algorithm is shown in Equations (10) and (10). We have also shown a block diagram of the quality assessment algorithm in **Figure 8**.

$$V_{svm} = SVM(f_c, f_n);\ V_{svm} \in \{0, 1\} \quad (9)$$

$$F_{Z|k+1} = F_{Z|k} + \delta F(1 - V_{svm}) \quad (10)$$

4. ROBOT ADMITTANCE CONTROL

Our admittance controller in the x-y-z direction keeps the robot in the original x-y position and updates the z position based on the image quality assessment algorithm, as mentioned earlier. We transform the force sensor data into the base frame of the robot. **Figure 1** shows the robot coordinate system during the experiments.

We use the output of the quality assessment algorithm in the loop controlling the force applied by the US probe to tissue. **Figure 9** shows the control loop for the z-axis used during the experiments. The admittance model calculates desired position of the robot based on the input force. K_θ is the gain for calculating how much torque should be applied at joints. The control loop works on two different frequencies. Dash lines in **Figure 9** represent image-quality feedback working on 30 *Hz*, and the solid

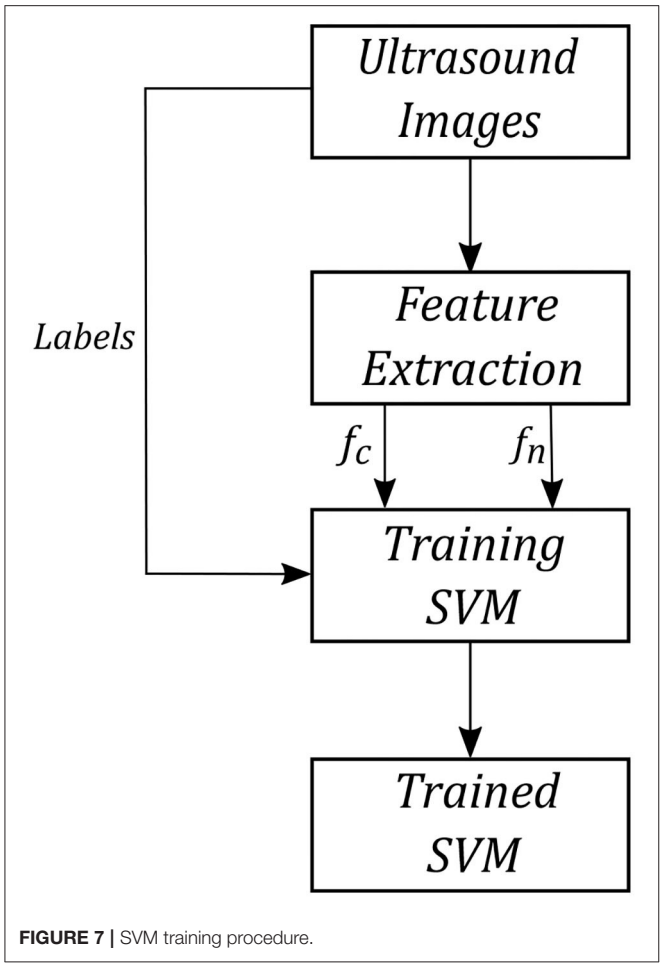

FIGURE 7 | SVM training procedure.

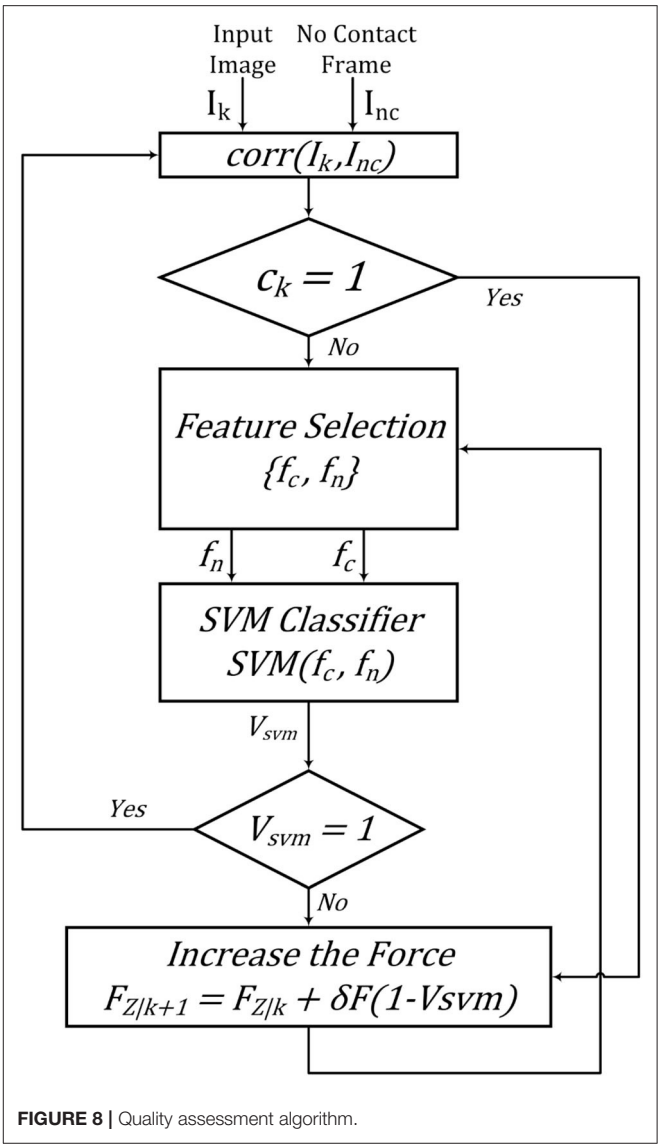

FIGURE 8 | Quality assessment algorithm.

lines represent robotic control working on 1 *kHz*. We reduced the sampling time of robotic control to 30 *Hz* to avoid discrepancies during our experiment.

The value of the force applied to the tissue in the z-direction is fed to the admittance controller. The transfer function describes the admittance model in (11). Where $X_k(s)$ is the desired Cartesian position in the robot base frame, and $F_k(s)$ is the force applied to the end effector in the robot base frame in the z-direction. **M** is the virtual mass matrix specified for the system. **B** and **K** represent specified damping and spring matrices, respectively. The matrices **M**, **B**, and **K** are shown in section 5. The admittance model in the feedforward finds the desired position for the system, while the feedback impedance model calculates the robot's current position. We multiply the error by inverse jacobian J^{-1} and K_θ to find the error in joint space, and torque should be applied at joints.

$$H(s) = \frac{X_k(s)}{F_k(s)} = \frac{1}{\mathbf{M}s^2 + \mathbf{B}s + \mathbf{K}} \tag{11}$$

For the experimental setup and results, which will be covered in (5), We chose the values of **M**, **B**, and **K** for the parameters of the admittance model, as shown in the following matrices. The matrix of **K** has only one non-zero parameter (in the z direction) that controls the US force applied to the tissue. The values of **M** and **K** are based on Piwowarczyk et al. (2020), and they were chosen empirically as a trade-off between sluggishness and control of the system. We calculated the value for **B** to have a critically damped response in the z direction. The threshold values in our quality assessment algorithm were found empirically based on the SVM response in our US image database, these values are $t_{corr} = 0.7$ and $t_{comp} = 20$.

$$\mathbf{M} = \begin{bmatrix} 5.625 & 0 & 0 \\ 0 & 5.625 & 0 \\ 0 & 0 & 5.625 \end{bmatrix} kg \tag{12}$$

$$\mathbf{B} = \begin{bmatrix} 33.54 & 0 & 0 \\ 0 & 33.54 & 0 \\ 0 & 0 & 33.54 \end{bmatrix} \frac{N \cdot sec}{m} \tag{13}$$

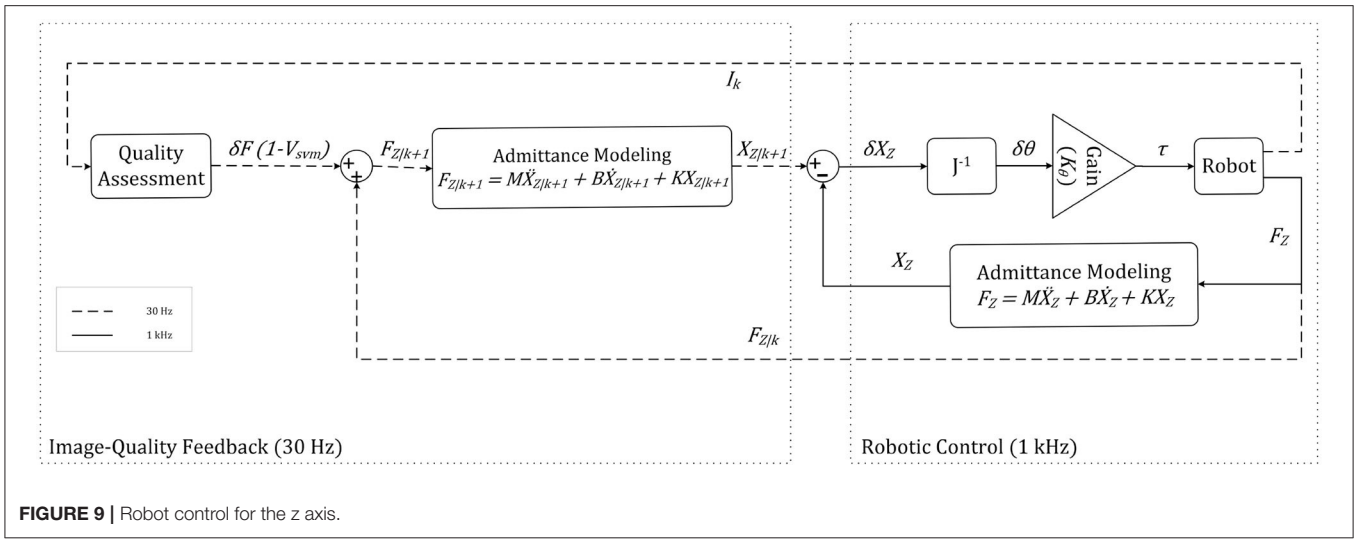

FIGURE 9 | Robot control for the z axis.

$$\mathbf{K} = \begin{bmatrix} 0 & 0 & 0 \\ 0 & 0 & 0 \\ 0 & 0 & 50 \end{bmatrix} \frac{N}{m} \tag{14}$$

5. EXPERIMENTAL SETUP AND RESULTS

In this study, an Axia80-M20 force-torque sensor (ATI Industrial Automation, Apex, NC, USA) was mounted on a Panda robotic arm (Franka Emika GmbH, Munich, Germany), which holds US probe (see **Figure 1**). We have used US machine for capturing images with an Epiphan DVI2USB3.0 (Epiphan Systems Inc, California, USA) for sending the image to the computer. The US machine used for the experiment was an Ultrasonix Touch with a 4DL14-5/38 Linear 4D transducer (Ultrasonix Corp, Richmond, BC, Canada). For this experiment, we only use the 2D functionality of the US probe. We used a tissue phantom made of plastisol as an artificial tissue for our experiment. The setup is shown in **Figure 1**.

The admittance controller was programmed and implemented in MATLAB 2019a (The Mathworks Inc., Natwick, MA, USA) and ran using Simulink on a PC running Ubuntu 16.04 LTS. The PC has an Intel Core i5-8400 running at 4.00 GHz. The communication between robot and computer was done over UDP, and the Epiphan was connected to the computer using a USB port.

To evaluate the image quality controller algorithm, we selected six spots on the surface of the plastisol tissue and ran the proposed method on those six locations. We then manually classified the acquired images and found the values of Structural Similarity Index Metric (SSIM) and Peak Signal to Noise Ratio (PSNR) between the output of our quality assessment algorithm and our manual subjective results. The calculation of SSIM is based on Wang et al. (2004). These values are reported in **Table 1**.

The experiments are designed to test the feasibility of incorporating our quality assessment algorithm into the control loop. The robot increases the force applied to the tissue by going down in the z-axis using an admittance controller. **Figure 10** shows the output of the quality assessment algorithm and the subjective result by the human operator. **Figure 10A** is the output of the quality assessment algorithm in one specific position and **Figure 10B** is the output of the manual classification of the image in that specific position. This will show that our proposed method provides US images of high quality similar to those taken by a sonographer.

TABLE 1 | Similarity metrics' value between quality assessment algorithm and subjective classification.

Location	SSIM	PSNR
First position	0.87	26.85
Second position	0.76	20.60
Third position	0.84	24.30
Fourth position	0.88	28.16
Fifth position	0.86	24.53
Sixth position	0.82	22.54

The values reported in **Table 1** show the US image captured using our proposed image quality assessment method is similar to the result of manual classification. The similarity between the values of SSIM and PSNR in all six positions proves the generality of the proposed quality assessment method. Being as PSNR only compare the values of intensities without analyzing general features of the image like the shape of the organ inside the tissue. The SSIM finds the similarities between two images based on structural analysis. The values of SSIM are high for our experiment, which proves our algorithm performs very close to a human operator.

We evaluated the performance of the proposed method experimentally by recording the values of each feature and the output of SVM by controlling the force applied to the tissue. **Figure 11** shows the average value of compression value with respect to the force applied to the tissue during the test

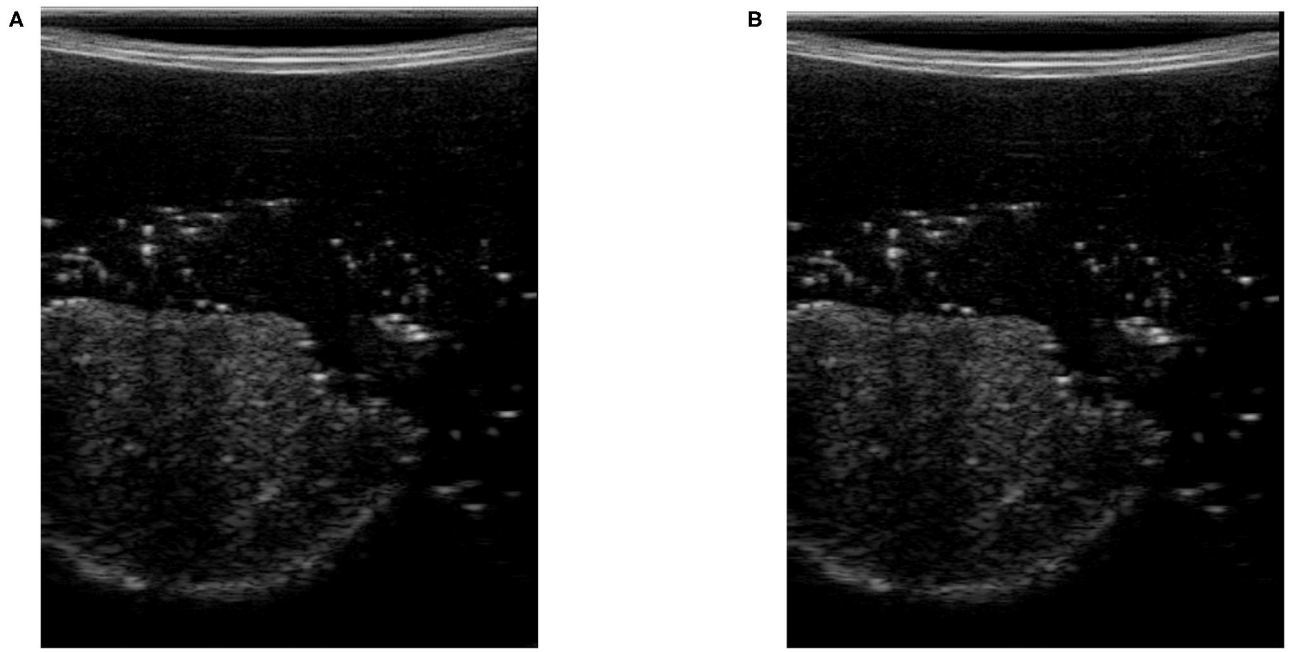

FIGURE 10 | Output of quality assessment algorithm and human subjective classification. **(A)** Quality assessment output. **(B)** Subjective result.

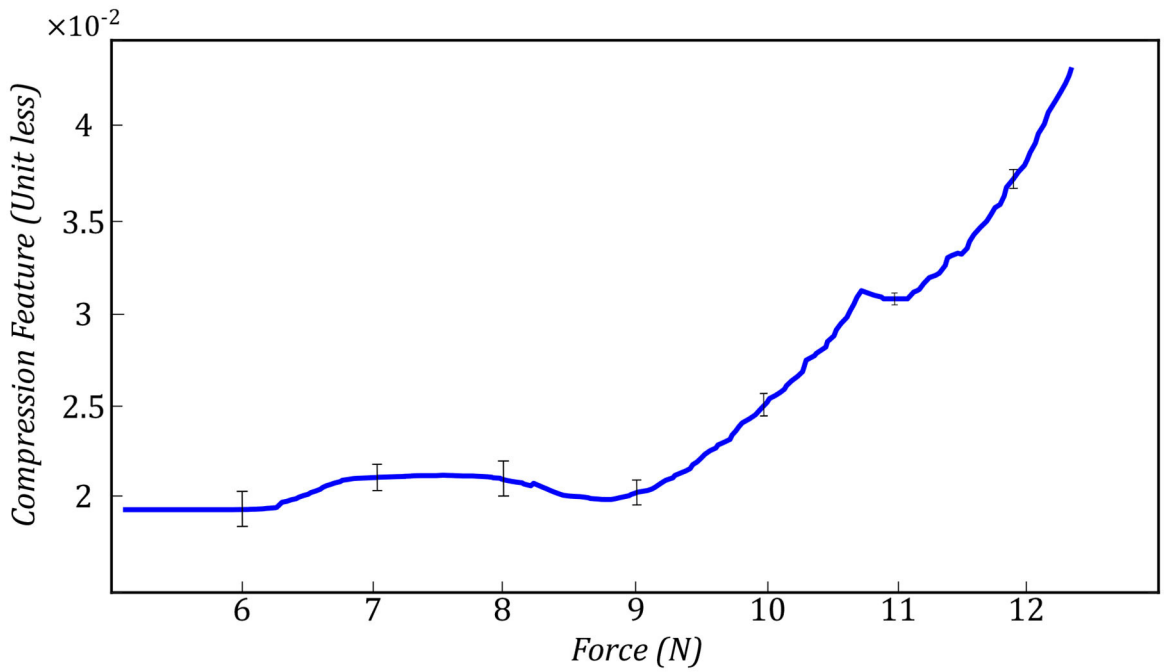

FIGURE 11 | Variation of compression feature during the test experiment in all six spots on the surface of the tissue.

experiment. The values reported in this figure, are the average compression feature values in six different spots on the surface of the tissue. The bar in each force value represents the variation of the compression feature at the corresponding force value at all six locations on the tissue. We also reported the same variation for noise feature in **Figure 12**. **Figure 13** shows the variation of SVM output during scanning of the tissue by increasing the force applied to it. The threshold value of t_{SVM} divides the graph to

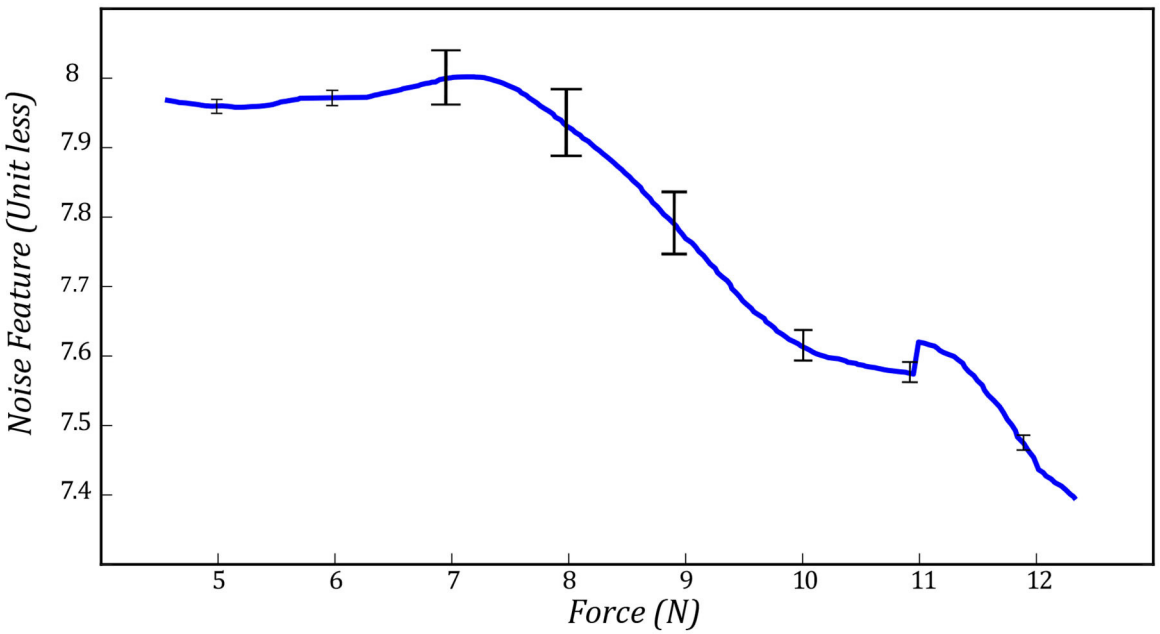

FIGURE 12 | Variation of noise feature during the test experiment in all six spots on the surface of the tissue.

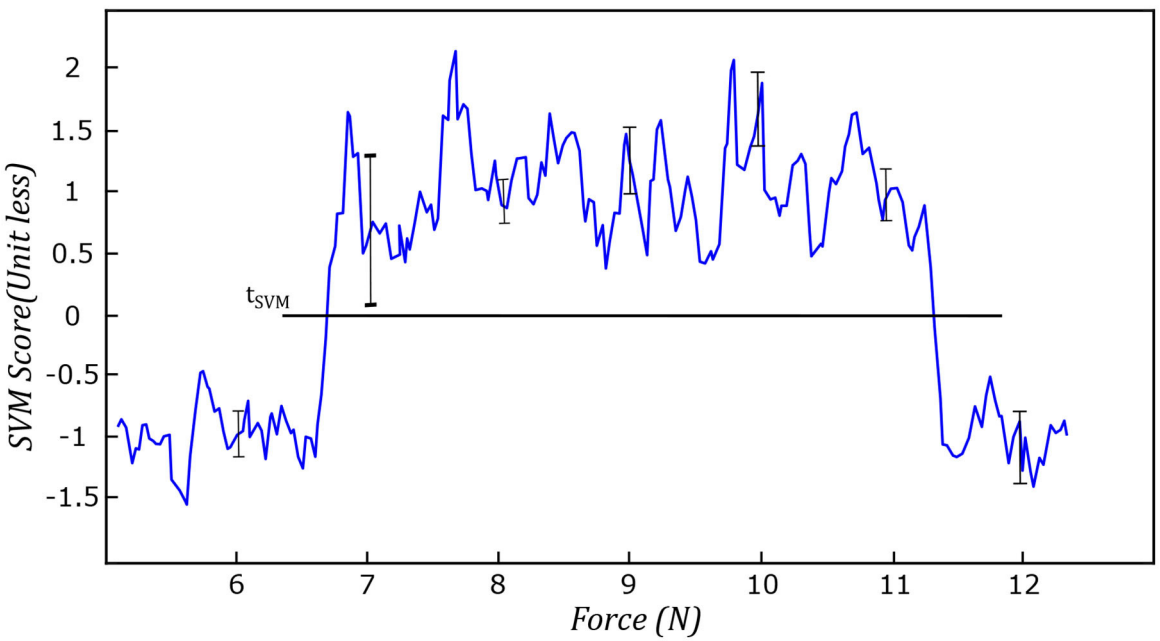

FIGURE 13 | Variation of SVM during the test experiment in all six spots on the surface of the tissue.

two separate classes in which the top part is associated with class of high-quality images and the bottom part is related to the low-quality images. These graphs prove the generality of our proposed method in different situations as the variation of each feature across the different levels of force was within the limited range in all six locations on the tissue.

The experiments conducted in this section shows us that the level of force applied to the tissue using the quality assessment algorithm is within a reasonable range, based on the results shown in **Figures 11–13**. The general trend and variation of these features during scanning are consistent with respect to the applied force, which proves the generality of the proposed

method. **Figure 10** and **Table 1** show us that the output of the quality assessment algorithm is very close to the desire of the sonographer that all the values reported in **Table 1** are within a reasonable range and the image acquired using image quality assessment algorithm and the subjective result are very close to each other in **Figure 10**.

6. CONCLUSION

This paper has presented US image quality assessment algorithm used for robotic control of US scanning. Our proposed quality assessment algorithm uses feature extraction and a SVM classifier to assess the acquired images' quality. The algorithm estimates the US image's quality based on correlation, compression, and noise features. These features are input into a SVM classifier to determine an image is of high quality or low quality. The algorithm was used as a part of the real-time control loop in the robotic US image scanning system. The user is able to put the US probe at a specific location on the tissue, and the algorithm will modulate the US scanning force applied to the tissue. An admittance controller was used internally to modulate the force. We evaluated the performance of the proposed system using different quality assessment metrics, showing close agreement between manual subjective assessment of the captured US image quality and the quality estimation from our algorithm.

This system is designed to enable isolation between patients and sonographers during the COVID-19 pandemic. In the future, we can control the US probe's orientation in an autonomous manner to enable six degrees of freedom of the US probe during scanning. We can also incorporate the quality assessment algorithm into a teleoperation system to enable remote control of a US scanning robot. Here, the user can remotely move the robot to the desired location, with the algorithm appropriately adjusting the US scanning force automatically.

DATA AVAILABILITY STATEMENT

The raw data supporting the conclusions of this article will be made available by the authors, without undue reservation.

AUTHOR CONTRIBUTIONS

This paper has been prepared by MA under the supervision of MT and JC. TM, RS, SH, and NU helped the research group by giving advisory comments. All authors contributed to the article and approved the submitted version.

ACKNOWLEDGMENTS

This research was supported by the Canada Foundation for Innovation (CFI), the Natural Sciences and Engineering Research Council (NSERC) of Canada, the Canadian Institutes of Health Research (CIHR), and the Alberta Jobs, Economy and Innovation Ministry's Major Initiatives Fund to the Center for Autonomous Systems in Strengthening Future Communities.

REFERENCES

AbbasiMoshaii, A., and Najafi, F. (2019). Design, evaluation and prototyping of a new robotic mechanism for ultrasound imaging. *J. Comput. Appl. Mech*. 50, 108–117. doi: 10.22059/JCAMECH.2018.257439.282

Abdel-Hamid, L., El-Rafei, A., El-Ramly, S., Michelson, G., and Hornegger, J. (2016). Retinal image quality assessment based on image clarity and content. *J. Biomed. Opt*. 21:096007. doi: 10.1117/1.JBO.21.9.096007

Antico, M., Sasazawa, F., Wu, L., Jaiprakash, A., Roberts, J., Crawford, R., et al. (2019). Ultrasound guidance in minimally invasive robotic procedures. *Med. Image Anal*. 54, 149–167. doi: 10.1016/j.media.2019.01.002

Buda, N., Segura-Grau, E., Cylwik, J., and Wełnicki, M. (2020). Lung ultrasound in the diagnosis of covid-19 infection-a case series and review of the literature. *Adv. Med. Sci* 65, 378–385. doi: 10.1016/j.advms.2020.06.005

Carriere, J., Fong, J., Meyer, T., Sloboda, R., Husain, S., Usmani, N., et al. (2019). "An admittance-controlled robotic assistant for semi-autonomous breast ultrasound scanning." in *2019 International Symposium on Medical Robotics (ISMR)* (Atlanta, GA: IEEE), 1–7. doi: 10.1109/ISMR.2019.8710206

Chatelain, P., Krupa, A., and Navab, N. (2015). "Optimization of ultrasound image quality via visual servoing," in *2015 IEEE International Conference on Robotics and Automation (ICRA)* (Seattle, WA: IEEE), 5997–6002. doi: 10.1109/ICRA.2015.7140040

Chen, W., Gu, K., Zhao, T., Jiang, G., and Le Callet, P. (2020). Semi-reference sonar image quality assessment based on task and visual perception. *IEEE Trans. Multimedia* 23, 1008–1020. doi: 10.1109/TMM.2020.2991546

Chow, L. S., and Paramesran, R. (2016). Review of medical image quality assessment. *Biomed. Signal Process. Control* 27, 145–154. doi: 10.1016/j.bspc.2016.02.006

Dimeas, F., and Aspragathos, N. (2016). Online stability in human-robot cooperation with admittance control. *IEEE Trans. Hapt*. 9, 267–278. doi: 10.1109/TOH.2016.2518670

Ebadollahi, S., Chang, S.-F., Wu, H. D., and Takoma, S. (2001). "Echocardiogram video summarization," in *Medical Imaging 2001: Ultrasonic Imaging and Signal Processing* (San Diego, CA: International Society for Optics and Photonics), 492–501. doi: 10.1117/12.4282290

Fang, T.-Y., Zhang, H. K., Finocchi, R., Taylor, R. H., and Boctor, E. M. (2017). Force-assisted ultrasound imaging system through dual force sensing and admittance robot control. *Int. J. Comput. Assist. Radiol. Surg*. 12, 983–991. doi: 10.1007/s11548-017-1566-9

Ferraguti, F., Talignani Landi, C., Sabattini, L., Bonfé, M., Fantuzzi, C., and Secchi, C. (2019). A variable admittance control strategy for stable physical human-robot interaction. *Int. J. Robot. Res*. 38, 747–765. doi: 10.1177/0278364919840415

Fong, J., and Tavakoli, M. (2018). "Kinesthetic teaching of a therapist's behavior to a rehabilitation robot," in *2018 International Symposium on Medical Robotics (ISMR)* (Atlanta, GA: IEEE), 1–6. doi: 10.1109/ISMR.2018.8333285

Hemmsen, M. C., Petersen, M. M., Nikolov, S. I., Nielsen, M. B., and Jensen, J. A. (2010). "Ultrasound image quality assessment: a framework for evaluation of clinical image quality," in *Medical Imaging 2010: Ultrasonic Imaging, Tomography, and Therapy* (San Diego, CA: International Society for Optics and Photonics). doi: 10.1117/12.840664

Jarvis, C. I., Van Zandvoort, K., Gimma, A., Prem, K., Klepac, P., Rubin, G. J., et al. (2020). Quantifying the impact of physical distance measures on the transmission of covid-19 in the UK. *BMC Med*. 18:124. doi: 10.1186/s12916-020-01597-8

Jin, Y.-H., Cai, L., Cheng, Z.-S., Cheng, H., Deng, T., Fan, Y.-P., et al. (2020). A rapid advice guideline for the diagnosis and treatment of 2019 novel coronavirus (2019-ncov) infected pneumonia (standard version). *Military Med. Res* 7:4. doi: 10.1186/s40779-020-0233-6

Karamalis, A., Wein, W., Klein, T., and Navab, N. (2012). Ultrasound confidence maps using random walks. *Med. Image Anal*. 16, 1101–1112. doi: 10.1016/j.media.2012.07.005

Keemink, A. Q., van der Kooij, H., and Stienen, A. H. (2018). Admittance control for physical human-robot interaction. *Int. J. Robot. Res.* 37, 1421–1444. doi: 10.1177/0278364918768950

Landi, C. T., Ferraguti, F., Sabattini, L., Secchi, C., and Fantuzzi, C. (2017). "Admittance control parameter adaptation for physical human-robot interaction," in *2017 IEEE International Conference on Robotics and Automation (ICRA)* (Singapore: IEEE), 2911–2916. doi: 10.1109/ICRA.2017.7989338

Li, Z., Huang, B., Ye, Z., Deng, M., and Yang, C. (2018). Physical human-robot interaction of a robotic exoskeleton by admittance control. *IEEE Trans. Indus. Electron.* 65, 9614–9624. doi: 10.1109/TIE.2018.2821649

Lim, J. S. (1990). Two-dimensional signal and image processing. Englewood Cliffs.

McDermott, C., Daly, J., and Carley, S. (2020). Combatting covid-19: is ultrasound an important piece in the diagnostic puzzle? *Emerg. Med. J.* 37, 644–649. doi: 10.1136/emermed-2020-209721

Morawska, L., and Milton, D. K. (2020). It is time to address airborne transmission of covid-19. *Clin. Infect. Dis.* 6:939. doi: 10.1093/cid/ciaa939

Moshaii, A. A., and Najafi, F. (2014). A review of robotic mechanisms for ultrasound examinations. *Indus. Robot Int. J.* 41, 373–380. doi: 10.1108/IR-01-2014-0304

Najafi, F., and Sepehri, N. (2011). A robotic wrist for remote ultrasound imaging. *Mech. Mach. Theory* 46, 1153–1170. doi: 10.1016/j.mechmachtheory.2011.03.002

NHL (2018). *Ultrasound Scanning*. Available online at: https://www.nhs.uk/conditions/ultrasound-scan (accessed May 25, 2018).

Piwowarczyk, J., Carriere, J., Adams, K., and Tavakoli, M. (2020). "An admittance-controlled force-scaling dexterous assistive robotic system," in *2020 Journal of Medical Robotics Research (JMRR)*, 1–16. doi: 10.1142/S2424905X20410020

Renieblas, G. P., Nogués, A. T., González, A. M., León, N. G., and Del Castillo, E. G. (2017). Structural similarity index family for image quality assessment in radiological images. *J. Med. Imaging* 4:035501. doi: 10.1117/1.JMI.4.3.035501

Sartori, E., Tadiello, C., Secchi, C., and Muradore, R. (2019). "Tele-echography using a two-layer teleoperation algorithm with energy scaling," in *2019 International Conference on Robotics and Automation (ICRA)* (Montreal, QC: IEEE), 1569–1575. doi: 10.1109/ICRA.2019.8794152

Schinaia, L., Scorza, A., Orsini, F., and Sciuto, S. (2017). "Feature classification in ultrasound textures for image quality assessment: a preliminary study on the characterization and selection of haralick parameters by means of correlation matrices," in *22nd IMEKO TC4 International Symposium and 20th International Workshop on ADC Modelling and Testing Supporting World Development through Electrical and Electronic Measurements* (Iaşi), 170–174.

Schwaab, J., Diez, Y., Oliver, A., Marti, R., van Zelst, J., Gubern-Mérida, A., et al. (2016). Automated quality assessment in three-dimensional breast ultrasound images. *J. Med. Imaging* 3:027002. doi: 10.1117/1.JMI.3.2.027002

Sharifi, M., Salarieh, H., Behzadipour, S., and Tavakoli, M. (2017). Tele-echography of moving organs using an impedance-controlled telerobotic system. *Mechatronics* 45, 60–70. doi: 10.1016/j.mechatronics.2017.05.006

Tavakoli, M., Carriere, J., and Torabi, A. (2020). Robotics, smart wearable technologies, and autonomous intelligent systems for healthcare during the covid-19 pandemic: an analysis of the state of the art and future vision. *Adv. Intell. Syst.* 2:2000071. doi: 10.1002/aisy.202000071

Wang, Z., Bovik, A. C., Sheikh, H. R., and Simoncelli, E. P. (2004). Image quality assessment: from error visibility to structural similarity. *IEEE Trans. Image Process.* 13, 600–612. doi: 10.1109/TIP.2003.819861

Welleweerd, M., de Groot, A., de Looijer, S., Siepel, F., and Stramigioli, S. (2020). "Automated robotic breast ultrasound acquisition using ultrasound feedback," in *2020 IEEE International Conference on Robotics and Automation (ICRA)* (Paris: IEEE), 9946–9952. doi: 10.1109/ICRA40945.2020.9196736

Wu, L., Cheng, J.-Z., Li, S., Lei, B., Wang, T., and Ni, D. (2017). FUIQA: fetal ultrasound image quality assessment with deep convolutional networks. *IEEE Trans. Cybernet.* 47, 1336–1349. doi: 10.1109/TCYB.2017.2671898

Yang, C., Peng, G., Li, Y., Cui, R., Cheng, L., and Li, Z. (2018). Neural networks enhanced adaptive admittance control of optimized robot-environment interaction. *IEEE Trans. Cybernet.* 49, 2568–2579. doi: 10.1109/TCYB.2018.2828654

Zemp, R. J., Abbey, C. K., and Insana, M. F. (2003). "Generalized neq for assessment of ultrasound image quality," in *Medical Imaging 2003: Physics of Medical Imaging* (San Diego, CA: International Society for Optics and Photonics), 391–402. doi: 10.1117/12.480134

Zeng, G., and Hemami, A. (1997). An overview of robot force control. *Robotica* 15, 473–482. doi: 10.1017/S026357479700057X

Zhang, L., Dudley, N. J., Lambrou, T., Allinson, N., and Ye, X. (2017). Automatic image quality assessment and measurement of fetal head in two-dimensional ultrasound image. *J. Med. Imaging* 4:024001. doi: 10.1117/1.JMI.4.2.024001

Zu, Z. Y., Jiang, M. D., Xu, P. P., Chen, W., Ni, Q. Q., Lu, G. M., et al. (2020). Coronavirus disease 2019 (covid-19): a perspective from China. *Radiology* 2:200490. doi: 10.1148/radiol.2020200490

Conflict of Interest: The authors declare that the research was conducted in the absence of any commercial or financial relationships that could be construed as a potential conflict of interest.

frontiers in Robotics and AI

ORIGINAL RESEARCH
published: 07 May 2021
doi: 10.3389/frobt.2021.580080

Cough Recognition Based on Mel-Spectrogram and Convolutional Neural Network

*Quan Zhou[1], Jianhua Shan[1], Wenlong Ding[1], Chengyin Wang[1], Shi Yuan[1], Fuchun Sun[2], Haiyuan Li[3] and Bin Fang[2]**

[1]Anhui Province Key Laboratory of Special Heavy Load Robot, Anhui University of Technology, Ma'anshan, China, [2]Beijing National Research Center for Information Science and Technology, Department of Computer Science and Technology, Tsinghua University, Beijing, China, [3]Robotics Institute, School of Automation, Beijing University of Posts and Telecommunications, Beijing, China

In daily life, there are a variety of complex sound sources. It is important to effectively detect certain sounds in some situations. With the outbreak of COVID-19, it is necessary to distinguish the sound of coughing, to estimate suspected patients in the population. In this paper, we propose a method for cough recognition based on a Mel-spectrogram and a Convolutional Neural Network called the Cough Recognition Network (CRN), which can effectively distinguish cough sounds.

Keywords: cough recognition, mel-spectrogram, CNN, deep learning, audio, COVID-19

OPEN ACCESS

Edited by:
Shalabh Gupta,
University of Connecticut,
United States

Reviewed by:
Jing Yang,
University of Connecticut,
United States
Shugong Xu,
Shanghai University, China

****Correspondence:***
Bin Fang
fangbin@mail.tsinghua.edu.cn

Specialty section:
This article was submitted to Smart Sensor Networks and Autonomy, a section of the journal Frontiers in Robotics and AI

Received: *04 July 2020*
Accepted: *09 April 2021*
Published: *07 May 2021*

Citation:
Zhou Q, Shan J, Ding W, Wang C, Yuan S, Sun F, Li H and Fang B (2021) Cough Recognition Based on Mel-Spectrogram and Convolutional Neural Network. Front. Robot. AI 8:580080. doi: 10.3389/frobt.2021.580080

INTRODUCTION

As a disease with a long incubation period and high infection rate, COVID-19 has caused millions of people to be infected and hundreds of thousands of people to died. How to avoid the rapid spread of the epidemic and effectively control the number of infected people has become an urgent issue. Asif et al. found that data from 10,172 COVID-19 laboratory-confirmed cases have shown a correlation with coughing in 54.08% (Sattar Hashmi and Asif, 2020). Therefore, coughing, as a typical symptom of pneumonia, is of great significance in controlling the potential infectious source if it can be quickly and accurately monitored in the population.

Many scholars have studied how to extract features of sound and recognize the sound. Mel Frequency Cepstrum Coefficient (MFCC), as a method of extracting audio features (Shintri and Bhatia, 2015), is widely used in various audio recognition tasks. Xie et al. used MFCC to recognize abnormal voice (Xie et al., 2012). Wang et al. proposed to recognize speech emotion based on improved MFCC (Wang and Hu, 2018). Suksri described a method that used MFCC extracted from the speech signals of spoken words for speech recognition (Ittichaichareon et al., 2012). The Fourier transform (FT) is also widely used in audio processing. Jozef et al. presented a new procedure for the frequency analysis of audio signals (Pucik et al., 2014).

Although these traditional methods are very effective for the extraction of audio features, considering the complexity of the real scene, the method of deep learning may achieve better results. With the development of deep learning, the neural network has played an important role in audio recognition. Oren et al. proposed spectral representations for convolutional neural networks (Rippel et al., 2015). Some LSTM-based networks for speech recognition are also presented (Pundak and Sainath, 2017; Trianto et al., 2018). Compared with traditional methods, deep learning can extract more complex and robust features.

For cough recognition, various methods are proposed. Cough signals are usually obtained by audio or inertial sensors, which can detect the vibration caused by coughing. These sensors include a

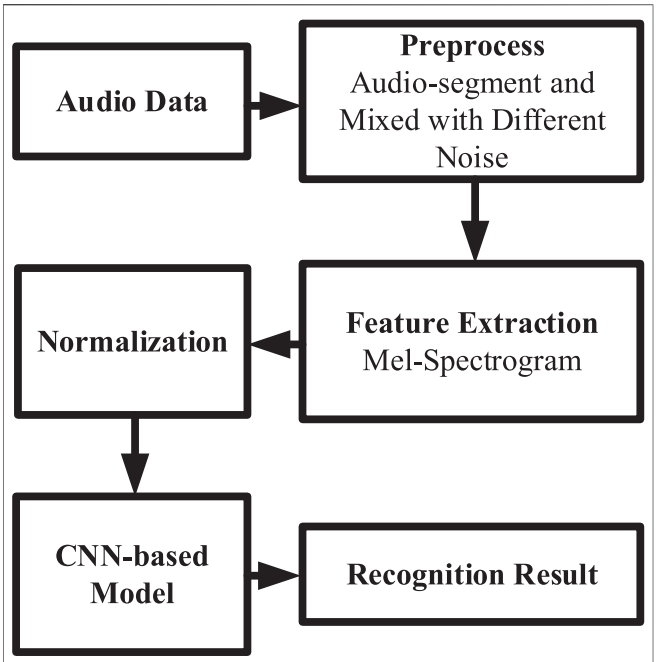

FIGURE 1 | The work-flow diagram.

microphone that can be worn or placed near the user, or a piezoelectric transducer and a high-sensitivity accelerator that can be placed in the throat or chest area (Drugman et al., 2013; Amoh and Odame, 2016; Elfaramawy et al., 2018).

Infante et al. used a machine learning method to recognize dry/wet cough (Infante et al., 2017). Semi-supervized Tree Support Vector Machine is proposed for cough recognition and detection (Hoa et al., 2011). K-NN is also an efficient tool that is often used for cough recognition (Hoyos Barcelo et al., 2017; Vhaduri et al., 2019).

In addition, the Artificial Neural Network (ANN), Gaussian Mixture Model (GMM), Support Vector Machine (SVM), and other methods are also used for cough recognition (Drugman et al., 2011).

The difficulty of cough recognition mainly lies in the distinction of background noise. There are many kinds of sound mixed together in daily scenes. How to effectively distinguish between coughing and other sounds has become a difficult problem to be solved.

In this paper, we propose a cough recognition method based on a Mel-spectrogram and a Convolutional Neural Network (CNN). First, we enhance the audio data and mix the voice in various complex scenes. Then, we preprocess the data to ensure the consistency of data length and convert it into a Mel-spectrogram. At last, we build a CNN-based model to classify the cough using the Mel-spectrogram. At the same time, we make comparisons with some other common methods. After the experiment result comparison, it can be seen that this method can effectively identify and detect coughing in complex scenes. It can be seen that the cough recognition model based on a Mel-spectrogram and a CNN can achieve good results.

MATERIALS AND METHODOLOGY

As shown in **Figure 1**, the work-flow of our cough classification model is presented.

Data Augmentation

Considering the natural environment, sound is not produced by a single sound source and the received sound is often the mix of multiple sounds. In order to improve the recognition effect and robustness, we enhance the data, using noise and human voice to mix the cough data.

We selected several audio datasets to make data augmentation, such as the ESC-50 dataset (Piczak, 2015) and the Speech Commands Data Set (Warden, 2018). All cough data comes from the ESC-50 dataset.

Positive Samples 1: Cough. After audio segmentation, we select all cough audio samples as positive samples. We also obtain more cough audio samples by increasing and decreasing the volume.

Positive Samples 2 and 3: Cough + Human Sound and Cough + Natural Sound. In order to enhance the robustness of the model, we also mix cough audio with natural sound (wind, rain, door-clock, footsteps, and other common noises) and human sound (mainly including commonly spoken words such as "go," "up," "right," and so on) respectively as positive samples 2 and 3.

In all the mixed audio, the volume of the coughing sound is adjusted to produce more mixed outcomes of different cough sounds and other sounds.

All of the original and processed cough audio data are labeled as "cough."

Negative Samples 1: Human Sound. We choose human sounds (mainly include "go," "up" and, some other common human noises, and all sounds come from different samples which are unused for cough augmentation) from the datasets above as one of the negative samples. So our model can distinguish between cough sounds and human sounds. And all human sounds were mixed with white noise, pink noise, and so on.

Negative Samples 2: Natural Sound: We choose natural noise (wind, rain, pouring-water, footsteps, and other common sounds. All sounds come from different samples which are unused for cough augmentation) from the datasets above as other negative samples.

All human sound and natural sound data are labeled as "others."

In the end, we have cough sounds, mixed cough audio with natural noise, and mixed cough audio with human sounds as positive samples. At the same time, human sounds and natural sounds are taken as negative samples.

Data Preprocess

Considering that audio with a too short length of time may make it difficult to recognize the sound, and that audio with a too long length of time may cause the superposition of a variety of uncorrelated sounds, we choose the length of 1 s as the input. And the duration of cough samples in the original dataset is different, so we select the audio containing coughing and divide it into seconds.

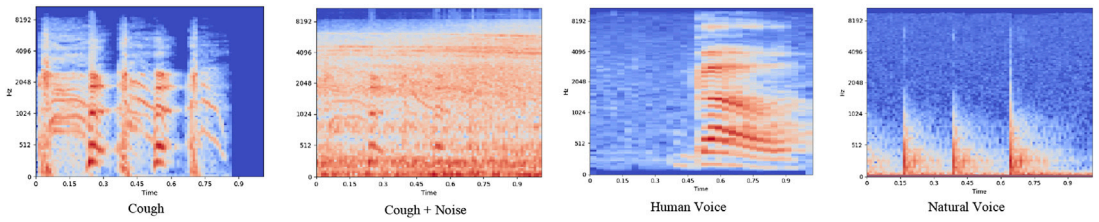

FIGURE 2 | Mel-spectrograms of different voices.

Mel-Spectrogram

The Mel spectrum contains a short-time Fourier transform (STFT) for each frame of the spectrum (energy/amplitude spectrum), from the linear frequency scale to the logarithmic Mel-scale, and then goes through the filter bank to get the eigenvector, these eigenvalues can be roughly expressed as the distribution of signal energy on the Mel-scale frequency.

After the audio data are processed into 1 s-long data, we transform all the data into Mel-spectrograms so that we can train the convolutional neural networks for recognition.

Audio data usually have complex features, so it is necessary to extract useful features to recognize the audio. The Mel-spectrogram is one of the efficient methods for audio processing and 8 kHz sampling is used for each audio sample.

In the experiment, we employ the Python package called librosa for data processing and all parameters are as follows: (n_fft = 1024, hop_length = 512, n_mels = 128). Then we call the power_to_db function to convert the power spectrum (amplitude square) to decibel (DB) units.

In **Figure 2**, we show some examples of Mel-spectrograms. As can be seen from the figure, there are some differences in different types of voices. But after mixing noise, some details will be covered, which is helpful for us to test the cough recognition effect of the model for the real scene. And we extract the features of the audio and transform them into feature images, so there are three channels like traditional color images.

Normalization

For image input, we normalize them to make the model converge faster. For the Mel-spectrogram, we calculate the mean and standard deviation of the three channels respectively and then normalize them. The normalization formula is as follows:

$$x_{\text{norm}} = \frac{x - \text{mean}(x)}{\text{std}(x)}, \tag{1}$$

where x denotes the values in different channels and x_{norm} denotes normalized values.

Loss Function

The recognition loss function of the model L_{rec} represents the cross-entropy loss:

$$L_{\text{rec}} = -\frac{1}{n}\sum\left[y ln\hat{y} + (1-y) ln(1-\hat{y})\right], \tag{2}$$

where $\hat{y}$ is the model output, y is the true label, and n is the number of samples.

Convolutional Neural Network

With the development of deep learning, more and more deep learning methods are applied to various scenarios, such as image recognition, image classification, speech recognition, machine translation, etc. As a kind of deep learning method, Convolutional Neural Networks (CNN) are widely used in the field of computer vision. In this section, we introduce the components of the proposed CNN-based network.

The convolutional layer is the key of a CNN model, it can effectively reduce the parameters of the model and make it possible for the model to optimize. The calculation formula for the convolutional layer is as follows:

$$x_j^n = f\left(\sum_{i \in M_j} x_i^{n-1} * \mathrm{k}_{\mathrm{ij}}^{\mathrm{n}} + \mathrm{b}_{\mathrm{j}}^{\mathrm{n}}\right), \tag{3}$$

where x_j^n is the output feature map, x_i^{n-1} is the input feature map, M_j is the selected area in the $n-1$ layer, k_{ij}^n is weight parameter, b_j^n is bias, and f is the activation function.

After each convolutional layer, we conduct batch normalization to make the outputs of the convolutional layer stay identically distributed, which can improve the performance of the model. The batch normalization formula is as follows:

$$y_i = \gamma \frac{x_i - u}{\sqrt{\sigma^2 + \varepsilon}} + \beta, \tag{4}$$

where x_i is the output of convolutional layer without activation, u is the mean of x, σ^2 is the variance of x, and γ and β are parameters to learn.

After feature extraction of the convolution layer, although the number of connections between layers has been significantly reduced, the number of neurons in the feature map group has not been significantly reduced. Therefore, like other common models, we add maximum pooling layers to solve this problem.

In the end, we use the fully connected layer as the output layer of the model. The calculation for the fully connected layer is:

$$y_j = f\left(\sum_{i=1}^{N} x_i * \mathrm{w}_{\mathrm{ij}} + \mathrm{b}_{\mathrm{j}}\right), \tag{5}$$

where x is the input layer, N is the number of input layer nodes, w_{ij} is the weight between the links x_i and y_j, b_j is the bias, and f is the activation function.

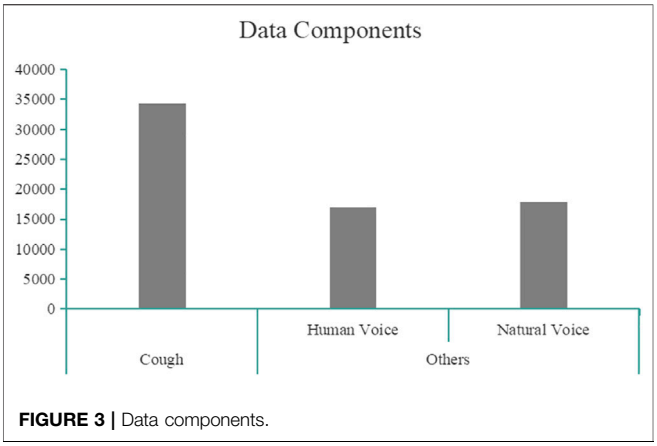

FIGURE 3 | Data components.

Experiment Approach

The CRN was trained by an Adam optimizer, whose learning rate is 0.0001. The max epoch and batch size were 20 and 64, respectively. The CRN was implemented by Pytorch and trained and tested on a computer with an Intel Core i7-8750H, two 8 GB memory chips (DDR4), and a GPU (Nvidia Geforce GTX 1060 6G).

Dataset Description

Before training, we need to preprocess the audio data. As mentioned in the second part, we obtained 34,320 cough samples augmented by different audio data, including 17,160 cough + human sound samples, 17,160 cough + natural sound samples, 17,050 human sounds, and 17,919 different noises. As shown in **Figure 3**, data components have been provided. In order to evaluate the model better, we use two ways to divide the processed dataset.

Random Division Dataset

After all data are processed, 80% are randomly selected as the training set, 10% as the verification set, and 10% as the test set. Considering that due to data augmentation, some data may leak the features of coughing.

No-Leakage Division Dataset

After all data are processed, we select almost 80% which we augment as the training set and 10% is augmented from completely different cough audio as the test set. In this way, the cough sounds of the training and test sets come from different original data, so that we can evaluate the generalization ability of the model.

After all data are split, the mean and variance of each channel are calculated. They are normalized to make the model converge better.

Performance Measurements

In order to better evaluate the performance of the model, we list several indicators used to evaluate the model.

Accuracy

The indicator that the samples with a correct reaction classification account for the total samples.

Recall

The ratio of the number of samples recognized correctly to the total number of samples recognized.

Precision

The ratio of the number of samples recognized correctly to the number of samples that should be recognized.

F1 Score

It is an index used to measure the accuracy of the binary classification model.

$$\text{Accuracy} = \frac{\text{TP} + \text{TN}}{\text{TP} + \text{TN} + \text{FP} + \text{FN}}, \tag{6}$$

$$\text{Recall} = \frac{\text{TP}}{\text{TP} + \text{FN}}, \tag{7}$$

$$\text{Precision} = \frac{\text{TP}}{\text{TP} + \text{FP}}, \tag{8}$$

$$\text{F1 Score} = \frac{2*\text{Precision}*\text{Recall}}{\text{Recall} + \text{Precion}}, \tag{9}$$

where TP (True Positive) denotes samples of coughing that are correctly recognized by the model. FP (False Positive) which denotes samples of coughing that are recognized as others by the model. TN (True Negative) which denotes samples of others that are correctly recognized by the model. FN (False Negative) which denotes samples of others that are incorrectly recognized as coughing by the model.

Experiment Based on Mel-Spectrogram + CNN

The Mel-spectrogram is an effective tool to extract hidden features from audio and visualize them as an image. A CNN model can effectively extract features from images, and then complete tasks such as classification and recognition. Therefore, we use the CNN model to effectively classify the audio and to realize the accurate recognition and detection of coughing. In **Figure 4**, the architecture of this model has been illustrated.

Considering the different positions of coughing in audio, the relative positions of coughing are also different. Before we feed the image into the network, we first unify the image size into 256×256, and then randomly select 224×224 size parts for the recognition of different cough positions.

RESULTS

After two methods of dataset division and training, we get the performance of the cough recognition task.

Experiment on Random Division Dataset

As shown in **Table 1**, we can find that Mel-Spectrogram + CNN can achieve the best performance in cough recognition than other methods. For randomly divided datasets, the correct recognition rate is 98%. It can be seen that the model can still achieve good recognition performance even

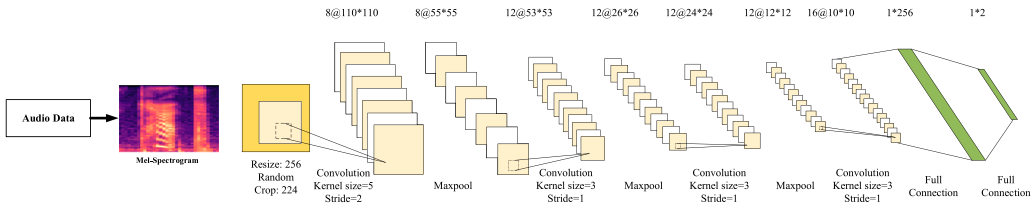

FIGURE 4 | The Architecture of the Mel-spectrogram and CNN model.

TABLE 1 | The comparison results of different methods.

Methods	Random division recognition task				No-leakage division recognition task			
	Accuracy (%)	Recall (%)	Precision (%)	F1 Score (%)	Accuracy (%)	Recall (%)	Precision (%)	F1 Score (%)
Mel-spectrogram + CNN	98.18	99.18	99.28	99.23	95.18	93.33	100	96.55
Mel-spectrogram + BP	94.34	87.50	100	93.33	91.44	93.75	93.75	93.75
MFCC + CNN	97.43	88.88	100	94.12	94.04	100	88.88	94.11
MFCC + BP	96.12	97.19	93.87	97.19	93.45	90.91	100	95.23
MFCC + SVM	95.76	96.99	94.57	95.77	93.29	93.56	91.79	92.67
MFCC + K-means	52.93	42.86	53.09	47.43	50.34	42.44	44.96	43.66
MFCC + Naive-bayes	88.57	95.31	83.83	89.20	78.81	82.43	73.87	77.92
MFCC + LightGBM	95.73	98.46	93.29	95.80	89.89	88.17	89.38	88.77

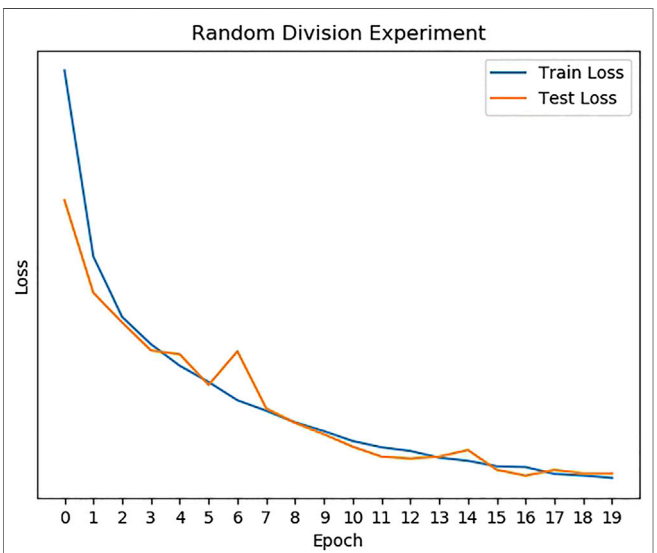

FIGURE 5 | The loss of the random division experiment.

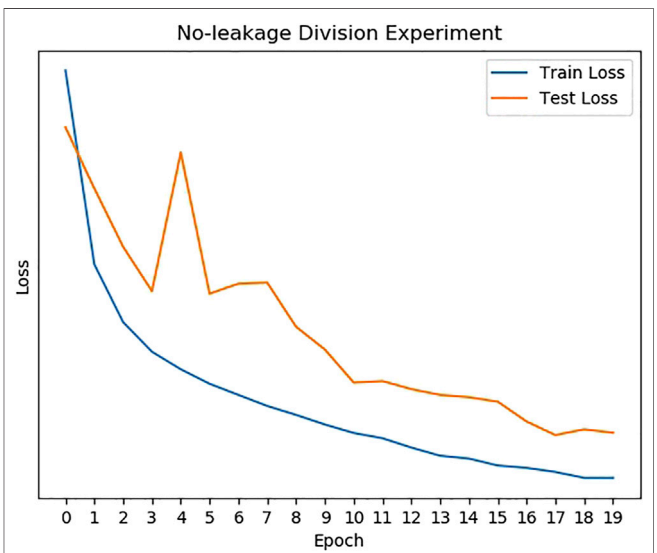

FIGURE 6 | The loss of the no-leakage division experiment.

if a variety of different sounds are mixed. The train/test loss curves are presented in **Figure 5**.

Experiment on No-Leakage Division Dataset

Considering that the model needs to cope with the cough sounds of different people, we add an experiment to estimate the generalization ability of the model. In this experiment, all the cough data are augmented, but the cough sound in the training set and the test set come from totally different collection objects. In this way, it can detect whether the model has the ability to recognize the cough sound produced by strange sound sources effectively.

The train/ test loss curves of no- leakage experiment are presented in **Figure 6** and the experiment result is shown in

Table 1. The no-leakage recognition accuracy is 95.18% and the F1 score is the highest of all methods. It can be seen that the model performs well during generalization cough recognition tasks.

Experiment Based On Other Traditional Methods

In order to prove the effectiveness of this method, we use several other methods for comparison.

MFCC

MFCC is an effective method to extract audio features. We use this method to preprocess the original audio data and then pass it to the different model. In order to make it suitable for the linear model, in the experiment, we take the average value on each dimension.

Back Propagation Network

BP is a multilayer feedforward network which has a strong nonlinear mapping ability. In our experiment, we build a four-layer BP neural network and the activation is ReLU.

Support Vector Machine

A Support Vector Machine (SVM) is a kind of generalized linear classifier that classifies data according to supervised learning.

K-Means

The K-means algorithm is an iterative clustering algorithm. Firstly, it randomly selects *K* objects as the initial clustering center. Then it calculates the distance between each object and each seed cluster center and assigns each object to the nearest cluster center.

Naive-Bayes

Naive Bayes is a classification method based on Bayes theorem and the independent hypothesis of characteristic conditions.

LightGBM

LighGBM is one of the boosting set models. It is an efficient implementation of the Gradient Boosting Decision Tree (GBDT) as XGBoost. In principle, it is similar to GBDT and XGBoost. It uses the negative gradient of loss function as the residual approximation of the current decision tree to fit the new decision tree.

All results based on these methods are shown in **Table 1**, and we can find that the CNN model is better than these methods in recognition accuracy and other indicators.

CONCLUSION

In this work, we proposed a cough recognition network (CRN) based on the CNN model and a Mel-spectrogram. From the experiments result based on random division and no-leakage division datasets, we can find that the proposed CRN can achieve excellent performance in cough recognition. Compared to other methods, the accuracy of CRN is highest and most of the indexes are the best. In order to estimate the generalization ability of the model, we have collected some cough sounds that were not included in training. We find that the CRN can also recognize them efficiency. Experiments show that the model can recognize coughing in complex scenes effectively, and can recognize coughing with various other sounds correctly, which is good for cough monitoring in daily life. Cough recognition is a potential solution for disease management during the COVID-19 pandemic and reduces epidemic prevention workers' exposure possibility.

Although the model has achieved good recognition results, there are still some problems that need to be further solved. For example, the audio length is now limited to 1 s. When the intercept position is not right, it may be misjudged.

DATA AVAILABILITY STATEMENT

Publicly available datasets were analyzed in this study. This data can be found here: https://github.com/karolpiczak/ESC-50 ESC-50 Dataset http://download.tensorflow.org/data/speech_commands_v0.02.tar.gz Speech Commands Dataset.

AUTHOR CONTRIBUTIONS

BF proposed the idea of the paper. QZ and JS designed the network and wrote the manuscript. WD, CW, and SY wrote the code and analyzed the results. FS and HL helped improve the paper.

FUNDING

This work supported by the National Key Research and Development Program of China (2017YFE0113200), National Natural Science Foundation of China (Grant No. 91848206), Beijing Science & Technology Project (Grant No. Z191100008019008) and Natural Science Foundation of university in Anhui Province (No.KJ 2019A0086).

REFERENCES

Amoh, J., and Odame, K. (2016). Deep Neural Networks for Identifying Cough Sounds. *IEEE Trans. Biomed. Circuits Syst.* 10, 1003–1011. doi:10.1109/TBCAS.2016.2598794

Drugman, T., Urbain, J., and Dutoit, T. (2011). "Assessment of Audio Features for Automatic Cough Detection," in 2011 19th European Signal Processing Conference., Barcelona, Spain, 29 Aug.-2 Sept. 2011 (IEEE), 1289–1293.

Drugman, T., Urbain, J., Bauwens, N., Chessini, R., Valderrama, C., Lebecque, P., et al. (2013). Objective Study of Sensor Relevance for Automatic Cough Detection. *IEEE J. Biomed. Health Inform.* 17, 699–707. doi:10.1109/jbhi.2013.2239303

Elfaramawy, T., Fall, C. L., Arab, S., Morissette, M., Lellouche, F., and Gosselin, B. (2019). A Wireless Respiratory Monitoring System Using a Wearable Patch Sensor Network. *IEEE Sensors J.* 19, 650–657. doi:10.1109/JSEN.2018.2877617

Hoa, H., Tran, A., and Dat, T. (2011). Semi-supervised Tree Support Vector Machine for Online Cough Recognition, *12th Annual Conference of the*

International SpeechCommunication Association. (Florence, Italy: . ISCA), 1637–1640. |

Hoyos-Barcelo, C., Monge-Alvarez, J., Zeeshan Shakir, M., Alcaraz-Calero, J.-M., and Casaseca-de-la-Higuera, P. (2018). Efficient K-NN Implementation for Real-Time Detection of Cough Events in Smartphones. *IEEE J. Biomed. Health Inform.* 22, 1662–1671. doi:10.1109/JBHI.2017.2768162

Infante, C., Chamberlain, D. B., Kodgule, R., and Fletcher, R. R. (2017). Classification of Voluntary Coughs Applied to the Screening of Respiratory Disease. *Annu Int. Conf. IEEE Eng. Med. Biol. Soc.* 2017, 1413–1416. doi:10.1109/EMBC.2017.8037098

Ittichaichareon, C., Suksri, S., and Yingthawornsuk, T. (2012). Speech Recognition Using Mfcc. *Int. Conf. Comp. Grap. Simula. Model.*, 135–138. doi:10.13140/RG.2.1.2598.3208

Piczak, K. J. (2015). Esc: Dataset for Environmental Sound Classification, 1015–1018. doi:10.1145/2733373.2806390

Pucik, J., Kubinec, P., and Ondracek, O. (2014). "Fft with Modified Frequency Scale for Audio Signal Analysis,"in International Conference Radioelektronika. Bratislava, Slovakia, 15-16 April 2014 (IEEE), 1–4.

Pundak, G., and Sainath, T. (2017). "Highway-LSTM and Recurrent Highway Networks for Speech Recognition," in Proceedings of Interspeech 2017, 1303–1307. doi:10.21437/Interspeech.2017-429

Rippel, O., Snoek, J., and Adams, R. P. (2015). Spectral Representations for Convolutional Neural Networks. *arXiv*.

Sattar Hashmi, H. A., and Asif, H. M. (2020). Early Detection and Assessment of Covid-19. *Front. Med.* 131, 311. doi:10.3389/fmed.2020.00311

Shintri, R. G., and Bhatia, S. K. (2015). Analysis of Mfcc and Multitaper Mfcc Feature Extraction Methods. *Int. J. Comput. Appl.* 131, 7–10. doi:10.5120/ijca2015906883

Trianto, R., Tai, T.-C., and Wang, J.-C. (2018). Fast-lstm Acoustic Model for Distant Speech Recognition. *IEEE Inter. Confer. Consu. Electro. (ICCE)* 2018, 1–4. doi:10.1109/ICCE.2018.8326195

Vhaduri, S., Kessel, T. V., Ko, B., Wood, D., Wang, S., and Brunschwiler, T. (2019). Nocturnal Cough and Snore Detection in Noisy Environments Using Smartphone-Microphones. *IEEE Inter. Conf. Health. Infor. (ICHI)*. 2019, 1–7. doi:10.1109/ICHI.2019.8904563

Wang, Y., and Hu, W. (2018). Speech Emotion Recognition Based on Improved Mfcc. *Inter. Confe. Compu. Sci. Appli. Engin* 88, 1–7. doi:10.1145/3207677.3278037

Warden, P. (2018). Speech Commands: A Dataset for Limited-Vocabulary Speech Recognition. *arXiv*. doi:10.2172/1635786

Xie, C., Cao, X., and He, L. (2012). Algorithm of Abnormal Audio Recognition Based on Improved Mfcc. *Proced. Eng.* 29, 731–737. doi:10.1016/j.proeng.2012.01.032

Conflict of Interest: The authors declare that the research was conducted in the absence of any commercial or financial relationships that could be construed as a potential conflict of interest.

frontiers in Robotics and AI

ORIGINAL RESEARCH
published: 25 May 2021
doi: 10.3389/frobt.2021.645756

Autonomous Robotic Point-of-Care Ultrasound Imaging for Monitoring of COVID-19–Induced Pulmonary Diseases

Lidia Al-Zogbi[1], Vivek Singh[2], Brian Teixeira[2], Avani Ahuja[3], Pooyan Sahbaee Bagherzadeh[2], Ankur Kapoor[2], Hamed Saeidi[1], Thorsten Fleiter[4] and Axel Krieger[1]*

[1]Laboratory for Computational Sensing and Robotics, Department of Mechanical Engineering, Johns Hopkins University, Baltimore, MD, United States, [2]Medical Imaging Technologies, Siemens Medical Solutions, Inc. USA, Princeton, NJ, United States, [3]Georgetown Day High School, WA, DC, United States, [4]R. Cowley Shock Trauma Center, Department of Diagnostic Radiology, School of Medicine, University of Maryland, Baltimore, MD, United States

OPEN ACCESS

Edited by:
Bin Fang,
Tsinghua University, China

Reviewed by:
Emmanuel Benjamin Vander Poorten,
KU Leuven, Belgium
Selene Tognarelli,
Sant'Anna School of Advanced Studies, Italy

***Correspondence:**
Lidia Al-Zogbi
lalzogb1@jh.edu

Specialty section:
This article was submitted to Biomedical Robotics, a section of the journal Frontiers in Robotics and AI

Received: *23 December 2020*
Accepted: *21 April 2021*
Published: *25 May 2021*

Citation:
Al-Zogbi L, Singh V, Teixeira B, Ahuja A, Bagherzadeh PS, Kapoor A, Saeidi H, Fleiter T and Krieger A (2021) Autonomous Robotic Point-of-Care Ultrasound Imaging for Monitoring of COVID-19–Induced Pulmonary Diseases. Front. Robot. AI 8:645756. doi: 10.3389/frobt.2021.645756

The COVID-19 pandemic has emerged as a serious global health crisis, with the predominant morbidity and mortality linked to pulmonary involvement. Point-of-Care ultrasound (POCUS) scanning, becoming one of the primary determinative methods for its diagnosis and staging, requires, however, close contact of healthcare workers with patients, therefore increasing the risk of infection. This work thus proposes an autonomous robotic solution that enables POCUS scanning of COVID-19 patients' lungs for diagnosis and staging. An algorithm was developed for approximating the optimal position of an ultrasound probe on a patient from prior CT scans to reach predefined lung infiltrates. In the absence of prior CT scans, a deep learning method was developed for predicting 3D landmark positions of a human ribcage given a torso surface model. The landmarks, combined with the surface model, are subsequently used for estimating optimal ultrasound probe position on the patient for imaging infiltrates. These algorithms, combined with a force–displacement profile collection methodology, enabled the system to successfully image all points of interest in a simulated experimental setup with an average accuracy of 20.6 ± 14.7 mm using prior CT scans, and 19.8 ± 16.9 mm using only ribcage landmark estimation. A study on a full torso ultrasound phantom showed that autonomously acquired ultrasound images were 100% interpretable when using force feedback with prior CT and 88% with landmark estimation, compared to 75 and 58% without force feedback, respectively. This demonstrates the preliminary feasibility of the system, and its potential for offering a solution to help mitigate the spread of COVID-19 in vulnerable environments.

Keywords: autonomous robotics, point-of-care ultrasound, force feedback, 3D landmark estimation, 3D deep convolutional network, COVID-19

1 INTRODUCTION

The COVID-19 pandemic has emerged as a serious global health crisis, with the primary morbidity and mortality linked to pulmonary involvement. Prompt and accurate diagnostic assessment is thus crucial for understanding and controlling the spread of the disease, with Point-of-Care Ultrasound scanning (POCUS) becoming one of the primary determinative methods for its diagnosis and staging (Buda et al., 2020). Although safer and more efficient than other imaging modalities (Peng et al., 2020), POCUS requires close contact of radiologists and ultrasound technicians with patients, subsequently increasing risk for infections (Abramowicz and Basseal, 2020). To that end, robotic solutions embody an opportunity to offer a safer and more efficient environment to help mitigate the critical need for monitoring patients' lungs in the COVID-19 pandemic, as well as other infectious diseases.

Tele-operated solutions allow medical experts to remotely control the positioning of an ultrasound (US) probe attached to a robotic system, thus reducing the distance between medical personnel and patients to a safer margin. Several tele-operated systems have been successfully tested amid the pandemic for various purposes. Ye et al. (2020) developed a 5G-based robot-assisted remote US system for the assessment of the heart and lungs of COVID-19 patients, whereby the system successfully evaluated lung lesions and pericardial effusions in patients with varying levels of disease progression. An MGIUS-R3 tele-echography system was also evaluated for remote diagnosis of pneumonia in COVID-19 patients (Wu et al., 2020). The physician successfully obtained a lung scan from 700 km away from the patient's site, allowing him to diagnose lung pneumonia characterized by pleural abnormalities. The system could also detect left ventricular systolic function, as well as other complications such as venous thrombosis (Wang et al., 2020). Yang et al. (2020) developed a tele-operated system that, in addition to performing robotized US, is capable of medicine delivery, operation of medical instruments, and extensive disinfection of high-touch surfaces.

Although a better alternative to traditional in-person POCUS, commercialized tele-operated solutions nonetheless typically involve the presence of at least one healthcare worker in close vicinity of the patient to initialize the setup and assist the remote sonographer (Adams et al., 2020). An autonomous robotic US solution would hence further limit the required physical interaction between healthcare workers and infected patients, while offering more accuracy and repeatability to enhance imaging results, and hence patient outcomes. An autonomous solution can additionally become a valuable tool for assisting less experienced healthcare workers, especially amid the COVID-19 pandemic where trained medical personnel is such a scarce resource. Mylonas et al. (2013) have trained a KUKA light-weight robotic arm using learning-from-demonstration to conduct autonomous US scans; however, the entire setup was trained and evaluated on Latin letters detection within a uniform and clearly defined workspace, which is not easily transferable to applications involving human anatomy. An autonomous US robotic solution has been developed by Virga et al. (2016) for scanning abdominal aortic aneurysms, whereby the optimal probe pressure is estimated offline for enhanced image acquisition, and the probe's orientation estimated online for maximizing the aorta's visibility. Kim et al. (2017) designed a control algorithm for an US scanning robot using US images and force measurements as feedback tested on a thyroid phantom. The authors developed their own robotic manipulator, which, however, has too limited of a reach to scan a human upper torso. Additionally, the phantom on which the experiments were conducted is flat without an embedded skeleton, impeding the solution's immediate translation to lung scanning. The aforementioned works show significant progress in the field; however, to the best of our knowledge, no system has been developed for performing US lung scans in particular. Robotic POCUS of lungs requires a more tailored approach due to 1) the large volume of the organ which cannot be inspected in a single US scan, implying that during each session, multiple scans from different locations need to be sequentially collected for monitoring the disease's progression; 2) the scattering of US rays through lung air, meaning that an autonomous solution needs to be patient-specific to account for different lung shapes and sizes to minimize this effect; and finally 3) the potential obstruction of the lungs by the ribcage, which would result in an uninterpretable scan.

We thus developed and implemented a protocol for performing autonomous robotic POCUS scanning on COVID-19 patients' lungs for diagnosis and monitoring purposes. The major contributions of our work are 1) improved lung US scans using solely force feedback, given a patient's prior CT scan; and 2) prediction of anatomical features of a patient's ribcage using only a surface torso model to eliminate the need for a CT scan, with

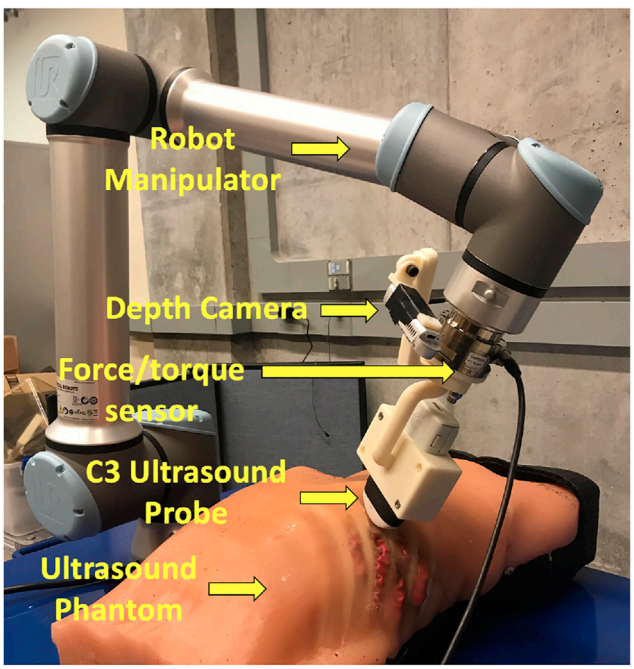

FIGURE 1 | Components of the autonomous robotic system setup.

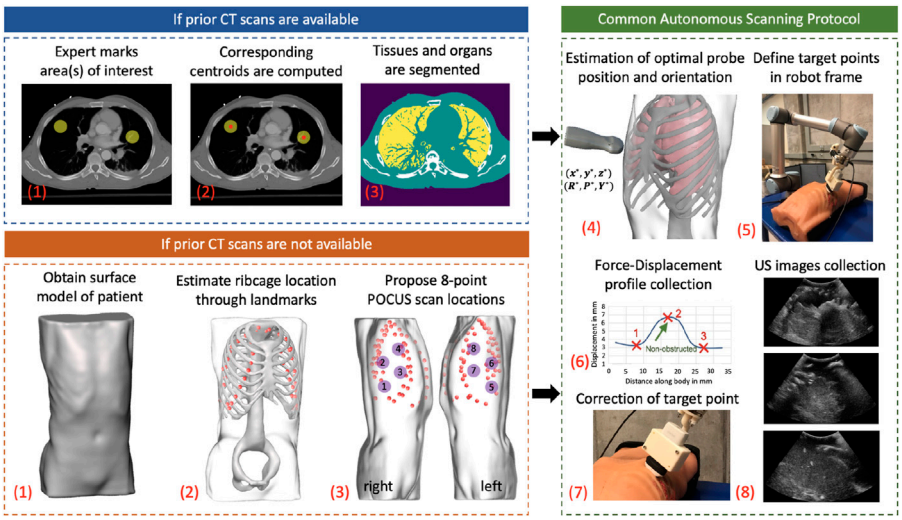

FIGURE 2 | General workflow of the autonomous robotic setup. Areas of interest in lungs are marked by an expert if a CT scan of a patient is available. The centroid of each area is computed, and an algorithm segments different organs in CT images. In the case where a CT is not available, a surface model of the patient is obtained using a depth camera, which acts as an input to a deep learning algorithm to estimate ribcage landmarks. The 8-point POCUS locations are subsequently manually proposed. In both cases, the optimal US probe positioning and orientation is estimated, which is relayed to the robotic system. During implementation, a force–displacement profile is collected, which is used to correct the end effector's position to avoid imaging of bones. US images of the target point are finally collected in a sweeping motion of $\pm 30^{\circ}$.

comparable results in terms of US scan accuracy and quality. This article is organized as follows: 1) Materials and Methods, which includes detailed information on the adopted robotic scanning procedure and algorithmic steps at every stage of the protocol; 2) Experiments and Results, which details the experimental setup used for validating the approach as well as the obtained results; 3) Discussion, providing an insightful analysis of aforementioned results and future work prospects; and finally 4) Conclusions, summarizing our key contributions and research outcomes.

2 MATERIALS AND METHODS

2.1 Testbed

The overall robotic setup is shown in **Figure 1**, which consists of a 6 degrees of freedom UR10e robot (Universal Robot, Odense, Denmark), a world frame color camera Intel RealSense D415 (Intel, Santa Clara, California, United States), a C3 wireless US probe (Clarius, Burnaby, British Columbia, Canada), and an SI-65-5 six-axis F/T Gamma transducer (ATI Industrial, Apex, North Carolina, United States). The US probe and camera are attached to the robot's end effector in series with the force sensor via a custom-designed 3D-printed mount for measuring the forces along the US probe's tip. The tool camera was positioned behind the probe to visualize it in the camera frame, as well as the scene in front of it. An M15 Alienware laptop (Dell, Round Rock, Texas, United States) with a single 6 GB NVIDIA GeForce GTX 1660 Ti GPU memory card was used for controlling the robot.

For the experimental validation of the results, we are using a custom-made full torso patient-specific ultrasound phantom that was originally developed for FAST scan evaluation, as it offers a realistic model of a patient's torso (Al-Zogbi et al., 2020). The phantom's geometry and organs were obtained from the CT scan of a 32-year-old anonymized male patient with low body mass index (BMI). The tissues were made of a combination of two different ballistic gelatin materials to achieve human-like stiffness, cast into the 3D-printed molds derived from the CT scan. The skeleton was 3D printed in polycarbonate, and the mechanical and acoustic properties of the phantom were evaluated, showing great similitude to human tissue properties. An expert radiologist has also positively reviewed the phantom under US imaging.

2.2 Workflow

Figure 2 shows the step-by-step workflow of the autonomous US scanning protocol of the robotic system, with and without prior CT scans. First, an expert radiologist marks on a chest CT of a patient regions of interest (typically but not necessarily containing infiltrates), which are to be observed over the course of coming days to evaluate the progression of the disease. An algorithm computes the spatial centroid of each region and returns optimal positions and orientations of an US probe on a subject's body, such that the resultant US image guarantees to contain the specified point of interest without skeletal obstruction. In the case where a CT scan is not available, landmarks of the ribcage are estimated using the patient's 3D mesh model, which is obtained through a depth camera. The scanning points are then manually selected on the model following the 8-point POCUS protocol (Blaivas, 2012). Goal positions and orientations are then relayed to the robotic system. Owing to possible kinematic and registration errors, the

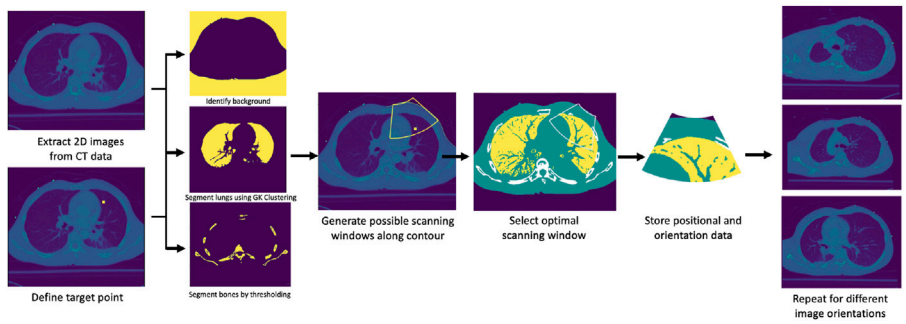

FIGURE 3 | Overview of steps for optimal scanning points selection algorithm.

positioning of the US probe may suffer from unknown displacements, which can compromise the quality and thus interpretability of the US scans. To mitigate this, the system employs a force–feedback mechanism through the US probe to avoid skeletal structures that will lead to shadowing. The specifics of this protocol are discussed in further detail in the following subsections.

The optimal US scanning position and orientation algorithm, as well as the ribcage landmark estimation, were implemented in Python, whereas the robot control, which includes planning and data processing algorithms, was integrated via Robot Operating System (Quigley et al., 2009). Kinematics and Dynamics Library (KDL) in Open Robot Control Systems (OROCOS) (Smits et al., 2011) is used to transform the task-space trajectories of the robot to the joint space trajectories, which are the final output of the high-level autonomous control system. The drivers developed by Universal Robot allow one to apply the low-level controllers to the robot to follow the desired joint-space trajectories.

2.3 Estimation of Optimal Ultrasound Probe Positioning and Orientation

A prior CT scan of a patient's chest is required for the algorithm's deployment. The possible scanning area on the body of a given patient is limited to the frontal and side regions. Given a region of interest in the lungs specified by a medical expert, its spatial centroid is computed first to define a target point. The procedure thus initially targets imaging a single point, followed by a sweeping motion about the contact line of the US probe to encompass the surrounding area. A set of images from the CT data containing the computed centroid is generated at various orientations, each of which is subsequently segmented into four major classes: 1) soft tissues, 2) lung air, 3) bones, and 4) background. First, the background is identified using a combination of thresholding, morphological transformations, and spacial context information. The inverse of the resultant binary mask thus delimits the patient's anatomy from the background. The inverse mask is next used to restrict the region in which lung air is identified and segmented through Gustafson–Kessel clustering (Elsayad, 2008). The bones are segmented using an intensity thresholding cutoff of 1,250, combined with spacial context information. Soft tissues are lastly identified by subtracting the bones and lung air masks from the inverse of the background mask. For simplicity's sake, identical acoustic properties are considered for all soft tissues within the patient's body. This assumption is justified by comparing the acoustic properties of various organs in the lungs' vicinity (soft tissue, liver, and spleen), which were shown to be sufficiently close to each other. **Figure 3** summarizes the workflow of the segmentation algorithms, as well as the final segmentation masks.

The objective is to image predetermined points within the lungs, while maximizing the quality of the US scan which is influenced by three major factors: 1) proximity of the target to the US probe, 2) medium through which the US beam travels, and 3) number of layers with different acoustic properties the beam travels across. The quality of an US scan is enhanced as the target is closer to the US probe. In the particular case of lung scanning, directing beams through air should be avoided due to the scattering phenomenon, which significantly reduces the interpretability of the resulting scan. Skeletal structures reflect US almost entirely, prompting the user to avoid them at all cost. Last, layers of medium with different attenuation coefficients induce additional refraction and reflection of the signal, negatively impacting the imaging outcomes.

The problem was therefore formulated as a discrete optimization solved by linear search, whereby the objective is to minimize the sum of weights assigned to various structures in the human body through which the US beam travels, along with interaction terms modeling refraction, reflection, and attenuation of the signal. Let $\overrightarrow{p}_i \in \mathbb{R}^2$ represent the 2D coordinates of a pixel i inside the ultrasound beam cone (see **Figure 3** for cone reference). Let $\overrightarrow{p}_{fc} \in \mathbb{R}^2$ represent the pixel corresponding to the focal point of the ultrasound probe. The attenuation of the ultrasound signal is evaluated through the following equation (Narayana et al., 1984):

$$w_{i,c} = w_{0,c}\left[\exp\left(-\alpha\Delta\left\|\overrightarrow{p}_i - \overrightarrow{p}_{fc}\right\|_2\right)\right]^{-1}, \quad (1)$$

whereby $w_{0,c}$ is the weight of the first pixel pertaining to the same class c, α is the attenuation coefficient of the medium, and Δ is the spatial resolution of the CT scan. To model the intensity reflection of the ultrasound beam at the interface of two different mediums, first the intensity reflection coefficient γ is

evaluated, and subsequently applied to the weight of the first pixel following the interface boundary (Laugier and Haïat, 2011):

$$\gamma = \frac{\left(\rho_2 v_2 - \rho_1 v_1\right)^2}{\left(\rho_2 v_2 + \rho_1 v_1\right)^2}, \tag{2}$$

$$w_{i,c}^{*} = w_{i,c}(\gamma)^{-1}, \tag{3}$$

with ρ being tissue density and v the speed of ultrasound. The term ρv effectively represents the impedance of the medium, with medium 1 preceding medium 2. The algorithm thus evaluates the weight of every pixel in between the first point of contact of the ultrasound probe and the target point, with higher weights assigned to more attenuated pixels, as they would drastically reduce the image quality. The US path that results in the lowest weight is selected as the optimal one.

To this end, bones were assigned the highest weight of 10^9, since US rays cannot travel past them. The second highest weight was assigned to lung air at 5, followed by soft tissues at 1. These weights were derived with the assistance of an expert sonographer. The assumed attenuation coefficients for skeletal tissue, lung air, and soft tissues are 1.1 dB/(mm × MHz), 1.2 dB/(mm × MHz), and 0.12 dB/(mm × MHz), respectively. The assumed densities of each class are 2000 kg/m^3, 1.225 kg/m^3, and 1,000 kg/m^3, whereas the speed of sound is 3,720 m/s, 330 m/s, and 1,575 m/s, respectively (Zagzebski, 1996; Etchison, 2011; Shung, 2015; Szalma et al., 2019). The weights are computed within an US cone that can only be instantiated from the surface of the patient's body across all generated images. The algorithm first determines the optimal scanning position and orientation of the probe for each individual image, and then selects the image with the overall lowest returned weight. The position of the US cone, as well as the orientation of the image, defines the optimal US scanning position and orientation in the CT coordinate frame. The solution was deployed on the Alienware laptop used for the robot control, and a pseudo-code is provided for reference in **Algorithm 1**.

Algorithm 1: Ultrasound Probe Optimal Scanning Position and Orientation

input: CT scan, target point $\overrightarrow{p}_t \in \mathbb{R}^3$, angle resolution $\Delta\beta = 5$, Δ in mm
procedure
extract $N \times M$ image I_0 from CT in axial plane s.t. $\overrightarrow{p}_t \in I_0$
extract $N' \times M'$ images I_i from CT in tilted planes at angles $\Delta\beta$ s.t. $\overrightarrow{p}_t \in I_i$
generate background masks $M_{BK,i}$ for $I_i, i: 0 \rightarrow k$
generate lung air masks $M_{L,i}$ for $I_i, i: 0 \rightarrow k$
generate bones masks $M_{BN,i}$ for $I_i, i: 0 \rightarrow k$
generate soft tissue masks $M_{T,i}$ for $I_i, i: 0 \rightarrow k$
replace I_i with. $M_i := M_{BK,1} + M_{T,i} + M_{L,i} + M_{BN,i}, i: 0 \rightarrow k$
initialize empty weight vector $W \in \mathbb{R}^{(k+1)\times L}$
For $i := 0$ to k do
generate L US beam cone contours C for I_i *s.t.* $\overrightarrow{p}_t \in A_l$, A_l: = area enclosed by contour
For $j := 0$ **to** $L - 1$ **do**
define. $\overrightarrow{d} := \overrightarrow{p}_t - \overrightarrow{p}_{fc}$
define $\overrightarrow{p}_{closest} := \text{argmin}\left(\left|\left|\overrightarrow{p}_{US} - \overrightarrow{p}_{fc}\right|\right|_2\right)$ *s.t.* $\overrightarrow{p}_{US} \in \overrightarrow{d}$
reinitialize $\overrightarrow{d} := \overrightarrow{p}_{closest} - \overrightarrow{p}_t$
define vector $\overrightarrow{p} := [M_i[\overrightarrow{p}_{closest}], \ldots, M_i[\overrightarrow{p}_t]]^T$ that contains all pixel values along $\overrightarrow{d}$
initialize $w = \overrightarrow{p}[0]$
initialize $w_{0,T} = 1$, $w_{0,L} = 5$ and $w_{0,B} = 10^9$
For $t := 1$ to length $(\overrightarrow{p})$ do
If $\overrightarrow{p}[t-1] \neq \overrightarrow{p}[t]$do
$\overrightarrow{p}[t:end] = \overrightarrow{p}[t:end]\left[\frac{(\rho_t v_t - \rho_{t-1} v_{t-1})^2}{(\rho_t v_t + \rho_{t-1} v_{t-1})^2}\right]^{-1}$
update $w_{0,c}$ according to $\overrightarrow{p}[t:end]$ for corresponding classes
$w = w + w_0\left[\exp\left(-\alpha_C \Delta \left|\left|\overrightarrow{p}_i - \overrightarrow{p}_{closest}\right|\right|_2\right)\right]^{-1}$
append w to W
return by linear search w_{min} : = Argmin W
return $\overrightarrow{p}_{goal} \in \mathbb{R}^3$ corresponding to w_{min} evaluated from plane transformation
return $R_{goal} \in SO(3)$ corresponding to w_{min} evaluated from plane transformation
output: R_{goal} and w_{min}

2.4 Force–Displacement Profiles Along the Ribcage

Uncertainties in patient registration and robot kinematics can result in a partial or complete occlusion of the region of interest due to the misplacement of the US probe. To mitigate this problem, a force–feedback mechanism is proposed, whereby we hypothesize that for a constant force application of 20 N, which is the recommended value for abdominal US imaging (Smith-Guerin et al., 2003), the probe's displacement within the phantom body will be higher in-between the ribs as opposed to being on the ribs. If the hypothesis is validated, one can thus generate a displacement profile across the ribcage of a patient to detect the regions obstructed by the ribs. The displacement on the phantom is expected to follow a sinusoidal profile, with peaks (i.e., largest displacements) corresponding to a region in-between the ribs, and troughs (i.e., smallest displacement) corresponding to a region on the ribs.

To evaluate this hypothesis, we have generated solid models of $n = 3$ patient torsos using anonymized CT scans, which were used to simulate displacements using finite element analysis (FEA) in ANSYS (ANSYS, Canonsburg, Philadelphia, United States). All image data are stripped from patient-identifying information, and are thus concordant with the exempt status described in 45 CFR §46.102. Two of the patients are female. The third patient is a male and was used as the model for the phantom's creation. All patients have varying BMI. The different organs of the patients were extracted from the CT scans using Materialize Mimics (Materialize NV, Southport, QLD 4222, Australia) software as STL files, and subsequently converted through SOLIDWORKS (SolidWorks Corp., Dassault Systemes, Velizy-Villacoublay, France) into IGS format, thus transforming the mesh surfaces into solid objects that can undergo material assignment and FEA simulations. The tissues' mechanical properties for the female patients were obtained from the literature, whereas those of the

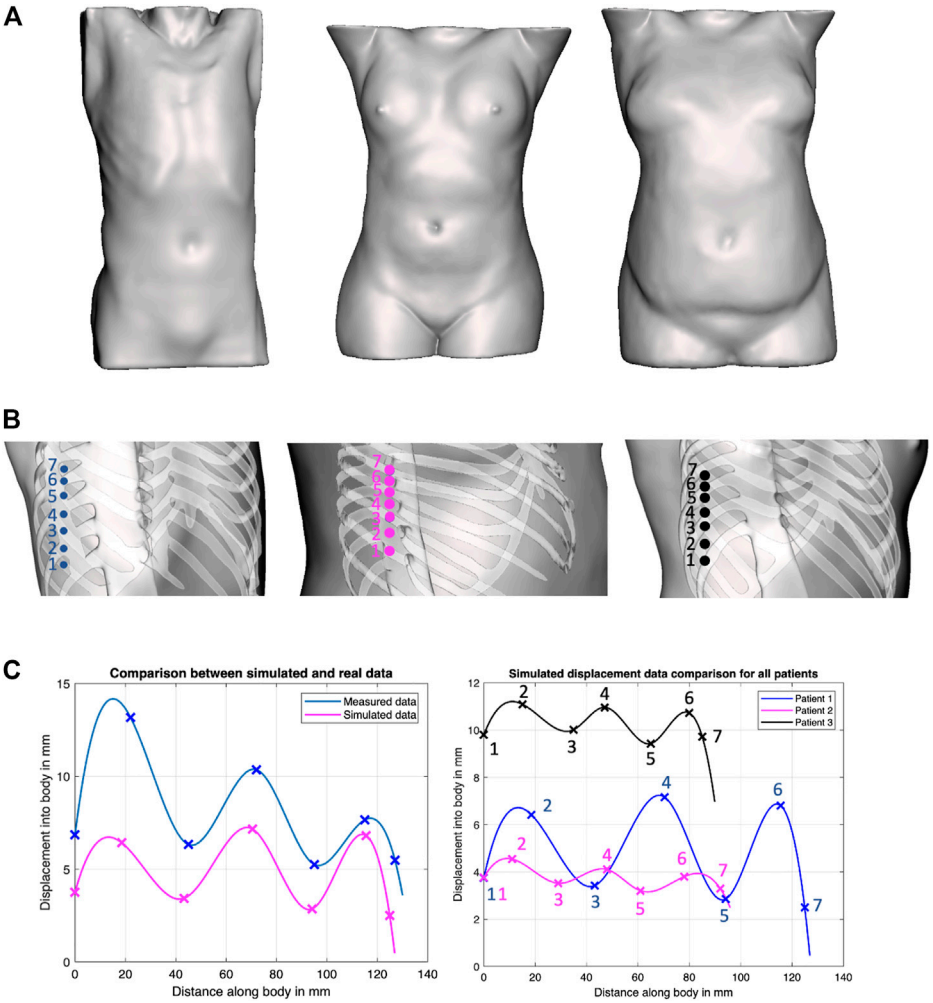

FIGURE 4 | Force–displacement validation experiments. **(A)** Surface models of the three patients considered in our work, covering both genders and various BMI; **(B)** positions on the phantoms where displacement profiles were collected in ANSYS simulations; **(C)** Comparison of experimental results between simulated data and actual phantom (patient 1, left plot), and comparison of simulated data between all patients (right plot).

phantom were measured experimentally (Al-Zogbi et al., 2020). In the FEA simulations, the force was transmitted onto the bodies through a CAD model of the ultrasound probe. In the robotic implementation, the ultrasound probe does not slip on a patient's body when contact is established because of the setup's rigidity. A lateral displacement of the probe in simulation would be erroneously translated into soft tissue displacement since the probe's tip displacement was used to represent the soft tissue displacement. Thus to ensure that the motion of the probe is confined to a fixed vector, the probe's motion was locked in all directions except in the z-axis. The force was directly applied to the probe through a force load that gradually increases from 0 to 20 N over a period of 5 s. The probe was initially positioned at a very close proximity from the torso; hence, its total displacement was considered to be a measure of the tissue's displacement. The simulations were deployed on a Dell Precision workstation 3620 with an i7 processor and 16 GB of RAM. Each displacement data point required on average 2.5 h to converge.

The location of the collected data points, as well as the returned displacement profile for all the three patients, is shown in **Figure 4**. Cubic splines were used to fit the data to better visualize the trend using MATLAB's curve fitting toolbox. Cubic splines were considered for better visualizing the profiles, assuming a continuous and differentiable function to connect data points. The actual displacements in between the minimum and maximum, however, need to be further validated, and may not match the displayed spline. To verify the outcome of the simulations, the corresponding displacement profiles were collected from the physical phantom, which are reported in **Figure 4** as well. Although the physical test demonstrates overall larger displacements, the physical displacement trend is similar to those of the simulated experiments. The results thus provide preliminary validation of our hypothesis of varying displacements associated with different positioning of an US probe with respect to the ribs. Therefore, we adopted this strategy in the robot's control process, whereby the system collects several displacement data points around the goal

position at 20 N, to ensure that the US image is obtained in-between the ribs.

2.5 Ribcage Landmark Prediction

This framework uses 3D landmarks defined on the ribcage to estimate the optimal probe's position. We trained a deep convolutional neural network to estimate the 3D position of 60 landmarks on the ribcage from the skin surface data. We define these landmarks using the segmentation masks of ribs obtained from the CT data. From the segmentation masks, we compute the 3D medial axis for each rib using a skeletonization algorithm (Lee et al., 1994). The extremities and center of each rib for the first 10 rib pairs (T1 to T10) are used as landmark locations. The three landmarks thus represent the rib–spine intersection, the center of the rib, and the rib–cartilage intersection.

Recent research in deep learning has shown encouraging progress in detecting 3D landmarks from surface data (Papazov et al., 2015; He et al., 2019; Liu et al., 2019). Teixeira et al. (2018) introduced a method to estimate 2D positions of internal body landmarks from a 2.5D surface image of the torso generated by orthographically projecting the 3D skin surface. Such methods, however, do not generalize to 3D data, since it would require representing landmark likelihood as a Gaussian distribution over a dense 3D lattice, and the memory required for representing 60 such lattices, one for each landmark, would be overwhelming. We address this by training a 3D deep convolutional network to directly estimate the landmark coordinates in 3D from the 3D volumetric mask representing the skin surface of a patient's torso. Given the skin mask, we estimate a 3D bounding box covering the thorax region, using jugular notch on the top and pelvis on the bottom. We then crop this region and resize to $128 \times 128 \times 128$ volume, which is used as input to a deep network. The network outputs a 3×60 matrix, which represents the 3D coordinates of the 60 rib landmarks. We adopt the DenseNet architecture (Huang et al., 2016) with batch normalization (Ioffe and Szegedy, 2015), and LeakyReLU activations (Xu et al., 2015) with a slope of 0.01 following the 3D convolutional layers with kernel size of 5x5x5. The network parameters were optimized using AdaDelta (Zeiler, 2012).

2.6 Control Strategy for Skeletal Structure Avoidance

The autonomous positioning of the US probe in contact with the patient's body necessitates motion and control planning. Let T_B^A denote the homogeneous transformation matrix from frames A to B, composed of a rotation matrix $R_B^A \in SO(3)$, and a translation vector $\overrightarrow{p}_B^A \in \mathbb{R}^3$. The global reference frame for the robotic implementation was chosen as the base frame of the robot, denoted by frame R. Let C and p represent the frames attached to the camera and tip of the US probe, as shown in **Figure 5**. Since both camera and probe are rigidly affixed to the robot's end effector, T_R^C and T_R^P are constant. T_R^C is estimated by performing an *eye-in-hand* calibration following the scheme presented in Tsai and Lenz (1989), whereas T_R^P is evaluated from the CAD model of the probe and its holder. Note that these transformations are composed of two transformations, namely,

$$T_R^C = T_R^{EE} T_{EE}^C, \tag{4}$$

$$T_R^P = T_R^{EE} T_{EE}^P, \tag{5}$$

whereby EE corresponds to the robot's end effector frame. The holder is designed such that the frame of the US probe would be translated by a fixed distance along the z-direction of the

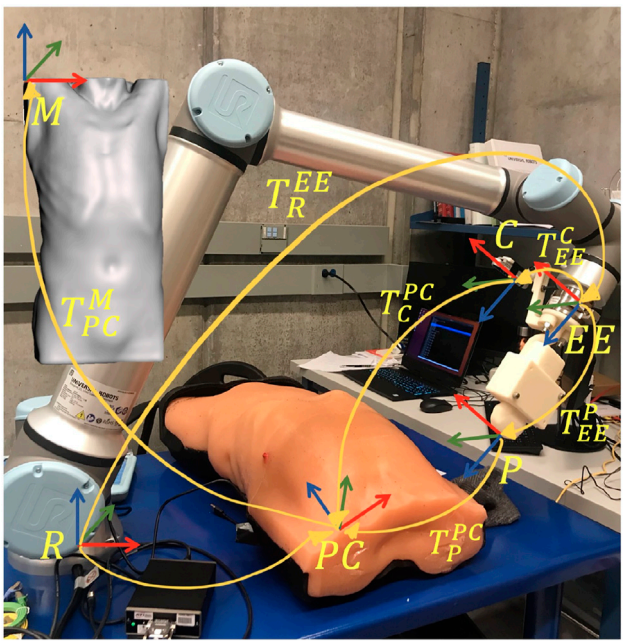

FIGURE 5 | Overview of the different reference frames used in the implementation, as well as the homogeneous transformations between them.

manipulator's end effector frame (see **Figure 5**). Thus, in the physical workspace, the relationship used to map out the point cloud data (frame *PC*) to the robot's base frame is

$$T_R^{PC} = T_R^C T_C^{PC}. \tag{6}$$

The anonymous CT patient scans (frame *CT*) were used to generate the mesh model (frame *M*) of the torsos, and hence the transformation between the two is known, set as $R_{CT}^M = I$ and $\overrightarrow{p}_{CT}^M = [0,0,0]^T$. The transformation T_{PC}^M between the point cloud data and the mesh model is estimated through the pointmatcher library using the iterative closest point approach (Pomerleau et al., 2013). Initial target points are either defined in the CT scans, or on the mesh models, both of which correspond to the *M* frame. Since the US probe target position and orientation need to be defined in the US probe frame (*p*), the following transformation is used:

$$T_P^M = T_R^{P-1} T_R^C T_C^{PC} T_{PC}^M. \tag{7}$$

The overall control algorithm can be described through three major motion strategies: 1) positioning of the US probe near the target point, 2) tapping motion along the ribcage in the vicinity of the target point to collect displacement data at 20 N force, and 3) definition of an updated scanning position to avoid ribs, followed by a predefined sweeping motion along the probe's *z*-axis.

The trajectory generation of the manipulator is performed by solving for the joint angles $\theta_i, i \in [0,5]$ through inverse kinematics computation facilitated by Open Robotics Control Software (OROCOS), and the built-in arm controller in the robot driver. Since obstacle avoidance has not been explicitly integrated into the robot's motion generator, we have defined a manipulator home configuration, from which the system can reach various target locations without colliding with the patient and the table. The home configuration is centered at the patient's torso at an elevation of 0.35°m from the body, with the $+z$ axis of the end effector corresponding to the $-z$ axis of the robot's base frame. The robot is driven to the home configuration before each target scan.

The force–displacement collection task begins with the robot maintaining the probe's orientation fixed (as defined by the goal), and moving parallel to the torso at regular intervals of 3 mm, starting at 15 mm away from the goal point, and ending 15 mm past the goal point, resulting in a total of 11 readings. The robot thus moves along the end effector's +z-axis, registering the probe's position when a force reading is first recorded, and when a 20 N force is reached. The L_2 norm of the difference of these positions is stored as a displacement data point. The two data points that represent the smallest displacements are assumed to be rib landmarks, and represent the center of the corresponding rib. The ideal direction of the applied force would be normal to the centerline of the curved section of the probe; however, it may not always be the case as some regions in the lungs might only be reachable with the resultant force pushing the probe on the side. In the case where the measured lateral forces contributed to the overall force by over 20%, the overall force was then considered in the computations. The center of mass of the probe holder is not in line with the assumed center; however, it is stiff enough to prevent bending.

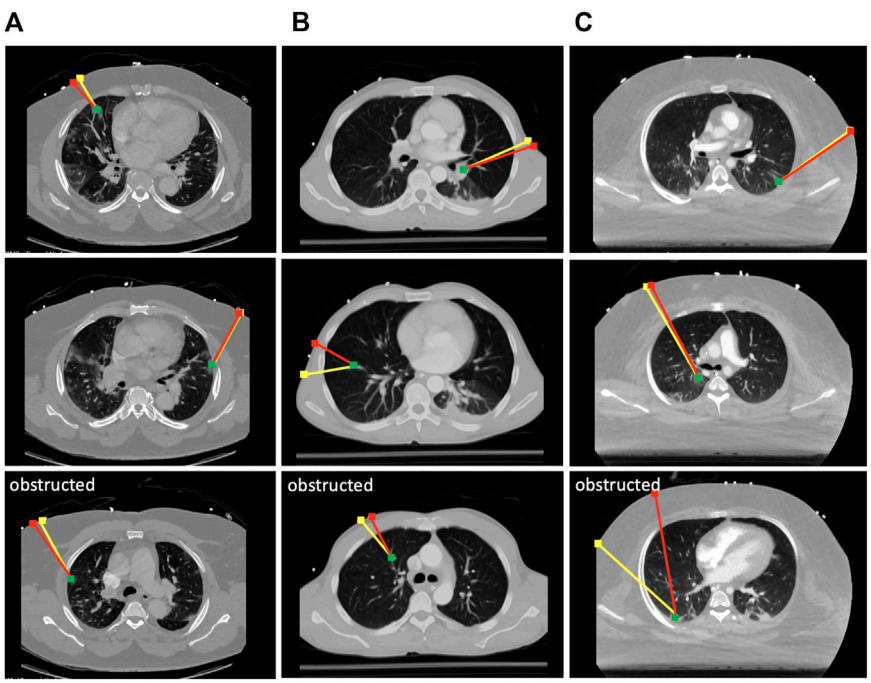

FIGURE 6 | Selected results from the optimal scanning algorithm compared to medical expert's selection. The yellow lines mark the expert's proposed paths, and the red lines are the ones proposed by the algorithm. The green dots are the target points that need to be imaged in the lungs. Paths returned by the expert that were obstructed by the ribs are marked as such. Each column of results corresponds to a CT scan of a different patient. **(A)** Results from COVID-19 patient 1; **(B)** results from a healthy patient; **(C)** results from COVID-19 patient 2.

TABLE 1 | Percentile distribution of the ribcage heights for training and testing the 3D landmark prediction algorithm.

	Percentile								
Ribcage height (mm)	10^{th}	20^{th}	30^{th}	40^{th}	50^{th}	60^{th}	70^{th}	80^{th}	90^{th}
Training set	282	293	304	321	344	372	388	407	428
Testing set	337	351	363	371	379	399	407	432	447

Since the goal point is always located between two ribs, it can hence be localized with respect to the center of the two adjacent ribs. The goal point is thus projected onto the shortest straight segment separating the center of the ribs, which is also closest to the goal point itself. Let the distance of the goal point from Rib 1 be d_1. Since the ribs are fairly close to each other, a straight line connecting the two is assumed to avoid modeling the curvature of a torso. Once two points with the smallest displacement are identified from the force collection procedure, a line connecting the two is defined in the end effector's coordinate frame, and distance d_1 is computed along that line from Rib 1 to define the position of the updated target point. Maintaining the same optimal orientation, the robot is thus driven to the updated goal point, the end effector then moves along the probe's +z-axis until a 20 N force is reached, followed by a sweeping motion of $\pm 30^{\circ}$ around the probe's line of contact with the patient.

3 EXPERIMENTS AND RESULTS

3.1 Scanning Points Detection

To evaluate the effectiveness of the scanning point detection algorithm, we asked an expert radiologist to propose scanning points on the surface of $n = 3$ patients using CT data in 3D Slicer. All image data are stripped from patient-identifying information, and are thus concordant with the exempt status described in 45 CFR §46.102. Two of the patients were positive for COVID-19 and exhibited significant infiltrate formation in their lungs, whereas the last patient was healthy with no lung abnormalities (see **Figure 6**). The medical expert selected 10 different targets within the lungs of each patient at various locations (amounting to a total of 30 data points), and proposed corresponding probe position and orientation on the CT scans that would allow them to image the selected targets through US. The medical expert only reviewed the CT slices along the main planes (sagittal, transverse, and coronal). The following metrics were used to compare the expert's selection to the algorithm's output: 1) bone obstruction, which is a qualitative metric that indicates whether the path of the US center beam to the goal point is obstructed by any skeletal structure; and 2) the quality of the US image, which was estimated using the overall weight structure discussed in the previous section, whereby a smaller scan weight signals a better scan, with less air travels, scattering, reflection, and refraction. For a fair initial comparison, we restricted the image search in the detection algorithm to the plane considered by the medical expert, i.e., the optimal scanning point was evaluated across a single image that passes through the target point. In this setting, the algorithm did not return solutions that were obstructed by bones, whereas five out of 30 of the medical expert's suggested scanning locations resulted in obstructed paths, as shown in **Figure 6**.

The quality of the scans has been compared on the remaining unobstructed 25 data points, and it was found that the algorithm returned paths with an overall 6.2% improvement in US image quality as compared with the expert's selection based on the returned sum of weights. However, when the algorithm is reset to search for optimal scanning locations across several tilted 2D images, the returned paths demonstrated a 14.3% improvement across the 25 data points, indicating that it can provide estimates superior to an expert's suggestion that was based on exclusively visual cues. The remaining five points have also been tested on the algorithm, and the optimal scanning locations were successfully returned. The average runtime for the detection of a single optimal scanning position and orientation is 10.5 ± 2.10 min, evaluated from the aforementioned 30 target points. The two most time-consuming tasks are the generation of oblique planes from the CT scans, and the Gustafson–Kessel clustering used to delineate lung air. Since this is a preprocessing step, the rather large time consumption is not a concern.

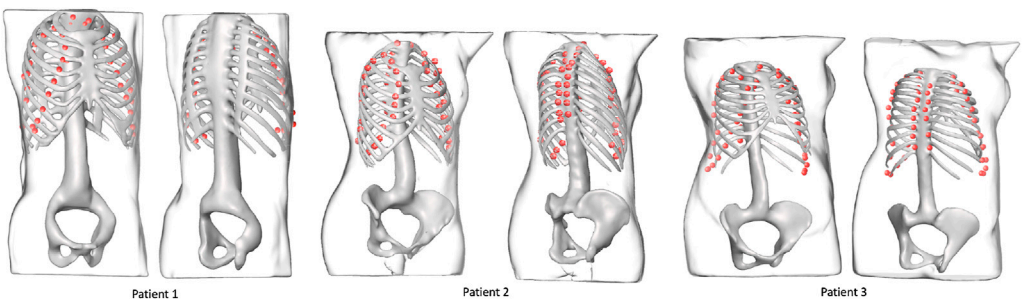

FIGURE 7 | Landmark outputs for every patient superimposed on the ribcages. The ribcage acts as ground truth for bone detection using the proposed landmarks. The skeletons are used for visualization purposes and were not part of the training process.

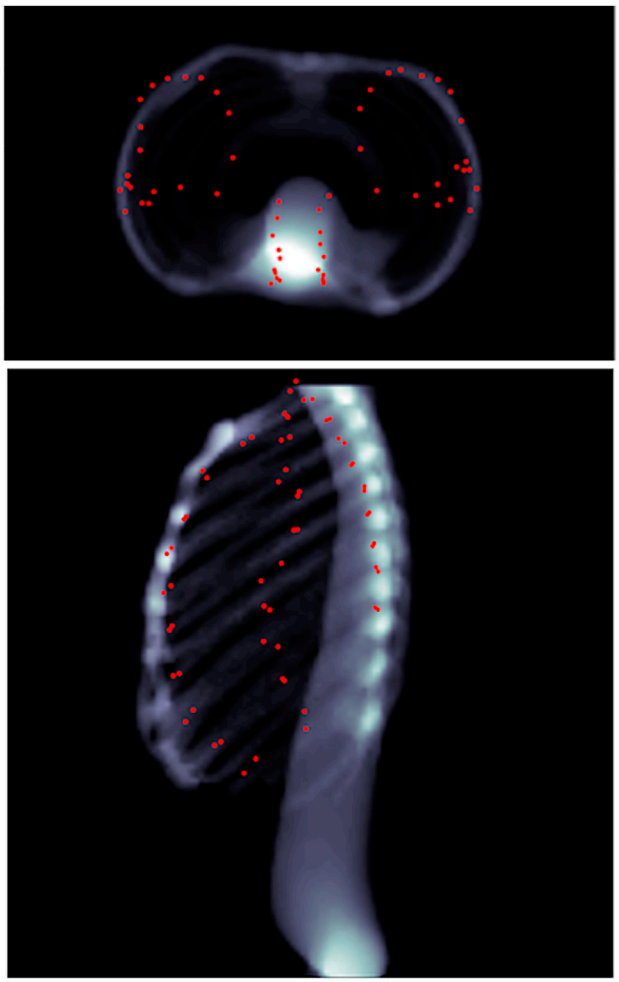

FIGURE 8 | Predicted landmarks (represented by red points) on patient 1 as seen through head–feet projection **(top)**, as well as lateral projection **(bottom)**. The landmarks are not part of the lungs, but merely appear so because of the projection.

3.2 Ribcage Landmark Prediction

A total of 570 volumes were prepared from thorax CT scans, 550 of which were used for training and 20 for testing. All image data are stripped from patient-identifying information and are thus concordant with the exempt status described in 45 CFR §46.102. Each of the 570 volumes is obtained from a different patient. In the training set, the minimum ribcage height was 195 mm and the maximum height was 477 mm, whereas in the testing set the minimum ribcage height was 276 mm and the maximum height was 518 mm. The percentile distribution of the training and testing ribcage heights is detailed in **Table 1**. The network was trained for 150 epochs optimizing the L_1 distance between the predicted coordinates and the Ground truth coordinates using the Adam optimizer (Kingma and Ba, 2015). The training took place on an NVIDIA Titan Xp GPU using the PyTorch framework (Paszke et al., 2017) and converged in 75 min. A mean Euclidean error of 14.8 ± 7.00 mm was observed on the unseen testing set, with a 95th percentile of 28 mm. The overall inference time was on average 0.15 s. **Figure 7** shows the landmark predictions obtained using the trained model on the three human subjects discussed in **Section 2.4**, by taking their corresponding skin surface masks as input. **Figure 8** shows the projected landmarks in 2D images.

3.3 Evaluation of Robotic System

A total of four experiment sets were devised to analyze the validity of our two main hypotheses, which involve the evaluation of the robotic system: 1) with prior CT scans without force feedback, 2) with prior CT scans with force feedback, 3) with ribcage landmark estimation without force feedback, and 4) with ribcage landmark estimation with force feedback. The overall performance of the robotic system is assessed in comparison with clinical requirements, which encompass three major elements: 1) prevention of acoustic shadowing effects whereby the infiltrates are blocked by the ribcage (Baad et al., 2017); 2) minimization of distance traveled by the US beam to reach targets, particularly through air (Baad et al., 2017); and last 3) maintaining a contact force below 20 N between the patient's body and US probe (Smith-Guerin et al., 2003).

3.3.1 Simulation Evaluation

Due to the technical limitations imposed by the spread of COVID-19 itself, the real-life implementation of the robotic setup was limited to $n = 1$ phantom. Additional results are thus reported using Gazebo simulations. The same three patients described in **Section 2.4** are used for the simulation. Since Gazebo is not integrated with an advanced physics engine for modeling tissue deformation on a human torso, we replaced the force sensing mechanism with a ROS node that compensates for the process of applying a force of 20 N and measuring the displacement of the probe through a tabular data lookup, obtained from the FEA simulations. In other words, when the US probe in the simulation approaches the torso, instead of pushing through and measuring the displacement for a 20 N force (which is not implementable in Gazebo for such complex models), we fix the end effector in place, and return a displacement value that was obtained from prior FEA simulations on the corresponding torso model.

To replicate a realistic situation with uncertainties and inaccuracies, the torso models are placed in the simulated world at a predefined location, corrupted with noise in the x, y, and z directions, as well as roll, pitch, and yaw angles. Errors were estimated based on reported camera accuracy, robot's rated precision, and variations between original torsos design and final model. The noises were sampled from Gaussian distributions with the precomputed means, using a standard deviation of 10% of the mean. The numerical estimates on the errors are reported in **Table 2**. The exact location of the torsos is thus unknown to the robot. For each torso model, a total of eight points were defined for the robot to image, four on each side. Each lung was divided into four quadrants, and the eight target points correspond to the centroid of each quadrant (see **Figure 9**). This approach is based on the 8-point POCUS of lungs. The exact location of the torso is used to assess the probe's position with respect to the torso, and provide predicted US scans using CT data. Two main evaluation metrics are considered: 1) the positional accuracy of the

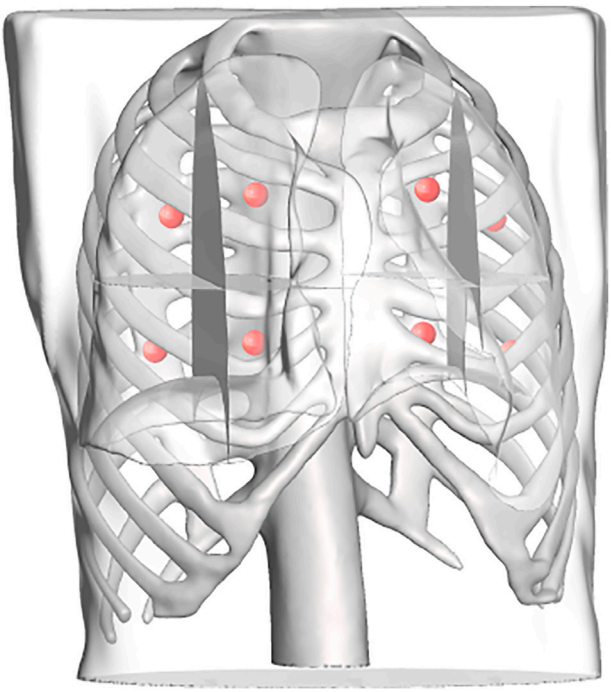

FIGURE 9 | Each lung is divided into four regions, the centroids of which are computed and used as target points in the scanning point detection algorithm.

TABLE 2 | Elements contributing to the overall error estimation. RPY stands for roll, pitch, and yaw. All values in the x, y, z directions are reported in mm, and the RPY values are in radians.

	x	y	z	R	*p*	Y
Registration	5	5	30	0.10	0.10	0.10
Robot	0.1	0.1	0.1	0.01	0.01	0.01
Model	10	10	10	0.05	0.05	0.05
Total	~15	~15	~40	0.16	0.16	0.16

TABLE 3 | Probe positioning error evaluation on the simulation experiments for the three patients. Experiments are divided by cases; case 1: using CT data without force feedback; case 2: using CT data with force feedback; case 3: using landmark prediction only without force feedback; case 4: using landmark prediction only with force feedback. All values are reported in mm.

	Case 1	Case 2	Case 3	Case 4
Patient 1				
Average error in x	13.7	9.40	16.5	12.3
Average error in y	12.7	10.1	14.6	6.70
Average error in z	30.3	11.5	31.2	8.10
Total error	35.5	17.9	38.1	16.1
Standard deviation	18.2	12.8	18.5	16.8
Patient 2				
Average error in x	14.2	13.2	12.4	11.2
Average error in y	10.5	8.70	15.3	13.4
Average error in z	41.0	13.5	35.6	15.1
Total error	44.6	20.7	40.6	23.0
Standard deviation	23.4	14.5	9.80	16.2
Patient 3				
Average error in x	17.8	15.0	19.8	11.3
Average error in y	13.6	13.9	12.4	10.9
Average error in z	35.6	11.1	39.1	13.2
Total error	42.0	23.2	45.5	20.5
Standard deviation	18.7	16.7	21.4	17.6

final ultrasound probe placement, which is the L_2 norm of the difference between the target ultrasound position, and the actual final ultrasound position; and 2) a binary metric for imaging the goal infiltrate or region, whereby it is either visualized or obstructed.

Each experiment set was repeated 10 times with different sampled errors at every iteration. The results of all four experiment sets are reported in **Table 3**. It is noticeable that the force feedback component has decreased the overall error on the probe's placement by 49.3% using prior CT scans, and 52.2% using predicted ribcage landmarks. The major error decrease was observed along the z-axis, since the force feedback ensured that the probe is in contact with the patient. It also provided additional information on the rib's placement near the target points, which were used to define the same target points' positions relative to the rib's location as well. For the US probe placement using only force–displacement feedback, we can observe that the average error across all three models is 20.6 ± 14.7 mm. Using the final probe's placement and orientation on the torso, we converted these data into CT coordinates to verify that the point of interest initially specified was imaged. In all of the cases, the sweeping motion allowed the robot to successfully visualize all the points of interest. When using ribcage landmark estimation, the displacement error with force feedback for all the three patients averaged at 19.8 ± 16.9 mm.

Similarly, the data were transformed into CT coordinates, showing that all the target points were also successfully swept by the probe. The average time required for completing an 8-point POCUS scan on a single patient was found to be 3.30 ± 0.30 min and 18.6 ± 11.2 min using prior CT scans with and without force feedback, respectively. The average time for completing the same scans was found to be 3.80 ± 0.20 min and 20.3 ± 13.5 using the predicted ribcage landmarks with and without force feedback, respectively. The reported durations do not include the timing to perform camera registration to the robot base, as it is assumed to be known a priori.

3.3.2 Phantom Evaluation

The same eight points derived from the centroids of the lung quadrants were used as target points for the physical phantom. Since the manufactured phantom does not contain lungs or visual landmarks, we are evaluating the methodology qualitatively, categorizing the images into three major groups: 1) completely obstructed by bones whereby 50–100% of the field of view is uninterpretable, with the goal point shadowed; 2) partially obstructed by bones, whereby <50% of the field of view is uninterpretable, with the goal point not shadowed; and 3) unobstructed, whereby <10% of the field of view is interpretable, and the goal point not shadowed. These groupings were developed in consultation with an expert radiologist. Since the scanning point algorithm focuses on imaging a target point in the center of the US window, we are also reporting this metric for completeness. The phantom was assessed by an expert radiologist, confirming that the polycarbonate from which the ribcage is made is clearly discernible from the rest of the gelatin tissues. It does, however, allow for the US beam to traverse it, meaning that the "shadow" resulting from the phantom's rib obstruction will not be as opaque as that generated by human bones. The robot manipulator is first driven to the specified goal point, and displacement profiles are collected in the vicinity of the target. The ribs' location is estimated from the force–displacement profile, and the final goal point is recomputed as a distance percentage offset from one of the ribs. Each experiment set was

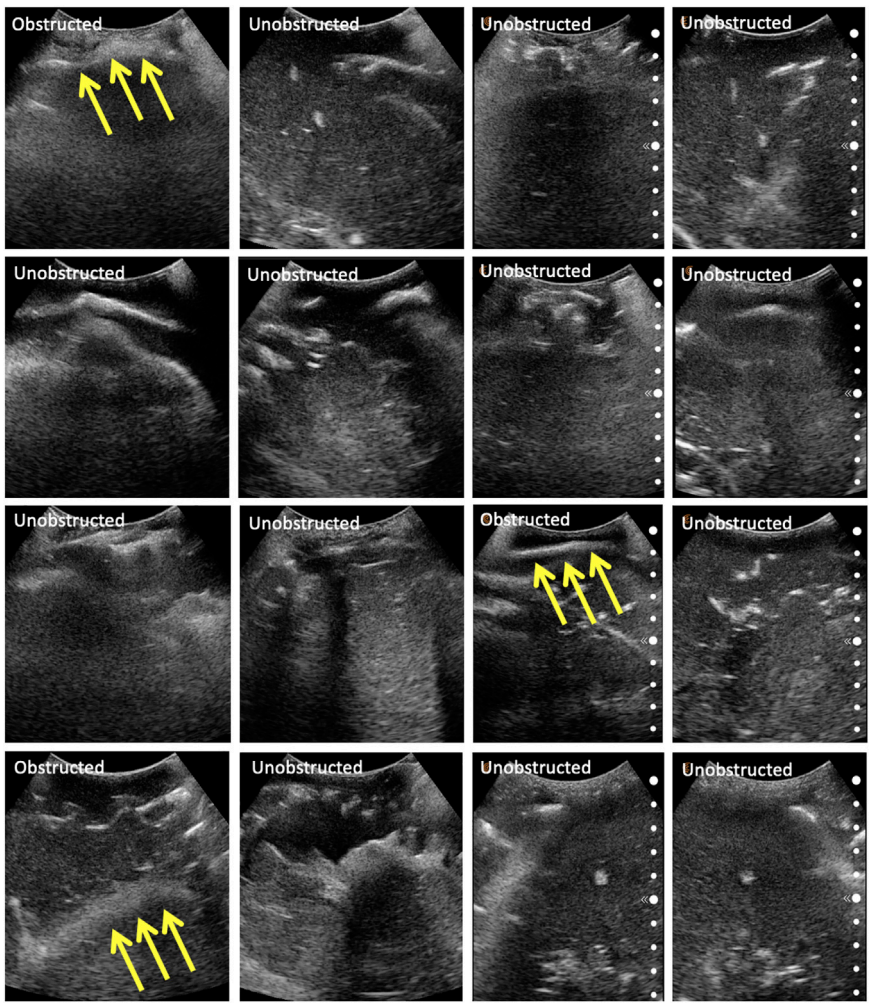

FIGURE 10 | Selected US scans obtained from the phantom through the different sets of experiments. Scans that are obstructed by bones are marked as such, with the arrows pointing toward the bone. Each column represents a different experiment, namely: **(A)** scans using CT data without force feedback; **(B)** scans using CT data with force feedback; **(C)** scans using landmark prediction only without force feedback; **(D)** scans using landmark prediction only with force feedback.

TABLE 4 | Qualitative categorization of all US images as evaluated by an expert radiologist. The US images were collected from the phantom. Experiments are divided by cases; case 1: using CT data without force feedback; case 2: using CT data with force feedback; case 3: using landmark prediction only without force feedback; case 4: using landmark prediction only with force feedback.

	Completely obstructed	Partially obstructed	Unobstructed	Visible center
Case 1	6	3	15	18
Case 2	0	4	20	24
Case 3	10	1	13	14
Case 4	3	3	16	19

repeated three times, the results of which are reported in **Table 4**. The evaluation of the US images was performed by an expert radiologist. The results show that the force feedback indeed assists with the avoidance of bone structures for imaging purposes, whereby 100% of the US scans using prior CT data were interpretable (i.e., with a visible center), and 87.5% of the scans were interpretable using landmark estimation. The results without using force feedback show that only 75% of the scans have a visible center region using prior CT scans, and 58.3% using predicted landmarks. The landmark estimation approach demonstrated worse results due to errors associated with the prediction, which can cause erroneous ribs' location estimation, and thus bad initial target points suggestions. Select images for all four experiments are shown in **Figure 10**. The average time required for completing an 8-point POCUS scan on the phantom was found to be 3.40 ± 0.00 min and 17.3 ± 5.10 min using prior CT scans with and without force feedback, respectively. The average time for completing the scans was found to be 3.30 ± 0.00 min and 25.8 ± 7.40 min using predicted ribcage landmarks with and without force feedback, respectively. Camera registration time was not included in reported durations.

4 DISCUSSION

The experimental results have demonstrated the preliminary feasibility of our robotic solution for diagnosing and monitoring COVID-19 patients' lungs, by successfully imaging specified lung infiltrates in an autonomous mode. In a real-life setting, a sonographer initially palpates the patient's torso to assess the location of the ribs for correctly positioning the US probe. We proposed a solution that autonomously replicates this behavior, by collecting force–feedback displacement data in real time. This approach has been assessed in simulation on three patients with varying BMI. We have evaluated our algorithm for proposing optimal US probe scanning positions and orientations given a patient's CT scan for generating target points for the robotic system. We also addressed the issue of potentially unavailable prior CT scans by developing a deep learning model for ribcage landmarks estimation. Our approach has demonstrated feasibility potential in both simulations and physical implementation, with a significant improvement in US image quality when using force feedback, and comparable results to CT experiments when using ribcage landmarks prediction only. The successful imaging of the target points in simulation, as well as the reduction in shadowing effects in the phantom experiments, is deemed to fulfill the clinical requirements defined in **Subsection 3.3**. This does not, however, imply the system's clinical feasibility, as additional experiments would be needed to support such claim. The current system is intended to alleviate the burden of continuously needing highly skilled and experienced sonographers, as well as to provide a consistent solution to lung imaging that can complement a clinician's expertise, rather than eliminating the need of a clinician's presence.

We acknowledge the limitations associated with the current implementation. The presented work is a study for demonstrating the potential of the methods' practical feasibility, laying down the foundation for more advanced experimental research. Although the simulated environment has been carefully chosen in an attempt to replicate real-life settings, and the physical phantom results have shown to support the simulated results, further experimentation is required to validate the outcomes. The simulated environment is incapable of capturing all the nuances of a physical setup—soft tissue displacements, for instance, have been acquired from a limited set of points on the patients' torsos using finite element simulations, with displacements in other locations obtained by interpolation. Elements such as breathing and movement of a patient during the scanning procedure are additional, albeit not comprehensive, factors too complex to be modeled in a robotic simulation, but ones that can negatively affect the outcome of the implementation.

Future work will focus on developing improved registration techniques to reduce the error associated with this step. An image analysis component as an additional feedback tool can further enhance the accuracy of the setup; force feedback ensures that the US probe is not positioned on ribs, and that it is in contact with the patient; however, it does not guarantee image quality. Additionally, a larger sample size of patients needs to be investigated to better validate the proposed force–displacement hypothesis. As was shown in **Figure 4**, different patients showed different displacement magnitudes, with the least noticeable differences pertaining to the patient with the highest BMI. It is important to understand in the future how well this approach scales with different body types and genders. The physical phantom used for the experimental setup does not contain lungs, has Polycarbonate bones, and embedded hemorrhages made of water balloons. These factors make the US image analysis quite challenging, with room for misinterpretation. Additional experiments need to be conducted on phantoms containing structures that can be clearly visualized and distinguished in US to better assess the experiments' outcome. Lastly, this study does not account for variations in patients' posture as compared to their posture when the CT scan was taken. The combination of CT data, ribcage landmark estimation, and force feedback will be investigated in future work for improved imaging outcomes.

5 CONCLUSION

We have developed and tested an autonomous robotic system that targets the monitoring of COVID-19-induced pulmonary diseases in patients. To this end, we developed an algorithm that can estimate the optimal position and orientation of an US probe on a patient's body to image target points in lungs using prior patient CT scans. The algorithm inherently makes use of the CT scan to assess the location of ribs, which should be avoided in US scans. In the case where CT data are not available, we developed a deep learning algorithm that can predict the 3D landmark positions of a ribcage given a torso surface model that can be obtained using a depth camera. These landmarks are subsequently used to define target points on the patient's body. The target points are relayed to a robotic system. A force–displacement profile collection methodology enables the system to subsequently correct the US probe positioning on the phantom to avoid rib obstruction. The setup was successfully tested in a simulated environment, as well as on a custom-made patient-specific phantom. The results have suggested that the force feedback enabled the robot to avoid skeletal obstruction, thus improving imaging outcomes, and that landmark estimation of the ribcage is a viable alternative to prior CT data.

DATA AVAILABILITY STATEMENT

The raw data supporting the conclusions of this article will be made available by the authors, without undue reservation.

AUTHOR CONTRIBUTIONS

LA-Z: responsible for the work on the ultrasound probe scanning algorithm, ANSYS simulations, robotic implementation, and drafting and revising the article. VS: responsible for the work on the 3D landmark estimation, and drafting and revising the manuscript. BT: responsible for the work on the 3D landmark estimation, and drafting and revising the manuscript. AA: contributed to the work on the segmentation of CT images. PB: responsible for the work on the 3D landmark estimation and supervising the team. AK: responsible for supervising the team and revising the manuscript. HS: contributed to the robotic implementation. TF: responsible for providing image data, designing and conducting the image analysis study, and revising and editing the manuscript. AK: responsible for designing the layout of the study, supervising the team, and revising the manuscript.

REFERENCES

Abramowicz, J. S., and Basseal, J. M. (2020). World Federation for Ultrasound in Medicine and Biology Position Statement: How to Perform a Safe Ultrasound Examination and Clean Equipment in the Context of Covid-19. *Ultrasound Med. Biol.* 46, 1821–1826. doi:10.1016/j.ultrasmedbio.2020.03.033

Adams, S. J., Burbridge, B., Obaid, H., Stoneham, G., Babyn, P., and Mendez, I. (2020). Telerobotic Sonography for Remote Diagnostic Imaging: Narrative Review of Current Developments and Clinical Applications. *J. Ultrasound Med.* doi:10.1002/jum.15525

Al-Zogbi, L., Bock, B., Schaffer, S., Fleiter, T., and Krieger, A. (2020). A 3-D-Printed Patient-specific Ultrasound Phantom for Fast Scan. *Ultrasound Med. Biol.* 47, 820–832. doi:10.1016/j.ultrasmedbio.2020.11.004

Baad, M., Lu, Z. F., Reiser, I., and Paushter, D. (2017). Clinical Significance of Us Artifacts. *Radiographics* 37, 1408–1423. doi:10.1148/rg.2017160175

Blaivas, M. (2012). Lung Ultrasound in Evaluation of Pneumonia. *J. Ultrasound Med.* 31, 823–826. doi:10.7863/jum.2012.31.6.823

Buda, N., Segura-Grau, E., Cylwik, J., and Wełnicki, M. (2020). Lung Ultrasound in the Diagnosis of Covid-19 Infection-A Case Series and Review of the Literature. *Adv. Med. Sci.*.

Elsayad, A. M. (2008). "Completely Unsupervised Image Segmentation Using Wavelet Analysis and Gustafson-Kessel Clustering," in 2008 5th International Multi-Conference on Systems, Signals and Devices, Amman, Jordan, September 26, 2008 (IEEE).

Etchison, W. C. (2011). Letter to the Editor Response. *Sports health* 3, 499. doi:10.1177/1941738111422691

He, Y., Sun, W., Huang, H., Liu, J., Fan, H., and Sun, J. (2019). PVN3D: A Deep Point-wise 3d Keypoints Voting Network for 6dof Pose estimationCoRR Abs/1911. Available at: arXiv:1911.04231 (Accessed November 11, 2019).

Huang, G., Liu, Z., and Weinberger, K. Q. (2016). Densely Connected Convolutional networksCoRR Abs/1608. Available at: arXiv:1608.06993 (Accessed August 25, 2016).

Ioffe, S., and Szegedy, C. (2015). Batch Normalization: Accelerating Deep Network Training by Reducing Internal Covariate Shift. *CoRR abs/* 1502, 03167.

Kim, Y. J., Seo, J. H., Kim, H. R., and Kim, K. G. (2017). Development of a Control Algorithm for the Ultrasound Scanning Robot (Nccusr) Using Ultrasound Image and Force Feedback. *Int. J. Med. Robotics Comp. Assist. Surg.* 13, e1756. doi:10.1002/rcs.1756

Kingma, D. P., and Ba, J. (2015). Adam: A Method for Stochastic Optimization. Available at: arXiv:1412.6980 (Accessed December 22, 2015).

Laugier, P., and Haïat, G. (2011). Introduction to the Physics of Ultrasound. *Bone Quantitative Ultrasound*, 29–45. doi:10.1007/978-94-007-0017-8_2

Lee, T. C., Kashyap, R. L., and Chu, C. N. (1994). Building Skeleton Models via 3-d Medial Surface axis Thinning Algorithms. *CVGIP: Graphical Models Image Process.* 56, 462–478. doi:10.1006/cgip.1994.1042

Liu, X., Jonschkowski, R., Angelova, A., and Konolige, K. (2019). Keypose: Multi-View 3d Labeling and Keypoint Estimation for Transparent Objects. *CoRR* abs/1912.02805

Mylonas, G. P., Giataganas, P., Chaudery, M., Vitiello, V., Darzi, A., and Yang, G.-Z. (2013). "Autonomous Efast Ultrasound Scanning by a Robotic Manipulator Using Learning from Demonstrations," in IEEE/RSJ International Conference on Intelligent Robots and Systems, Birmingham, UK, April 24–26, 2003 (IEEE), 3256.

Narayana, P. A., Ophir, J., and Maklad, N. F. (1984). The Attenuation of Ultrasound in Biological Fluids. *The J. Acoust. Soc. America* 76, 1–4. doi:10.1121/1.391097

Papazov, C., Marks, T. K., and Jones, M. (2015). Real-time Head Pose and Facial Landmark Estimation from Depth Images Using Triangular Surface Patch Featuresdoi:10.1109/cvpr.2015.7299104

Paszke, A., Gross, S., Chintala, S., Chanan, G., Yang, E., DeVito, Z., et al. (2017). *NIPS-W*.Automatic Differentiation in Pytorch

Peng, Q.-Y., Wang, X.-T., and Zhang, L.-N. (2020). Chinese Critical Care Ultrasound Study Group (CCUSG) (2020). Findings of Lung Ultrasonography of Novel Corona Virus Pneumonia during the 2019–2020 Epidemic. *Intensive Care Med.* 46, 849–850. doi:10.1007/s00134-020-05996-6

Pomerleau, F., Colas, F., Siegwart, R., and Magnenat, S. (2013). Comparing Icp Variants on Real-World Data Sets. *Auton. Robot* 34, 133–148. doi:10.1007/s10514-013-9327-2

Quigley, M., Conley, K., Gerkey, B., Faust, J., Foote, T., Leibs, J., et al. (2009). "Ros: an Open-Source Robot Operating System," in ICRA Workshop on Open Source Software, Kobe, Japan.

Shung, K. K. (2015). *Diagnostic Ultrasound: Imaging and Blood Flow Measurements*. Boca Raton, FL: CRC Press.

Smith-Guerin, N., Al Bassit, L., Poisson, G., Delgorge, C., Arbeille, P., and Vieyres, P. (2003). "Clinical Validation of a Mobile Patient-Expert Tele-Echography System Using Isdn Lines," in 4th International IEEE EMBS Special Topic Conference on Information Technology Applications in Biomedicine, Birmingham, UK, April 24–26, 2003 (IEEE), 23–26.

Smits, R., Bruyninckx, H., and Aertbeliën, E. (2011). *Kdl: Kinematics and Dynamics Library*. doi:10.1037/e584032011-011

Szalma, J., Lovász, B. V., Vajta, L., Soós, B., Lempel, E., and Möhlhenrich, S. C. (2019). The Influence of the Chosen In Vitro Bone Simulation Model on Intraosseous Temperatures and Drilling Times. *Scientific Rep.* 9, 1–9. doi:10.1038/s41598-019-48416-6

Teixeira, B., Singh, V., Chen, T., Ma, K., Tamersoy, B., Wu, Y., et al. (2018). Generating Synthetic X-Ray Images of a Person from the Surface Geometry. doi:10.1109/cvpr.2018.00944

Tsai, R. Y., and Lenz, R. K. (1989). A New Technique for Fully Autonomous and Efficient 3D Robotics Hand/eye Calibration. *IEEE Trans. Robot. Automat.* 5, 345–358. doi:10.1109/70.34770

Virga, S., Zettinig, O., Esposito, M., Pfister, K., Frisch, B., Neff, T., et al. (2016). "Automatic Force-Compliant Robotic Ultrasound Screening of Abdominal Aortic Aneurysms," in IEEE/RSJ International Conference on Intelligent Robots and Systems, Daejeon, Korea, December 9–14, 2016 (Piscataway, NJ: IEEE), 508–513.

Wang, J., Peng, C., Zhao, Y., Ye, R., Hong, J., Huang, H., et al. (2020). Application of a Robotic Tele-Echography System for Covid-19 Pneumonia. *J. Ultrasound Med.* 40, 385–390. doi:10.1002/jum.15406

Wu, S., Li, K., Ye, R., Lu, Y., Xu, J., Xiong, L., et al. (2020). Robot-assisted Teleultrasound Assessment of Cardiopulmonary Function on a Patient with Confirmed Covid-19 in a Cabin Hospital. *AUDT* 4, 128–130. doi:10.37015/AUDT.2020.200023

Xu, B., Wang, N., Chen, T., and Li, M. (2015). Empirical Evaluation of Rectified Activations in Convolutional Network. Available at: arXiv:1505.00853 (Accessed May 5, 2015).

Yang, G., Lv, H., Zhang, Z., Yang, L., Deng, J., You, S., et al. (2020). Keep Healthcare Workers Safe: Application of Teleoperated Robot in Isolation Ward for Covid-19 Prevention and Control. *Chin. J. Mech. Eng.* 33, 1–4. doi:10.1186/s10033-020-00464-0

Ye, R., Zhou, X., Shao, F., Xiong, L., Hong, J., Huang, H., et al. (2020). Feasibility of a 5g-Based Robot-Assisted Remote Ultrasound System for Cardiopulmonary Assessment of Patients with Covid-19. *Chest* 159, 270–281. doi:10.1016/j.chest.2020.06.068

Zagzebski, J. A. (1996). *Essentials of Ultrasound Physics*. Maryland Heights, MO: Mosby.

Zeiler, M. D. (2012). Adadelta: An Adaptive Learning Rate Method. Preprint repository name [Preprint]. Available at: arXiv:1212.5701 (Accessed December 22, 2012).

Conflict of Interest: Authors VS, BT, PSB, and AK are employed by company Siemens Medical Solutions, Inc. USA.

The remaining authors declare that the research was conducted in the absence of any commercial or financial relationships that could be construed as a potential conflict of interest.

frontiers in Robotics and AI

REVIEW
published: 26 August 2021
doi: 10.3389/frobt.2021.611978

Delivery of Healthcare Resources Using Autonomous Ground Vehicle Convoy Systems: An Overview

Calvin Cheung[1], *Alireza Mohammadi*[1]*, *Samir Rawashdeh*[1] *and Stanley Baek*[2]

[1]*Electrical and Computer Engineering, University of Michigan, Dearborn, MI, United States,* [2]*Academy Center for UAS Research, Department of Electrical and Computer Engineering, United States Air Force Academy (USAF Academy), Colorado Springs, CO, United States*

Utilizing military convoys in humanitarian missions allows for increased overall performance of healthcare logistical operations. To properly gauge performance of autonomous ground convoy systems in military humanitarian operations, a proper framework for comparative performance metrics needs to be established. Past efforts in this domain have had heavy focus on narrow and specialized areas of convoy performance such as human factors, trust metrics, or string stability analysis. This article reviews available Army doctrine for manned convoy requirements toward healthcare missions and establishes a framework to compare performance of autonomous convoys, using metrics such as spacing error, separation distance, and string stability. After developing a framework of comparison for the convoy systems, this article compares the performance of two autonomous convoys with unique convoy control strategies to demonstrate the application and utility of the framework.

Keywords: convoy, platooning, medical transport, military doctrine, convoy performance metrics

OPEN ACCESS

Edited by:
John Oyekan,
The University of Sheffield,
United Kingdom

Reviewed by:
Florian Georg Jentsch,
University of Central Florida,
United States
Khalid Mirza,
Oakland University, United States

***Correspondence:**
Alireza Mohammadi
amohmmad@umich.edu

Specialty section:
This article was submitted to Biomedical Robotics, a section of the journal Frontiers in Robotics and AI

Received: *29 September 2020*
Accepted: *21 July 2021*
Published: *26 August 2021*

Citation:
Cheung C, Mohammadi A, Rawashdeh S and Baek S (2021) Delivery of Healthcare Resources Using Autonomous Ground Vehicle Convoy Systems: An Overview. Front. Robot. AI 8:611978. doi: 10.3389/frobt.2021.611978

INTRODUCTION

From a military perspective, a ground vehicle convoy is a column of two or more vehicles under a single leader, traveling from a set origin to an objective destination (Center for Army Lessons Learned, 2010). Military utilization of convoys has a long history, with doctrine on convoy utilization for the United States (U.S.) Army being described as early as 1847 in "An Elementary Treatise on Advanced-Guard, Out-Post, and Detachment Service of Troops" (Killblane, 2005). While the battlefield and vehicles have changed drastically throughout the years, the purpose of convoys has remained consistent: to control road movements to meet various logistical needs, such as movement of supplies, personnel, and equipment toward humanitarian and medical needs (Layer, 1993). Even though the topic of convoys has been thoroughly dissected and studied by the Army (Killblane, 2013; Killblane, 2015; MPRI Kuwait Observer Controller Team, 2003), the advent of autonomous vehicles has led to modernization efforts to improve convoys through the addition of autonomy. These efforts aim to improve convoy efficiency and performance, reduce the risks to the Soldier[1], and decrease the overall cost of operations (Green, 2011).

In addition to military research, there are various other civilian organizations looking to develop and utilize autonomous ground convoy (AGC) systems. Efforts such as the Netherlands' European Truck Platooning Challenge (European Truck Platooning, 2021) and the European Commission's

[1]In this article, we use the preferred spelling of "Soldier" under the U.S. DoD guidance

Safe Road Trains for the Environment Project (Waibel, 2011) demonstrated the interest of civilian governments in maturing autonomous convoy technology for improvements in safety, reduction in fuel consumption, and reduction of traffic congestion. In support of these efforts and commercial development, many companies, such as Peloton Technology (King, 2017), Scania (Francis, 2019), Daimler, Volvo, and Volkswagen (Vincent, 2016), are researching and developing autonomous convoy solutions.

At a high level, AGC systems have a lead vehicle and follower vehicles. Follower vehicles keep pace and formation with the lead per system requirements. This is normally done through the sharing of vehicle kinematics, intended maneuvers, or sensor data (cameras, GPS, LIDAR, wheel encoders, etc.) between the vehicles, which allows separate vehicles to actuate appropriately to meet the desired speed and formation (Nardini et al. 2018; Virdis et al., 2018; Campolo et al., 2018; Molinaro et al., 2018; Stea et al., 2018). The data are distributed wirelessly via a variety of different methods, such as vehicular ad hoc networks (VANET), Vehicle-to-Vehicle (V2V) communications, and Vehicle-to-Infrastructure (V2I) communications (Uysal et al., 2015; Jia et al., 2016; Lu et al., 2016; Wang et al., 2016; Zhang et al., 2016; Shen et al., 2016). Several different standards and protocols are used for network communications, such as dedicated short-range communications (DSRC) radios, 3G/4G Long Term Evolution (LTE) cellular networks, and roadside wireless sensor networks, to improve network coverage and throughput.

To properly gauge the performance of AGC systems, a proper framework for comparative performance metrics needs to be established. Past efforts in this domain have had heavy focus on narrow and specialized areas of convoy performance without considering the complex requirement of AGVs performing logistical operations, such as human factors, trust metrics (Davis et al., 2008), or string stability analysis (Feng, et al., 2019). We remark that developing human trust metrics about the performance of autonomous vehicles is a vibrant research area. In a recent work in Seet et al. (2020), Harvy et al. (2020), Bose et al. (2020), Dragomir et al. (2020), it is demonstrated that automation malfunctions such as deceleration failures do not deteriorate human trust by themselves. But rather the human driver's inability for adaptive mitigation of the risk of negative outcomes such as risk of crashing resulting from those malfunctions adversely impacts the human trust. In Seet et al. (2020), Harvy et al. (2020), Bose et al. (2020), Dragomir et al. (2020), the human trust metric is reflected in changes in brain activity associated with action planning and motivational state. In addition, broad assumptions and simplifications were used in the analysis, such as the removal of lateral position considerations for convoy member vehicles, or the consistent existence in an information flow topology for robust inter-vehicle communications (Eben Li, et al., 2019). While the constraints, assumptions, and narrow focus areas of performance metrics that have been previously discussed are highly valuable for their intended purposes, a more generalizable approach is needed to compare performance across a larger swathe of autonomous convoy systems. The goal of this effort is to establish a framework for performance metrics of AGC systems for military humanitarian healthcare delivery missions by performing a review of AGC literature and comparing the findings to requirements found in Army doctrine relating to manned convoy systems. Based on these two critical pieces of information, we propose metrics for military AGCs. We will start with a brief historical exploration of the needs for autonomy in ground vehicle convoys and their utilization and benefits in humanitarian military delivery of healthcare. This will be followed by an exploration of overall manned convoy requirements. From there, we will survey the field of AGC efforts to determine common threads in the performance metrics to establish a generalized AGC performance metric framework to be used to compare the performance of future AGC efforts. Owing to military and commercial efforts having separate sets of needs and requirements, this article will focus on AGCs in the military domain, with an emphasis on humanitarian healthcare delivery, to be able to perform an in-depth look at the topic area.

The use of ground convoys to perform supply operations has been codified as an important part of an efficient strategy for the U.S. military as early as 1847 (Killblane, 2005). While modern military operations include more modern transportation systems such as rail lines, aircraft, and helicopters, ground vehicles still account for a significant portion of supply and equipment distribution. This reliance on ground vehicles was evident in Operation Iraqi Freedom, in which 98 percent of the military's supplies and equipment were distributed by ground transportation (Green, 2011). In addition to general supply and equipment transport, humanitarian military missions and military healthcare support leverage convoys for delivery of healthcare personnel and resources to areas of conflict that nongovernment organizations are unable to safely assist. U.S. military medical units support remote regions of the world to provide medical support toward humanitarian aid (Gomez et al., 1996; Poropatich et al., 1996; Karinch et al., 1996; Zajtchuk et al., 1996). Depending on the location, humanitarian aid convoys can be leveraged to provide several tasks, such as protection *via* greater physical and psychological security when transporting healthcare supplies, escorting medical practitioners to areas of confrontation, and performing medical evacuations (Wolfson and Wright, 1995). Furthermore, medical aid may potentially be applied within the convoy vehicles themselves, depending on the extent of the need (Headquarters United States Army Reserve Command, 1997). Given the warfare scenarios and battlefields in which current military operations take place, the danger to the Warfighter and need for medical aid in convoys continue to grow (Harrell et al., 2007).

Vehicle platooning refers to linking of two or more vehicles in a convoy. In this article, we use the terms "platoon" and "convoy" interchangeably.

Need for Military Autonomous Convoys

The unprecedented challenge of COVID-19 global pandemic requires an unprecedented global response. Given the military

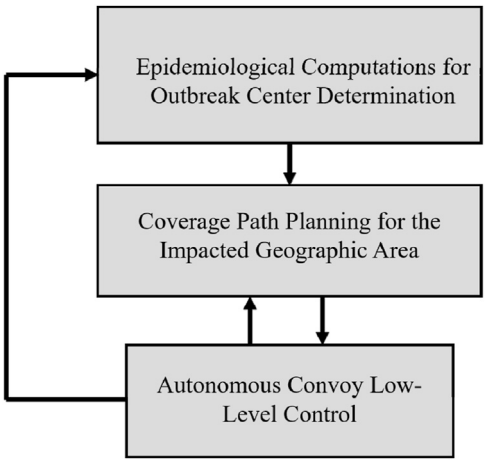

FIGURE 1 | A hierarchical decision-making framework for deployment of military AGCs in combat against pandemics.

historical superiority in providing medical and humanitarian logistics, a very efficient way of distributing vaccine and pandemic-fighting supplies would be through military convoys. The global nature of the pandemic and the need for reaching out to the most remote areas necessitate the use of autonomous and robotic technologies. As an instance of medical logistics delivery, the autonomous military convoys can deliver screening devices for biosampling and image-guided diagnosis tools to an outbreak area. In particular, the autonomous convoys deployed to an outbreak area can install remote sensing devices (Di Lallo et al., 2021) such as the recently developed "Levelogger" machine[2] for the rapid detection of the circulation of the COVID-19 virus within the impacted communities by sampling and testing wastewater in sewers and at wastewater treatment plants for the presence of the virus.

The coordination and command of such autonomous convoys need to be done in a proper hierarchical structure. At a higher level of hierarchy, there is a need for a supervisory control scheme that deploys the autonomous convoys to the areas that require mass vaccination and/or health service administration. For instance, the authors in David et al (2020), Baldassi et al (2020), Pio et al (2020) propose using Spatiotemporal Epidemiological Modeler (STEM) that can efficiently locate the centers of outbreaks and the course of epidemic trends. The obtained results on epidemic trends can then be used in coverage path planners (see, e.g., Nasirian et al. (2021)) that would ensure all the given points in an outbreak center are visited in a proper order. After the desired paths for an autonomous convoy in a geographic area are determined, low-level controllers will ensure that the trajectory tracking control objectives for the convoy are achieved (see **Figure 1**). This article is mainly concerned with achieving low-level control objectives in autonomous military convoys.

"Linear" and "Nonlinear" warfare scenarios are among the two main scenarios that can be defined for military autonomous convoys. In what follows, we argue that nonlinear warfare scenarios are more appropriate for medical logistics. In "linear warfare" scenarios, convoy operations are not prone to be attacked (Layer, 1993), where linear warfare is defined by conflicts in which opposing enemy forces generally proceeded forward. The geometry of a linear warfare battlefield implies that there is a "front" in which direct contact between forces is made, two "side" flanks that are often protected, and a secure "rear" area. Advancement in linear warfare means that forces at the front advance forward to clear and secure land. As the front moves forward, the noncombat assets in the rear progress as well, pushing forward and extending the secure rear (Harrell et al., 2007). Because of the aforementioned geometry, convoy operations are viewed as low risk in linear battlefields. Convoys are used to bring supplies and personnel from the rear to a forward position, traveling through secured areas that were far away from enemy combatants at the front battlefields. Many conflicts in U.S. history, including World War I, World War II, and Desert Storm, were linear warfare campaigns.

Despite the relative safety of convoy operations in linear battlefields, many modern conflicts and military operations in peacekeeping and humanitarian efforts are on a nonlinear battlefield. Indeed, in the epidemic spread models, computed using complex algorithms such as STEM (David et al., 2020; Baldassi et al., 2020; Pio et al., 2020), it can be observed that in contrast to linear battlefields, coverage areas do not have a defined front and secure rear area. Hence, there exists a need to use nonlinear battlefield techniques to deliver medical logistics to the outbreak area. The battlefield has a 360° area of operation with the center being a main operating base. In addition, many modern conflicts are against combatants that are using asymmetrical tactics. Asymmetrical tactics are strategies designed to harm a military's assets without going up against the primary defenses and forces (Harrell et al., 2007). Prime examples of this are the targeting of unarmored convoys during supply operations with improvised explosive devices (IED), snipers, and sudden ambushes on stopped vehicles (Killblane, 2005; Layer, 1993). Past examples of U.S. military operations in nonlinear battlefields against combatants using asymmetrical tactics include the Vietnam War, humanitarian efforts on Bosnia and Somalia, and the conflicts in Iraq and Afghanistan throughout the first quarter of the 21st century (Layer, 1993; Harrell, et al., 2007). U.S. Department of Defense studies project most future conflicts will be on nonlinear battlefields against combatants using asymmetrical tactics, indicating a continued threat to the personnel and resources needed for convoy operations (Harrell et al., 2007). Given the threat of asymmetrical tactics on nonlinear battlefields, the U.S. Army is looking to leverage AGC systems for strategic and logistical benefits including reduction of danger to personnel and reduction in the costs of logistics.

Considering the recent COVID-19 events, the pandemic-induced supply chain requirements have been demonstrated to be different from traditional supply chains (see, e.g., Rutner et al. (2012), for the pre-pandemic status-quo views on commercial and logistical operations), where efficiencies are usually realized

[2]https://www.michigan.gov/egle/0,9429,7-135-3313_71618-545670–,00.html

as cost savings. In particular, the main objective for distributing the COVID-19 vaccines (or in other future similar scenarios) has been to have a high throughput across the supply chain[3]. For this specific reason, the COVID-19-related logistical operations have been oriented toward humanitarian and wartime-like logistics, where highly responsive supply chains are constructed by the military in a way to meet the demand at any cost. With the surge of the COVID-19 variants across the globe, we believe that similar large-scale military supported logistical operations will be carried out to combat the pandemic. Indeed, the COVID-19 vaccine supply chain is set up in a completely different manner that is centered on the short-term measure of securing a sufficient supply of vaccines for the population spread across a vast geographic area.

The greatest threat to the safety of the personnel performing convoy operations in a nonlinear, asymmetrical battlefield are IEDs. IEDs are the main cause of battlefield casualties in Iraq and Afghanistan, accounting for 44% of the roughly 36,000 casualties from 2005 to 2009 (Green, 2011). By leveraging AGCs, vehicles can be operated with reduced direct human intervention, reducing the number of people needed in an operation, and thereby reducing the risk to human life by removing the personnel from dangerous situations. In addition to the lifesaving benefits, utilization of AGCs would provide tremendous cost savings as well. The cost of deploying a Soldier is estimated to be $2.1 M a year (Krumboltz, 2013), which means reduction of personnel needed has a built-in financial benefit. Furthermore, the use of autonomy in a convoy allows for greater precision in vehicle spacing due to the removal of human error, allowing for decreased spacing between vehicles. This decrease in spacing would reduce overall convoy length and provide fuel savings, which had been previously estimated to be between eight to twelve percent depending on the separation distance (Browand et al., 2004; McArthur et al., 2004; Radovich et al., 2004). Finally, from the humanitarian and healthcare mission perspective, increasing the autonomy of ground convoys reduces crew sizes, which is valuable in preventing the spread of infectious respiratory diseases, such as COVID-19. According to the Centers for Disease Control and Prevention, of the primary methods for protective against COVID-19 is to avoid close contact with others (Centers for Disease Control and Prevention, 2020). By leveraging greater levels of autonomy in convoys, the vectors of disease spread are decreased for both the warfighter and potential patients they may encounter as part of humanitarian military missions.

To reduce the threat to personnel, materiel, and medical supplies, and to reduce costs associated with convoy operations, the U.S. Army is looking to increase the utilization of autonomy in future operational concepts. Precision logistics, which entails the use of robotic autonomous delivery, is highlighted as a required Army capability set for sustained support of multi-domain operations (U.S. Army Training and Doctrine Command, 2018). In addition, the U.S. Army Robotic and Autonomous System Strategy specifically calls out autonomous convoys as a tool to enhance soldier survivability and reduce their exposure to hazardous situations (Maneuver Aviation and Soldier Division Army Capabilities Integration Center, 2017). With the high-level need being evident and understood by military leadership, a proper examination of the requirements is needed to be able to define metrics of success for an AGC system.

MANNED CONVOY REQUIREMENTS

Military doctrine outlines the fundamental set of principles that guides military forces in support of meeting its objectives (North Atlantic Treaty Organization Standardization Office, 2019). There exist four general types of military doctrine: Joint, Multinational, Multi-Service, and Service. While Joint, Multinational, and Multi-Service doctrine addresses processes common between multiple services (and nations, in the case of Multinational), every Service of the United States Armed Forces outlines Service specific doctrine defined to meet their idiosyncratic goals (U.S. Army Training and Doctrine Command, 2019). A thorough review of military doctrine can be performed to determine metrics and requirements of specific processes and systems for military needs. In this effort, we reviewed military doctrine to determine performance metrics for manned convoys. To limit the scope of the effort, we focused on service-specific doctrine from the U.S. Army due to their mission being most closely tied to the sustained utilization of ground convoys. In particular, our service-specific investigated topic is that of delivering medical logistics to the epidemic/pandemic outbreak areas.

All Army doctrine fits into a hierarchical structure with one of three classifications: Army Doctrine Publications (ADP), Field Manuals (FM), and Army Techniques Publications (ATP) (U.S. Army Training and Doctrine Command, 2019). Each of these publications serves a distinct purpose. ADPs contain the fundamental principles and foundations that guide Army actions in support of its objectives. FMs contain the tactics, procedures, and other relevant information in the execution of the principles described in the ADP. ATPs detail the flexible, non-prescriptive techniques to be used to perform Army missions, functions, and tasks. The doctrine has a hierarchy, with ADP on top, followed by FM, followed by ATP.

In addition to the doctrine, the Army also publishes training material, such as Training Circulars (TC) and Soldier Training Publications (STP). These documents can also contain information pertinent to the desired system performance and outcomes that are valuable in determining performance metrics. These documents, along with the aforementioned Army doctrine documents, are published from the Army Publishing Directorate (APD, 2021).

Table 1 lists the Army publications found to be relevant to convoy performance. An important characteristic of DoD publications is the Distribution Statement. Publications that

[3]See the following DoD News network article for more details: https://www.defense.gov/Explore/News/Article/Article/2393298/military-to-play-logistics-only-role-in-covid-19-vaccine-effort/

TABLE 1 | Current Army publications relevant to convoy performance.

Publication number	Publication name	Distribution statement
ATP 4-01.45	MULTI-SERVICE TACTICS, TECHNIQUES, AND PROCEDURES FOR TACTICAL CONVOY OPERATIONS	Distribution D
ATP 4-11	ARMY MOTOR TRANSPORT OPERATIONS	Distribution A
STP 55-88M14-SM-TG	SOLDIER'S MANUAL AND TRAINER'S GUIDE MOS 88M, MOS 88 M MOTOR TRANSPORT OPERATOR, SKILL LEVELS 1, 2, 3, AND 4	Distribution A
TC 21-305-20	MANUAL FOR THE WHEELED VEHICLE OPERATOR	Distribution A
TC 4-11.46	CONVOY PROTECTION PLATFORM (CPP) COLLECTIVE LIVE FIRE EXERCISES	Distribution C

have a Distribution Statement A label have been reviewed through the DoD Operational Security process and have been approved for public release (Office of the Under Secretary of Defense for Acquisition and Sustainment, 2012). Any other Distribution Statements, such as C or D, have restricted access and are not available to the general public. Owing to the limitation of availability in the information, the contents of those publications are not considered in this effort. However, they are included in **Table 1** for the sake of completeness. The remaining Army publications that are approved for public release and pertinent to convoys are ATP 4-11 Army Motor Transport Operations; STP 55-88M14-SM-TG Soldier's Manual and Training Guide MOS 88 M MOTOR TRANSPORT OPERATOR, SKILL LEVELS 1, 2, 3, and 4; and TC 21-305-20 Manual for the Wheeled Vehicle Operator. In the following sections, we will give a brief overview of the purpose of the publication, discuss its relationship to the convoy mission, and lay out the requirements that can be extracted toward the development of convoy performance metrics.

ATP 4-11 Army Motor Transport Operations details the Army's doctrine in the utilization of motor transportation in the support of operations (United States Army Combined Arms Support Command, 2013). This support includes the movement of personnel, units, supplies, and equipment by vehicles. By performing these functions, motor transports allow for essential distribution capabilities, force sustainment, and extended operational reach, making them an integral part of the Army's support and force sustainment. ATP 4-11 has information on the fundamentals, operations, and unit elements that make up motor transport operations. While the doctrine itself explicitly states that it does not go into details about convoy operations and battle drills, it still contains relevant information on how convoys are utilized, since they are used for motor transport. In the document, a convoy is defined as "a group of vehicles moving from the same origin to a common destination and organized under a single commander for the purpose of control." This definition of a convoy is important to note, since the statement gives the following high-level requirement:

> Requirement 1 - Two or more vehicles must be able to travel to a specified point.[4]

In addition, the various types of hauling required of motor transports specify the potential need for vehicles to make repeated trips, indicating the following requirement:

> Requirement 2 - A convoy must have the ability to return to the original location after initially reaching the destination.

From the perspective of overall convoy system parameters, ATP 4-11 details multiple planning factors needed for convoy missions that shape the performance requirements of a convoy system. One important planning factor is the "rate of march." The rate of march of a convoy mission is the average distance expected to be traveled by a given period of time. The need to be able to set a rate of march parameter indicates the following requirement:

> Requirement 3 - Convoy system must have an adjustable rate of march.

In addition to the rate of march, multiple planning factors related to convoy elements and associated gaps are discussed. A convoy can be broken down into smaller elements for organizational purposes. The smallest element is a march unit, which can have up to 25 vehicles. Next is a serial, which can consist of two to five march units. Following that is a column, which can consist of two or more serials. **Figure 2** illustrates the breakdown of the described convoy elements. The proper gap spacing considerations of a convoy differ between vehicles and convoy elements. For vehicles, the gaps are defined by distance between vehicles, with the exact distance being set by a Convoy Commander. This indicates the following requirement:

> Requirement 4 - Convoy system must have an adjustable gap distance[5] between vehicles.

While convoy vehicles define the gap by distance, convoy element gaps are defined by a time gap. A time gap is the amount of time measured between convoy elements as they pass a specified point. Different convoy elements can have unique time gaps, such as march unit gaps and serial gaps, and are

[4]In the context of the control of autonomous vehicle platoons, this is known as an autonomous rendevousz requirement

[5]Numerous adaptive control techniques such as extremum seeking control (Dadras, 2017) and model reference adaptive control (MRAC) (Dixit et al., 2020; Montanaro et al., 2020; Dianati et al., 2020; Mouzakitis et al., 2020; Fallah et al., 2020) can be employed to achieve this requirement in the context of AGCs

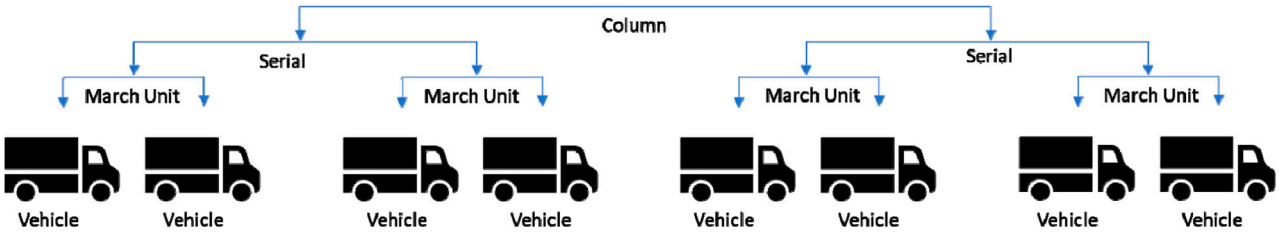

FIGURE 2 | Convoy elements.

also set at the discretion of the Convoy Commander. This indicates the following requirement:

> Requirement 5 - Convoy system must have an adjustable gap time between convoy elements.

Finally, ATP 4-11 also indicates that if a vehicle in a convoy is involved in a motor accident, then only the afflicted vehicle and its immediate successor should stop. All other vehicles in the convoy should continue the path when possible. This gives the following requirement:

> Requirement 6 - Convoy systems must be able to complete its route even in the event of one or more vehicles leaving the system.

STP 55-88M14-SM-TG Soldier's Manual and Trainer's Guide MOS 88 M identifies the training requirements for Soldiers serving in the Military Occupational Specialty (MOS) of 88M, which is the designation for motor transport operators (U.S. Army Training and Doctrine Command, 2013). Rather than providing doctrinal guidance, STPs provide task summaries to help plan, conduct, and evaluate individual training in units. The task summaries provide information and instructions such as task conditions, task standards, performance steps, evaluation preparation, and performance measures[6]. Much of the information covers the processes necessary in performing motor transport, such as mission preparation, transportation of cargo, and motor pool management. In reviewing the task summaries, certain portions of the text were found to reinforce the need of the requirements identified in ATP 4-11. Specific training tasks indicated a need for a convoy to increase transit speeds in kill-zones, reinforcing the adjustable rate of march in Requirement 3. In addition, the need to situationally set gaps between convoy vehicles and elements depending on the desired convoy formation reinforced the Requirement 4 and Requirement 5. Aside from the reinforcement of previously described requirements, STP 55-88M14-SM-TG also identifies a new requirement based on the responsibilities attributed to the Convoy Commander relating to catch-up speed. Convoy Commanders are to set a catch-up speed that convoy followers must abide by. This indicates the following requirements:

> Requirement 7 - Convoy system must be able to specify a maximum catch-up speed for individual convoy vehicles that fall behind.

The final convoy related publication available for public release is TC 21-305-20 Manual for the Wheeled Vehicle Operator. This TC describes operating practices, procedures, and techniques to efficiently operate a wheeled vehicle, including a chapter devoted to motor marches and convoys (U.S. Army Training and Doctrine Command, 2016). In this chapter, proper gap and vehicle speeds are discussed. The catch-up speed referenced in Requirement 7 is further enforced, and a speed-based gap distance is suggested as follows:

$$g = m*s$$

with gap distance in yards (g), speedometer multiplier (m), and speed of the vehicle in miles per hour (s). The value of m is typically set at two but is variable as determined by the Convoy Commander. This adjustable gap calculation further emphasizes the need for Requirement 4 and Requirement 5.

In addition to the publications available for public release, **Table 1** shows two additional documents: TC 4-11.46 Convoy Protection Platform (CPP) Collective Live Fire Exercises and ATP 4-01.45 Convoy Protection Platform (CPP) Collective Live Fire Exercises. TC 4-11.46 deals primarily with gunnery and training it handling threats (Frembling, 2012; Brooks, 2012), rather than topics pertaining to mobility performance requirements. ATP 4-01.45 "Multi-Service Tactics, Techniques, and Procedures for Tactical Convoy Operations," contains tactics, techniques, and procedures relevant to leading of troops, employment of gun trucks, battle drills, and IED handling (ALSA, 2021). Both publications are restricted from public release to protect the information contained, and as such, are noted only for completeness.

Challenges for Military Autonomous Convoys

In military healthcare delivery missions, there is a need for the autonomous convoy to be deployed to remote/rural areas, where the vehicles, which can belong to the class of Light Armored Vehicles (LAVs) or High Mobility Multi-purpose Wheeled

[6]We remark that the terms "measures"/"metrics" are used interchangeably in this article.

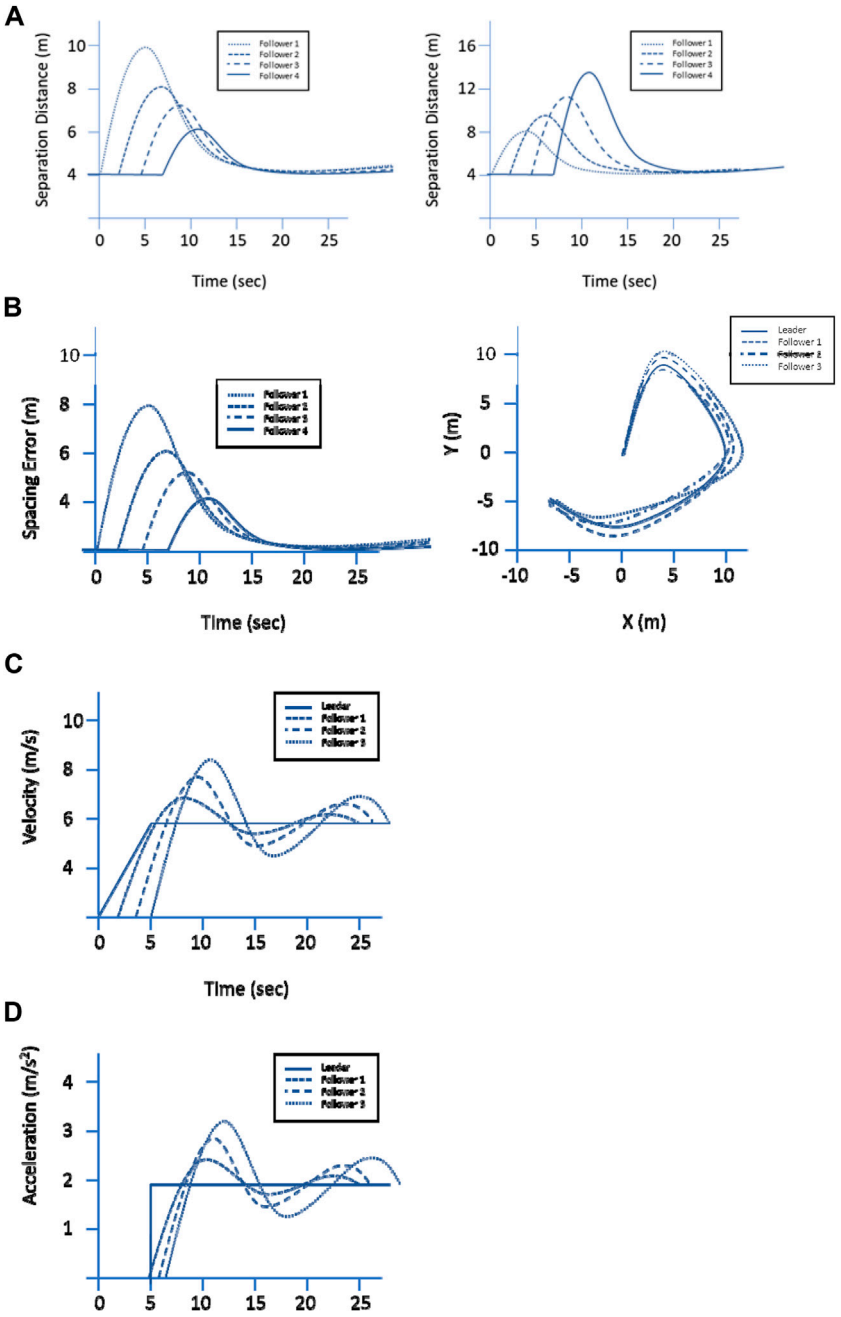

FIGURE 3 | Prevalent metrics for Convoy Vehicle Performance for **(A)** separation distance, **(B)** spacing error, **(C)** vehicle velocity, and **(D)** vehicle acceleration.

Vehicles (HMMWVs), need to move on deformable terrains. Accurate and efficient tire models for deformable terrain operations are essential for performing low-level vehicle control (Taheri et al., 2015). As opposed to civilian truck convoys that often move on roads, a direct application of on-road tire models to simulate tire behavior on a deformable terrain such as soft soil is not viable. Therefore, the methods for performance evaluation and modeling of the wheeled vehicles on deformable terrains are affected by various terrain properties in addition to design and operational parameters. For instance, ruts that are formed into the ground by the travel of wheels and tracks can cause deterioration of vehicle mobility (Liu et al., 2009). Consequently, for each convoy member, there is a need for using advanced control schemes such as terramechanics-based path-tracking control laws that consider mismatched uncertainties due to interaction with soft soils (Taghavifar and Rakheja, 2019). In addition to issues arising from interaction with soft soil, the communication channels in-between the convoy members are subject to communication delay and packet losses (Pawar and Pan, 2016). This problem will become more

TABLE 2 | Categorized manned convoy requirements.

Category	Requirement
Goal Specification	Requirement 1—Two or more vehicles must be able to travel to a specified point Requirement 2—A convoy must have the ability to return to the original location after initially reaching the destination Requirement 6—Convoy systems must be able to complete its route even in the event of one or more vehicles leaving the system
Spacing Policy	Requirement 4—Convoy system must have an adjustable gap distance between vehicles Requirement 5—Convoy system must have an adjustable gap time between convoy elements
System Parameters	Requirement 3—Convoy system must have an adjustable rate of march Requirement 7—Convoy system must be able to specify a maximum catch-up speed for individual convoy vehicles that fall behind

pronounced if the convoy is being teleoperated from a remote base. Therefore, there is a need for delay prediction/compensation algorithms for control of these autonomous convoys in the field (Lu et al., 2018).

There exist numerous efforts in the development and improvement of AGC systems that focus on a number of different areas, such as control objectives, VANET factors, and control strategies (Jia et al., 2016; Lu et al., 2016; Wang et al., 2016; Zhang et al., 2016; Shen et al., 2016). Each effort defines customized measures of performance and success based on the research goals, but there is not a standardized set of high-level metrics to be used across AGC systems. Despite the lack of standardization, there is nonetheless commonality between how AGC efforts measure their system's performance due to the common problem space that is being explored. The most common subjects that AGC efforts look to investigate are spacing policy and string stability; two closely related topic areas. By looking at metrics utilized in research efforts exploring these topics, we attempt to discern common threads in AGC metrics that can be used as a performance metrics framework for AGC systems for military utilization.

Spacing policy is the collection of methods, actions, and plans by which a convoy sets the desired distance between the vehicles (Rödönyi at al., 2014; Gáspár at al., 2014; Bokor at al., 2014; Palkovics at al., 2014). In general, the two most widely used platoon spacing policies are constant spacing and variable spacing. In a constant spacing policy, the separation distance between platoon members is independent of the speed of the controlled vehicle. The spacing error, $\varepsilon_j(t)$, of the *j*th vehicle, is as follows (Swaroop et al., 1994; Hedrick et al., 1994; Chien et al., 1994; Ioannou et al., 1994):

$$\varepsilon_j(t) = x_{j-1}(t) - x_j(t) - L_j$$

where x_j is the *j*th vehicle's position, x_{j-1} is the *j*th vehicle's leader, and L_j is the following distance. In variable spacing, the spacing of the convoy vehicles is related to the vehicle's speed, typically using a constant time headway approach. The spacing error δ_j is defined as follows (Ali et al., 2015; Garcia et al. 2015; Martinet et al. 2015):

$$\delta_j(t) = x_{j-1}(t) - x_j(t) - L_j - h_w v_j$$

where h_w is the time headway constant and v_j is the velocity of the vehicle j.

One of the primary goals of a convoy system is to reduce spacing error in accordance with the chosen spacing policy, which necessitates changes in control input to the follower vehicles. These changes and errors have the potential to propagate and amplify throughout the convoy, as each follower vehicle attempts to adjust their control parameters to reduce the error. A convoy system's reaction to this propagation of error is referred to as "string stability," with a convoy system being "string stable" if errors decrease, rather than increase, as they propagate through the convoy (Klančar et al., 2011). Intuitively, loss of string stability in a group of vehicles moving on a highway leads to undesired phenomenon such as the "accordion effect," which leads to accidents and/or traffic jam.

More formally (Lu et al., 2017; Li et al., 2017; Huang et al., 2017):

$$\|H(s)\|_\infty \le 1$$
$$h(t) > 0$$

where $h(t)$ represents the ratio of spacing error between two consecutive vehicles and $H(s)$ represents the Laplace transform of this function as follows.

$$h(t) = \frac{\varepsilon_j(t)}{\varepsilon_{j-1}(t)}$$
$$H(s) = \mathcal{L}(h(t))$$

presuming constant spacing, with $\delta_j(t)$ replacing $\varepsilon_j(t)$ for variable spacing.

It has been shown that string stability can be achieved in a convoy system with a variable spacing policy without any V2V communication, in contrast to constant spacing policy convoys that require some level of V2V communications to achieve stability (Guo and Yue, 2012). Experimental verification of string stability and adherence to spacing policy is often performed to validate that AGC systems are meeting the designed intent. The most prevalent metrics for experimentation can be split into separation distance, spacing error, velocity, and acceleration comparisons. Sample graphs for the various metrics can be seen in **Figure 3**.

When separation distance metrics are used, it presumes that the convoy vehicles start off with the desired spacing distance in a stopped state and looks at how the separation distance changes as the convoy system progresses throughout time. Given that the

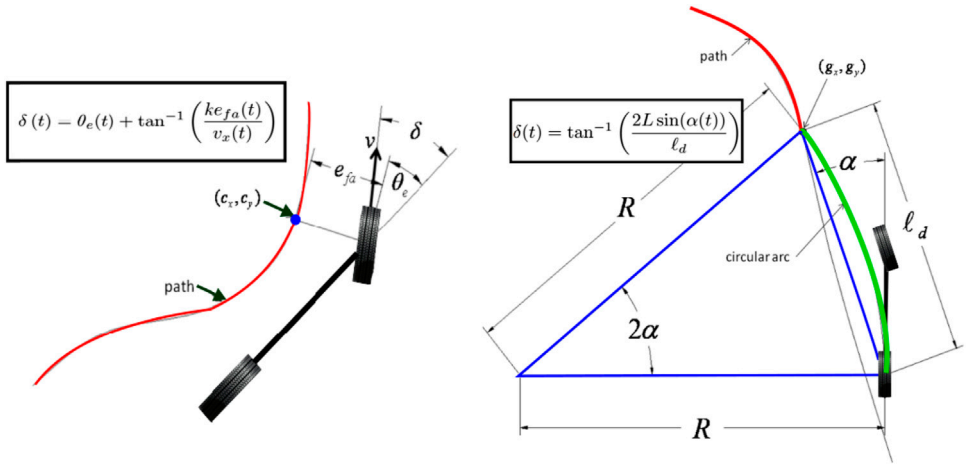

FIGURE 4 | Stanley (left) and pure pursuit (right) controller schematic diagrams (recreated from the schematic diagrams in Sinder, 2009).

separation distance is not static in a convoy system using a variable spacing policy, this metric is normally used when examining convoy controllers using a constant spacing policy (Guo and Yue, 2012; Ali et al., 2015; Garcia and Martinet, 2015; Lu et al., 2017; Li and Huang, 2017). **Figure 3A** shows a representative separation distance graph, with a string stable system on the left, and a string unstable system on the right.

Another metric that is often used in gauging autonomous convoy performance is spacing error over time. Convoy systems that leverage variable spacing tend to use spacing errors as the experimental metric, given the variable nature of separation distance between the member vehicles. Convoy systems that are string stable will show spacing errors that decrease along the follower vehicles (Li and He, 2018; Rödönyi et al., 2014; Gáspár et al., 2014; Bokor and Palkovics, 2014; Liu et al., 2014; Gao et al., 2014; Xu et al., 2014; Liu and Cheng, 2014; Gong et al., 2016; Shen and Du, 2016), as shown on the left side of **Figure 3B**. A separate way that spacing error is commonly used is in comparing convoy member vehicle offset to the desired trajectory, which is known as path following error (Klančar et al., 2011; Zhao et al., 2017; Goi et al., 2010; Klančar et al., 2009), as shown on the right side of **Figure 3B**. The path offset is then used to calculate an error metric, such as with a root mean squared error approach. This is typically used when systems are looking to examine path replication, rather than string stability.

An additional common metric that was discovered in gauging autonomous convoy performance was vehicle velocity. Given that the primary goal of a convoy in motion is to have followers maintain a certain gap distance with a lead vehicle, followers will always be aiming to converge to a velocity that matches its leader (Lu et al., 2017; Li and Huang, 2017). As such, it is important to note if a convoy's ability to have the vehicles reach a desired velocity is string stable. Since disturbances that are exerted on an individual convoy member can adversely deteriorate the string stability of the whole convoy, ensuring disturbances to vehicle velocity are not amplified throughout a convoy's followers, and noting time to convergence at the desired velocity, are important factors when examining performance (Guo and Yue, 2012; Liu et al. 2014; Gao et al. 2014; Xu et al. 2014; Liu and Cheng, 2014; Gong et al. 2016; Shen and Du, 2016; Lu et al., 2017; Li and Huang, 2017; Li and He, 2018). **Figure 3C** shows a representative velocity graph for a system that is not string stable in terms of velocity.

The final metric we reviewed in gauging autonomous convoy performance is control effort acceleration for the vehicles. If the control effort is not string stable, the reliability of vehicle operation can be put into jeopardy, as amplification of acceleration requests can exceed the limits of the vehicle's capabilities (Öncü, 2013). As such, string stability for acceleration is important for not only convoy performance, but overall safety and maintenance of the vehicles. Indeed, since the acceleration is proportional to exerted forces, acceleration string stability metric can be directly used to study the effect of exerted disturbances on the convoy dynamics and its position/velocity string stability metrics. Ensuring disturbances to control effort are not amplified throughout a convoy's followers, and noting time to convergence at the desired acceleration, are important factors when examining performance (Guo and Yue, 2012; Liu et al., 2014; Gao et al., 2014; Xu et al., 2014; Liu and Cheng, 2014; Rödönyi et al., 2014; Gáspár et al., 2014; Bokor and Palkovics, 2014; Gong et al., 2016, Shen and Du, 2016; Li and He, 2018). **Figure 3D** shows a representative acceleration graph for a system that is not string stable in terms of acceleration.

FRAMEWORK FOR COMPARING AUTONOMOUS CONVOYS FOR MILITARY USE

Through analyzing Army doctrine, we have derived generalized requirements that can be leveraged to apply to autonomous ground vehicle convoys in assessing their ability to perform Army missions. By leveraging common autonomous convoy

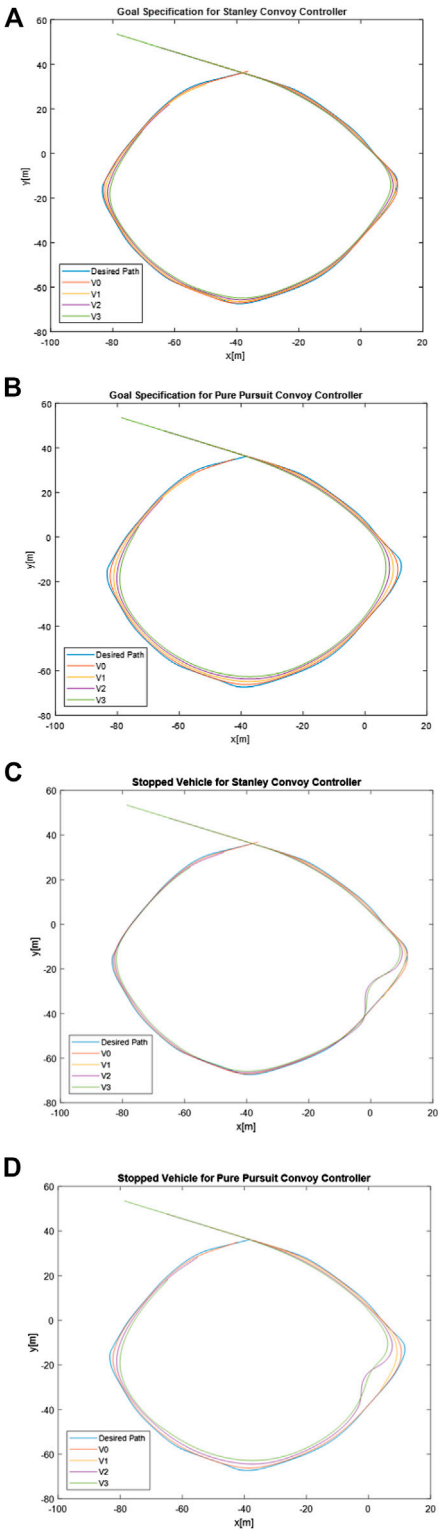

FIGURE 5 | Planned path and taken path of convoy vehicles for Requirement 1 using **(A)** Stanley and **(B)** Pure Pursuit and Requirement 6 using **(C)** Stanley and **(D)** Pure Pursuit.

performance metrics to gauge how well the requirements are being met, we can develop a framework that can be used to assess AGC performance across different systems. For greater clarity, we will be classifying the manned convoy requirements into three categories of analysis: Goal Specification, Spacing Policy, and System Parameters. Refer to **Table 2** for the specific categorization of requirements. The following sections will examine which metrics are best utilized for comparison for each different category of requirements. An example application of the framework will then be shown by examining a simulated AGC.

Goal Specification

Per Army doctrine, a convoy system must be able to travel to a designated point (Requirement 1) and optionally return to the original point of departure (Requirement 2) as dictated by mission needs. This indicates that there is a desired path and goal that the AGC is meant to follow as closely as possible, and deviation from said path is undesirable. Given these needs, offset spacing error, as shown on the right in **Figures 3B**, is the most appropriate metric to compare the performance of AGC systems. The desired position of lead vehicles and the relative position of the follower vehicles can be used to calculate the offset between the desired and actual positions. This metric can be used for both Requirement 1 and Requirement 2, since Requirement 2 can be considered an extension of Requirement 1 with multiple goal points. To evaluate overall offset spacing error performance, we will adapt evaluation metrics for position tracking from the domain of computer vision (Needham and Boyle, 2003) due to the similar goals between leader following and position tracking.

Another aspect of goal specification is that convoy systems must be able to complete their route even if one or more vehicles leave the convoy (Requirement 6). Once again, this looks at how well an AGC follows the path of a lead vehicle, with the added complexity of having a convoy follower needing to modify which vehicle it is following to ensure that a disabled follower vehicle does not cause all followers to halt. This also can be examined by leveraging spacing offset error, as shown in **Figure 3B**, as a metric of comparison. Vehicles that are unable to continue with the convoy will produce a greater overall error in the system, giving a data point to compare between different AGC implementations.

Spacing Policy

As previously defined, spacing policy is the collection of methods, actions, and plans by which a convoy sets the desired distance between the vehicles (Rödönyi et al., 2014; Gáspár et al., 2014; Bokor and Palkovics, 2014). The two primary categories of spacing policies are constant spacing and variable spacing. The doctrinal requirements align with the two categories of spacing policy, with the need for an adjustable gap distance (Requirement 4) aligning with constant spacing, and the need for adjustable gap time (Requirement 5) aligning with variable spacing. The key areas of comparison for spacing policy performance are string stability and time to convergence. A string stable system will not propagate errors throughout a convoy, meaning that convoy

TABLE 3 | Comparison metrics for path offset error.

		Vehicle 0 path offset error (m)		Vehicle 1 path offset error (m)		Vehicle 2 path offset error (m)		Vehicle 3 path offset error (m)	
		Stanley	Pure Pursuit	Stanley	Pure Pursuit	Stanley	Pure Pursuit	Stanley	Pure Pursuit
Req. 1	Mean	0.7149	0.5975	1.7203	2.0791	4.0645	4.5741	7.1026	7.9936
	St. Dev	0.5568	0.3086	3.1583	3.0689	7.9315	7.7624	13.4847	13.1704
Req. 6	Mean	0.7156	0.5725	N/A	N/A	4.2375	4.7396	7.4087	8.2358
	St. Dev	0.5571	0.3085	N/A	N/A	7.9525	7.7913	13.5224	13.1862

followers will more closely adhere to the desired speed and position. In addition, string stability allows the overall convoy to reach its desired end state more rapidly, meaning that the time needed for each follower vehicle to converge to the desired system parameter is lower. Therefore, string stability-related metrics, such as amplification of the response of follower vehicles and overall time it takes for the follower vehicles to converge to the steady state (Guo and Yue, 2012; Liu et al., 2014; Gao., 2014; Xu., 2014; Liu and Cheng, 2014; Rödönyi et al., 2014; Gáspár et al., 2014; Bokor and Palkovics, 2014; Gong et al., 2016; Shen and Du, 2016; Li and He, 2018), are appropriate tools for comparison. Examples can be seen in **Figure 3**. The choice of which area to examine for string stability (spacing, velocity, acceleration, etc.) is dependent on the mission goals that the AGC is attempting to meet.

System Parameters

The requirements categorized under System Parameters deal with overall convoy system settings. Army doctrine defines the need for an adjustable rate of march (Requirement 3) and an ability to set a maximum catch-up speed for the convoy follower vehicles (Requirement 7). Overall, they impose qualifiers and restrictions to how the AGVC meets spacing policy requirements. These requirements can be analyzed with a binary success or failure by monitoring the overall convoy velocity and the speed of the individual vehicles. If comparisons of greater granularity are needed, the distinction can be made by examining the string stability-related metrics described in Spacing Policy at different rates of march and catch-up speeds. This would entail examining multiple runs of a convoy system and changing the system parameter to be evaluated between each run. The results of each run can be examined for string stability-related metrics, such as amplification of the response of follower vehicles and overall time it takes for the follower vehicles to converge to the steady state. The examples can be seen in **Figure 3**. Changes in these measurements between the various runs can then be noted for an AGC system, which could then be compared with how changes affected performance for other AGC systems.

APPLICATION OF FRAMEWORK

To apply our framework for comparing autonomous convoys, we leveraged the Autonomous Navigation Virtual Environment Laboratory (ANVEL), "an interactive, real-time engineering modeling and simulation (M&S) software tool built specifically to assist in the research, design, testing, and evaluation of intelligent ground vehicles (Quantum Signal, 2018)." ANVEL features Python application programmer interfaces to set up and control autonomous convoys in an M&S environment.

Two different convoy following controllers were used in our application of the framework. One convoy controller utilized a Pure Pursuit method for geometric path tracking, in which the center of the rear axle is used as the reference point on the vehicle to compute a steering angle toward a look-ahead point at a fixed distance (Amidi and Thorpe, 1991). The other convoy controller utilized the Stanley method for geometric path tracking, in which the front axle is used as the reference point, and both the heading error and cross-track error are used to find the proper steering angle (Thrun et al., 2006). These two control schemes represent the two ends of the spectrum of geometric/kinematic controllers in terms of dependency on the number of to-be-tuned parameters where the Pure Pursuit controller relies less on the system parameters while the Stanley controller, which was the winner of DARPA challenge 2005 (Buehler et al., 2007) relies on more tunable parameters.

The following schematic diagrams depict the schematic diagrams associated with the Stanley and pure pursuit control schemes. Some remarks are in order (see, e.g. Snider, 2009, for more detailed explanations). Both pure pursuit and Stanley controllers belong to the family of path tracking algorithms, namely, algorithms that make a vehicle to execute a globally defined geometric path by applying appropriate steering commands that guide the vehicle along the path. The goal of any path tracking algorithm is to simultaneously minimize the lateral distance between the vehicle and the defined path, to constrain the steering control inputs to smooth input commands, and to minimize the heading of the vehicle and the defined path heading.

As it is demonstrated in Snider (2009), pure pursuit controllers are essentially proportional controllers with a proportional gain of $2/l_d^2$ acting on the steering angle dynamics. Indeed, if the curvature of the circular arc in **Figure 4** (right) is given by κ, then it can be shown that $\kappa = (2/l_d^2)e_{l_d}$, where $e_{l_d} := l_d \sin(\alpha)$ is the cross-track error. A geometric interpretation of the parameter l_d in the gain $2/l_d^2$ is that it provides a kind of look-ahead distance. As is customary in the pure pursuit control literature, the look-ahead distance is tuned to be stable at several constant speeds. If the look-ahead distance is a function of the speed of the vehicle, then gain-scheduling and linear parameter varying control (LPV)

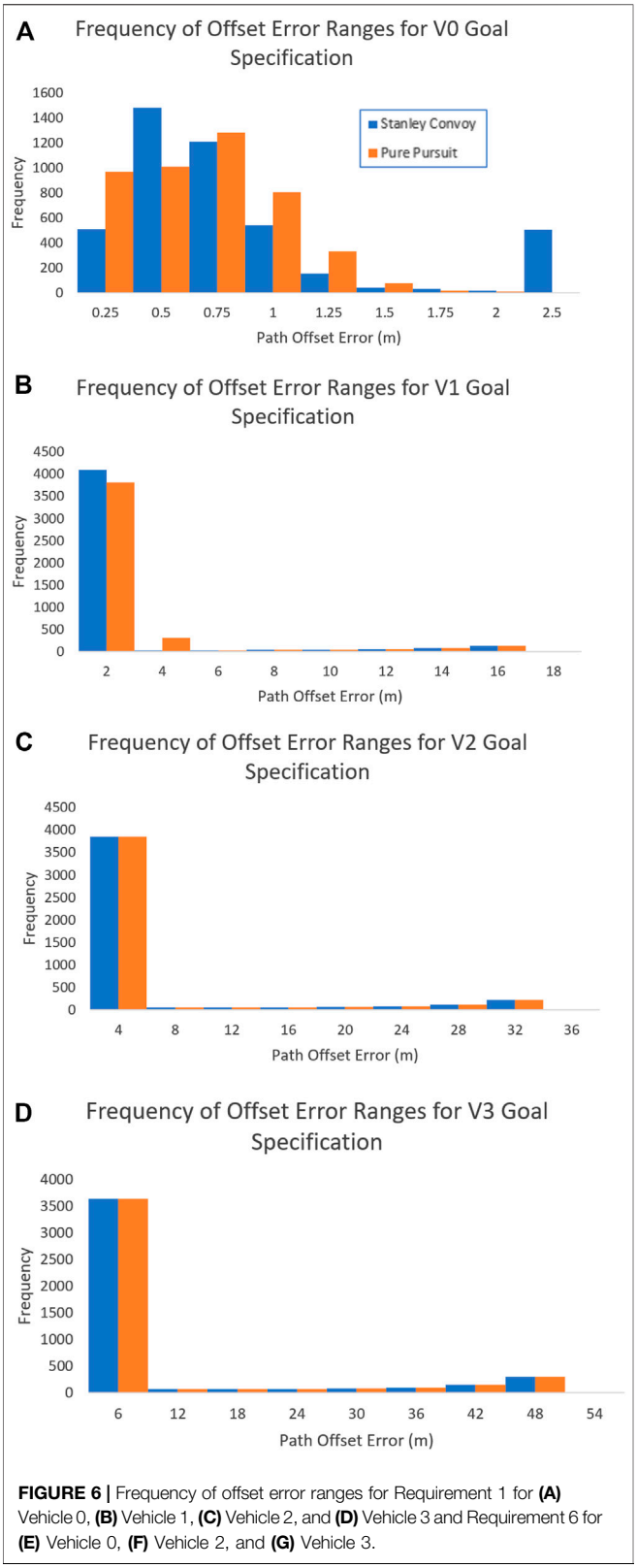

FIGURE 6 | Frequency of offset error ranges for Requirement 1 for **(A)** Vehicle 0, **(B)** Vehicle 1, **(C)** Vehicle 2, and **(D)** Vehicle 3 and Requirement 6 for **(E)** Vehicle 0, **(F)** Vehicle 2, and **(G)** Vehicle 3.

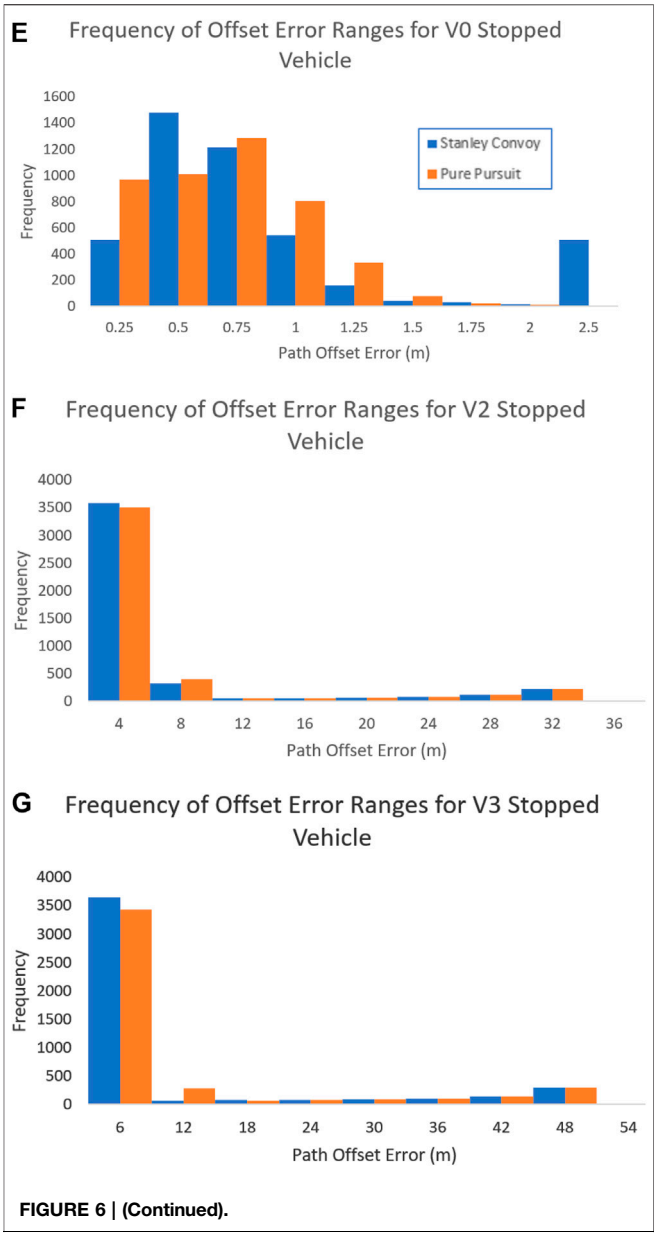

FIGURE 6 | (Continued).

techniques can be used to analyze the stability of the resulting closed-loop dynamics (see, e.g., the recent work by Kapsalis, et al. (2021)). The nonlinear feedback control law associated with Stanley controller, on the other hand, relies on the cross track error e_{f_a} from the center of the front axle to the nearest path point. The intuition behind Stanley control scheme is that the larger the cross-track error from the path, the further the steering of the wheels toward the path. Despite the demonstrated superiority of Stanley controller in the DARPA challenge, in extremely rare maneuvers, pure pursuit controllers demonstrate more robustness with respect to sudden lane changes. On the other hand, pure pursuit controllers have shown miserable failures under paths with fast varying curvatures (see, Snider (2009) for further details).

By studying such extremes of Stanley and pure pursuit control schemes in our simulations, we highlight the results that can be expected for low-level control of military autonomous convoys across the spectrum of trajectory-tracking control schemes. The

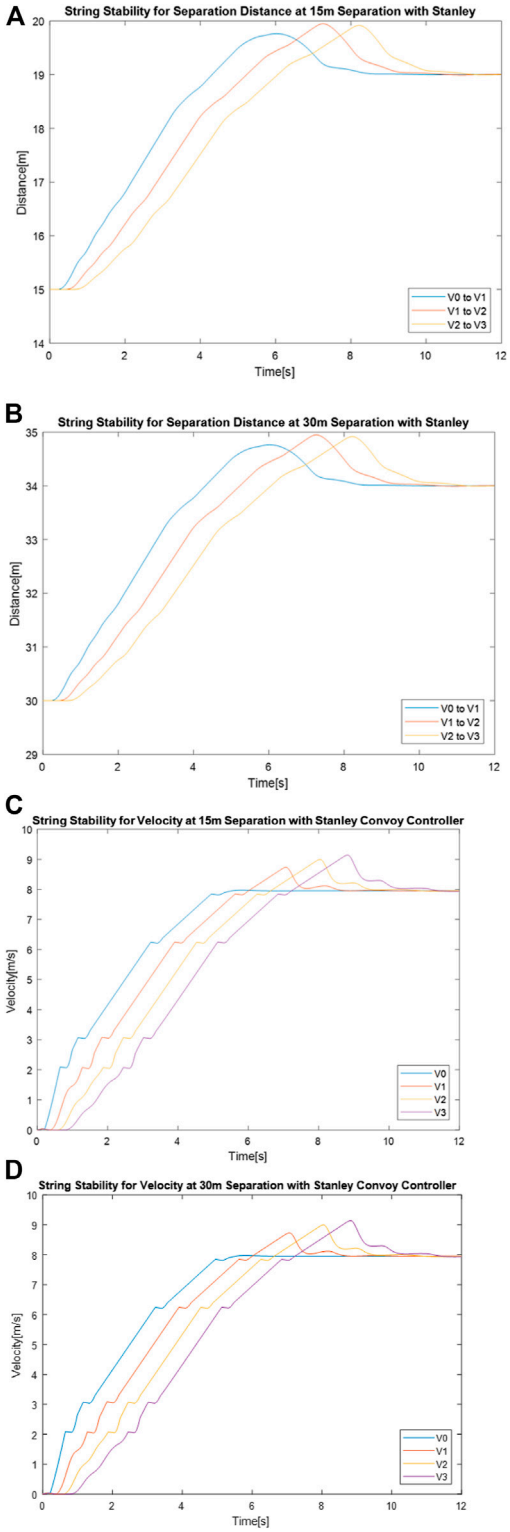

FIGURE 7 | Stanley convoy controller performance for separation distance between vehicles with a gap distance of **(A)** 15 m and **(B)** 30 m and velocity of vehicles over time with a gap distance of **(C)** 15 m and **(D)** 30 m.

network topology of the convoy is configured so that each vehicle only has information of its adjacent leader and follower. We compared the convoy controllers within the three categories defined by the framework: goal specification, spacing policy, and system parameters. In goal specification, we are concerned with the amount of deviation of autonomous convoy members from a given specified path. In spacing policy, we are concerned with maintaining a desired distance between the autonomous convoy members. Finally, in system parameters, we are concerned with the controller parameters that need to be tuned to achieve a given control objective. The results of the comparison are as follows.

Goal Specification

To compare performance in Goal Specification, a circular route was created. Per the framework detailed in this effort, vehicle offset from the desired path is the most appropriate metric to use for comparison between convoy controllers for the Goal Specification requirements. The two Goal Specification requirements that we will examine in this comparison are Requirement 1 and Requirement 6. The overall convoy vehicle positions for the two different convoy controllers applied to Requirement 1 are shown in **Figure 5A** and **Figure 5B**. Circular paths provide proper test cases where one is interested in studying the effectiveness of the proposed controllers in minimizing the deviation of each autonomous convoy member from the desired paths. The Spacing Policy studies, which are concerned with maintaining proper distances in-between the convoy members, are discussed in the next section (i.e., Section 6.2).

To compare path offset performance of the convoy controllers, we leveraged metrics used in positional tracking (Needham and Boyle, 2003) due to the similarities between vehicle path following and trajectory tracking in computer vision. The metrics and results for Goal Specification are shown in **Table 3**. In addition, **Figure 6A**, **Figure 6B**, **Figure 6C**, and **Figure 6D** demonstrate the frequency distribution of the path offset to show the spread of the error for Requirement 1.

As evident in **Table 3**, the lead convoy vehicle performed better in adhering to the desired path for the Pure Pursuit controller as opposed to the Stanley controller, with a lower mean offset error and standard deviation. However, the subsequent Stanley convoy followers had a lower mean offset error when compared to Pure Pursuit, with similar distributions of error, as shown in **Figures 6B–D**. This indicates that if the requirement of Goal Specification is the most important factor, the convoy overall performs better utilizing a Stanley convoy controller. While the lead vehicle performed better with Pure Pursuit compared to Stanley, we are comparing autonomous following performance in an AGC and not the performance of solely the lead vehicle.

To compare path offset performance of the convoy controllers for Requirement 6, we utilized the same path and convoy controllers but modified the experiment so that Vehicle 1

TABLE 4 | Gap range for different gap settings.

		15 m Gap setting			30 m Gap setting		
		V0 to V1	V1 to V2	V2 to V3	V0 to V1	V1 to V2	V2 to V3
Stanley	Min gap (m)	15.000	15.000	15.000	30.000	30.000	30.000
	Max gap (m)	19.762	19.947	19.917	34.762	34.947	34.917
	Range (m)	4.762	4.947	4.917	4.762	4.947	4.917
Pure Pursuit	Min gap (m)	15.000	15.000	14.999	30.000	30.000	30.000
	Max gap (m)	19.792	19.944	19.892	34.782	34.936	34.919
	Range (m)	4.792	4.944	4.892	4.782	4.936	4.919

TABLE 5 | Average velocity per vehicle using for different gap settings.

		Vehicle 0	Vehicle 1	Vehicle 2	Vehicle 3
Stanley	Average velocity for 15 m gap (m/s)	7.127	6.927	6.727	6.527
	Average velocity for 30 m gap (m/s)	7.127	6.927	6.727	6.527
	Difference (m/s)	0.000	0.000	0.000	0.000
Pure Pursuit	Average velocity for 15 m gap (m/s)	6.577	6.244	5.91	5.577
	Average velocity for 30 m gap (m/s)	6.577	6.244	5.91	5.577
	Difference (m/s)	0.000	0.000	0.000	0.000

stopped motion at 17.71 s into the run. At that time, Vehicle 2 modifies its leader to ignore Vehicle 1 and follow Vehicle 0 directly, while Vehicle 3 continues to follow Vehicle 2 per the initial setup. The overall convoy vehicle positions for the two different convoy controllers applied to Requirement 6 are shown in **Figure 5C** and **Figure 5D**. As with the initial Goal Specification experiment, we leveraged metrics used in positional tracking. The metrics and results for Stopped Vehicle are shown in **Table 3**. In addition, **Figure 6E**, **Figure 6F**, and **Figure 6G** show the frequency distribution of the path offset to show the spread of the error.

For the Stopped Vehicle experiment, the results of Vehicle 1 were omitted due to that vehicle leaving the convoy shortly after the experiment began. As evident in **Table 3**, the lead convoy vehicle once again performed better in adhering to the desired path for the Pure Pursuit controller as opposed to the Stanley controller, with a lower mean offset error and standard deviation. Likewise, the subsequent Stanley convoy followers performed better in terms of mean offset error when compared to Pure Pursuit, with similar distributions of error, as shown in **Figures 6F, G**. This indicates that if the requirement of Stopped Vehicle convoy recovery is the most important factor, the convoy overall performs better utilizing a Stanley convoy controller yet again.

Overall, the Goal Specification requirements favored the Stanley convoy controller in terms of performance based on the metrics discussed in this effort.

Spacing Policy

To compare performance in Spacing Policy, a straight-line path was created in ANVEL. As previously described, a convoy system's string stability is the most appropriate metric to use for comparison between convoy controllers for Spacing Policy requirements. The Spacing Policy requirement that we will examine in this comparison is Requirement 4. To compare performance of this requirement between the convoy controllers, two gap distances were used: 15 and 30 m. For both the Stanley convoy controller and the Pure Pursuit convoy controller, a test run with a 15 m gap distance was recorded, followed by a run with a 30 m gap distance, both with a convoy speed set at 8 m/s in both instances. Because the requirement is for adjustable gap distance, we will compare how performance changes between the 15 and 30 m for both controllers to determine which one better handled adjusting of distances. Although the spacing policy simulations are being done along a straight-line path for the sake of brevity, the convoy controllers are general enough to regulate the distancing between the autonomous convoy members in more complex situations such as roads on curvy hills. In particular, one can use the longitude and latitude of the autonomous convoy members and then compute their distance from the Haversine equation (Amer et al., 2018).

Figures 7A, B shows separation distance between vehicles over time for 15 and 30 m using the Stanley convoy controller, while **Figure 7C** and **Figure 7D** shows the vehicle velocity over time for those same convoy settings.

As seen in **Table 4**, the performance characteristics between 15 and 30 m for the Stanley controller did not change. While the minimum and maximum separation distance increased when the convoy gap distance was changed from 15 to 30 m, the overall range of the distances remained consistent. This indicates that adjusting the gap distance had no detrimental effect on performance regarding separation distance error. In addition, the changes in velocity between the 15 m gap setting and the 30 m gap setting were negligibly low, as shown by the difference

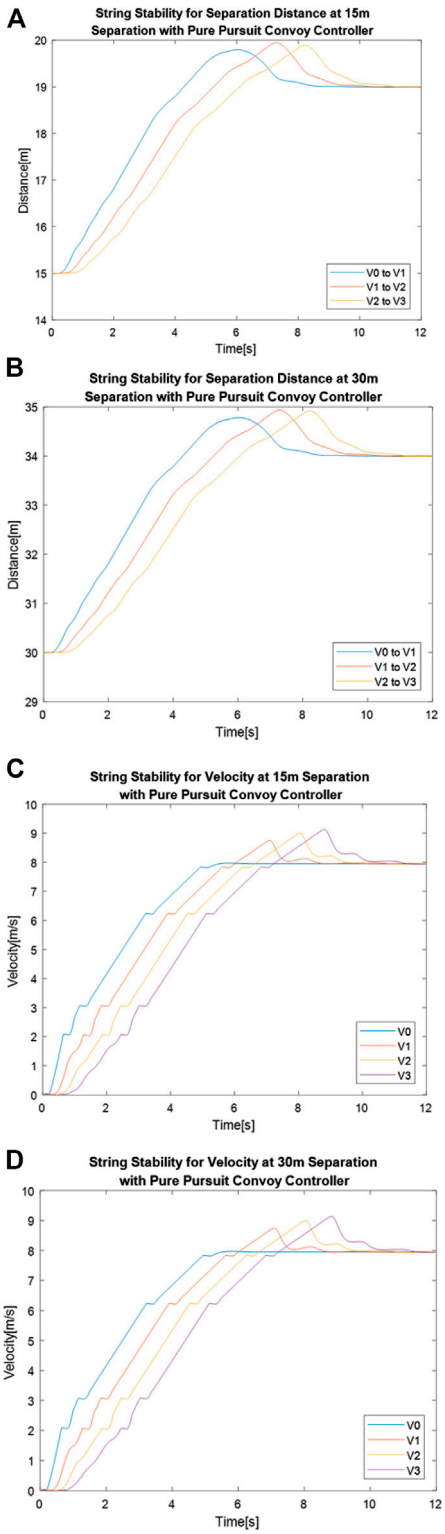

FIGURE 8 | Pure Pursuit convoy controller performance for separation distance between vehicles with a gap distance of **(A)** 15 m and **(B)** 30 m and velocity of vehicles over time with a gap distance of **(C)** 15 m and **(D)** 30 m.

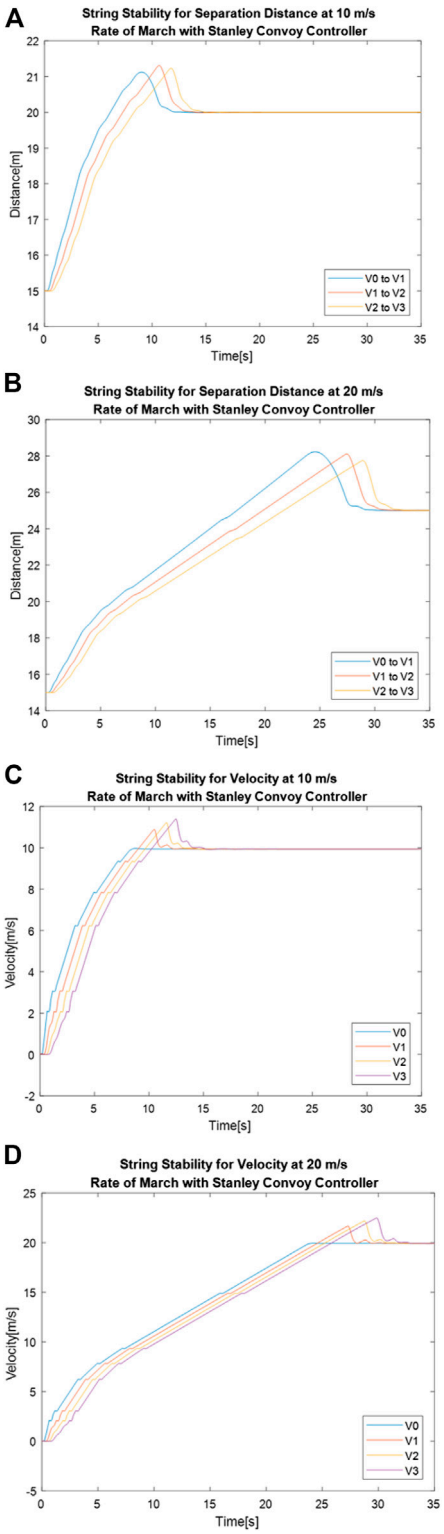

FIGURE 9 | Stanley convoy controller performance for separation distance between vehicles with a rate of march of **(A)** 10 m/s and **(B)** 20 m/s and velocity of vehicles over time with a gap distance of **(C)** 10 m/s and **(D)** 20 m/s.

TABLE 6 | Maximum gap distance for different Rate of March settings.

		10 m/s rate of March			20 m/s rate of March		
		V0 to V1	V1 to V2	V2 to V3	V0 to V1	V1 to V2	V2 to V2
Stanley	Maximum gap (m)	21.125	21.312	21.235	28.226	28.107	27.741
	% Change from previous gap distance	N/A	0.876%	–0.361%	N/A	–0.424%	–1.319%
Pure Pursuit	Maximum gap (m)	21.166	21.302	21.202	28.321	28.062	27.672
	% Change from previous gap distance	N/A	0.64%	–0.47%	N/A	–0.92%	–1.41%

TABLE 7 | Maximum vehicle velocities for different Rate of March settings.

			Vehicle 0	Vehicle 1	Vehicle 2	Vehicle 3
Stanley	10 m/s Rate of March	Maximum velocity (m/s)	9.968	10.887	11.212	11.390
		% Change from max velocity of preceding vehicle	N/A	8.441%	2.898%	1.562%
	20 m/s Rate of March	Maximum velocity (m/s)	19.968	21.680	22.194	22.494
		% Change from max velocity of preceding vehicle	N/A	7.896%	2.314%	1.337%
Pure Pursuit	10 m/s Rate of March	Maximum velocity (m/s)	9.968	10.908	11.218	11.382
		% Change from max velocity of preceding vehicle	N/A	8.62%	2.76%	1.45%
	20 m/s Rate of March	Maximum velocity (m/s)	19.968	21.709	22.198	22.488
		% Change from max velocity of preceding vehicle	N/A	8.02%	2.21%	1.29%

between the mean values in **Table 5**. Comparing the performance of the two systems with four significant figures shows no change in velocity for all vehicles, indicating no detrimental effect on velocity performance in regard to adjusting gap distance. Overall, adjusting gap distance showed little to no detrimental effect on convoy performance when using the Stanley convoy controller.

Figures 8A, B shows separation distance between vehicles over time for 15 and 30 m using the Pure Pursuit convoy controller, while **Figure 8C** and **Figure 8D** shows the vehicle velocity over time for those same convoy settings.

When using the Pure Pursuit convoy control, there were performance differences between the 15 and 30 m gap distance setting. Unlike in the Stanley convoy controller case, the overall range of the distances between vehicles changes between the two gap distance settings, as seen in **Table 4**. The range of separation distances between "V1 to V2" and "V2 to V3" increases by 0.35 m when the gap distance is increased from 15 to 30 m, indicating that an increase in gap distance affects how well the system can correct for the propagation of separation distance error. Despite the performance differences in separation distance, the changes in velocity between the 15 m gap setting and the 30 m gap setting were negligibly low, as shown by the difference between the mean values in **Table 5**. Comparing the performance of the two systems with four significant figures shows no change in velocity for all vehicles, indicating no detrimental effect on velocity performance in regard to adjusting gap distance. Overall, adjusting gap distance showed a slight detrimental effect on convoy performance for string stability of the separation distance when using the Pure Pursuit convoy controller.

When examining both Stanley and Pure Pursuit performance as a whole given spacing policy requirements, the Stanley convoy controller performs better when considering the metrics discussed in this effort.

System Parameters

To compare performance in System Parameters, the same straight-line path used in Spacing Policy was used for test runs. As previously described, a convoy system's string stability is the most appropriate metric to use for comparison between convoy controllers for System Parameter requirements. The System Parameter requirement that we will examine in this comparison is Requirement 3. To compare performance of this requirement between the convoy controllers, two velocities were used: 10 and 20 m/s. For both the Stanley convoy controller and Pure Pursuit convoy controller, an experiment was run with a desired convoy velocity of 10 m/s, followed by a run with a desired convoy velocity of 20 m/s. Both runs set the separation distance at 15 m. Because the requirement is for adjustable rate of march, we will compare how performance changes between 10 and 20 m/s for both controllers to determine which one better handled adjusting of rates of march.

Figures 9A, B shows separation distance between vehicles over time for 10 and 20 m/s rate of marches respectively, using the Stanley convoy controller, while **Figure 9C** and **Figure 9D** shows the vehicle velocity over time for those same convoy settings. The convoy achieves string stability when the rate of march is increased from 10 m/s, as seen in **Figure 9A**, to 20 m/s, as seen in **Figure 9B**, for the Stanley convoy controller. This can be seen by looking at the peaks of the separation distance measurements and noting that the error decreases throughout the convoy followers, as seen in **Figure 9B**, as opposed to increasing, as seen in **Figure 9A**. This is noted in **Table 6** by reviewing the percentage changes of maximum gap distances. As seen in **Figure 9C** and **Figure 9D**, the Stanley convoy controller fails to achieve string stability for velocity regardless of the rate of march. **Table 7** shows the maximum velocities member vehicles reached, along with the percentage difference between the maximum velocities between vehicles. While both rates of

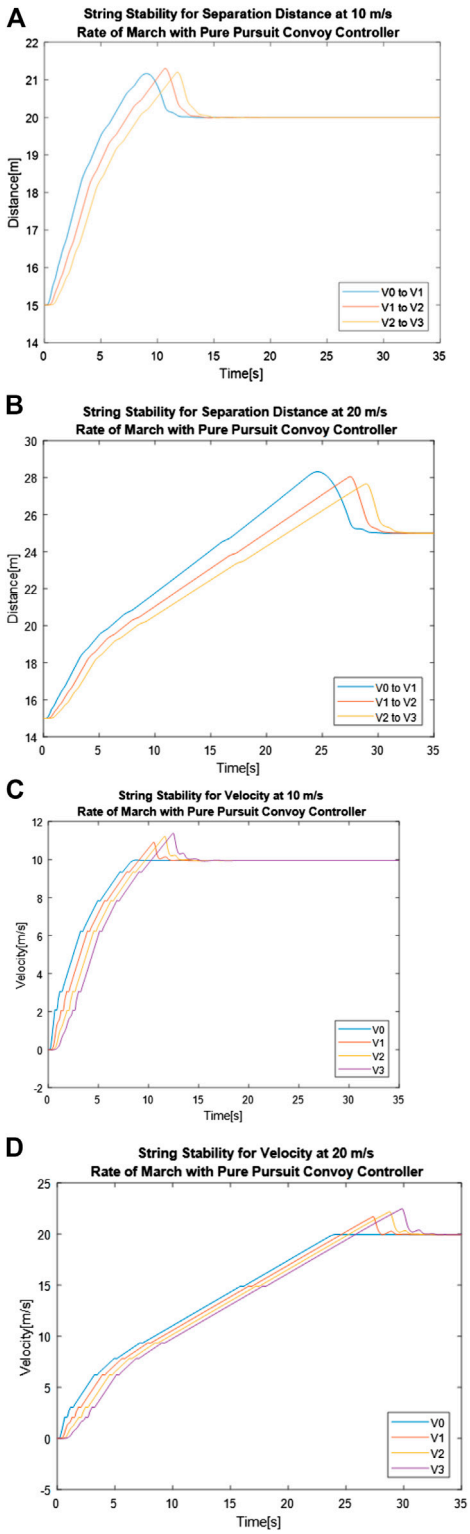

FIGURE 10 | Pure Pursuit convoy controller performance for separation distance between vehicles with a rate of march of **(A)** 10 m/s and **(B)** 20 m/s and velocity of vehicles over time with a gap distance of **(C)** 10 m/s and **(D)** 20 m/s.

march failed to achieve string stability for velocity, the percentage changes show that the 10 m/s Rate of March created greater error propagation down the line of the convoy.

Figures 10A, B shows separation distance between vehicles over time for 10 and 20 m/s rates of marches respectively using the Pure Pursuit convoy controller, while **Figure 10C** and **Figure 10D** shows the vehicle velocity over time for those same convoy settings. These results tracked closely to what was seen with the Stanley convoy controller. The convoy achieves string stability when the rate of march is increased from 10 to 20 m/s for the Pure Pursuit convoy controller, much like with the Stanley convoy controller. This can be seen once again by looking at the peaks of the separation distance measurements and noting that the error decreases throughout the convoy followers, as seen in **Figure 10A** and **Figure 10B**. This is noted in **Table 6** by reviewing the percentage changes of maximum gap distances. While the 10 m/s rate of march shows a positive and negative fluctuation of the separation distance, the 20 m/s rate of march only decreases, indicating that error does not propagate through. As seen in **Figure 10C** and **Figure 10D**, the Pure Pursuit convoy controller fails to achieve string stability for velocity regardless of the rate of march. **Table 7** shows the maximum velocities member vehicles reached, along with the percentage difference between the maximum velocities when comparing vehicles with their predecessor. While both rates of march failed to achieve string stability for velocity, the percentage changes show that the 10 m/s Rate of March created greater error propagation down the line of the convoy.

Overall, adjusting the rate of march affected the convoy controllers differently depending on the metric being analyzed. From the perspective of separation distance, changing the rate of march from 10 to 20 m/s reduced the propagation of error down the convoy in both Stanley and Pure Pursuit, but the reduction of error was greater for Pure Pursuit. This indicates that Pure Pursuit performs better in increasing the rate of march from the perspective of maintaining the desired separation difference. From the perspective of velocity, both the Stanley and Pure Pursuit convoy controller showed string instability, regardless of the rate of march. Neither controller showed a consistent reduction of instability between vehicles in adjusting the rate of march, indicating that in this application, separation distance should be the determining factor of performance. This means that for the System Parameters requirement analyzed here, the Pure Pursuit convoy controller should be used for optimal performance.

DISCUSSION

By reviewing and analyzing both Army doctrine and the field of AGC research, we were able to develop a framework for comparison of AGC performance as it relates to military convoy needs. With humanitarian military efforts relying on

convoys for supply delivery, medical practitioner transportation, and medical evacuation, it is important to understand what autonomous convoy technology best serves the needs of healthcare resource delivery. Requirements 1, 2, and 6 directly relate to Goal Specification objectives of autonomous convoy control framework. Furthermore, Requirements 4 and 5 are related to Spacing Policy objective of the autonomous convoy control framework. As it can be seen from the simulation results presented, Stanley Controller demonstrates a more robust performance in fulfilling the Spacing Policy requirement over a range of gap distances. Finally, Requirements 3 and 7 are related to System Parameters. As it is demonstrated in simulation, the Pure Pursuit Controller had a better performance in fulfilling the Spacing Policy requirement.

Even with the framework however, comparative performance is highly dependent on the requirement needs to be prioritized. No sole factor singularly defines the quality of a convoy, and considerations such as terrain, hostile forces, and size of the convoy elements may change what can be considered the best choice for an AGC solution working toward military requirements. The purpose of the framework is to provide a way to compare different AGC efforts, but the user must have a strong understanding of the baseline mission needs to make a meaningful comparison. For a healthcare delivery perspective, a convoy commander will have to make the same considerations, with added logistical complexity of the placement of medical vehicles within the convoy. The intended outcome of this effort is to better understand how AGC technologies perform relative to one another given the needs of healthcare delivery in a medical context, in order to have metrics to improve upon between the research and development of new systems.

CONCLUSION

In this effort, we performed a review of Army doctrine to derive requirements for convoy performance toward delivery of healthcare resources. After discussing a hierarchical decision-making, we argued for using nonlinear battlefield techniques for delivering healthcare logistics to remote pandemic outbreak areas. Through examining publicly available doctrine, we identified seven key requirements to be met when in developing AGCs for a military context. By doing a survey of AGC efforts, we found that metrics related to spacing policy and string stability were commonly used and could be leveraged as the basis for a framework of performance comparison between different AGC systems. With that framework in hand, we showed a sample application, comparing the performance of a Stanley convoy controller and a Pure Pursuit convoy controller. By creating this framework, we look to enable future AGC development efforts to properly baseline and compare performance between existing systems, to find optimal solutions for delivery of healthcare resources using AGCs.

AUTHOR CONTRIBUTIONS

CC and SB developed the initial concept. SR and AM provided direction and guidance to refine the effort. CC performed the research and authored the article, with revisions from SR and AM.

REFERENCES

Ali, A., Garcia, G., and Martinet, P. (2015). The Flatbed Platoon Towing Model for Safe and Dense Platooning on Highways. *IEEE Intell. Transport. Syst. Mag.* 7, 58–68. doi:10.1109/mits.2014.2328670

ALSA (2021). Air Land See Application Center. Retrieved from: https://www.alsa.mil/mttps/tco/(Accessed August 1, 2020).

Amer, N. H., Hudha, K., Zamzuri, H., Aparow, V. R., Abidin, A. F. Z., Kadir, Z. A., et al. (2018). Adaptive Modified Stanley Controller with Fuzzy Supervisory System for Trajectory Tracking of an Autonomous Armoured Vehicle. *Robotics Autonomous Syst.* 105, 94–111. doi:10.1016/j.robot.2018.03.006

Amidi, O., and Thorpe, C. E. (1991). *Integrated Mobile Robot Control*. Pittsburgh, Pennsylvania: Mobile Robots V.

APD (2021). Army Publishing Directorate. Retrieved from: https://armypubs.army.mil/(Accessed March 16, 2020).

Browand, F., McArthur, J., and Radovich, C. (2004). *Fuel Saving Achieved in the Field Test.* Los Angeles, CA: California Partners for Advanced Transit and Highways.

Brooks, T. N. (2012). *Sustainment Battalion Convoy Protection Platform Gunnery*. Fort Lee, Virginia: Army Sustainment, 33–37.

Buehler, M., Iagnemma, K., and Singh, S. (2007). *The 2005 DARPA Grand Challenge: The Great Robot Race*. Springer.

Center for Army Lessons Learned (2010). *Convoy Operations in Afghanistan Handbook*. Fort Leavenworth, KS: U. S. Army Combined Arms Center.

Centers for Disease Control and Prevention (2020). *How to Protect Yourself and Others*. Atlanta, GA: CDC. Retrieved from: https://www.cdc.gov/coronavirus/2019-ncov/prevent-getting-sick/prevention.html.

Dadras, S. (2017). *Path Tracking Using Fractional Order Extremum Seeking Controller for Autonomous Ground Vehicle. No. 2017-01-0094.* Warrendale, Pennsylvania: SAE Technical Paper.

David, W., Baldassi, F., and Pio, S. E. (2020). "Combining Epidemiologal and Constructive Simulations for Robotics and Autonomous Systems Supporting Logistic Supply in Infectious Diseases Affected Areas," in *Modelling and Simulation for Autonomous Systems: 7th International Conference* (Prage, Czech Republic: Spinger Nature), 86.

Davis, J., Animashaun, A., Schoenherr, E., and McDowell, K. (2008). Evaluation of Semi-autonomous Convoy Driving. *J. Field Robotics* 25, 880–897. doi:10.1002/rob.20263

Di Lallo, A., Murphy, R., Krieger, A., Zhu, J., Taylor, R. H., and Su, H. (2021). Medical Robots for Infectious Diseases: Lessons and Challenges from the COVID-19 Pandemic. *IEEE Robot. Automat. Mag.* 28 (1), 18–27. doi:10.1109/mra.2020.3045671

Dixit, S., Montanaro, U., Dianati, M., Mouzakitis, A., and Fallah, S. (2020). *Integral MRAC with Bounded Switching Gain for Vehicle Lateral Tracking*. IEEE Transactions on Control Systems Technology, 1–16. doi:10.1109/tcst.2020.3024586

Eben Li, S., Zheng, Y., Wu, Y., Hedrick, J., Gao, F., Li, K., et al. (2019). *Dynamical Modeling and Distributed Control of Connected and Automated Vehicles: Challenges and Opportunities*. IEEE Intelligent Transportation Systems Magazine, 46–58.

European Truck Platooning (2021). European Truck Platooning Challenge - EU Truck Platoon Challenge. Retrieved from: https://eutruckplatooning.com/default.aspx.

Feng, S., Zhang, Y., Li, S. E., Cao, Z., Liu, H. X., and Li, L. (2019). String Stability for Vehicular Platoon Control: Definitions and Analysis Methods. *Annu. Rev. Control.* 47, 81–97. doi:10.1016/j.arcontrol.2019.03.001

Francis, S. (2019). Robotics & Automation News. Retrieved from: https://roboticsandautomationnews.com/2019/10/02/scania-unveils-new-driverless-concept-truck/26036/.

Frembling, J. B. (2012). *Training and Certification for Convoy Escort Teams*. Fort Lee, Virginia: Army Sustainment, 41–43.

Goi, H. K., Giesbrecht, J. L., Barfoot, T. D., and Francis, B. A. (2010). Vision-based Autonomous Convoying with Constant Time Delay. *J. Field Robotics* 27, 430–449. doi:10.1002/rob.20344

Gomez, E., Poropatich, R., Karinch, M. A., and Zajtchuk, J. (1996). Tertiary Telemedicine Support during Global Military Humanitarian Missions. *Telemed. J.* 2, 201–210. doi:10.1089/tmj.1.1996.2.201

Gong, S., Shen, J., and Du, L. (2016). Constrained Optimization and Distributed Computation Based Car Following Control of a Connected and Autonomous Vehicle Platoon. *Transportation Res. B: Methodological* 94, 314–334. doi:10.1016/j.trb.2016.09.016

Green, D. A. (2011). *The Future of Autonomous Ground Logistics: Convoys in the Department of Defense*. Fort Leavenworth, KS: United States Army Command and General Staff College School of Advanced Military Studies.

Guo, G., and Yue, W. (2012). Autonomous Platoon Control Allowing Range-Limited Sensors. *IEEE Trans. Veh. Technol.* 61, 2901–2912. doi:10.1109/tvt.2012.2203362

Harrell, M. C., Werber, L., Schirmer, P., Hallmark, B. W., Kavanagh, J., Gershwin, D., et al. (2007). *Assessing the Assignment Policy for Army Women*. Santa Monica, CA: RAND Corporation.

Headquarters United States Army Reserve Command (1997). *Surface Transportation Convoy Commander's Guide*. McPherson, Georgia, USA: DEPARTMENT OF THE ARMY.

Jia, D., Lu, K., Wang, J., Zhang, X., and Shen, X. (2016). A Survey on Platoon-Based Vehicular Cyber-Physical Systems. *IEEE Commun. Surv. Tutorials* 18 (1), 263–284. doi:10.1109/comst.2015.2410831

Kapsalis, D., Sename, O., Milanes, V., and Molina, J. J. M. (2021). "Design and Experimental Validation of an LPV Pure Pursuit Automatic Steering Controller," in *16th IFAC Symposium on Control in Transportation Systems*.

Killblane, R. E. (2005). *Circle the Wagons: The History of US Army Convoy Security*. Fort Leavenworth, KS: Combat Studies Institute Press.

Killblane, R. E. (2013). *Convoy Ambush Case Studies Volume I - Korea and Vietnam*. Fort Lee, VA: US Army Transportation School.

Killblane, R. E. (2015). *Convoy Ambush Case Studies Volume II - Iraq and Afghanistan*. Fort Lee, VA: US Army Transportation School.

King, I. (2017). *Peloton Technology Raises Cash for Automated Truck Convoy Technology*. New York, NY: Bloomberg.

Klančar, G., Matko, D., and Blažič, S. (2011). *A Control Strategy for Platoons of Differential Drive Wheeled Mobile Robot*. Amsterdam, Netherlands: Robotics and Autonomous Systems, 57–64.

Klančar, G., Matko, D., and Blažič, S. (2009). *Wheeled Mobile Robots Control in a Linear Platoon*. Berlin, Germany: Journal of Intelligent and Robotic Systems, 709–731.

Krumboltz, M. (2013). It Costs $2.1 Million Per Year for Each Soldier Deployed in Afghanistan: Report. Retrieved from: https://www.yahoo.com/news/it-costs–2-1-million-per-year-for-each-soldier-deployed-in-afghanistan–report-133150602.html (Accessed March 2, 2020).

Layer, B. R. (1993). *Some Principles of Convoy Operations in Operations Other than War*. Fort Leavenworth, KS: School of Advanced Military Studies United Staets Army Command and General Staff College.

Li, Y., and He, C. (2018). "Connected Autonomous Vehicle Platoon Control Considering Vehicle Dynamic Information," in *2018 37th Chinese Control Conference (CCC)* (Wuhan: IEEE), 7834–7839. doi:10.23919/chicc.2018.8483514

Liu, K., Ayers, P., Howard, H., and Anderson, A. (2009). Influence of Turning Radius on Wheeled Military Vehicle Induced Rut Formation. *J. Terramechanics* 46 (2), 49–55. doi:10.1016/j.jterra.2009.02.004

Liu, Y., Gao, H., Xu, B., Liu, G., and Cheng, H. (2014). Autonomous Coordinated Control of a Platoon of Vehicles with Multiple Disturbances. *IET Control. Theor. Appl.* 8, 2325–2335. doi:10.1049/iet-cta.2014.0172

Lu, D., Li, Z., and Huang, D. (2017). "Platooning as a Service of Autonomous Vehicles," in *2017 IEEE 18th International Symposium on A World of Wireless, Mobile and Multimedia Networks (WoWMoM)* (Maccau: IEEE), 1–6. doi:10.1109/wowmom.2017.7974353

Lu, S., Zhang, M. Y., Ersal, T., and Yang, X. J. (2018). "Effects of a Delay Compensation Aid on Teleoperation of Unmanned Ground Vehicles," in *Companion of the 2018 ACM/IEEE International Conference on Human-Robot Interaction* (ACM/IEEE), 179–180.

Maneuver, Aviation and Soldier Division Army Capabilities Integration Center (2017). *The U.S. Army Robotic and Autonomous Systems Strategy*. Fort Eustis, VA: U.S. Army Training and Doctrine Command.

MPRI Kuwait Observer Controller Team. (2003). *Convoy Leader Training Handbook*. Kuwait: DohaMPRI KOCT.

Nardini, G., Virdis, A., Campolo, C., Molinaro, A., and Stea, G. (2018). Cellular-V2X Communications for Platooning: Design and Evaluation. *Sensors* 18 (5), 1527–1549. doi:10.3390/s18051527

Nasirian, B., Mehrandezh, M., and Janabi-Sharifi, F. (2021). Efficient Coverage Path Planning for Mobile Disinfecting Robots Using Graph-Based Representation of Environment. *Front. Robotics AI* 8, 4. doi:10.3389/frobt.2021.624333

Needham, C. J., and Boyle, R. D. (2003). "Performance Evaluation Metrics and Statistics for Positional Tracker Evaluation," in *International Conference on Computer Vision Systems* (Graz: Springer), 278–289. doi:10.1007/3-540-36592-3_27

North Atlantic Treaty Organization Standardization Office (2019). *AAP-06*. Brussels, Belgium: North Atlantic Treaty Organization Standarization Office.

Office of the Under Secretary of Defense for Acquisition and Sustainment (2012). *Department of Defense Instruction 5230.24 Distribution Statements on Technical Documents*. Washington, DC: Department of Defense.

Öncü, S. (2013). *String Stability of Interconnected Vehicles: Network-Aware Modelling, Analysis and Experiments*. Eindhoven: Technische Universiteit Eindhoven.

Pawar, A., and Pan, Y. J. (2016). "Leader-following Consensus Control of Multi-Agent Systems with Communication Delays & Random Packet Loss," in *2016 American Control Conference (ACC)* (IEEE), 4464–4469.

Quantum Signal (2018). ANVEL (Autonomous Navigation Virtual Environment Laboratory) from Quantum Signal LLC. Retrieved from: https://www.youtube.com/watch?v=nd1P4KpBmTk.

Rödönyi, G., Gáspár, P., Bokor, J., and Palkovics, L. (2014). Experimental Verification of Robustness in a Semi-autonomous Heavy Vehicle Platoon. *Control. Eng. Pract.* 28, 13–25. doi:10.1016/j.conengprac.2014.02.014

Rutner, S. M., Aviles, M., and Cox, S. (2012). Logistics Evolution: a Comparison of Military and Commercial Logistics Thought. *Int. Jrnl Logistics Manag.* 23, 96–118. doi:10.1108/09574091211226948

Seet, M., Harvy, J., Bose, R., Dragomir, A., Bezerianos, A., and Thakor, N. (2020). *Differential Impact of Autonomous Vehicle Malfunctions on Human Trust*. IEEE Transactions on Intelligent Transportation Systems, 1–10. doi:10.1109/tits.2020.3013278

Snider, J. M. (2009). *Automatic Steering Methods for Autonomous Automobile Path Tracking*. Pittsburgh, PA, Tech: Robotics Institute.

Swaroop, D., Hedrick, J. K., Chien, C. C., and Ioannou, P. (1994). A Comparision of Spacing and Headway Control Laws for Automatically Controlled Vehicles1. *Vehicle Syst. Dyn.* 23, 597–625. doi:10.1080/00423119408969077

Taghavifar, H., and Rakheja, S. (2019). A Novel Terramechanics-Based Path-Tracking Control of Terrain-Based Wheeled Robot Vehicle with Matched-Mismatched Uncertainties. *IEEE Trans. Vehicular Tech.* 69 (1), 67–77.

Taheri, S., Sandu, C., Taheri, S., Pinto, E., and Gorsich, D. (2015). A Technical Survey on Terramechanics Models for Tire-Terrain Interaction Used in Modeling and Simulation of Wheeled Vehicles. *J. Terramechanics* 57, 1–22. doi:10.1016/j.jterra.2014.08.003

Thrun, S., Montemerlo, M., Dahlkamp, H., Stavens, D., Aron, A., Diebel, J., et al. (2006). Stanley: The Robot that Won the DARPA Grand Challenge. *J. Field Robotics* 23, 661–692. doi:10.1002/rob.20147

United States Army Combined Arms Support Command (2013). *ATP 4-11 Army Motor Transport Operations*. Fort Lee, VA: Department of the Army.

U.S. Army Training and Doctrine Command (2019). *ADP 1-01 Doctrine Primer*. Fort Belvoir, VA: Department of the Army.

U.S. Army Training and Doctrine Command (2013). *STP 55-88m14-SM-TG Soldier's Manual and Training Guide*. Arlington County, VA: United States Department of the Army.

U.S. Army Training and Doctrine Command (2016). *TC 21-305-20/AFMAN 24-306(I) Manual for the Wheeled Vehicle Operator*. Arlington County, VA: United States Department of the Army.

U.S. Army Training and Doctrine Command (2018). *The U.S. Army in Multi-Domain Operations 2028*. Fort Eustis, VA: U.S. Army Training and Doctrine Command.

Uysal, M., Ghassemlooy, Z., Bekkali, A., Kadri, A., and Menouar, H. (2015). Visible Light Communication for Vehicular Networking: Performance Study of a V2V System Using a Measured Headlamp Beam Pattern Model. *IEEE Veh. Technol. Mag.* 10 (4), 45–53. doi:10.1109/mvt.2015.2481561

Vincent, J. (2016). Self-driving Truck Convoy Completes its First Major Journey across Europe - the Verge. Retrieved from: https://www.theverge.com/2016/4/7/11383392/self-driving-truck-platooning-europe (Accessed January 1, 2019).

Waibel, M. (2011). *SARTRE: Autonomous Car Platoons*. IEEE Spectrum. Retrieved from: https://spectrum.ieee.org/automaton/robotics/industrial-robots/sartre-autonomous-car-platoons (Accessed January 1, 2019).

Wolfson, S., and Wright, N. (1995). *A UNHCR Handbook for the Military on Humanitarian Operations*. Suisse: Office of the United Nations High Commissioner for Refugees.

Zhao, X., Yao, W., Li, N., and Wang, Y. (2017). "Design of Leader's Path Following System for Multi-Vehicle Autonomous Convoy," in *2017 IEEE International Conference on Unmanned Systems (ICUS)* (Beijing: IEEE), 132–138. doi:10.1109/icus.2017.8278329

Author Disclaimer: Distribution Statement A. Approved for Public Release: Distribution Unlimited. The views expressed in this article are those of authors and not necessarily those of the U.S. Air Force Academy, the U.S. Air Force, the Department of Defense, or the U.S. Government. PA#: USAFA-DF-2020-352.

Conflict of Interest: The authors declare that the research was conducted in the absence of any commercial or financial relationships that could be construed as a potential conflict of interest.

Publisher's Note: All claims expressed in this article are solely those of the authors and do not necessarily represent those of their affiliated organizations, or those of the publisher, the editors and the reviewers. Any product that may be evaluated in this article, or claim that may be made by its manufacturer, is not guaranteed or endorsed by the publisher.

Advantages of publishing in Frontiers

OPEN ACCESS
Articles are free to read for greatest visibility and readership

FAST PUBLICATION
Around 90 days from submission to decision

HIGH QUALITY PEER-REVIEW
Rigorous, collaborative, and constructive peer-review

TRANSPARENT PEER-REVIEW
Editors and reviewers acknowledged by name on published articles

Frontiers
Avenue du Tribunal-Fédéral 34
1005 Lausanne | Switzerland

Visit us: www.frontiersin.org
Contact us: frontiersin.org/about/contact

REPRODUCIBILITY OF RESEARCH
Support open data and methods to enhance research reproducibility

DIGITAL PUBLISHING
Articles designed for optimal readership across devices

FOLLOW US
@frontiersin

IMPACT METRICS
Advanced article metrics track visibility across digital media

EXTENSIVE PROMOTION
Marketing and promotion of impactful research

LOOP RESEARCH NETWORK
Our network increases your article's readership